Superbubbles and the origin of Cosmic Rays

Thibault Vieu

Université de Paris

Ecole doctorale 560

Sciences de la Terre et de l'Environnement et Physique de l'Univers

Laboratoire AstroParticule et Cosmologie

Superbubbles and the origin of Cosmic Rays

Par **Thibault Vieu**

Thèse de doctorat de Physique de l'Univers

Dirigée par **Stefano Gabici** et **Vincent Tatischeff**

Présentée et soutenue publiquement le 30 septembre 2021

Devant un jury composé de :

Etienne Parizot Professeur, Université de Paris	Président
Andrei Bykov Professeur, Institut Ioffe, Saint-Pétersbourg	Rapporteur
Alexandre Marcowith Directeur de recherche, LUPM, Montpellier	Rapporteur
Fiorenza Donato Professeur, Université de Turin	Examinatrice
Stefano Gabici Chargé de recherche, APC, Paris	Directeur de thèse
Vincent Tatischeff Directeur de recherche, IJCLab, Orsay	Codirecteur de thèse

Title: Superbubbles and the origin of cosmic rays

Abstract:

It has been known for more than a century that the interstellar medium is full of charged particles called cosmic rays. These particles are crucial agents in the galactic ecosystem. Not only do they influence the properties of space plasmas and magnetic fields, they also impact the gas dynamics, drive the evolution of molecular clouds and regulate the formation of the stars. Yet, there is still no definite answer to the question of their sources. Given the gigantic energies that some of these particles carry when they impact the Earth atmosphere, they are much likely produced in the most energetic astrophysical systems of the galaxy such as massive stars eventually exploding as supernovae. During the last decades, the supernova remnant shocks have indeed been proved to efficiently accelerate particles up to high energies. Although appealing from a global energetic point of view, this scenario of cosmic ray production is nowadays challenged by a number of arguments, including the difficulty to account for the cosmic rays of very high energies as well as the peculiarities of the cosmic ray spectrum measured near Earth. On the other hand, most of the massive stars which end their lives as supernovae are believed to be born within clusters formed inside dense molecular clouds. During their lives, the clustered stars collectively carve galactic-scale cavities, called superbubbles, in their parent environment. The stellar winds and subsequent supernova explosions deposit a large amount of mechanical, thermal and turbulent energy within these superbubbles, which makes them appealing candidates as cosmic ray sources. However, the acceleration of particles in these environments has been scarcely considered. This thesis therefore aims at reviewing the relevant fundamental mechanisms of acceleration in superbubbles in order to provide an investigation by means of semi-analytical modelling derived from first principles. Collective effects such as shock collisions and successive events of particle reacceleration are discussed. A self-consistent model accounting for the nonlinear feedback of the particles on the environment is described. The hydromagnetic turbulence, the multiple supernovae and the stellar winds are found to be efficient sources of cosmic rays. The spectrum of the accelerated particles is not only influenced by the collective effects and the propagation in the bubble interior, but also by the magnetised supershell which surrounds the bubble and the intermittency of the mechanical power delivered by the stars. The overall contribution of galactic star clusters and superbubbles to the cosmic ray spectrum is eventually discussed, as well as recent gamma-ray observations.

Keywords: Cosmic rays; Interstellar medium; Superbubbles; Supernova remnants; Massive stars; Turbulence; Particle acceleration.

Titre : Les superbulles et l'origine des rayons cosmiques

Résumé :

Il a été découvert il y a plus d'un siècle que le milieu interstellaire est rempli de particules chargées appelées rayons cosmiques. Ces particules sont des composantes de premier-plan dans l'écosystème galactique. Non seulement elles influencent les propriétés des plasmas et des champs magnétiques, mais elles impactent également la dynamique des gaz, régissent l'évolution des nuages moléculaires et régulent la formation des étoiles. Cependant, la question de leurs sources reste sans réponse définitive. Les énergies gigantesques que certaines de ces particules atteignent lorsqu'elles impactent l'atmosphère terrestre suggèrent qu'elles doivent être produites dans les systèmes astrophysiques les plus puissants de la galaxie, comme les étoiles massives qui finissent par exploser en supernovae. Au cours des dernières décennies, il a été démontré que les vestiges de supernovae accélèrent en effet des particules. Bien que séduisant d'un point de vue énergétique, ce scénario de production de rayons cosmiques est aujourd'hui ébranlé par un certain nombre d'arguments, incluant la difficulté de rendre compte des rayons cosmiques de très hautes énergies ainsi que des particularités du spectre mesuré sur Terre. D'un autre côté, la plupart des étoiles massives qui explosent en supernovae à la fin de leur vie sont supposées naître au sein d'amas formés à l'intérieur de nuages moléculaires denses. Durant leur vie, les étoiles creusent autour des amas des cavités qui atteignent des dimensions galactiques et que l'on appelle des superbulles. Les vents stellaires et les explosions de supernovae déposent une grande quantité d'énergie mécanique, thermique et turbulente à l'intérieur de ces cavités, ce qui en font des candidates de choix comme sources du rayonnement cosmique. Pourtant, l'accélération des particules dans ces environnements a été rarement considérée. Cette thèse a donc pour but de récapituler les mécanismes d'accélérations fondamentaux supposés agir à l'intérieur des superbulles, afin de produire des modèles semi-analytiques dérivés d'équations fondamentales. Des effets collectifs comme les collisions entre ondes de choc et les réaccélérations successives des particules confinées sont discutés. Un modèle auto-consistant, prenant en compte la réponse non-linéaire des particules sur leur environnement, est décrit. Il est montré que la turbulence hydromagnétique, les multiples supernovae et les vents stellaires produisent efficacement des rayons cosmiques. Le spectre des particules accélérées est non seulement influencé par les effets collectifs et la propagation dans l'intérieur de la bulle, mais aussi par la coquille magnétisée qui délimite la bulle et le caractère intermittent de la puissance mécanique délivrée par les étoiles. La contribution globale des amas stellaires et des superbulles galactiques au spectre des rayons cosmiques est finalement discutée, ainsi que des observations récentes en rayons gamma.

Mots Clefs : Rayons cosmiques ; Milieu interstellaire ; Superbulles ; Vestiges de supernovae ; Etoiles massives ; Turbulence ; Accélération de particules.

Remerciements

C'est loin d'être par pure forme que je remercie mes deux directeurs de thèse, Stefano et Vincent. Issu d'une formation en physique théorique, je ne connaissais rien du domaine des astroparticules à l'aube de ce doctorat. Stefano et Vincent m'ont tout appris, des mécanismes fondamentaux d'accélération des particules cosmiques aux subtilités de leur composition. J'ai eu cette chance d'être encadré par un duo complémentaire, toujours encourageant et bienveillant, qui m'a laissé une grande liberté. Grazie, Stefano, pour m'avoir appris à estimer des temps caractéristiques avant d'écrire des équations. Merci, Vincent, pour avoir éveillé mon intérêt quant aux aspects plus observationnels. Last but not least, I can't thank both of you enough for carefully reviewing the manuscript.

Merci papa merci maman, comme le veut la coutume mais surtout, en ces circonstances particulières, pour le rôle majeur que vous avez joué dans le bon déroulement de mon doctorat, en m'offrant un cadre de travail idéal loin des folies de ces temps tourmentés. Nous avons réussi à trouver un équilibre pour que chacun continue à travailler sereinement, en particulier grâce au dévouement de maman, que l'on ne souligne pas assez. Merci au reste de la famille, que je n'ai pas eu l'occasion de beaucoup voir ces derniers temps mais que je n'oublie pas.

Merci Anne-Stylite pour m'avoir aidé à garder un contrepied littéraire durant ces trois années. Je devrais être bientôt de nouveau dispo, sur les terres tourmentées de Skandyar, dans les méandres célestiniens, dans des lieux et des temps qui restent à décrire.

Merci Charlotte pour ton soutien, au terme de ce bout de chemin commun. Je suis désolé de n'avoir pu t'offrir ce dont tu avais besoin. Puisses-tu trouver la voie.

Merci à mes amis et collègues de l'APC, Minh, Baptiste, Pierre, Makarim etc. pour les bons moments et les discussions fructueuses, en particulier lors des "PhD seminars", autant d'ouvertures sur d'autres domaines de la physique et au-delà. Un grand merci à Lioni-Moana et Sruthi qui ont contribué en m'aidant, dans les dernières semaines, à tracer les données du spectre primaire et à calculer les spectres gamma. Une pensée aussi aux amis croisés à l'occasion d'écoles d'été, en particulier Adrien et Lucía.

Merci enfin à Alexandre et Etienne, membres de mon comité de suivi annuel, pour leurs suggestions éclairées, et à Andrei Bykov et Fiorenza Donato pour avoir accepté de faire partie du jury.

À Clément,

pour que tu te sentes obligé de lire ces 200 pages.
Merci pour ton soutien, nos discussions sans fin.
Je te souhaite le meilleur pour ta troisième année,
et à très vite pour de nouvelles aventures !

Cheers to all, including who I forgot.
Paris, le 16 juillet 2021.

Note

Qui ne comprend pas l'anglais pourra lire le résumé général en français à la fin du manuscrit.

Qui n'a pas de formation scientifique pourra lire l'introduction, que j'espère pédagogique, ou simplement jeter un œil aux images du premier chapitre. De là naît la fascination.

Contents

Abstract i

Résumé ii

Remerciements iii

Introduction: Cosmic Rays 1
A cosmic ray journey . . . 3
The high energy universe . . . 7
Modern stakes . . . 9
The supernova paradigm . . . 11
Superbubbles as sources of cosmic rays . . . 13
Goals and outline of the thesis . . . 14
References . . . 14

1 Superbubbles: formation and evolution 19
1.1 Stellar clusters . . . 19
1.1.1 Cluster formation . . . 19
1.1.2 Cluster properties . . . 20
1.1.3 Massive stars . . . 22
1.1.4 Supernova remnants . . . 23
1.2 Bubble structure and evolution . . . 29
1.2.1 Hydrodynamic theory of wind-driven bubbles . . . 29
1.2.2 Supernova-driven superbubbles . . . 34
1.2.3 Radiative cooling . . . 35
1.2.4 Shell instabilities . . . 36
1.2.5 Magnetised medium . . . 38
1.2.6 Recent numerical simulations . . . 39
1.2.7 The fate of the bubble . . . 40
1.3 Turbulence generation . . . 41
1.4 Observations of superbubbles . . . 43
1.4.1 Circumstellar bubbles . . . 43
1.4.2 Interstellar bubbles . . . 47
1.4.3 Galactic superbubbles . . . 48
1.4.4 Superbubbles in the Large Magellanic Cloud . . . 51
1.5 Energy crisis . . . 54
1.6 Summary . . . 58
References . . . 60

2 Cosmic rays in turbulence **71**
2.1 Interstellar turbulence . . . 71
2.1.1 Magnetohydrodynamic waves . . . 71
2.1.2 Turbulence spectrum . . . 72
2.1.3 Turbulence dynamics . . . 73
2.2 Particle scattering on turbulence . . . 75
2.2.1 Wave-particle interaction . . . 75
2.2.2 The quasi-linear approximation . . . 76
2.2.3 Pitch-angle scattering and momentum diffusion . . . 76
2.2.4 The diffusion approximation . . . 78
2.2.5 Perpendicular diffusion . . . 80
2.2.6 Calculation of the diffusion coefficients . . . 82
2.2.7 Beyond the quasi-linear approximation . . . 84
2.3 Stochastic particle reacceleration . . . 85
2.4 The particle feedback on the waves . . . 86
2.4.1 Non-thermal wave damping . . . 88
2.4.2 Streaming instability . . . 89
2.5 Summary . . . 90
References . . . 90

3 Particle acceleration at shock fronts **95**
3.1 Interstellar shocks . . . 95
3.2 Thermal leakage injection . . . 97
3.3 Energy gain . . . 99
3.4 Particle spectrum . . . 100
3.5 Maximum energy . . . 101
3.6 Diffusive shock acceleration from first principles . . . 102
3.6.1 Transport equation in the presence of large-scale motions . . . 102
3.6.2 Infinite plane parallel stationary shock . . . 104
3.6.3 Generalisations . . . 105
3.7 Nonlinear diffusive shock acceleration . . . 106
3.7.1 Wave and fluid equations . . . 106
3.7.2 Kinetic equation . . . 107
3.7.3 Method of solution . . . 108
3.7.4 Numerical solution . . . 109
3.7.5 Non-resonant field amplification . . . 111
3.8 Summary . . . 112
References . . . 113

4 Particle acceleration at colliding shocks **117**
4.1 Motivation . . . 117
4.2 Physical setup . . . 118
4.2.1 Model . . . 118
4.2.2 Timescales . . . 120
4.3 Numerical solution . . . 121
4.3.1 Methods . . . 121
4.3.2 Results . . . 122
4.4 Analytic approach . . . 125
4.4.1 The self-similarity hypothesis . . . 125

4.4.2 Time-dependent shock velocity . . . 127
4.4.3 The self-similar transport equation . . . 128
4.4.4 Maximum energy . . . 130
4.4.5 Time integrated spectrum of cosmic rays accelerated at converging shocks . . . 131
4.5 Spectrum of cosmic rays reaccelerated by converging supernovae shocks . . . 132
4.6 Colliding winds . . . 135
4.7 Summary . . . 136
References . . . 136

5 Particle acceleration by multiple shocks 139
5.1 Particle acceleration in supersonic turbulence . . . 139
5.1.1 High momenta . . . 140
5.1.2 Low momenta . . . 140
5.1.3 Supersonic turbulence in superbubbles . . . 142
5.2 Successive shocks . . . 143
5.3 A nonlinear model of shock reacceleration . . . 145
5.3.1 Kinetic equation . . . 146
5.3.2 Fluid equations . . . 147
5.3.3 Method of solution . . . 147
5.3.4 Adiabatic decompression and escape flux . . . 148
5.4 Reacceleration of seed particles . . . 149
5.5 Particle acceleration by successive nonlinear shocks . . . 151
5.5.1 Identical shocks . . . 151
5.5.2 Heating . . . 153
5.5.3 Towards cosmic ray production in superbubbles . . . 154
5.6 Summary . . . 156
References . . . 157

6 Cosmic ray production in superbubbles 159
6.0 Notations . . . 159
6.1 Superbubble properties . . . 159
6.1.1 Bubble structure . . . 159
6.1.2 Turbulence generation . . . 162
6.2 Particle acceleration and transport in superbubbles . . . 164
6.2.1 Particle acceleration at stellar wind termination shocks . . . 164
6.2.2 Particle reacceleration at supernova remnant shocks . . . 165
6.2.3 Stochastic acceleration . . . 168
6.2.4 Spatial diffusion and escape . . . 169
6.3 Results . . . 171
6.3.1 Timescales . . . 171
6.3.2 Cosmic ray energetics in superbubbles . . . 171
6.3.3 Intermittency . . . 173
6.3.4 Spectra . . . 175
6.4 Two-zone model . . . 177
6.4.1 Diffusion in a two-zone model . . . 177
6.4.2 Cosmic ray reacceleration in compact clusters . . . 179
6.4.3 Modelling the supershell . . . 181
6.5 Superbubble contribution to galactic cosmic rays . . . 182

6.6 Gamma-ray spectra . . . 184
6.7 Summary . . . 185
References . . . 186

Conclusions and perspectives **191**
General summary . . . 191
Perspectives . . . 192
References . . . 195

Résumé substantiel **197**
Résumé chapitre par chapitre . . . 197
Bilan général . . . 200

Introduction: Cosmic Rays

Norway, XIIIth century

As to that matter which you have often inquired about, what those lights can be which the Greenlanders call the northern lights, I have no clear knowledge. I have often met men who have spent a long time in Greenland, but they do not seem to know definitely what those lights are. However, it is true of that subject as of many others of which we have no sure knowledge, that thoughtful men will form opinions and conjectures about it and will make such guesses as seem reasonable and likely to be true. [...]

The men who have thought about and discussed these lights have guessed at three sources, one of which, it seems, ought to be the true one. Some hold that fire circles about the ocean and all the bodies of water that stream about on the outer sides of the globe; and since Greenland lies on the outermost edge of the earth to the north, they think it possible that these lights shine forth from the fires that encircle the outer ocean. Others have suggested that during the hours of night, when the sun's course is beneath the earth, an occasional gleam of its light may shoot up into the sky; for they insist that Greenland lies so far out on the earth's edge that the curved surface which shuts out the sunlight must be less prominent there. But there are still others who believe (and it seems to me not unlikely) that the frost and the glaciers have become so powerful there that they are able to radiate forth these flames. I know nothing further that has been conjectured on this subject, only these three theories that I have presented; as to their correctness I do not decide, though the last mentioned looks quite plausible to me.

The King's Mirror, around 1250 A.D.[1] (translation Larson, 1917)

Do northern lights originate from the ices and fires of Earth or from the sky? Are they flames radiated by the Nordic glaciers or remnants of the Sun's light? The observation by the Nordic folks of this outstanding manifestation of charged particles ejected from a star and arriving on Earth contains the embryo of what modern times will call *Astroparticle Physics*.

Austria[2], 1912

The field will however only rise in the early XXth century, a few years after the discovery of radioactivity. At that time, scientists were measuring radiations using electroscopes.

[1] *The King's Mirror* is a remarkable work reviewing the geography, climate, politics, moral, justice and philosophy of the Nordic folks in the middle-age. I encourage the interested reader to have a look, in particular at the first part describing the Nordic lands and climate as well as several natural phenomena such as the course of the sun, the winds, the volcanoes etc., all described in a scientific prosaic style.

[2] Now Czech Republic.

Surprisingly, these would discharge even in the absence of any close radioactive source, suggesting the presence of a background of charged particles on Earth. A crucial question was raised: does this "natural radioactivity" originate from the ground, or from space? It is to answer this very question that an air balloon takes off on August 7th 1912, at 6:12 am from Aussig. On board, a young scientist named Victor Hess is excited, on the dawn of his seventh scientific flight. The sky is clear, apart from some vapourish clouds on the western horizon. Attached to the basket, three electroscopes are measuring the level of radiation of the atmosphere, which is carefully read by Hess every hour as the balloon rises. The landscape appears as a quiet green land crossed by the sinuous Elbe which looks like a blue snake. The balloon is heading north over Peterswalde, Struppen, Bischofswerda, Cottbus. Now the cumulus are distinguishable on the horizon, while the Sun light diffuses onto high altitude vapours. It is now 10h45 above 5000 m. Hess has read the instruments, and even though one electroscope was unintentionally discharged during the manipulation, the two others show exciting results. Over the 4000 m of ascent, the number of discharges increased by a factor of about two. The frequency will then consistently decrease as the balloon goes down over the green lands of the German countryside until the landing at Pieskow in the end of the morning.

This was the seventh and last balloon flight which Hess performed from April to August 1912. He will then come to the following conclusion:

> *The results of the present observations seem most likely to be explained by the assumption that radiation of very high penetrating power enters from above into our atmosphere, and even in its lowest layers causes part of the ionization observed in closed vessels.*
>
> Hess 1912 (translation Hess, 2018)

At the time of Hess' experiments, it was thought that the observed radiation was of electromagnetic origin, i.e., *rays* of light. Even though it was later demonstrated that it mainly originates from charged particles interacting with the atmosphere, the discovery of its cosmic origin gave birth to what is still (mis)called the field of *Cosmic Ray Physics*.

It should be mentioned that the conclusion made by Hess did not only result from its own flights, but is rather the achievement of a decade of experiments and debates, starting from Wilson's measurements in tunnels, followed by many other measurements in various places from salt mines to over the ocean, the pioneering though not conclusive experiment by Wulf on top of the Eiffel Tower, and then the breakthrough by Pacini who found that the radioactivity was significantly reduced under the surface of the sea, followed by the first balloon flight by Gockel up to 4000 m, and the confirmation of Hess's results by Kolhörster in 1914 in several flights up to 9000 m. Even after World War I, the origin and nature of the radiation were still strongly debated. In 1928, Clay discovered the dependency of the cosmic ray flux on latitude, which was confirmed a few years later by Compton's survey. The correlation with the geomagnetic field shed a new light on the nature of cosmic rays. If they are deflected by a magnetic field, they cannot be photons, but rather charged particles such as protons and electrons. At about the same time, Rossi discovered the air-showers of particles induced by incident energetic particles colliding with the atmosphere, a phenomenon which will be extensively studied by Pierre Auger in the late 1930's.

Argentina, 2020

Let us now imagine ourselves transported into the Andes, on the west of Argentina. In front of us lies a great arid plateau, coloured with red and ochre shades. A few thorny bushes are disseminated here and there, and at the horizon rise snow capped mountains. It is the beginning of the afternoon, at the end of the austral summer. The weather is hot. Squinting the eyes, we can see little shiny domes of human size. They are aligned in a curious perspective. The space separating them is so large that we can barely count five of them before our eyes encounter the horizon.

Behind us stands a no-frill building. Could we guess the excitement of the astronomer who sits inside it? On his computer screen, a ramified cascade of coloured rays develops dynamically. Something happened above the sierra. A proton hit the upper layers of the atmosphere, interacted with the nitrogen, has been disintegrated in multiple secondary particles, which in turn decayed in a shower cascading down like an invisible rain on the desert. Several of the little domes have detected them. Just before vanishing in the pure water contained in the tanks, the particles have emitted a bluish flash, their swan song listened by very sensitive photomultipliers and sent to the observatory.

Even though charged particles from the cosmos disintegrate permanently in the atmosphere, the Auger observatory has been designed to probe the highest incident energies. This event which made the astronomer's day, was induced by a *single* microscopic particle containing more kinetic energy than a marble of one gram launched at 10 km/h. An energy thousand times larger than what could be achieved in the most sophisticated human-made particle accelerators. Despite the inconceivable area of 3000 km^2 covered by the network of 1600 water tanks, there is barely one such event detected per month in the Auger observatory.

From air balloon experiments to Auger measurements, many installations disseminated all over the world and in space nowadays detect particles of all kinds, from the low energy solar electrons and protons producing the auroras which have fascinated the Nordic folks for ages to galactic relativistic nuclei producing the cosmic radiation discovered at the time of Victor Hess and eventually extragalactic nuclei which create the extended air showers observed by detector arrays.

From the ancient times to the modern days, the questions have evolved, though not fundamentally changed. What is the nature of these particles? Which phenomena do they induce in the atmosphere? Where do they come from? What happened to them during their cosmic journey for they have accumulated such energy?

A cosmic ray journey

The story begins in some place of the galaxy or beyond, where a charged particle encounters an electric field. This may happen in a great variety of astrophysical environments, including (but not limited to) supersonic winds of massive stars or pulsars, plasma jets, magnetic turbulence, expanding shocks. Local[3] changes in the electromagnetic fields accelerate charged particles by means of the Lorentz force, for a particle of elementary charge experiencing one volt gains a kinetic energy of one *electronvolt* (eV), which is equal to

[3]It is important to keep in mind that *global* electric fields can be changed into magnetic fields by means of a Lorentz transform and therefore cannot accelerate charged particles. This is a major difficulty in the quest of fundamental acceleration mechanisms. The only ways to alleviate this issue is to either consider non-static or non-uniform fields.

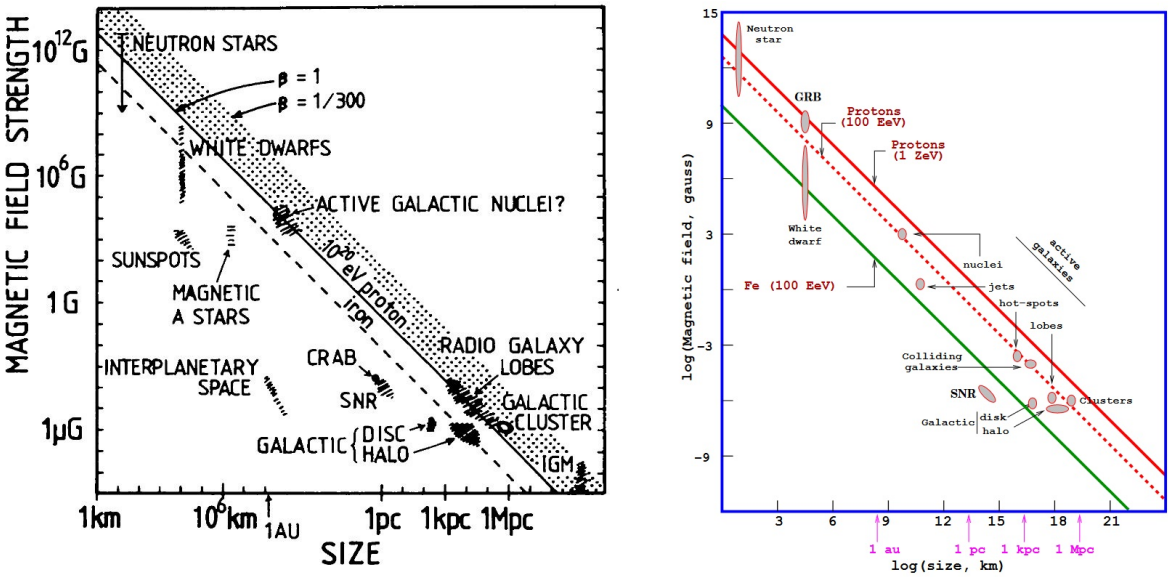

Figure 0.1: Hillas diagrams. Left: original figure adopted from Hillas (1984). Right: more recent version by Murat Boratav (2000).

about 1.6×10^{-19} J. Repeated interactions may push the particles to very high kinetic energies until they leave the system, either because they are transported too far away from the accelerator, or because they have gained so much energy that they don't interact with the accelerator anymore. The latter happens typically when the mean free path of the particles, that is their Larmor radius p/qB, where p and q are respectively the momentum and charge of the particle and B is the background magnetic field, becomes of the order of the size of the system. A simple upper limit on the maximum energy of a relativistic particle of charge Zq attainable in a source of size L and magnetic field B can therefore be derived as:

$$E_{max} < 0.9 \text{ PeV} \frac{ZB}{\mu\text{G}} \frac{L}{\text{pc}} . \tag{0.1}$$

Once a particle reaches such energy, it is not confined anymore within the accelerator and escapes without being accelerated further. This is the so-called Hillas criterion (Hillas, 1984). Although being generally the less stringent upper bound one could derive, it is a very powerful universal argument providing an absolute limitation for any kind of candidate accelerator. According to this criterion, astrophysical objects can be classified in a diagram as function of their magnetic field and size. Figure 0.1 provides two examples of these so-called Hillas diagrams. We see that protons can be accelerated by galactic sources at most up to about 1 EeV ($= 10^{18}$ eV≈ 0.16 J!). Galactic accelerators include large weakly magnetised objects such as supernova remnants or star clusters, as well as highly magnetised compact objects such as neutron stars. As for the extragalactic candidates, they include active galaxies, black holes, gamma-ray bursts... In the following we will however restrict ourselves to the study of galactic sources.

Once they have escaped their galactic accelerators, particles join the bulk of galactic cosmic rays whose energy density is estimated around 1 eV/cm^3. These particles are mostly protons (89%) but there are also about 10% of Helium nuclei, about 1% of electrons and around 1% of heavier nuclei. The abundances of nuclei relative to the composition of the local interstellar medium are displayed in Figure 0.2. Two comments are in order. First, nuclei with even charge number are generally more abundant than those with odd

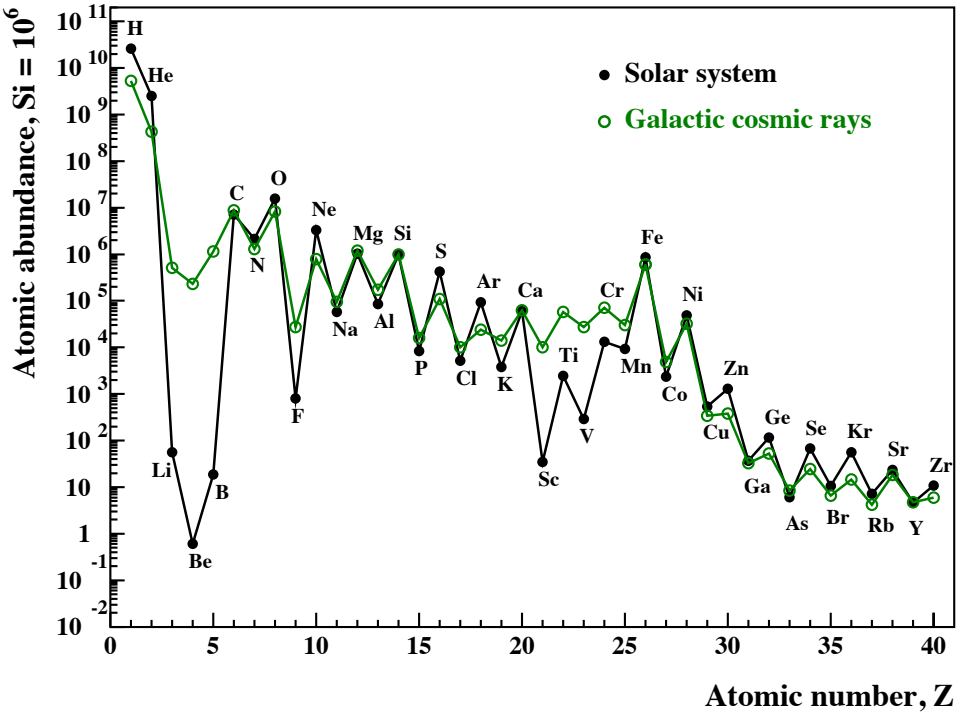

Figure 0.2: Composition of galactic cosmic rays compared to the solar composition. Adopted from Tatischeff and Gabici (2018).

charge number. This is a consequence of the former being more stable than the latter, which decay more frequently, and of the stellar nuclear reaction channels which combine helium nuclei rather than hydrogen to produce heavier nuclei. Second, we notice an excess of the light elements lithium, beryllium, boron and the sub-iron elements scandium, titanium, vanadium, chromium, manganese in the galactic cosmic rays over the local abundances. This is because these elements are created from primary nuclei interacting with the interstellar gas during their galactic journey. This process during which a heavy nuclei hit by an incident particle loses several nucleons to produce a secondary lighter nucleus is called *spallation*. The relative abundance of secondary to primary particles gives crucial clues about the transport of cosmic rays in the galactic disk. Indeed, the production rate of secondaries is proportional to the density of primaries. On the other hand, all particles diffusing in the galactic disk are expected to escape in the galactic halo after a typical residence time, such that an equilibrium should be established with the following ratio of secondaries to primaries:

$$n_s/n_p = n_{ISM}\sigma_s\tau_{res}c\,. \tag{0.2}$$

Experiments performed on Earth provide measurements of the spallation cross-sections σ_s. Then the residence time τ_{res} can be infered from the secondary to primary ratios (e.g. boron to carbon) and is currently estimated around a few Myr for particles of 1 GeV (Gabici et al., 2019).

On the other hand, one would naively estimate the residence time of relativistic cosmic rays to be about H/c, where $H \sim 1$ kpc is the height of the galactic disk and c the speed of light. As this represents only a few kyr, it implies that the transport of cosmic rays in the galaxy is by no means ballistic, but rather diffusive. Cosmic rays being charged particles, they are deflected by the large scale galactic magnetic fields as well as the small-scale magnetic turbulence. Assuming a purely diffusive regime, the diffusion coefficient

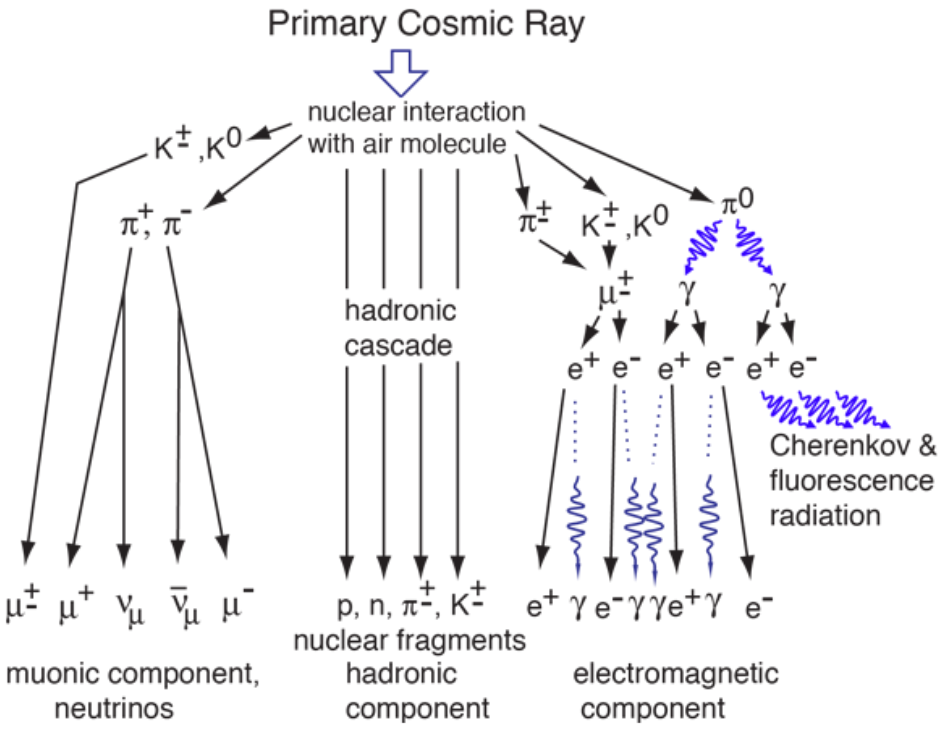

Figure 0.3: Air shower produced by an incident energetic particle. From http://hyperphysics.phy-astr.gsu.edu/hbase/Astro/cosmic.html.

is estimated around 10^{28} cm^2/s although one should keep in mind that the above picture is oversimplified, for we neglected inelastic collisions, we assumed homogeneity of the interstellar gas, turbulence, and cosmic ray propagation. The transport of cosmic rays in the galaxy is still poorly understood. For instance, recent models suggest that most of the residence time could be spent near the sources (e.g. D'Angelo et al., 2018). The origin of the magnetic turbulence on which cosmic rays scatter is yet unknown as well. It could be excited by the feedback of massive stars and supernova explosions, but also by the charged particles themselves via streaming instabilities (e.g. Blasi et al., 2012).

Nevertheless, it is expected that cosmic rays trapped in galactic magnetic fields repeatedly scatter on turbulence, changing direction again and again, until they eventually interact with matter and decay, or escape in the intergalactic space. Secondary to primary ratios also provide constraints on the average grammage $\Lambda = \rho_{ISM}\tau_{res}c$ accumulated by the cosmic rays during their journey. Values around 10 g/cm^2 are inferred for GeV particles, which represents several times the mean surface density of the galaxy. This means that the distribution of cosmic rays is isotropised and that any information about their original sources is lost. The distribution of cosmic rays arriving on Earth is indeed very close to isotropy, despite small variations at a level around 0.1% for GeV particles but increasing to about 10% for EeV particles, a matter which is still actively debated (e.g. Giacinti and Kirk, 2017).

At the end of their journey, cosmic rays may eventually reach the Earth and be detected. Space-based observatories such as the AMS detector on board of the International Space Station or air-balloon experiments such as the ATIC probe flying over Antarctica are able to directly detect the primary cosmic rays below the TeV bands. On the other hand, cosmic rays of very high and ultra-high energies do not reach the Earth frequently

enough to be detected by small detectors with significant statistics. Indirect ground-based techniques have been developed to probe higher energy bands. When a very energetic charged particle penetrates the atmosphere, it can interact with a nitrogen atom and decay into multiple secondary hadrons, leptons and photons, which is referred to as an air shower, as depicted in Figure 0.3.

The Cherenkov and fluorescence radiation produced in the atmosphere can be detected by Cherenkov telescopes while the particles at the end of the shower eventually reach the ground where they can be detected by arrays of detectors. This is for instance the working principle of the Tibet, Kascade or Auger observatories. Eventually, all the data obtained by a variety of techniques and installations all over the world can be combined in a single *cosmic ray spectrum*, which shows the flux of particles per energy band. This is displayed in Figure 0.4. One should take a moment to realise that each point on this plot is the result of decades of work done by international collaborations gathering thousands of researchers, engineers and technicians, the outcome of a century of technological improvement and cosmic ray dedication.

The high energy universe

Since cosmic rays are deflected in the galactic magnetic fields, it is in principle impossible to relate the direction of an incident particle to a specific source, which is one of the main difficulty of Cosmic Rays Physics. The diffuse cosmic ray flux measured near Earth is the primary source of information on these charged particles. On the other hand, cosmic rays are tightly linked with two other astrophysical messengers: photons and neutrinos. Indeed, while part of the charged particles may freely escape from the accelerators as mentioned above, a substantial fraction is expected to interact via various processes which will result in the production of photons and neutrinos near the source. Such interactions include for instance Coulomb and ionisation processes, production of pions, synchrotron interactions, the bremsstrahlung effect or the inverse Compton scattering.

Already in the 1930's astronomers started to look at the sky with radio antennas listening to the echoes of the Milky Way. A number of sources were detected from stars to radio galaxies. Astrophysical radio emissions are closely related to cosmic rays since radio waves are mainly produced by low-energy electrons deflected in magnetic fields. This motivated the early theoretical works on particle acceleration, such as Fermi's genuine intuition in 1949 that repeated interactions with magnetised inhomogeneities could accelerate particles to high energies.

In the second half of the XXth century, great progress have been made in the field of X-ray and γ-ray astronomy with the development of more and more sophisticated observatories. Nowadays, space-based observatories such as Chandra, XMM-Newton or NuStar probe the X-ray sky, while the Fermi-LAT telescope is looking at gamma-ray emissions. Ground-based Atmospheric Cherenkov Telescopes (ACTs) such as HESS in Namibia, Magic in the Canary Islands or Veritas in the United States have been developed to detect the Cherenkov signature of very high energy gamma-rays interacting in the atmosphere. In the last decades, arrays of detectors such as HAWC in Mexico or the very recent LHAASO observatory in China have been installed to probe the gamma-ray sky above TeV bands, by detecting the electromagnetic air-showers. It is nowadays a great time for Astrophysics as we are able to observe the sky in all wavelengths from radio bands to gamma-rays, as shown in Figure 0.5.

Besides the intrinsic advantage of multi-wavelengths observations to probe the physics

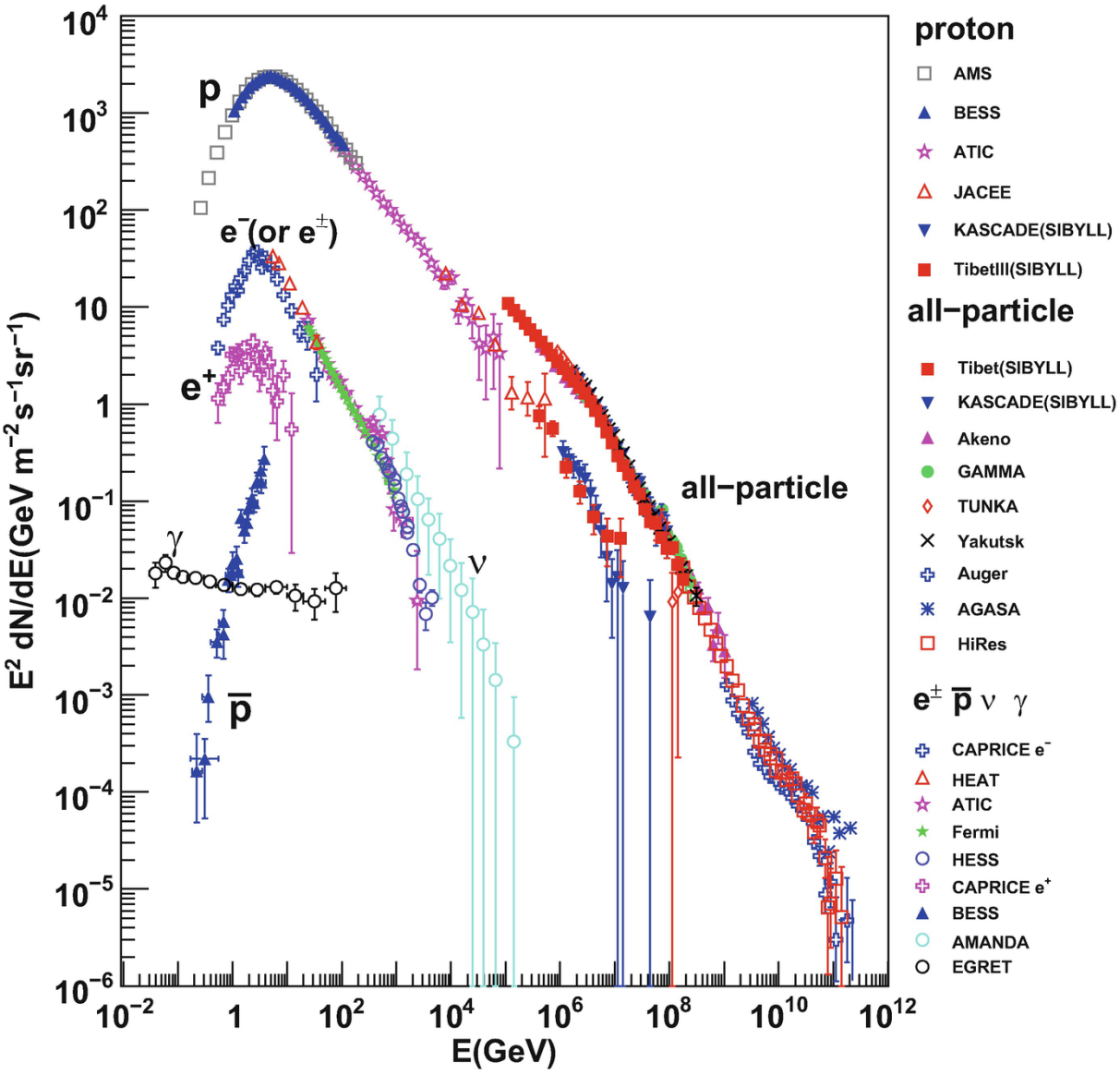

Figure 0.4: Cosmic ray spectrum as detected by various collaborations. Adopted from Morlino, 2017.

of a celestial object, high energy photons are tracers of accelerated cosmic rays. With the help of the aforementioned observatories, X and gamma-ray emissions of specific galactic objects or extended regions can be detected in correlation with nearby particle acceleration. Figure 0.6 shows the Crab nebula as example of a cosmic object observed in six energy bands. The electrons deflected by the ambient magnetic fields and scattered by photons produce a diffuse emission in all wavelengths from radio to gammas. The optical and infrared observations further show the filamentary structure of the nebula which are produced in the course of the expansion of a *supernova remnant shock*. The X-ray image provide an outstanding view of the inner ring surrounding the central *pulsar* as well as the perpendicular jets. The gamma-ray view likely originates from the synchrotron radiation of energetic electrons trapped in strong magnetic fields, an evidence of in-site particle acceleration.

With the recent construction of the IceCube observatory in Antarctica, the neutrino counterparts of specific sources have started to be detected as well and more is expected

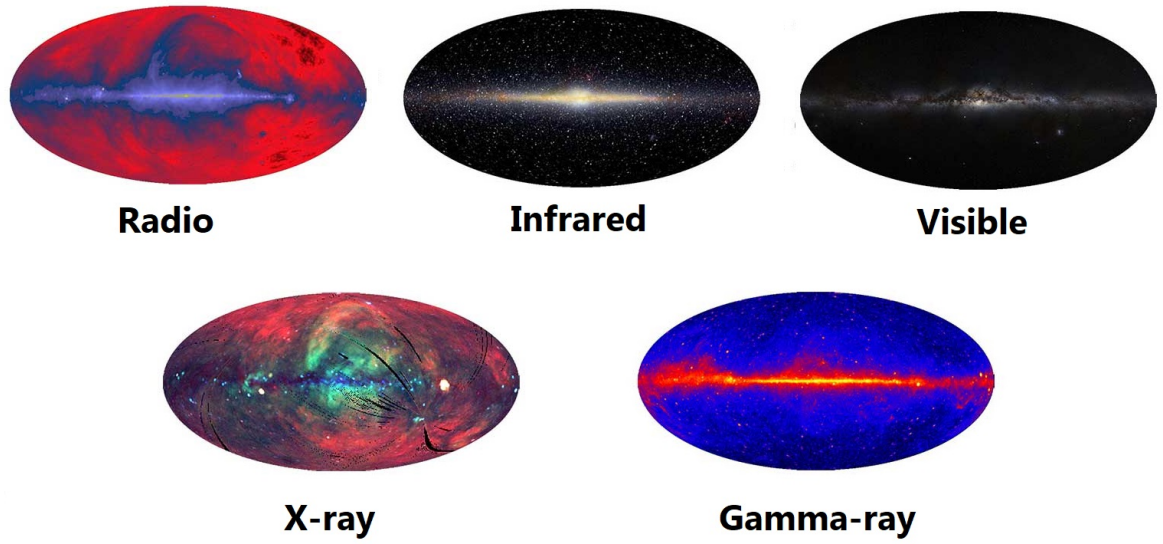

Figure 0.5: The sky observed in different energy bands. Radio emission is mainly produced by electrons moving in magnetic fields. The infrared emission traces the interstellar dust and gas. Stars are seen in visible light. X-rays trace very hot gas and non-thermal phenomena, for instance around supernova remnants or pulsars. Gamma-rays probe the most energetic regions of the universe, from compact clusters of massive stars to accreting black holes. The diffuse gamma-ray emission is due to the cosmic ray interactions with the interstellar matter.
Credits: Haslam et al. 1982 (radio), NASA (IR), ESO/S. Brunier (optical), MPE and S. L. Snowden (X-ray), NASA/DOE/Fermi-LAT Collaboration (γ-ray).

in a near future with the Baikal Deep Underwater Neutrino Telescope in development below the surface of the Baikal lake in Russia and the Km3net observatory currently in construction in the depths of the Mediterranean sea. On the other hand, gravitational waves interferometers are now sensitive enough to detect the gravitational counterpart of very energetic processes such as the merging of binary stars. Astrophysical sources can now be studied in the context of *multi-messengers* astronomy.

Modern stakes

Via their interactions with interstellar matter and magnetic fields, cosmic rays produce some of the most fascinating phenomena in our galaxy. Understanding the non-thermal[4] universe can only be achieved via the comprehension of cosmic ray acceleration, transport and interaction at the sources and nearby. The most energetic astrophysical systems of our Universe including massive stars, supernovae, pulsars or black holes are still not well understood, and their non-thermal emission is a unique way to probe their intrinsic physical mechanisms.

However, the stakes of cosmic ray physics are not limited to the study of astrophysical objects. Being accelerated inside the most powerful astrophysical systems, they represent an overall energy density comparable to the magnetic and thermal content of the galaxy. Through their ionising properties, they are believed to play important roles on gas dynamics, and in particular on the process of star formation and evolution since they are able to penetrate deep inside molecular clouds. Not only do they drive the chemistry

[4] A *non-thermal* distribution of particles or radiation is one which is not in thermal equilibrium, that is, which is accelerated mechanically or results from interactions involving accelerated particles. In the following, *non-thermal particles*, *accelerated particles* and *cosmic rays* designate the same physical objects.

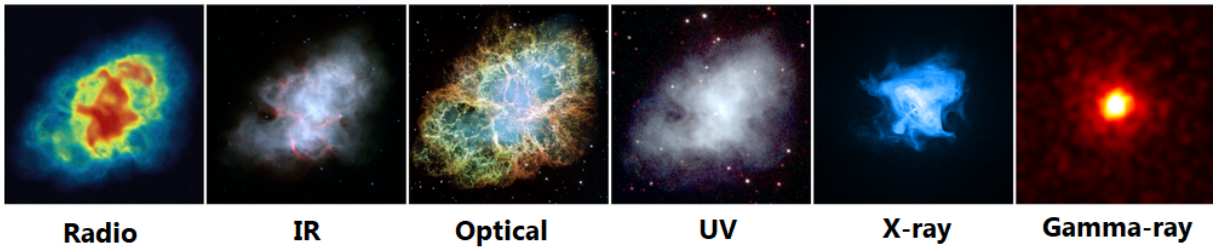

Figure 0.6: The Crab nebula observed in different energy bands.
Credits: NRAO/AUI and M. Bietenholz, J.M. Uson, T.J. Cornwell (radio), NASA/JPL-Caltech/R. Gehrz (IR), NASA, ESA, J. Hester and A. Loll (optical), NASA/Swift/E. Hoversten (UV), NASA/CXC/SAO/F. Seward et al. (X-ray), NASA/DOE/Fermi-LAT/R.Buehler (γ-ray).

and evolution of star forming regions, but also the physics of space plasmas, triggering instabilities and bending magnetic fields. In many aspects, cosmic rays are crucial actors in the galactic ecosystem.

On Earth, secondary particles such as muons and electrons resulting from atmospheric air-showers may have played a crucial role on the origin of life. It is yet unclear how the complex molecules which are the building blocks of life have been synthesised. Did comets transport them? Have they been synthesised by the volcanic activity deep in the oceans? Or have they been produced by sparks, as early suggested by the Miller-Urey experiment (Miller, 1953)? This last hypothesis was disfavoured as it was long thought sparks were not frequent enough, until it was discovered that cosmic rays could greatly enhance them (Erlykin and Wolfendale, 2010). Then, cosmic rays may have further influenced the evolution by their direct interactions with complex molecules, possibly explaining the chirality of life (Globus and Blandford, 2020) and more generally inducing the random mutations at the basis of the natural selection mechanism (Todd, 1994). The impact of cosmic ray radiation on the human cells has gained a rising interest ever since humans are sent into space, for they are energetic enough to damage the DNA and induce cancers. This is a long-standing threat over any interplanetary journey.

The study of cosmic rays is also the opportunity to probe fundamental physics. In fact, the discovery of cosmic rays in the early XXth century was the birth of Particle Physics. The positrons, muons, pions, were the first building block of the Standard Model discovered in the sky rather in underground accelerators. Even now, modern accelerators cannot compete with the energies reached by cosmic particles and astroparticles offer a chance to probe the fundamental laws of nature such as the Lorentz invariance at the basis of field theories (e.g. Bietenholz, 2011), the neutrinos oscillations which give constraints on their mass, or the nature of dark matter (Conrad and Reimer, 2017).

Although cosmic rays are of prime importance to understand the evolution of galaxies, the ionisation of the interstellar medium, the formation of stars, the physics of many compact objects as well as extended regions, and possibly the appearance and evolution of life on Earth, they are admittedly still poorly understood. We do know now that the northern lights observed by the Nordic folks are not "glacier radiation" but rather low energy solar particles interacting in the atmosphere. However, as far as more energetic "non thermal" cosmic particles are concerned, there are still many doubts on several aspects and in particular on the sources, propagation and interactions (see Gabici et al., 2019, for a review). Among the modern issues of Cosmic Ray Physics we find the uncertainty on the ionisation rate of molecular clouds (Phan, 2020), which not only determines the composition of the gas but also drives the formation of stars. Several anomalies on the composition of cosmic rays are still debated. The overabundance of the isotopes ^{22}Ne

and ^{58}Fe suggests for instance that cosmic rays are accelerated from materials enriched by products of massive star nucleosynthesis rather than standard interstellar material. The small-scale anisotropies are not completely understood, and ironically the fact that the distribution remains very close to isotropy up to very high energies is a mystery as well, as high energy cosmic rays are expected to be much less deflected. Finally, one of the long-standing mystery of cosmic rays is the origin of the ultra high energy flux. It is yet unclear which are the galactic and extragalactic sources able to accelerate charged particles up to energies thousands if not millions of times higher than the Large Hadron Collider at CERN.

As far as the primary spectrum is concerned, many difficulties are still to be solved. The low-energy bands are not well understood, in particular because they are affected by the modulation due to the solar wind which contains low-energy protons and electrons. Great progress have been done on the observational side since the Voyager probes crossed the heliopause, although it raised more questions than answers[5]. One of the great mysteries of the cosmic ray spectrum in the GeV band is the excess of antiparticles (positrons and antiprotons), with an observed secondary to primary ratio *rising* above 8 GeV, in contrast with the theoretical predictions. Possible explanations include the direct acceleration of antimatter in sources such as pulsars (Profumo, 2012), dark matter (Bergström et al., 2008), or propagation effects (Burch and Cowsik, 2010). Finally, the intermediate and high energy bands of the proton spectrum present several anomalies which will be discussed below.

It is very difficult to reconcile all the available observables in a consistent "Standard Model of Cosmic Rays". While more and more precise measurements have been performed for half a century, there is still no convincing theory of particle acceleration, propagation and interaction. In particular, the main sources are still not unambiguously identified. As soon as *supernovae* were discovered in 1934 (Baade and Zwicky, 1934b), it was realised from a simple energetic argument that they could explain the bulk of cosmic rays (Baade and Zwicky, 1934a). In 1949, Fermi shed light on the matter when he suggested a rather simple acceleration mechanism (the derivation holds in one notebook page!) where *energy* [is] *acquired in collisions against cosmic magnetic fields*(sic: Fermi, 1949). However the process in its original form was too inefficient in regard to radiative losses to explain the very high energy cosmic rays and it was only in the 70's that the connection between Fermi's idea and shock waves was made in four seminal papers published almost simultaneously by various authors (Axford et al., 1977; Krymskii, 1977; Bell, 1978; Blandford and Ostriker, 1978). This is still nowadays at the basis of the standard model of galactic cosmic rays.

The supernova paradigm

The spectrum of cosmic ray protons is almost a power law over more than ten decades in energy. This extraordinary result suggests that there exists a somewhat universal acceleration mechanism in our galaxy. Ones of the most promising cosmic accelerators are the shocks produced by supernova explosions which expand into the interstellar medium during several thousands years. These so-called *supernova remnants* are ones of the most energetic systems of our galaxy, with a mechanical power estimated around 10^{42} erg/s. On

[5]This is admittedly the fate of any field of research, however it seems that as far as cosmic ray physics is concerned, every new measurement systematically conspires to disprove the existing theories.

the other hand, the cosmic ray power can be estimated from the gamma-ray luminosity of the galaxy (fifth map of Figure 0.5) around 7×10^{40} erg/s (Strong et al., 2010), which would consistently maintain a cosmic ray energy density of 1 eV/cm^3 against the diffusive escape outside of the galaxy assuming that the volume of the galactic disk is about 400 kpc^3 and the residence time about 3 Myr. To sustain the observed spectrum of cosmic rays, supernova remnants must therefore transfer a few percent of their energy into particle acceleration, which is a very reasonable possibility. Moreover, the mechanism of acceleration by diffusion around strong shock waves is expected to produce universal power laws in relativistic energy bands of the form $f(E) \propto E^{-2}$, which makes supernova remnants good candidates to explain both the normalisation and the slope of the diffuse cosmic ray spectrum observed near Earth (Figure 0.4). Furthermore, there is nowadays no doubt that supernova remnants are efficient cosmic ray accelerators, as proven by their gamma-ray emission (Giordano et al. 2012; Aharonian 2013; Ackermann et al. 2013; see Hillas 2005 for a review of the supernova paradigm).

On the other hand, the acceleration of particles around supernova remnant shocks suffers several limitations. The strongest one is the maximum attainable energy, which is limited both by the age of the remnant and its size. Both criteria lead to a maximum energy of the order of 100 TeV in the most optimistic scenarios, which is two orders of magnitude below the high energy tail of the galactic proton spectrum. Furthermore, isolated supernova remnants producing perfect power laws can hardly account for the observed irregularities of the CR spectrum, in particular the steepening called the "knee" around 3 PeV where the spectral index suddenly steepens from -2.7 to -3.1, and the hardening called the "ankle" around 3 EeV where the spectral index goes back to -2.7. Although the knee could arise due to the superposition of the high energy depletions of various species (e.g. Stanev et al., 1993; Thoudam et al., 2016), this cannot explain the steepening of the proton spectrum alone. Alternative scenarios include for instance the contribution from a single nearby source (e.g. Erlykin and Wolfendale, 2001; Bouyahiaoui et al., 2019), but there is still no consensus about the origin of this PeV break. On the other hand, it is now widely believed that the ankle originates from the transition between galactic and extragalactic sources (Parizot, 2014). Indeed, EeV protons have a Larmor radius of the order of the width of the galactic disk, which means that they should escape in the intergalactic space quickly after they have been accelerated.

With the rise of more and more sensitive detectors, smaller anomalies have been observed in the cosmic ray spectrum, such as the hardening around 300 GeV detected by the PAMELA, AMS-02 and CREAM experiments (Aguilar et al., 2015). Possible interpretations, including a change in the galactic diffusion regime (Génolini et al., 2017), are still speculative. Finally, theoretical computations of particle acceleration at shocks and subsequent propagation in the galaxy predict a spectral index near Earth of about -2.3 to -2.5. Although this is close to the observed value of -2.7, explaining the discrepancy is far from being straightforward. In particular, propagation effects from the source to the Earth are not expected to steepen the spectrum that much. Furthermore, the nonlinear backreaction of cosmic rays on the shock waves is expected to curve the spectra in a non-universal way.

To summarise in one sentence, it is not exaggerated to say that even the *bulk* of cosmic rays remains mysterious nowadays.

Superbubbles as sources of cosmic rays

Many efforts have been made in the past decades to find alternative scenarios of cosmic ray acceleration. One promising possibility are the *superbubbles* carved in the interstellar medium by the interactions of massive stars born inside clusters. Inside superbubbles, star winds and supernovae combine to inject mechanical energy in the surrounding medium under the form of shock waves and turbulence. It was early realised (e.g. Montmerle, 1979) that this could lead to an interesting scenario of particle acceleration, which would still fundamentally rely on shock acceleration with all its aforementioned qualities, but modulated by collective effects such as shock interactions or stochastic acceleration in turbulence. Despite the fact that most massive stars are believed to be born inside clusters, the standard supernova paradigm only considers isolated supernovae and few attempts have been made to model clusters and superbubbles acting as a whole in a self-consistent way.

In the 90's, Bykov and Toptygin developed renormalisation methods to solve the transport of particles into a strongly turbulent medium characterised by an ensemble of stochastic shocks (Bykov and Toptygin, 1993). This was then applied to model the acceleration of particles inside young superbubbles with promising consequences regarding the shape of the spectrum and maximum energy (Bykov et al., 1995; Bykov, 2001). At the same time, Klepach et al. (2000) considered the acceleration of cosmic rays either at the collective termination shock produced by the winds of the stars in a compact cluster, or around the multiple winds in the case of a loose cluster. They also found that the maximum energy could be increased by up to two orders of magnitude compared to the acceleration at a single shock, and that the more efficient acceleration would lead to hard spectra. A model of acceleration at the collective wind of a compact cluster was solved recently by Morlino et al. (2021) who showed that the maximum energy of accelerated protons could exceed PeV energies only if the magnetic field close to the termination shock is efficiently amplified, which is required to confine the particles of very high energies around the shock. The stochastic acceleration in the turbulent medium was not included in these two last models. As far as the acceleration by repeated shocks is concerned, apart from the analytic proof of strong spectral hardening given by Melrose and Pope (1993), there has been one modelling developed by Ferrand and Marcowith (2010) who considered successive supernovae explosions inside superbubbles. The acceleration of particles was solved during the whole superbubble lifetime, with several limitations, including a fully linear treatment of the acceleration and transport as well as the assumption that winds and losses would provide negligible modulations. More recently, Tolksdorf et al. (2019) solved the transport of cosmic rays around superbubbles. They showed that interstellar particles could be efficiently reaccelerated in the turbulent interior. The primary acceleration at shock waves was however disregarded.

Efforts to model the acceleration of particles in interacting shocks, such as colliding winds or supernova remnants, have been made in a series of paper by Bykov and collaborators (Bykov et al., 2013; Bykov et al., 2018). It was shown that very hard spectra could be expected in the idealised case of stationary plane infinite shocks. An attempt to include geometrical effects has been performed in Bykov et al. (2015), although a complete solution of the problem is still missing.

The aforementioned works are to my knowledge the only existing attempts to model the acceleration of particles inside superbubbles from first principles. A number of phenomenological studies (e.g. Higdon et al., 1998; Parizot and Drury, 1999; Higdon and

Lingenfelter, 2006) support the superbubble origin of cosmic rays. In particular, it was early realised that the reacceleration of enriched stellar material in superbubbles could explain the ^{22}Ne excess (Higdon and Lingenfelter, 2003), as confirmed by recent numerical simulations (Gupta et al., 2020), as well as other composition anomalies (Tatischeff and Gabici, 2018). Besides, particle reacceleration in multiple shocks and strong turbulence is expected to be more efficient than the acceleration around a single supernova, such that one can hope to push the maximum energy above the spectral "knee", as required to explain the transition between the galactic and extragalactic components. In large-scale superbubbles, the Hillas criterion is furthermore not a limitation anymore. On the other hand, the fundamental mechanism of acceleration remains the diffusion around shock waves or magnetic inhomogeneities, with all its appealing properties such as its universality and a spectral slope not far from what is observed. In some sense, superbubbles are a natural extension of the standard supernova model, in particular because most supernova remnants are actually believed to explode within associations of massive stars (Higdon and Lingenfelter, 2005). Although this scenario for the origin of cosmic rays was only marginally studied a decade ago (see the reviews by Parizot et al., 2004; Bykov, 2014; Lingenfelter, 2018; Bykov et al., 2020), the interest has been rising since the recent gamma-ray detections of star clusters and superbubbles in the Milky Way as well as in the Large Magellanic Cloud (Aharonian et al., 2007; Abramowski et al., 2012; Ackermann et al., 2011; Abramowski et al., 2015; Katsuta et al., 2017; Aharonian et al., 2019). This confirms that stellar clusters and superbubbles are important sources of cosmic rays.

Goals and outline of the thesis

While a number of theoretical and observational arguments support the superbubble origin of cosmic rays, a comprehensive self-consistent modelling remains to be developed. This will be the main goal of the present work.

In Chapter 1, I review the modelisations and observations of superbubbles, from the formation of stellar clusters to the expansion of supershells. Chapter 2 is devoted to the description of the transport of charged particles in a turbulent medium, which is at the basis of any theory of particle acceleration and transport. The mechanism of diffusive acceleration around shock waves is then detailed in Chapter 3. This acceleration mechanism is applied to a system of colliding fronts in Chapter 4 and to a collection of shocks in Chapter 5. Chapter 6 describes a self-consistent modelling of cosmic ray production in superbubbles, including the contribution of supernovae, winds and turbulence as well as the nonlinear feedback of the non-thermal particles. Conclusions are drawn on the energetics, intermittency, spectra and composition of cosmic rays. The model is refined accounting for a diffusion in two zones, which allows in particular to investigate the effect of the supershell and eventually to compute the gamma-ray counterpart of the nonthermal protons.

References

Abramowski, A. et al. (Jan. 2012). "Discovery of extended VHE gamma-ray emission from the vicinity of the young massive stellar cluster Westerlund 1". In: A&A 537, A114, A114. DOI: 10.1051/0004-6361/201117928.

Abramowski, A. et al. (Jan. 2015). "The exceptionally powerful TeV γ-ray emitters in the Large Magellanic Cloud". In: *Science* 347.6220, pp. 406–412. DOI: 10.1126/science.1261313.

Ackermann, M. et al. (Nov. 2011). "A Cocoon of Freshly Accelerated Cosmic Rays Detected by Fermi in the Cygnus Superbubble". In: *Science* 334.6059, p. 1103. DOI: 10.1126/science.1210311.

Ackermann, M. et al. (Feb. 2013). "Detection of the Characteristic Pion-Decay Signature in Supernova Remnants". In: *Science* 339.6121, pp. 807–811. DOI: 10.1126/science.1231160.

Aguilar, M. et al. (Apr. 2015). "Precision Measurement of the Proton Flux in Primary Cosmic Rays from Rigidity 1 GV to 1.8 TV with the Alpha Magnetic Spectrometer on the International Space Station". In: *Phys. Rev. Lett.* 114 (17), p. 171103. DOI: 10.1103/PhysRevLett.114.171103.

Aharonian, F. A. (2013). "Gamma rays from supernova remnants". In: *Astroparticle Physics* 43. Seeing the High-Energy Universe with the Cherenkov Telescope Array - The Science Explored with the CTA, pp. 71–80. ISSN: 0927-6505. DOI: https://doi.org/10.1016/j.astropartphys.2012.08.007.

Aharonian, F. et al. (June 2007). "Detection of extended very-high-energy gamma-ray emission towards the young stellar cluster Westerlund 2". In: A&A 467.3, pp. 1075–1080. DOI: 10.1051/0004-6361:20066950.

Aharonian, F., Yang, R., and de Oña Wilhelmi, E. (Mar. 2019). "Massive stars as major factories of Galactic cosmic rays". In: *Nature Astronomy* 3, pp. 561–567. DOI: 10.1038/s41550-019-0724-0.

Axford, W. I., Leer, E., and Skadron, G. (Jan. 1977). "The Acceleration of Cosmic Rays by Shock Waves". In: *International Cosmic Ray Conference*. Vol. 11. International Cosmic Ray Conference, p. 132.

Baade, W. and Zwicky, F. (1934a). "Cosmic Rays from Super-Novae". In: *Proceedings of the National Academy of Sciences* 20.5, pp. 259–263. ISSN: 0027-8424. DOI: 10.1073/pnas.20.5.259.

Baade, W. and Zwicky, F. (May 1934b). "On Super-novae". In: *Proceedings of the National Academy of Science* 20.5, pp. 254–259. DOI: 10.1073/pnas.20.5.254.

Bell, A. R. (Jan. 1978). "The acceleration of cosmic rays in shock fronts - I." In: MNRAS 182, pp. 147–156. DOI: 10.1093/mnras/182.2.147.

Bergström, L., Bringmann, T., and Edsjö, J. (Nov. 2008). "New positron spectral features from supersymmetric dark matter: A way to explain the PAMELA data?" In: Phys. Rev. D 78.10, 103520, p. 103520. DOI: 10.1103/PhysRevD.78.103520.

Bietenholz, W. (Aug. 2011). "Cosmic rays and the search for a Lorentz Invariance Violation". In: Phys. Rep. 505.5, pp. 145–185. DOI: 10.1016/j.physrep.2011.04.002.

Blandford, R. D. and Ostriker, J. P. (Apr. 1978). "Particle acceleration by astrophysical shocks." In: ApJ 221, pp. L29–L32. DOI: 10.1086/182658.

Blasi, P., Amato, E., and Serpico, P. D. (Aug. 2012). "Spectral Breaks as a Signature of Cosmic Ray Induced Turbulence in the Galaxy". In: Phys. Rev. Lett. 109.6, 061101, p. 061101. DOI: 10.1103/PhysRevLett.109.061101.

Bouyahiaoui, M., Kachelriess, M., and Semikoz, D. V. (Jan. 2019). "Vela as the source of Galactic cosmic rays above 100 TeV". In: J. Cosmology Astropart. Phys. 2019.1, 046, p. 046. DOI: 10.1088/1475-7516/2019/01/046.

Burch, B. and Cowsik, R. (Sept. 2010). "On the Positron Fraction and Cosmic-Ray Propagation Models". In: *arXiv e-prints*, arXiv:1009.1361.

Bykov, A. M., Gladilin, P. E., and Osipov, S. M. (Mar. 2013). "Non-linear model of particle acceleration at colliding shock flows". In: MNRAS 429.3, pp. 2755–2762. DOI: 10.1093/mnras/sts553.

Bykov, A. M., Ptuskin, V. S., and Toptygin, I. N. (Jan. 1995). "Spectrum of Ultra-High Energy Cosmic Rays Acceleration in Superbubbles". In: *International Cosmic Ray Conference*. Vol. 3. International Cosmic Ray Conference, p. 337.

Bykov, A. M. et al. (Oct. 2015). "Ultrahard spectra of PeV neutrinos from supernovae in compact star clusters". In: MNRAS 453.1, pp. 113–121. DOI: 10.1093/mnras/stv1606.

Bykov, A. M. et al. (Nov. 2018). "Supernovae in compact star clusters as sources of high-energy cosmic rays and neutrinos". In: *Advances in Space Research* 62.10, pp. 2764–2772. DOI: 10.1016/j.asr.2017.05.043.

Bykov, A. M. (Oct. 2001). "Particle Acceleration and Nonthermal Phenomena in Superbubbles". In: Space Sci. Rev. 99, pp. 317–326. DOI: 10.1023/A:1013817721725.

Bykov, A. M. (Nov. 2014). "Nonthermal particles and photons in starburst regions and superbubbles". In: A&A Rev. 22, 77, p. 77. DOI: 10.1007/s00159-014-0077-8.

Bykov, A. M. and Toptygin, I. (Nov. 1993). "Reviews of topical problems: Particle kinetics in highly turbulent plasmas (renormalization and self-consistent field methods)". In: *Physics Uspekhi* 36.11, pp. 1020–1052. DOI: 10.1070/PU1993v036n11ABEH002179.

Bykov, A. M. et al. (Apr. 2020). "High-Energy Particles and Radiation in Star-Forming Regions". In: Space Sci. Rev. 216.3, 42, p. 42. DOI: 10.1007/s11214-020-00663-0.

Conrad, J. and Reimer, O. (Mar. 2017). "Indirect dark matter searches in gamma and cosmic rays". In: *Nature Physics* 13.3, pp. 224–231. DOI: 10.1038/nphys4049.

D'Angelo, M. et al. (Feb. 2018). "Diffuse gamma-ray emission from self-confined cosmic rays around Galactic sources". In: MNRAS 474.2, pp. 1944–1954. DOI: 10.1093/mnras/stx2828.

Erlykin, A. D. and Wolfendale, A. W. (Jan. 2001). "Models for the origin of the knee in the cosmic-ray spectrum". In: *Advances in Space Research* 27.4, pp. 803–812. DOI: 10.1016/S0273-1177(01)00125-9.

Erlykin, A. D. and Wolfendale, A. W. (July 2010). "Long Term Time Variability of Cosmic Rays and Possible Relevance to the Development of Life on Earth". In: *Surveys in Geophysics* 31.4, pp. 383–398. DOI: 10.1007/s10712-010-9097-8.

Fermi, E. (Apr. 1949). "On the Origin of the Cosmic Radiation". In: *Physical Review* 75.8, pp. 1169–1174. DOI: 10.1103/PhysRev.75.1169.

Ferrand, G. and Marcowith, A. (Feb. 2010). "On the shape of the spectrum of cosmic rays accelerated inside superbubbles". In: A&A 510, A101, A101. DOI: 10.1051/0004-6361/200913520.

Gabici, S. et al. (Jan. 2019). "The origin of Galactic cosmic rays: Challenges to the standard paradigm". In: *International Journal of Modern Physics D* 28.15, 1930022-339, pp. 1930022–339. DOI: 10.1142/S0218271819300222.

Génolini, Y. et al. (Dec. 2017). "Indications for a High-Rigidity Break in the Cosmic-Ray Diffusion Coefficient". In: Phys. Rev. Lett. 119.24, 241101, p. 241101. DOI: 10.1103/PhysRevLett.119.241101.

Giacinti, G. and Kirk, J. G. (Feb. 2017). "Large-scale Cosmic-Ray Anisotropy as a Probe of Interstellar Turbulence". In: ApJ 835.2, 258, p. 258. DOI: 10.3847/1538-4357/835/2/258.

Giordano, F. et al. (Jan. 2012). "Fermi Large Area Telescope Detection of the Young Supernova Remnant Tycho". In: ApJ 744.1, L2, p. L2. DOI: 10.1088/2041-8205/744/1/L2.

Globus, N. and Blandford, R. D. (May 2020). "The Chiral Puzzle of Life". In: ApJ 895.1, L11, p. L11. DOI: 10.3847/2041-8213/ab8dc6.

Gupta, S. et al. (Apr. 2020). "Realistic modelling of wind and supernovae shocks in star clusters: addressing $^{22}Ne/^{20}Ne$ and other problems in Galactic cosmic rays". In: MNRAS 493.3, pp. 3159–3177. DOI: 10.1093/mnras/staa286.

Hess, V. (July 2018). "On the Observations of the Penetrating Radiation during Seven Balloon Flights". In: *arXiv e-prints*, arXiv:1808.02927. translated, commented by Alessandro De Angelis, Cornelia Arcaro b. Schultz.

Higdon, J. C. and Lingenfelter, R. E. (June 2003). "The Superbubble Origin of ^{22}Ne in Cosmic Rays". In: ApJ 590.2, pp. 822–832. DOI: 10.1086/375192.

Higdon, J. C. and Lingenfelter, R. E. (Aug. 2005). "OB Associations, Supernova-generated Superbubbles, and the Source of Cosmic Rays". In: ApJ 628.2, pp. 738–749. DOI: 10.1086/430814.

Higdon, J. C. and Lingenfelter, R. E. (Jan. 2006). "The superbubble origin for galactic cosmic rays". In: *Advances in Space Research* 37.10, pp. 1913–1917. DOI: 10.1016/j.asr.2005.07.071.

Higdon, J. C., Lingenfelter, R. E., and Ramaty, R. (Dec. 1998). "Cosmic-Ray Acceleration from Supernova Ejecta in Superbubbles". In: ApJ 509.1, pp. L33–L36. DOI: 10.1086/311757.

Hillas, A. M. (Jan. 1984). "The Origin of Ultra-High-Energy Cosmic Rays". In: ARA&A 22, pp. 425–444. DOI: 10.1146/annurev.aa.22.090184.002233.

Hillas, A. M. (May 2005). "TOPICAL REVIEW: Can diffusive shock acceleration in supernova remnants account for high-energy galactic cosmic rays?" In: *Journal of Physics G Nuclear Physics* 31.5, R95–R131. DOI: 10.1088/0954-3899/31/5/R02.

Katsuta, J., Uchiyama, Y., and Funk, S. (Apr. 2017). "Extended Gamma-Ray Emission from the G25.0+0.0 Region: A Star-forming Region Powered by the Newly Found OB Association?" In: *The Astrophysical Journal* 839.2, p. 129. DOI: 10.3847/1538-4357/aa6aa3.

Klepach, E. G., Ptuskin, V. S., and Zirakashvili, V. N. (May 2000). "Cosmic ray acceleration by multiple spherical shocks". In: *Astroparticle Physics* 13.2-3, pp. 161–172. DOI: 10.1016/S0927-6505(99)00108-5.

Krymskii, G. F. (June 1977). "A regular mechanism for the acceleration of charged particles on the front of a shock wave". In: *Akademiia Nauk SSSR Doklady* 234, pp. 1306–1308.

Larson, L. M. (1917). *The king's mirror (Speculum regale - Konungs skuggsjá)*. Unknown author around 1250 A.D. The American-Scandinavian Foundation.

Lingenfelter, R. E. (Nov. 2018). "Cosmic rays from supernova remnants and superbubbles". In: *Advances in Space Research* 62.10, pp. 2750–2763. DOI: 10.1016/j.asr.2017.04.006.

Melrose, D. B. and Pope, M. H. (Jan. 1993). "Diffusive Shock Acceleration by Multiple Shocks". In: *Proceedings of the Astronomical Society of Australia* 10.3, p. 222.

Miller, S. L. (1953). "A Production of Amino Acids Under Possible Primitive Earth Conditions". In: *Science* 117.3046, pp. 528–529. ISSN: 0036-8075. DOI: 10.1126/science.117.3046.528.

Montmerle, T. (July 1979). "On gamma-ray sources, supernova remnants, OB associations, and the origin of cosmic rays." In: ApJ 231, pp. 95–110. DOI: 10.1086/157166.

Morlino, G. et al. (Mar. 2021). "Particle acceleration in winds of star clusters". In: MNRAS. DOI: 10.1093/mnras/stab690.

Morlino, G. (2017). "High-Energy Cosmic Rays from Supernovae". In: *Handbook of Supernovae*. Ed. by A. W. Alsabti and P. Murdin. Cham: Springer International Publishing, pp. 1711–1736. ISBN: 978-3-319-21846-5. DOI: 10.1007/978-3-319-21846-5_11.

Parizot, E. and Drury, L. (Sept. 1999). "Superbubbles as the source of (6) Li, Be and B in the early Galaxy". In: A&A 349, pp. 673–684.

Parizot, E. et al. (Sept. 2004). "Superbubbles and energetic particles in the Galaxy. I. Collective effects of particle acceleration". In: A&A 424, pp. 747–760. DOI: 10.1051/0004-6361:20041269.

Parizot, E. (Nov. 2014). "Cosmic Ray Origin: Lessons from Ultra-High-Energy Cosmic Rays and the Galactic/Extragalactic Transition". In: *Nuclear Physics B - Proceedings Supplements* 256-257, pp. 197–212. ISSN: 0920-5632. DOI: 10.1016/j.nuclphysbps.2014.10.023.

Phan, V. H. M. (2020). "Cosmic ray interaction in molecular environment". 2020UNIP7070. PhD thesis.

Profumo, S. (Feb. 2012). "Dissecting cosmic-ray electron-positron data with Occam's razor: the role of known pulsars". In: *Central European Journal of Physics* 10.1, pp. 1–31. DOI: 10.2478/s11534-011-0099-z.

Stanev, T., Biermann, P. L., and Gaisser, T. K. (July 1993). "Cosmic rays. IV. The spectrum and chemical composition above 10^4 GeV". In: A&A 274, p. 902.

Strong, A. W. et al. (Oct. 2010). "Global Cosmic-ray-related Luminosity and Energy Budget of the Milky Way". In: ApJ 722.1, pp. L58–L63. DOI: 10.1088/2041-8205/722/1/L58.

Tatischeff, V. and Gabici, S. (Oct. 2018). "Particle Acceleration by Supernova Shocks and Spallogenic Nucleosynthesis of Light Elements". In: *Annual Review of Nuclear and Particle Science* 68.1, pp. 377–404. DOI: 10.1146/annurev-nucl-101917-021151.

Thoudam, S. et al. (Oct. 2016). "Cosmic-ray energy spectrum and composition up to the ankle: the case for a second Galactic component". In: A&A 595, A33, A33. DOI: 10.1051/0004-6361/201628894.

Todd, P. (Oct. 1994). "Cosmic radiation and evolution of life on earth: Roles of environment, adaptation and selection". In: *Advances in Space Research* 14.10, pp. 305–313. DOI: 10.1016/0273-1177(94)90483-9.

Tolksdorf, T. et al. (July 2019). "Cosmic Rays in Superbubbles". In: *The Astrophysical Journal* 879.2, p. 66. DOI: 10.3847/1538-4357/ab24c6.

Chapter 1

Superbubbles: formation and evolution

This chapter aims at reviewing the current understanding of the formation of massive stellar clusters and the properties of the superbubbles which evolve in the interstellar medium. The analytic theories are discussed as well as numerical simulations and observations.

1.1 Stellar clusters

1.1.1 Cluster formation

The Milky Way is the most efficient star factory in the local group, with a formation rate of 2 solar masses per year (Molinari et al., 2014). The main sites of star formation are believed to be dense molecular clouds, mostly made of molecular hydrogen, which condense due to gravitational instabilities. The largest molecular cloud complex in the Milky Way, located in the galactic centre region, has a total mass of 10^7 $M_\odot$ (e.g. Ferrière et al., 2007). Dense evolved clouds are far from being homogeneous. They rather display a fractal morphology made of clumps and filaments (Elmegreen and Falgarone, 1996). On small scales, density fluctuations may collapse gravitationally if the magnetic fields and supersonic turbulence are not able to sustain the infall of the mass. On the other hand, small scales are fed by largest scales, which gives rise to a *mass cascade* similar to the energy cascade describing turbulent systems (Field et al., 2008). The collapse of a dense molecular cloud therefore proceeds hierarchically.

Clumps are stretched during their collapse, flattening towards sheets of matter and eventually one-dimensional filaments which feed small-scale dense clouds within the original large-scale molecular cloud (Vázquez-Semadeni et al., 2017). Massive stars are believed to form in these very dense regions (McKee and Ostriker 2007; Longmore et al. 2014; see Krause et al. 2020 for a recent review). As soon as they are lit, stars start to feed back the surrounding medium by emitting outflows and radiation. The nearby gas is quickly swept up. The stellar feedback eventually disrupts the local parent cloud such that stars and gas decouple, leaving a low-density region carved inside the original molecular cloud and containing a large number of active stars which is called a *stellar cluster* if the stars are gravitational bound together or an *association* in the opposite case (Krumholz et al., 2019). At late times, the large-scale molecular cloud may be completely destructed by the newborn stars gathered within several nascent clusters or associations, leaving a complex *star forming region*.

According to this model of collective star formation, most massive stars are expected to lit inside embedded clusters or associations (Kruijssen, 2012). The radial dispersion

in such groups is of the order of a few parsecs per Myr (Mathieu, 1986), which means that most of the massive stars are expected to stay inside the cluster during their (short) lives (the lifetime of 8 $M_\odot$ stars being about 35-40 Myr). This is confirmed by the observations of the mass distribution of star clusters in the galaxy, compared to the initial mass function of individual stars, which suggest that about 75% of massive stars explode in clusters or associations (Higdon and Lingenfelter, 2005; Lingenfelter, 2018). Assuming that the distribution of massive stars is homogeneous in a cluster, the mean distance between neighbours is typically of the order of 10 pc. The actual distance between stars is however expected to be much smaller as the OB associations are often subdivided into subclusters containing tens of stars in a few parsecs.

The most massive star clusters, often referred to as *superclusters*, contain thousands of massive stars. In the inner parts of the Milky Way, radio, infrared and X-ray observations reveal young superclusters such as the Arches and the Quintuplet (e.g. Figer, 2004). Closer to the sun lie the Westerlund 1 and 2 clusters (e.g. Clark et al., 2005). The latter is shown in Figure 1.1 for illustration: the optical diffuse emission reveals the dense molecular clouds in which the stars are formed, while the X-ray emission shows the point-like sources corresponding to the positions of massive stars. Smaller clusters are observed in the Orion nebula, which contains a hierarchical structure of clusters and subclusters, or the W3 complex which contains several associations of compact clusters and subclusters, with more than 5 hierarchical levels from galactic to stellar scales. Extragalactic clusters are observed for instance in the Large Magellanic Cloud within the Tarantula nebula (e.g. De Marchi et al., 2011).

The formation of stars is a non-universal nonlinear process. The stars of the first generations exert a strong feedback on the surrounding gas as well on the whole galaxy dynamics. Thus, star formation can only be understood in light of the global galactic evolution including all relevant agents such as the large-scale motions of the interstellar gas enriched by massive stars, the condensation of dust, the generation and dynamics of magnetic fields and turbulence, as well as the local properties of gas clouds and plasmas, and eventually the ionising agents such as cosmic rays and radiation, either produced locally by the feedback of the stars or diffusing throughout the galaxy.

1.1.2 Cluster properties

The content of a given star cluster is statistically described by the *initial mass function* $\xi(M)$, which is defined as:

$$\mathrm{d}N = \xi(M)\mathrm{d}M\,, \tag{1.1}$$

such that $\mathrm{d}N$ is the number of stars with masses between M and $M + \mathrm{d}M$, and the normalisation $\int \mathrm{d}M\xi(M)$ gives the total number of stars in the cluster. In a seminal statistical analysis of massive stars in the solar neighbourhood, Salpeter (1955) derived $\xi(M) \propto M^{-\alpha}$ with $\alpha = 2.35$. This value was later find remarkably accurate and universal for stars heavier than the sun, with typical variations of the order 10% (Kroupa, 2002; Chabrier, 2003).

Three main parameters characterise star clusters: their mass, their size and their age. Masses and ages are inferred from the properties of the stellar content while sizes are obtained from direct observations of the stellar density distributions. The size of a cluster is conveniently defined as the half-mass radius r_h, that is, the radius of a sphere containing half the total mass of the cluster. From statistical studies, one can infer the mass, size and age distributions of stellar clusters in the Milky Way and in the Large

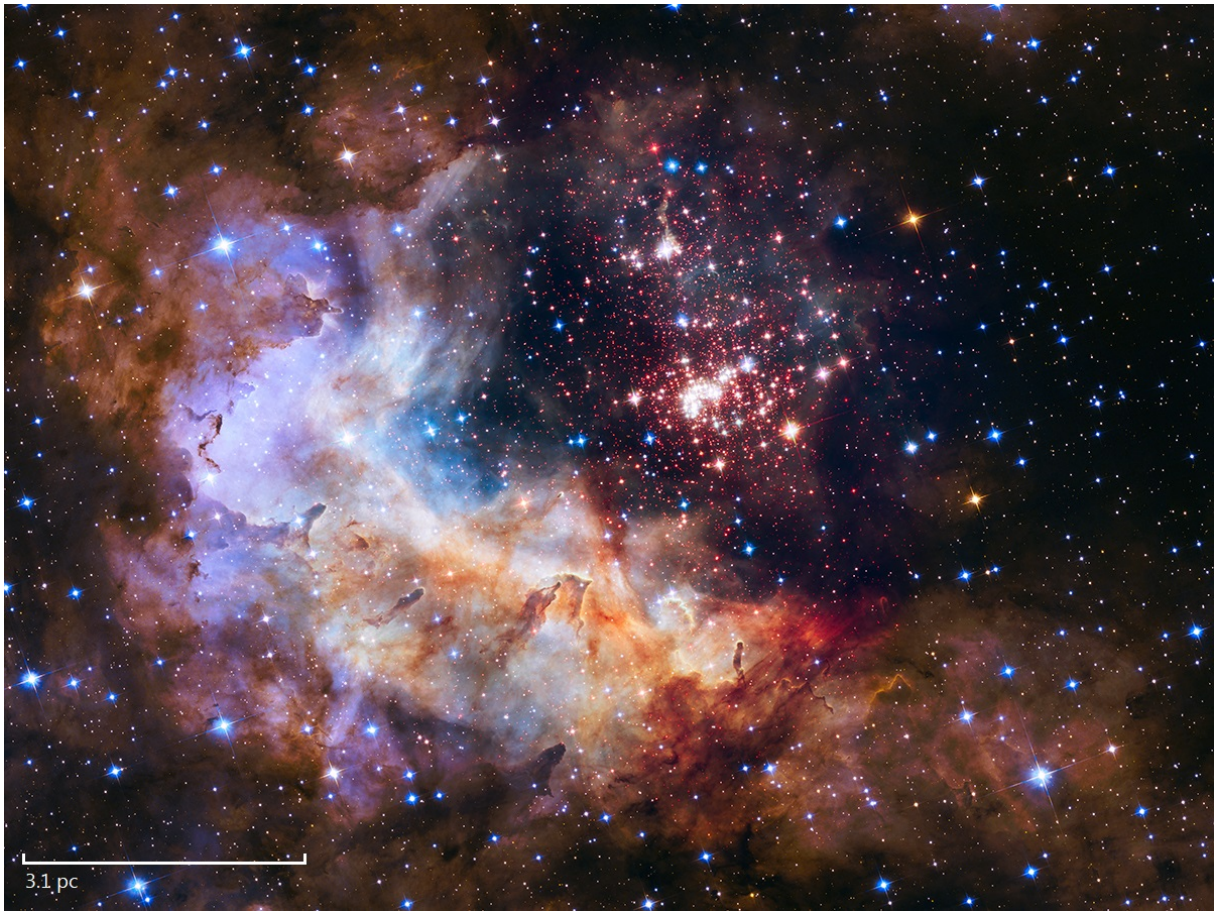

Figure 1.1: Westerlund 2 seen by the Hubble Space Telescope and the Chandra X-ray observatory (blue: optical 555 nm, green: optical 814 nm, red: IR 1.25 µG). Credits: NASA, ESA, the Hubble Heritage Team (STScI/AURA), A. Nota (ESA/STScI), and the Westerlund 2 Science Team.

Magellanic Cloud (e.g. Portegies Zwart et al., 2010; Krumholz et al., 2019). Although the stellar density seems roughly distributed along a universal value of about $100 M_\odot/\mathrm{pc}^3$, which suggests the scaling $r_h \propto M^{1/3}$, the variance is so large that we still lack evidence of a correlation between the mass and the size of a cluster. The ages of massive clusters are decorrelated as well, which is expected if clusters have formed at a constant rate in the past 40 million years, which is the typical lifetime of a massive cluster. Indeed, such timescale is more than one order of magnitude below the disruption time, which implies that the ages of massive clusters should be uniformly distributed. This is however not the case for other types of clusters, such as globular clusters, which are created by similar mechanisms but contain hundreds of thousands of low-mass stars gravitationally bounded in small regions (typically 10 pc^3). These clusters can shine during billions of years. However low-mass stars do not produce strong outflows so these clusters are not expected to be favourable sites of cosmic ray production and will be disregarded in this work, although their dynamics is crucial to understand the galactic ecosystem (see the recent review by Krumholz et al., 2019).

1.1.3 Massive stars

We define *massive stars* as stars with an initial mass higher than 8 $M_\odot$. This therefore includes B-type stars with masses ranging from 8 $M_\odot$ to 15 $M_\odot$ and O-type stars heavier than 15 $M_\odot$ and up to the highest end of the galactic initial mass function around 120 $M_\odot$. As such, associations of massive stars are often called *OB associations*. Both O- and B-type massive stars are very luminous blue stars which, apart from their discriminant spectral properties, follow similar evolutions. The latter is non-universal as it depends on several stellar parameters such as the rotation properties, the metallicity or the magnetic field strength and geometry (see Woosley et al., 2002, for a review)

The *main sequence* of stellar evolution begins with hydrogen burning in the very dense core of the star. In massive stars, the hydrogen continuously fusions into helium through the CNO (carbon-nitrogen-oxygen) catalytic cycle. The energy released by the nuclear fusion generates a pressure sufficient to sustain the gravitational force exerted on the core, while the outer layers are accelerated to supersonic velocities into the surrounding medium under the form of *winds* (Abbott, 1979), which produce a termination shock at a distance of a few parsecs from the star. The emission of these winds depletes the stellar mass. Over the main sequence, about 60% of the initial mass is lost, with 50% under the form of hydrogen, 8% under the form of helium and 4% under the form of carbon and oxygen. A massive star of initial mass $15M_\odot$ typically ejects $10^{-8}M_\odot$ per year at 2400 km/s. More massive stars, e.g. initially around $40M_\odot$, eject about $10^{-6}M_\odot$/yr with similar velocities. The most massive stars can reach more than $120M_\odot$. They eject more than $10^{-5}M_\odot$/yr at velocities which can reach 3000 km/s. The more massive stars exhaust more rapidly their hydrogen supplies. The main sequence of a $100M_\odot$ star ends after about 3 Myr, while a $8M_\odot$ B-type star will blow strong winds during almost 40 Myr (Seo et al., 2018, and references therein)

When most of the hydrogen supply is exhausted, massive stars cool down. If their initial mass is below $\sim 40\ M_\odot$, they undergo a transition toward the red supergiant phase, sustained by the fusion of the helium core, and then of all the heavier elements up to iron. Stars with initial masses above $\sim 20\ M_\odot$ will eventually become Wolf-Rayet stars after the hydrogen supply is exhausted. The stellar atmospheres of Wolf-Rayet stars are enriched in heavy elements and produce strong enriched stellar winds until the fusion reactions end up producing an iron core. At this stage, the star is characterised by an "onion-like" structure with successive layers of different composition, from the heavier elements near the core to the lighter elements far away in the atmosphere.

Because iron cannot fusion, the gas pressure cannot sustain the gravitational collapse of the star. It follows a runaway endothermic instability which makes the stellar core to shrink up to nuclear densities, at which point a compact neutron core is formed, on which the infalling layers bounce. Neutrinos created via inverse beta decay are released and their pressure launches a strong shock which blows the outer layers of the star away within a few milliseconds. The star explodes, expelling its former atmosphere in the interstellar medium at a highly supersonic velocity. This explosion, referred to as a core-collapse supernova, suddenly releases an enormous amount of energy in the surrounding medium, with a luminosity similar to that of the entire galaxy. This phenomenon, sometimes visible by eye, marks the death of a star. The mechanisms driving the explosion are still not well understood. In particular, after the bouncing of the layers on the compact core, the energy of the shock created by the supersonic infall of material is expected to be rapidly dissipated by photodesintegration, unless an additional mechanism rapidly launches it in the interstellar medium. While neutrinos are promising candidates to explain this

shock reactivation, sophisticated numerical models still struggle to simulate supernova explosions (see Janka, 2012, for a review of the collapse and explosion mechanisms).

After the supernova explosion, if the initial mass of the star was rather small ($8 - 20 M_\odot$), the dense core becomes a neutron star. On the other hand, if the initial mass was higher than about 30 $M_\odot$, it is believed that the star collapses onto a black hole. It should be noted however that the collapse of massive stars and the subsequent supernova explosion are still poorly understood. In particular, simulations suggest that very massive stars ($>$ 20-40 $M_\odot$) may only produce a weak supernova, as the infalling rate of the dense outer layers could dramatically slow down the blastwave, producing a *failed supernova*. This possibility has been investigated in the recent years, with rising interest as it could explain the lack of observation of core-collapse supernovae with very massive Wolf-Rayet progenitors (Smartt, 2015). Already twenty years ago, Fryer (1999) and Fryer (2003) suggested that supernova shocks originating from stars of masses between 20 and 40 $M_\odot$ may quickly slow down below the escape velocity of the compact remnant and fall back onto it, while stars with masses higher than 40 $M_\odot$ may not explode at all and directly collapse onto a black hole. This is believed to happen because the collapse is so fast in this case that the neutrinos produced by inverse beta decay in the core do not have enough pressure to overcome the in-falling matter and blow out the external layers. All layers then collapse on the core whose mass exceeds the neutron star limit and a compact remnant is formed without releasing energy in the interstellar medium (the mass of the remnant is then equal to the mass of the progenitor star). A few observational surveys have been performed in the past year to look at the fading of massive stars, and several possible candidates have been identified (Reynolds et al., 2015; Adams et al., 2017; Neustadt et al., 2021).

There is still no consensus nowadays about the fate of massive stars. It may well be the case that only narrow mass bands allow for a powerful supernova explosion (Sukhbold et al., 2016; Ebinger et al., 2020). The result strongly depends on star properties such as the metallicity (e.g. Heger et al., 2003), the mass loss rate in the red supergiant or Wolf-Rayet phases (e.g. Gofman et al., 2020), the rotation (Powell and Müller, 2020, e.g.) or the magnetic field (e.g. Matsumoto et al., 2020). Numerical simulations are furthermore challenging as high resolutions should be achieved in particular to resolve the turbulent stress induced by the neutrinos (Nagakura et al., 2019). Three-dimensional models are also needed to capture the physics accurately (Müller, 2019).

Disregarding these issues, we will assume in the following that all massive stars, i.e. with mass higher than 8 $M_\odot$, explode in a powerful supernova. It is worth keeping in mind that this may not be the case at all. In a typical cluster characterised by a Salpeter initial mass function, 25% of the stars have a mass higher than 20 $M_\odot$, with controversial fates. If this does not change fundamentally the acceleration of cosmic rays, it may have important consequences on the composition of the escaping particles from evolved massive stellar clusters, as enriched Wolf-Rayet material may not be accelerated efficiently if there is no subsequent supernova explosion.

1.1.4 Supernova remnants

When a star explodes as a supernova, a powerful blast wave is released far away from the compact core, with an energy of the order 10^{51} erg (Woosley and Weaver, 1995), which is in first approximation independent of the initial mass of the star (e.g. Ebinger et al., 2019). There are two main types of supernovae: core-collapse (type II, Ib, Ic), and thermonuclear

(type Ia). The former, which as discussed above result from the gravitational collapse of massive stars at the end of their burning cycles, occur in the Milky Way at a rate of about 2 per century. The latter occur in binary systems when the mass of a white dwarf accreting matter from a nearby star exceeds a critical threshold ($\approx 1.4 M_\odot$), which leads to a thermonuclear explosion. The type Ia supernovae eject few material ($0.8-1.4 M_\odot$) at velocities around 10^4 km/s (Chevalier, 1982a; Marietta et al., 2000; Scalzo et al., 2014), while core-collapse supernovae eject about 5-10 $M_\odot$ at $3-5\times10^3$ km/s (Chevalier, 1982b; Woosley and Weaver, 1995; Prantzos, 2012; Ebinger et al., 2019). Because these velocities are highly supersonic (even in a 10^6 K medium, the sound speed is "only" about 100 km/s), supernovae explosions launch strong shock waves in the interstellar medium.

In the early stage of the shock expansion, its radius increases in first approximation as $R \approx V_e t$, where V_e is the velocity of the ejecta[1]. This is called the *free expansion phase*. The free expansion phase ends when the interstellar material swept up by the forward shock becomes non-negligible when compared to the mass of the ejecta. This occurs at a time around 1500 yr for core-collapse supernovae expanding in a uniform medium of density 1 cm^{-3} (Truelove and McKee, 1999). Then begins the *Sedov-Taylor phase*, which corresponds to an adiabatic expansion of the shock. In this phase, the ejected material is negligible when compared to the swept-up gas. What is left is an expanding bubble of shocked hot ($\sim 10^8$ K) interstellar gas. The radius of the shock, driven by energy conservation, evolves as $R_s \approx (2E_{SN}t^2/\rho_0)^{1/5}$. The shock therefore slows down and cools up to the point where the radiative cooling of the post-shock material cannot be neglected anymore, which occurs after about 30 kyr in a medium of density 1 cm^{-3} (Blondin et al., 1998). All the energy of the explosion is then radiated away and the expansion of the shell continues only because of the conservation of its own momentum. This is called the "snow-plow" phase. The shock eventually fades when its velocity becomes comparable to the speed of sound (10-100 km/s).

During the expansion of the shock, the post-shock material is heated to very high temperatures (up to 10^8 K) and thermal X-rays are emitted in the keV bands. On the other hand, ions and electrons accelerated by the shock and interacting with the ambient matter and magnetic fields produce non-thermal photons from the radio to the gamma-ray bands. The shell of shocked matter can be observed in multiple wavelengths during several tens of thousand years. These objects, referred to as *supernova remnants*, produce some amongst the most impressive astrophysical pictures, which reveal a variety of physical phenomena in diverse environments.

The explosion which precedes the expansion of the remnant is so luminous that it can sometimes be observed by eye. Several remnants observed today can be related to the sudden appearance of "guest stars" in historical records, and a precise explosion date can be attributed in some cases. Supernova remnants are not only remnants of dead stars, but also remnants of our past. This remark gave rise to a fascinating field at the interface between physics and history, reviewed in the book by Clark and Stephenson (1977), which provides an exhaustive list of historical testimonies. All of them are worth reading and a few excerpts will be reproduced below for illustration.

[1] In reality the velocity is not constant in this early phase but obeys a slow self-similar decrease which behaviour depends on the properties of the ambient medium (Chevalier, 1982a; Truelove and McKee, 1999). I should not enter into these subtleties now.

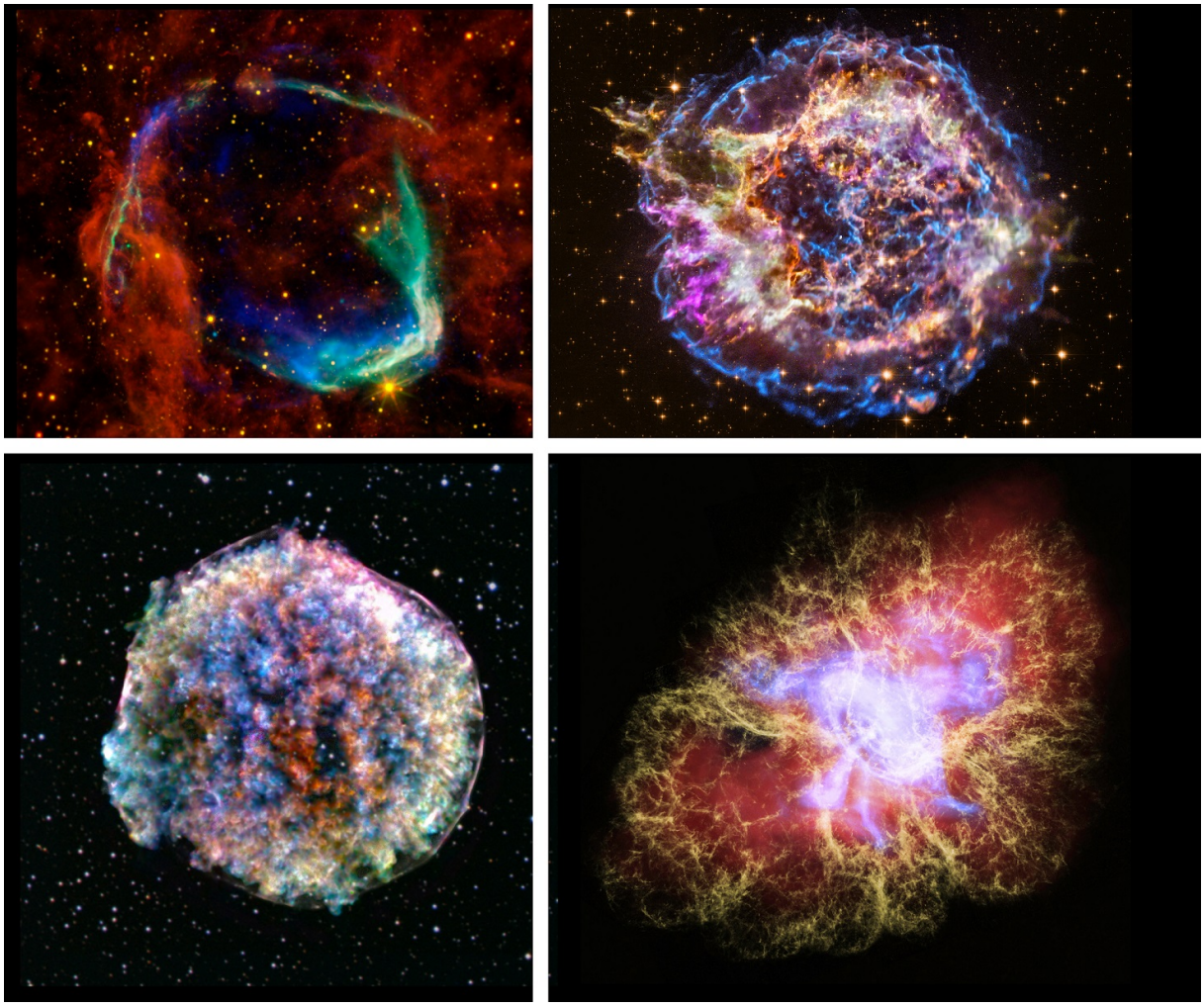

Figure 1.2: Multi-wavelength observations of four supernova remnants "superstars". Top left: RCW86. Top right: Cassiopeia A. Bottom left: Tycho remnant. Bottom right: Crab nebula. From the Chandra observatory website.
Credits: NASA/CXC/SAO&ESA (RCW86 X-ray), NASA/JPL-Caltech/B. Williams (RCW86 IR), NASA/CXC/RIKEN/T. Sato et al. (CasA X-ray), NASA/STScI (CasA optical, Crab optical), NASA/CXC/SAO (Crab and Tycho X-ray), NASA/JPL-Caltech (Crab IR), DSS (Tycho optical)

RCW86

The oldest established historical supernova exploded in 185. It is mentioned in the *Hou-han-shu*, a East-Asian historical record. The relevant excerpt is translated as follows by Clark and Stephenson (1977):

2nd year of the Chung-p'ing reign period, 10th month, day kuei-hai, a guest star appeared within Nan-men [α and β Centaurii]. *It was as large as half a mat; it was multicoloured and it scintillated. It gradually became smaller and disappeared in the 6th month of the year after next. According to the standard prognostication this means insurrection. When we come to the 6th year, the governor of the metropolitan region Yü an-shou punished and eliminated the middle officials. Wu-kuang attacked and killed Ho-miao, the general of chariots and cavalry, and several thousand people were killed.*

The date of first appearance corresponds in our calendar to December 7th 185 A.D. It is not entirely sure that this would have corresponded to a supernova explosion, in particular because there is no other known record mentioning it, but the duration of the reported event disfavours a nova or a comet. Moreover, there does exist a supernova

remnant in the corresponding region, with an age of about 2000 yr. It is designated as RCW86, has a radius of about 18 pc and has likely resulted from an extremely bright type Ia supernova which would have been visible by eye during 20 months. A composite image of the remnant is shown in the top left panel of Figure 1.2. The blue and green colours correspond to the thermal X-ray emission of the gas heated to millions of degrees. The infrared band in red originates from the radiation of warm dust.

Under the reign of the successive East-Asian dynasties, several other "guest stars" have been reported in historical records such as the *Sung-shu* or the *Chin-shu*. Possible supernova explosions might have been observed in 369, 386, 393. It is likely that the latter corresponds to the remnant RX J1713.7-3946, which has a compatible position and estimated age.

SN 1006

Six centuries later, several Asian, Arabic and European records mention the appearance of a very bright new star. Here follow two testimonies, one Arabic and one European, compiled in Clark and Stephenson (1977).

I will now describe a "spectacle"[2] *which I saw at the beginning of my studies. This spectacle appeared in the zodiacal sign Scorpio, in opposition to the Sun. The Sun on that day was 15 degrees in Taurus and the spectacle in the 15th degree of Scorpio. This spectacle was a large circular body, 2.5 to 3 times as large as Venus. The sky was shining because of its light. The intensity of its light was a little more than a quarter of that of moonlight. It remained where it was and it moved daily with its zodiacal sign until the Sun was in sextile with it in Virgo, when it disappeared at once.* [Follows a list of the positions of the planets in the sky at the time of the observation]. *The spectacle occurred in the 15th degree of Scorpio.* [...] *Because the zodiacal sign Scorpio is a bad omen for the Islamic religion, they bitterly fought each other in great wars and many of their great countries were destroyed. Also many incidents happened to the king of the two holy cities. Drought, increase of prices and famine occurred, and countless thousands died by the sword as well as from famine and pestilence. At the time when the spectacle appeared calamity and destruction occurred which lasted for many years afterwards.*

All ibn Ridwan, *Commentary on the Tetrabiblos of Ptolemy.*

1006. A new star of unusual size appeared, glittering in aspect, and dazzling the eyes, causing alarm. In a wonderful manner this was sometimes contracted, sometimes diffused, and moreover sometimes extinguished. It was seen likewise for three months in the inmost limits of the south, beyond all the constellations which are seen in the sky.

Annales Sangallenses Majores (monastic chronicles).

This type Ia supernova is thought to be the most luminous of all historical supernovae. Its remnant is nowadays observed as a clumpy sphere in X-rays. Its gamma-ray emission is a valuable source of information for probing on-site particle acceleration.

[2] In order to not overinterpret the words *athar* and *nayzak*, Clark and Stevenson chose to translate them invariably by *spectacle*.

Crab nebula

The crab nebula (see Figures 0.6 and 1.2) is an outstanding region in the Taurus constellation which displays a variety of phenomena, from plasma instabilities to particle acceleration. At the centre of the nebula, a highly magnetised pulsar is spinning at a very fast speed, ejecting a wind in its equatorial plane and jets of matter from its poles. The nebula blown by the pulsar wind is 1000 years old with a diameter of about 3 pc. It displays a filamentary structure which is caused by the Rayleigh-Taylor instability. Its non-thermal X-ray and gamma-ray emission are due to the interactions of very energetic electrons. Being the brightest gamma-ray source in the sky, it is the *standard candle* of gamma-ray astronomy and has been extensively studied.

In comparison to that of SN 1006, the explosion at the origin of the Crab nebula in 1054 was rather faint. Nevertheless, several records make mention of its appearance, with details about its size, brightness and colorimetry (although one should take caution in interpreting the latter literally). Among the numerous records, two from East Asia are particularly suggestive, mentioning a star "visible in daytime" and "as large as Jupiter":

Earlier, during the 5th month in the 1st year of the Chih-ho reign period [the guest star] *appeared in the morning in the east guarding T'ien-kuan. It was visible in the daytime, like Venus. It had pointed rays on all sides and its colour was reddish-white. Altogether it was visible for 23 days.*

Sung-hui-ya o ("Essentials of Sung History"), Chang Te-hsiang, under Sung Dynasty.

2nd year, chia-wu (of the Tenki reign period), 4th month. A great star appeared in the degrees of Tsui and Shen. It was seen in the east and flared up at T'ien-kuan. It was as large as Jupiter.

Ichidai yoki (volume l), unknown author.

Tycho supernova

Jumping several centuries later, we arrive at one of the most famous historical supernova, which has been observed in Europe by the Danish astronomer Tycho Brahe. The event is detailed in the report *De Nova Stella* published in 1573. From the indications given by Brahe, the position of the remnant can be narrowed down to a few arc minutes and there is no doubt that it corresponds to what is now called the Tycho remnant.

The description of Brahe's first observation is written in *Astronomiae Instauratae Progymnasmata*:

When on the above mentioned day [November 11 1572] *, a little before dinner I was returning to that house, and during my walk contemplating the sky here and there since the clearer sky seemed to be just what could be wished for in order to continue observations after dinner, behold, directly overhead, a certain strange star was suddenly seen, flashing its light with a radiant gleam and it struck my eyes. Amazed, and as if astonished and stupefied, I stood still, gazing for a certain length of time with my eyes fixed intently upon it and noticing that same star placed close to the stars which antiquity attributed to Cassiopeia. When I had satisfied myself that no star of that kind had ever shone forth before, I was led into such perplexity by the unbelievability of the thing that I began to doubt the faith of my own eyes, and so, turning to the servants who were accompanying me, I asked them whether they too could see a certain extremely bright star when I pointed out the place directly overhead.* [...] *And at length, having confirmed that my vision was not deceiving me, but in fact that an unusual star existed there, beyond all type, and marvelling*

that the sky had brought forth a certain new phenomenon to be compared with the other stars, immediately I got ready my instrument. I began to measure its situation and distance from the neighbouring stars of Cassiopeia, and to note extremely diligently those things which were visible to the eye concerning its apparent size, form, colour and other aspects.

Indeed, the observations made by Brahe were very detailed and accurate. In Europe, this supernova explosion created many debates and somehow a scientific revolution since it showed that the universe was not immutable, in contrast with the Aristotelian modelling of the universe which was still the dominant theory in the XVIth century.

Today, Tycho's supernova remnant is observed in X-rays as a very clumpy sphere of diameter about 12 pc (see bottom left panel of Figure 1.2). The origin of the clumps is still discussed. A possible explanation is that the type Ia explosion was asymmetric and triggered at multiple positions at the same time Ferrand et al. (2019).

As Tycho Brahe died in 1601, he could not see the event which occurred three years later, in 1604. Fortunately for us, Johannes Kepler, born in 1571, was there to witness it and describe it in details in his *De Stella Nova in Pede Serpentarii*. This other historical supernova has been named after him.

Cassiopeia A and modern observations

Cassiopeia A is a young remnant which originated from a type IIb supernova, with a current age of approximatively 300 yr and a diameter about 3 pc. In X-ray it is seen as a very aesthetic object, as displayed in the top right panel of Figure 1.2. The white dot at the centre of the image is the neutron star onto which the massive star has collapsed. The filaments of cool gas (around 10^4 K) are observed in visible yellow light. The blue false colour traces the high energy X-ray emission at the location of the blast wave, while other colours track the emission of different elements: silicon in red, sulphur in yellow, calcium in green, iron in purple.

Although the star at the origin of Cassiopeia A is expected to have exploded in the late XVIIth century, there is no established historical record mentioning it, apart maybe from John Flamsteed's catalog (1680), but the position given by Flamsteed is about 10 arcmin away from the observed remnant, which is much larger than the typical error of his other observations (Green and Stephenson, 2003). Interestingly, the fact that Cassiopeia A was not observed by eye imposes an upper bound on the luminosity of the explosion, which is a crucial information for the study of the remnant.

With modern telescopes, many remnants have been spotted whose explosion could not be seen by eyes. In 1987, a supernova was caught in the Large Magellanic Cloud, which gave the opportunity to study a remnant in the first decades of its expansion.

Up to now, 294 supernova remnants have been identified in the Milky Way (Green, 2019) and many others in nearby galaxies such as the Large Magellanic Cloud (Maggi et al., 2016; Bozzetto et al., 2017), the Small Magellanic Cloud (Maggi et al., 2019) or M31 and M33 (e.g. Sasaki, 2020, and references therein)

If the appearance of "guest stars" have amazed civilisations for millennia, affecting folks in such a deep way that it could sometimes justify wars, or revolutionising the human comprehension of the nature of the universe, it is still wondering to witness the evolution of very distant astronomical objects over human timescales (see e.g. https://chandra.harvard.edu/photo/2019/firstlight/).

1.2 Bubble structure and evolution

Having discussed the properties of massive clusters and massive stars, let us now consider the stellar feedback on their surrounding medium. At the smallest scales within dense molecular clouds, the feedback from recently formed massive stellar clusters in the surrounding gas carves several local cavities which are called *wind-driven bubbles*. These bubbles are pressurised by the mechanical input imparted by the stars so they rapidly expand within the molecular cloud and eventually coalesce, forming large-scale *superbubbles*. I shall now review the hydrodynamic theory of superbubbles.

1.2.1 Hydrodynamic theory of wind-driven bubbles

Point-like energy deposition

The hypothesis at the basis of the standard theory of interstellar bubbles is that there is an input of mechanical luminosity[3] L_* in some region of space, under the form of a supersonic matter outflow of velocity V_w which creates an expanding shock far away from the region of energy injection. The first derivation of the bubble structure and evolution in such context was established by Avedisova (1972), Falle (1975), and Castor et al. (1975), where the mechanical input was assumed to be imparted by a single star in a uniform medium. This modelling can be equally applied to the case of a star cluster, providing that the mean distance between the stars is much smaller than the radius of the bubble.

Unlike isolated supernova remnants, wind-bubbles are driven by a constant input of matter. Their total mass therefore increases progressively. At the early stage of the bubble evolution, the dynamics of the bubble is exclusively driven by the cluster luminosity and the density of the external medium ρ_0. The expansion of the external shock follows an adiabatic evolution: $R_b = \alpha(L_* t^3/\rho_0)^{1/5}$, with $\alpha = O(1)$ a numerical constant. During this early phase, most of the swept-up mass is accumulated in a shell delimiting the boundary of the bubble.

The bubble can be described as sketched in Figure 1.3. Mechanical energy is injected under the form of a supersonic steady wind around the cluster. This creates a termination shock at a radius R_s. Beyond this radius lies the bubble *interior* through which flow the shocked winds. The interior is limited by a contact discontinuity at a radius R_c, which corresponds to the transition between the shocked winds and the shocked interstellar medium[4]. The interstellar medium is indeed shocked at a radius R_b, which corresponds to the position of the external bubble shock. The region between R_c and R_b is referred to as the *shell*.

As it expands, the external shock slows down and the shocked material accumulated in the shell cools down. The cooling time of the shell is estimated as $t_c \sim 10\,(L_{38}^3/n^8)^{1/11}$ kyr, where L_{38} is the mechanical power of the cluster in units of 10^{38} erg/s and n the number density in units of cm^{-3} (Koo and McKee, 1992a). Different assumptions for the functional form of the cooling function lead to similar estimates. The shell therefore becomes radiative very early in the bubble evolution and collapses onto a thin region, such that $R_b \sim R_c \gg R_s$. In contrast, the cooling time of the bubble interior as computed by

[3] As it is customary in the field, throughout this manuscript we may use the term "mechanical luminosity" or "luminosity" in short to refer to the mechanical power of the stars or clusters.

[4] In this chapter and in most of the following, the "interstellar medium" refers to the medium beyond the forward shock of the superbubble. The hot phase inside the superbubble is referred to as the "interior".

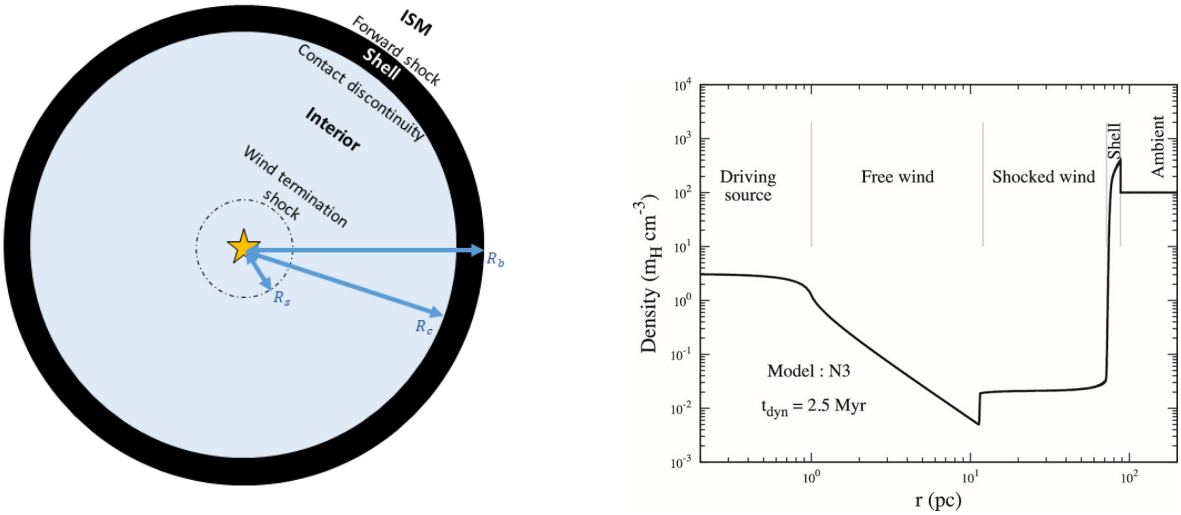

Figure 1.3: Left: Sketch of an interstellar bubble. Right: Density profile computed in numerical simulations, adopted from Gupta et al. (2018).

McCray and Kafatos, 1987 reads, as function of the frequency of supernova explosions ν:

$$t_{c,int} \approx 12 \left(\frac{\nu}{\mathrm{Myr}^{-1}}\right)^{0.3} \left(\frac{n_0}{1\ \mathrm{cm}^{-3}}\right)^{-0.7} \mathrm{Myr}\,. \tag{1.2}$$

As shown by the recent simulations performed by El-Badry et al. (2019), this is only a rough scaling which actually underestimates the interior cooling time as it does not take into account the cooling at the interface, which modifies the properties of the interior. El-Badry et al. (2019) concluded that the interior would actually never become radiative before the end of the cluster life, a statement which is valid in a broad region of the parameter space. Radiative losses in the interior region are usually neglected.

Under the assumption that the shell is very thin, its dynamics is only determined by the pressure of the bubble interior P. Conservation of momentum accross the interface reads:

$$\frac{\mathrm{d}}{\mathrm{d}t}\left(M\dot{R}_b\right) = 4\pi R_b^2 P\,, \tag{1.3}$$

where $M = \int_0^{R_b} 4\pi r^2 \rho_0 \mathrm{d}r = 4\pi R_b^3 \rho_0/3$ is the total mass swept up and accumulated in the shell over the expansion of the bubble in a uniform medium of density ρ_0. On the other hand, the equation for energy conservation in the bubble interior determines the variation of the internal energy as:

$$\frac{\mathrm{d}U}{\mathrm{d}t} = L_* - 4\pi R_b^2 \dot{R}_b P - L_r\,, \tag{1.4}$$

where L_r encompasses the losses, for instance the radiative losses or the energy lost by thermal conduction across the shell.

Since the bubble expands adiabatically, the internal energy is related to the pressure through $U = PV/(1-\gamma)$ where V is the volume of the bubble interior and γ the adiabatic index of the gas. The system of differential equations described above can then be solved to obtain the radius of the superbubble at a given time. In the following I provide a simplified treatment of the losses based on the assumption that one can define a fraction ξ such that $L_r = (1-\xi)L_*$. In reality, the loss term is a complicated function which not only depends on the cooling function, but also rely on the instability mechanisms driving

the generation of the turbulence, or the interactions with non-thermal particles. More realistic models and simulations will be discussed later. Under the assumption that the losses are proportional to the luminosity, a simple self-similar scaling is obtained as:

$$R_b = \left(\frac{125}{154\pi}\right)^{1/5} \left(\frac{\xi L_* t^3}{\rho_0}\right)^{1/5} , \tag{1.5}$$

$$P \approx 0.16 \left(\xi L_*\right)^{2/5} \rho_0^{3/5} t^{-4/5} , \tag{1.6}$$

where $n_0 = \rho_0/(1.4 m_H)$ is the ambient atomic number density, and where we assumed an adiabatic index $\gamma = 5/3$ appropriate for a (nearly) monoatomic gas. In numbers this gives, for the outer radius:

$$R_b = 27 \text{ pc} \left(\frac{\xi L_*}{10^{36} \text{ erg/s}}\right)^{1/5} \left(\frac{n_0}{1 \text{ cm}^{-3}}\right)^{-1/5} \left(\frac{t}{1 \text{ Myr}}\right)^{3/5} . \tag{1.7}$$

The pressure of the bubble interior determines the location of the wind termination shock, for it equilibrates the wind ram pressure as:

$$\frac{\dot{M} V_w}{4\pi R_s^2} = P . \tag{1.8}$$

Using the expression for the pressure obtained above we get, assuming an adiabatic index $\gamma = 5/3$:

$$\begin{aligned} R_s &= \xi^{-1/5} \left(L_*/\rho_0\right)^{3/10} V_w^{-1/2} t^{2/5} \\ &= 6.4 \text{ pc} \left(\frac{L_*}{10^{36} \text{ erg/s}}\right)^{3/10} \xi^{-1/5} \left(\frac{n_0}{1 \text{ cm}^{-3}}\right)^{-3/10} \left(\frac{V_w}{10^3 \text{ km/s}}\right)^{-1/2} \left(\frac{t}{1 \text{ Myr}}\right)^{2/5} . \end{aligned} \tag{1.9}$$

Thermal conduction and mass loading

The interior of the bubble is heated by the energy deposition of the stars, while the mass accumulated in the thin shell cools rapidly to reach a temperature similar to that of the interstellar medium ($T \sim 10^4$ K). There is therefore a thermal flux at the contact discontinuity $r = R_c$, through which thermal energy is tranfered into the shell in exchange to an inward flow of cold shocked interstellar matter which evaporates once it goes through the contact discontinuity. The mass flux from the cold shell to the hot interior is obtained within the classical evaporation theory as (Cowie and McKee, 1977):

$$\dot{M}_b = \frac{16\pi\mu C}{25k} T^{5/2} R_c , \tag{1.10}$$

where T is the temperature of the interior, $\mu \approx 0.6 m_H$ is the mean mass per particle in the interstellar medium beyond the superbubble and $C = 6 \times 10^{-7}$ erg K$^{-7/2}$/s/cm determines the thermal conductivity $\kappa = C T^{5/2}$ (Spitzer, 1962). On the other hand, the average temperature of the interior is by definition obtained from the thermal energy: $E_{th} = 3/2 (M_b/\mu) kT$, which is identified with the internal energy in the case of an ideal gas[5]. Assuming $R_c \approx R_b$, the solution to both equations provide the mean temperature

[5]In fact, turbulence and nonthermal particles may act as energy reservoirs storing a substantial part of the mechanical energy, which would decrease the thermal energy and therefore lower the temperature and density. This will be discussed later.

and atomic density in the interior of the bubble as:

$$n \approx 9 \times 10^{-3}\ \mathrm{cm}^{-3} \left(\frac{\xi L_*}{10^{36}\ \mathrm{erg/s}}\right)^{6/35} \left(\frac{n_0}{1\ \mathrm{cm}^{-3}}\right)^{19/35} \left(\frac{t}{\mathrm{Myr}}\right)^{-22/35}, \tag{1.11}$$

$$T \approx 1.4 \times 10^{6}\ \mathrm{K} \left(\frac{\xi L_*}{10^{36}\ \mathrm{erg/s}}\right)^{8/35} \left(\frac{n_0}{1\ \mathrm{cm}^{-3}}\right)^{2/35} \left(\frac{t}{\mathrm{Myr}}\right)^{-6/35}. \tag{1.12}$$

A detailed resolution of the energy density conservation equation in the bubble interior further provides the radial density and temperature profiles as $n \propto (1 - r/R_b)^{-2/5}$ and $T \propto (1-r/R_b)^{2/5}$ (Weaver et al., 1977). The interior is therefore isobaric as $P \propto nT$, which is expected since the sound crossing time $R_b/c_s < 1$ Myr is smaller than the dynamical time.

Since the works by Weaver et al. (1977), numerous hydrodynamic simulations have been performed, showing a very good agreement with the analytic theory. However the results change significantly when one considers the cooling of the shell, which I will discuss below.

Extended deposition region

In typical clusters, stars are distributed in a region of a few pc[3] (Krumholz et al., 2019). Although this implies that the termination shock is often beyond the cluster, thus produced by the collective outflows of the stars, it also means that the extension of the cluster is not negligible such that the injection of energy can hardly be assumed to be point-like.

The generalisation of the above derivation to the case of a finite distribution of sources was investigated by Chevalier and Clegg (1985) and Cantó et al. (2000). An additional region must be considered in this case, namely the inner part of the cluster delimited by the sphere of radius R_*. Chevalier and Clegg (1985) demonstrated that for $r < R_*$, the velocity profile of the collective wind is an increasing linear function of the radial coordinate. At the boundary of the cluster, beyond which there is no direct injection of mechanical energy, there is a smooth transition from a subsonic to a supersonic flow. For $r > R_*$, the velocity profile is nearly constant and equal to the expected asymptotic value V_w, while the sound speed $c_s = (\gamma P/\rho)^{1/2}$ decreases. The solution computed by Chevalier and Clegg (1985) for a monoatomic gas in the region $R_* \ll r < R_s$ shows that the velocity and density profiles are identical to those obtained in the case of a point-like injection. This implies that the position of the termination shock is unchanged as well, providing it stands far away from the cluster, which is expected given the scaling obtained above. The properties of the region beyond R_s, in particular the expansion of the outer shock and the internal pressure of the bubble, are neither affected by the extension of the cluster. The only variable which is affected in the region $R_* < r < R_s$ is the thermodynamic pressure, which reads:

$$P = 0.011 \left(\dot{M} L_*\right)^{1/2} R_*^{4/3} r^{-10/3}. \tag{1.13}$$

In the limit of point-like injection, i.e. $R_* \to 0$, the pressure is identically zero: a strong wind is emitted which advects all the gas such that the fluid is cold. In this case, the termination shock will be very strong whatever its size. On the other hand, when $R_* > 0$, the radial profile of the pressure decreases faster than the density ($\rho \propto r^{-2}$ and the sound speed $c_s = \sqrt{\gamma P/\rho}$ decreases. The termination shock will therefore be weak if its position

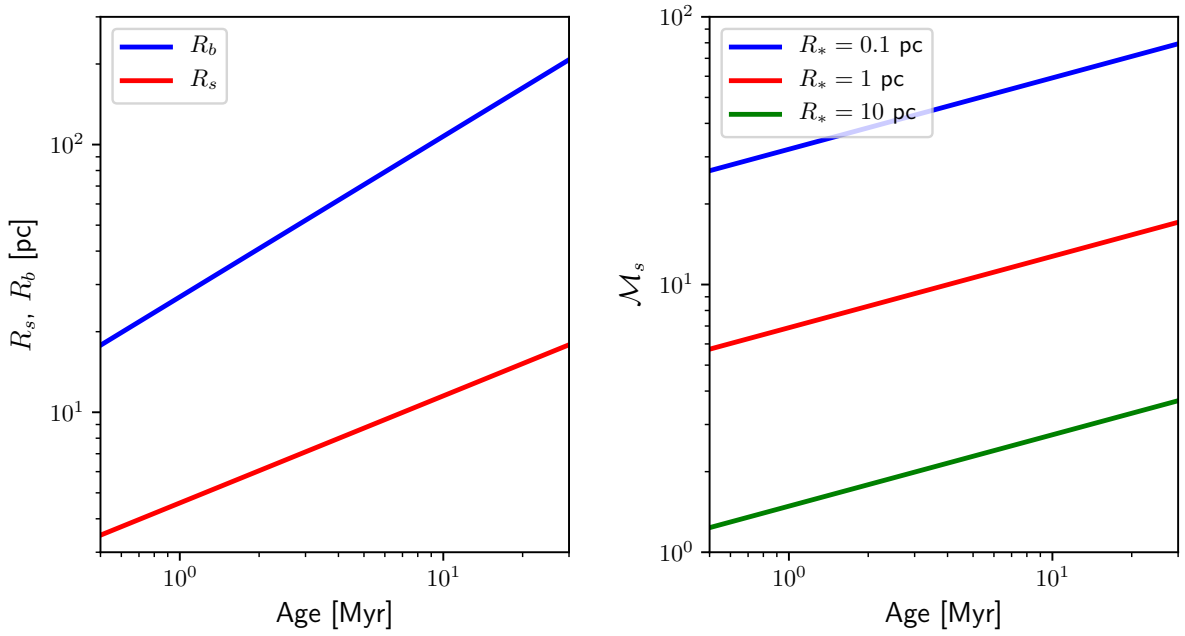

Figure 1.4: Evolution of the structure of a typical superbubble with luminosity 10^{38} erg/s, emitting a collective outflow at 2000 km/s, and with a forward shock expanding in a medium of density 100 cm^{-3} (we assumed $\xi = 1$). Left: Radius of the forward shock R_b and radius of the wind termination shock (reverse shock) R_s. Right: Mach number of the wind termination shock assuming various cluster sizes.

is close to the radius of the cluster. The Mach number of the fluid at $r = R_s$ reads:

$$\mathcal{M}_s \approx 2.5 \left(\frac{R_s}{R_*}\right)^{2/3} \tag{1.14}$$

$$\approx 2.5 R_*^{-2/3} \xi^{-2/15} \left(L_*/\rho_0\right)^{1/5} V_w^{-1/3} t^{4/15} . \tag{1.15}$$

In principle $\mathcal{M}_s$ is not the Mach number of the shock but the Mach number of the flow at the radial coordinate $r = R_s$. The discrepancy is due to the expansion of the shock, which for typical values of the parameters becomes quickly negligible when compared with the velocity of the flow.

In the case of a point-like energy injection, the wind is cold thus the shock is always strong. However, when the extension of the cluster is accounted for, the Mach number becomes time-dependent. As the termination shock expands, the incoming fluid is cooler and cooler and the strength of the shock increases.

As seen in the right panel of Figure 1.4, the termination shock is generally weak in the early phase of the cluster history, unless the cluster is confined within a very small radius (< 0.1 pc). The shock becomes strong ($\mathcal{M}_s > 10$) typically after a few Myr for a compact cluster ($R_* = 1$ pc). On the other hand, in the case of an extended cluster ($R_* = 10$ pc), it remains weak ($\mathcal{M}_s < 5$) until the end of the cluster life.

Cantó et al. (2000) performed numerical simulations of a realistic cluster of randomly distributed massive stars. The properties of the collective wind were found in remarkable agreement with the analytical theory. Inside the cluster, a stratified flow was obtained, reflecting the interactions between the individual stars as local features such as bow shocks. Even in this inhomogeneous region, the average profiles were found in good agreement with the analytic scalings, e.g. $u \propto r$.

It should be noted that the above expressions for the size and strength of the wind termination shock have been obtained assuming that the stars supply a constant power over the cluster lifetime, which is not the case in reality. Indeed, after about 10 Myr, all the Wolf-Rayet stars have exploded and the remaining main-sequence stars can barely maintain a collective wind termination shock unless the cluster is very compact. This is not expected to change the dynamics of the superbubble. Individual strong wind termination shocks will form around each massive star, as in the case of a loose association.

Loose associations

If the extension of the stellar cluster is larger than the radius R_s given by Equation 1.9, a collective termination shock cannot form. In this case the group of massive stars is called a loose association, or open cluster. Although the standard theory of wind-driven spherically symmetric bubbles cannot strictly be applied to this system, the expansion of the outer shock (which results from the merging of the *external* individual wind shocks) and the general properties of the bubble interior are expected to be qualitatively similar. The main difference is that massive stars inside loose associations are surrounded by their own wind termination shocks. The modelling of Chevalier and Clegg (1985) can still be applied locally, defining the boundary of the region of energy injection as the smooth transition where the stellar wind becomes supersonic (Gupta et al., 2020). This transition is generally close to the photospheric radius, which is much smaller than the radius of the termination shock (Pauldrach et al., 1986). The energy injection is therefore nearly point-like and the termination shock is very strong.

1.2.2 Supernova-driven superbubbles

The evolution of supernova remnants critically depends on the density of the surrounding medium. In particular, the adiabatic Sedov-Taylor phase starts only when the swept-up mass is equal to the mass of the ejecta, which occurs at a radius and time:

$$r_{ST} = 22 \left(\frac{M_{ej}}{10 M_\odot}\right)^{1/3} \left(\frac{n}{0.01\ \mathrm{cm}^{-3}}\right)^{-1/3} \mathrm{pc}\,, \tag{1.16}$$

$$t_{ST} = 7 \left(\frac{M_{ej}}{10 M_\odot}\right)^{1/3} \left(\frac{n}{0.01\ \mathrm{cm}^{-3}}\right)^{-1/3} \left(\frac{V_{ej}}{3000\ \mathrm{km/s}}\right)^{-1} \mathrm{kyr}\,, \tag{1.17}$$

where M_{ej} and V_{ej} are respectively the mass and velocity of the supernova ejecta, and $n \approx \rho/(1.4 m_p)$ is the atomic number density of the superbubble interior. In the adiabatic phase, the velocity decreases as $v(t) \approx 0.46\,(E_{SN}/\rho)^{1/5}\, t^{-3/5}$, where $E_{SN} \approx 10^{51}$ erg is the energy of the explosion, such that the shock becomes subsonic at the following time and corresponding radius:

$$t_{sub} = 0.18 \left(\frac{E_{SN}}{10^{51}\ \mathrm{erg}}\right)^{1/3} \left(\frac{n}{0.01\ \mathrm{cm}^{-3}}\right)^{-1/3} \left(\frac{T}{5\times 10^6\ \mathrm{K}}\right)^{-5/6} \mathrm{Myr}\,, \tag{1.18}$$

$$R_{sub} = 101 \left(\frac{E_{SN}}{10^{51}\ \mathrm{erg}}\right)^{1/3} \left(\frac{n}{0.01\ \mathrm{cm}^{-3}}\right)^{-1/3} \left(\frac{T}{5\times 10^6\ \mathrm{K}}\right)^{-1/3} \mathrm{pc}\,. \tag{1.19}$$

On the other hand, the radiative cooling becomes important when the age of the remnant equals the cooling time (Blondin et al., 1998):

$$t_{rad} \approx 0.33 \left(\frac{E_{SN}}{10^{51}\ \mathrm{erg}}\right)^{4/17} \left(\frac{n}{0.01\ \mathrm{cm}^{-3}}\right)^{-9/17} \mathrm{Myr}\,. \tag{1.20}$$

Similar estimates are obtained by accounting for a decreasing density profile (Mac Low and McCray, 1988). Many works aimed at modelling and simulating the evolution of supernova remnants in various media, including stratification, inhomogeneities etc. (e.g. Tenorio-Tagle et al., 1991; Tang and Wang, 2005; Jiménez et al., 2019). I shall not review this literature here. For the purpose of this chapter, it is enough to keep in mind the following estimates: supernova remnants in low-density superbubbles expand adiabatically during a few 100 kyr, and reach a radius of about 100 pc. One concludes that the remnants are generally not expected to reach the superbubble shell unless they explode very close to it. This is a convenient simplifying assumption. Indeed, if the momentum of the remnant shell is not directly transferred into the superbubble shell, the shock merges with the ambient material in the hot interior and convert its mechanical energy into heat. The hot interior therefore acts as a buffer storing the energy suddenly injected by supernovae and releasing it progressively. Under this assumption, the dynamics of supernova-driven superbubbles becomes similar to that of wind-driven bubbles, with an equivalent luminosity $L_{SN} = \nu E_{SN}$, where $\nu \approx N_*/35$ Myr is the mean supernova rate assuming that all massive stars explode at the end of their lives (Mac Low and McCray, 1988). Simulations show that only a few supernovae are required to create a superbubble (e.g. Tenorio-Tagle et al., 1987; Krause et al., 2013). The latter are therefore very natural structures.

The overall time-averaged mechanical input of a massive cluster is $L_* = N_* \times 10^{36}$ erg/s, with supernovae contributing up to 90% and winds up to 10%. Again, only a fraction (which we will denote ξ also when supernovae are taken into account) of this available energy is expected to be later transferred into the superbubble shell, even though the remnants never becomes radiative (El-Badry et al., 2019). In particular, the supernova shocks induce random plasma motions, excite hydromagnetic waves and accelerate thermal particles during their expansion, all of these becoming energy reservoirs.

One should keep in mind that if the efficiency ξ is much smaller than unity, or if the external cloud is dense, e.g. 100 cm^{-3} (which is a typical density for molecular clouds), the superbubble is expected to be much smaller and the above approximation may break down. Moreover, the hypothesis of constant mechanical power may not be realistic even for winds, because the Wolf-Rayet winds, which last about 300 kyr, are about two orders of magnitude more powerful than the main sequence winds. Thus, at the end of its life, a star will be, during a short time, as powerful as a whole cluster of a hundred massive stars. Finally, even though star births are correlated in time, the correlation time can be as large as 10 Myr (e.g. Herbst and Miller, 1982; Massey et al., 1989), that is, the luminosity of the cluster is expected to rise as more and more massive stars lit over an extended period. The consequences on the shell dynamics have been investigated in Shull and Saken (1995). They showed that the shell growth is underestimate by a factor of 2-3 in models with constant luminosity, as there should actually be a peak around 15 Myr corresponding to the time where many stars start their Wolf-Rayet phases.

1.2.3 Radiative cooling

As already mentioned, the cooling time of superbubble shells is about 10-100 kyr, which implies that very early in the superbubble evolution the shell collapses into a thin radiative layer, while the radiative losses are always negligible in the interior. If radiative losses are only relevant in a very thin region, one could wonder why we cannot neglect them completely. In fact, a substantial fraction of the internal energy is transferred to the shell

by thermal conduction, without any work done on the shell. This energy is then quickly radiated away at the interface and effectively lost. El-Badry et al. (2019) extended the analytical theory to properly account for the conduction and subsequent cooling in the shell. They defined the fraction θ of input energy lost in the shell, which is analogous to the fraction $1-\xi$ which we introduced above. As far as the radius of the bubble is considered, they retrieved the expectation that the cluster power L_* should be replaced by $(1-\theta)L_*$ in the self-similar scalings. Besides, their numerical estimates provided $\theta \approx 60-80\%$ depending on the interstellar density and more importantly on the efficiency of nonlinear mixing at the interface due to shell instabilities. Indeed, these instabilities modulate the azimuthal profile of the interface, which increases the contact surface and enhances the conduction. Instabilities such as the Rayleigh-Taylor instability also induce more mixing between phases of different temperature. In fact, El-Badry et al. (2019) concluded that the conduction was primarily *driven* by the instabilities. Unfortunately their one-dimensional modelling could not encompass these effects in a proper way and they had to implement an artificial diffusion around the interface. Nevertheless, this provides an interesting order of magnitude estimate for our fraction ξ, which could be as high as few tens of percent.

In the previous section, we computed the internal density and temperature assuming that the classical evaporation theory would hold even in the presence of losses, provided we multiply the cluster luminosity by the fraction ξ. As far as cooling losses are concerned, this is an oversimplification, for the conductive heat flux at the interface should be modified by the cooling. In a attempt to properly describe the mean internal properties of the bubble in this case, El-Badry et al. (2019) derived the following scalings[6]:

$$T \approx 4.5\times10^6\ \mathrm{K}\frac{\theta^{2/7}}{(1-\theta)^{2/35}}\left(\frac{\nu}{\mathrm{Myr}^{-1}}\right)^{8/35}\left(\frac{n_0}{1\ \mathrm{cm}^{-3}}\right)^{2/35}\left(\frac{t}{\mathrm{Myr}}\right)^{-6/35}, \tag{1.21}$$

$$n \approx 5\times10^{-2}\ \mathrm{cm}^{-3}\frac{(1-\theta)^{16/35}}{\theta^{2/7}}\left(\frac{\nu}{\mathrm{Myr}^{-1}}\right)^{6/35}\left(\frac{n_0}{1\ \mathrm{cm}^{-3}}\right)^{19/35}\left(\frac{t}{\mathrm{Myr}}\right)^{-22/35}. \tag{1.22}$$

Equations 1.11 are not retrieved in the limit $\theta \to 0$ because El-Badry et al. (2019) worked out the derivation under the simplifying assumption of a cold shell. For reasonable values of θ (e.g. 50%), the orders of magnitude are similar to that obtained without considering the cooling (a supernova rate of 1 per Myr providing a mean cluster luminosity $L_* \approx 3\times10^{37}$ erg/s). On the other hand, a higher cooling rate (i.e. a higher θ) is expected to *increase* the internal temperature, in contrast with the "naive" scaling which predicted a decrease of both the density and the temperature. This somewhat counter-intuitive result comes from the fact that the internal temperature is primarily determined by the evaporation at the interface. The latter is significantly reduced when the shell is radiative, which overcompensates the heat lost by conduction.

1.2.4 Shell instabilities

In the course of its expansion in the dense interstellar medium, the shell is subjected to various instabilities. These have been briefly reviewed by Ntormousi et al. (2017). The most important ones are the following.

[6] I have corrected a typo in the expression for the density.

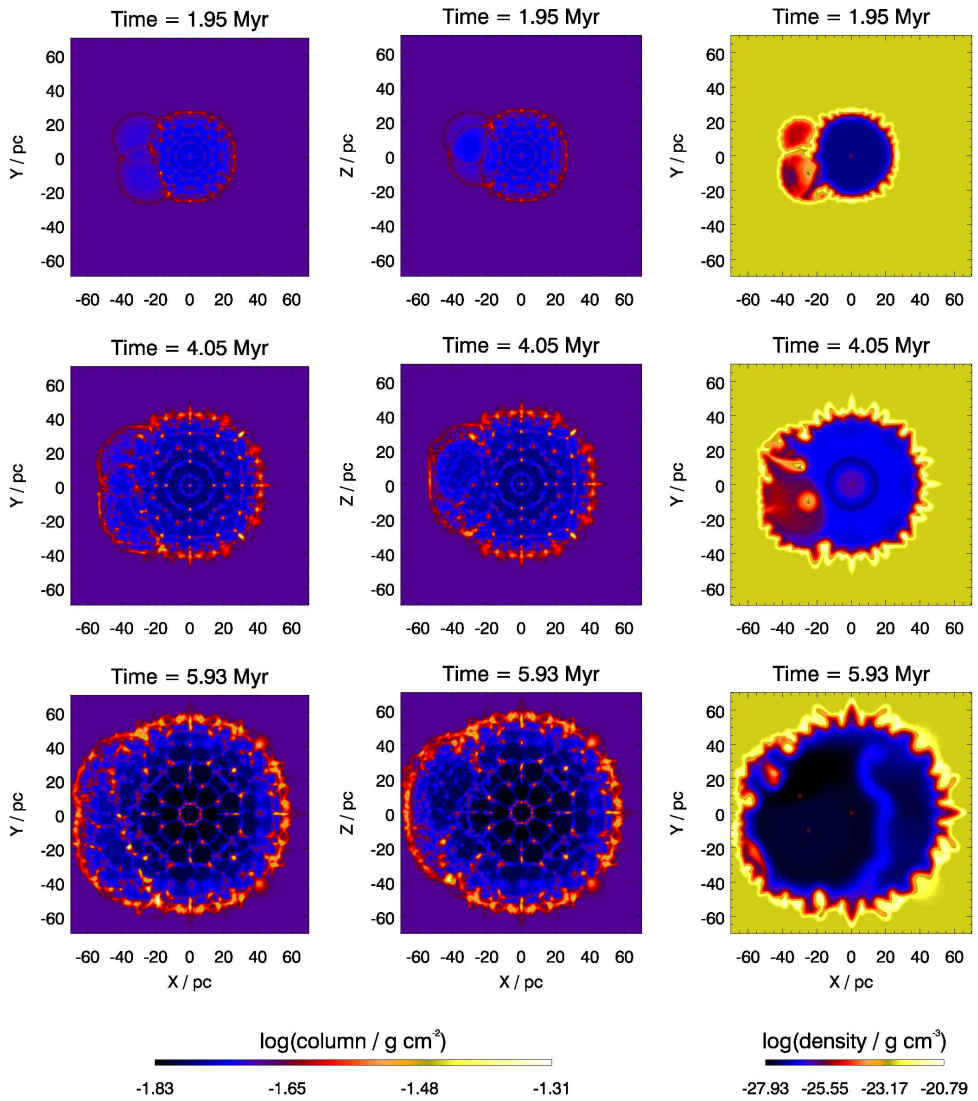

Figure 1.5: Evolution of the column and mid-plane densities of a simulated superbubble following the explosion of three supernovae. The figure is adopted from Krause et al. (2013).

Vishniac instability

When a thin spherical supersonic radiative shell propagates, it converts the ram pressure of the upstream flow into isotropic thermal pressure downstream. The momentum is therefore transferred from the radial to the tangential direction, which ripples the surface of the shell. If the wavelength of the perturbation is larger than the shell thickness, it will grow, deform significantly the surface and may even fragment it. This is a striking property of superbubble shells typically obtained in realistic simulations such as the ones performed by Krause et al. (2013), as shown in Figure 1.5. The growth rate of the instability scales as the inverse of the sound crossing time of the shell (Vishniac, 1983), which gives a fragmentation time of the order of 100 kyr for superbubble environments. The instability is therefore expected to develop very early. As it develops, it increases dramatically the surface of the interface between the interior and the shell, which enhances the thermal conduction.

Rayleigh-Taylor instability

The Rayleigh-Taylor instability is a classical hydrodynamic instability which occurs when a fluid characterised by a density gradient is subjected to a force opposite to the density gradient (Chandrasekhar, 1961). The denser parts of the fluid are more accelerated and penetrate into the more diffuse regions under the form of filaments. The most striking astrophysical example is probably the Crab nebula, which displays extended filaments in visible light.

In the case of an expanding superbubble, the dilute phase is the interior of the bubble (0.01 cm^{-3}), while the denser phase is the interstellar medium or the surrounding molecular cloud (1-100 part/cm^{-3}). The Rayleigh-Taylor instability will appear if the expansion is accelerated, which is a possibility if the bubble expands in the stratified interstellar medium.

Kelvin-Helmholtz instability

If two superimposed fluids move with a non-zero relative velocity, any normal perturbation will grow as an eddy and induce turbulence mixing near the interface (Chandrasekhar, 1961). This instability would not occur if the superbubble shell was expanding purely in the radial direction. However this is not expected in reality, first and foremost because of the aforementioned instabilities. Both Vishniac "ripples" and Rayleigh-Taylor "fingers" are eventually expected to trigger the formation of eddies of various scales. This will generate hydrodynamic turbulence, as we shall discuss later.

Thermal instability

If for some reason a small density fluctuation appears locally in the radiative shell, it will cool faster than the environment and thus the pressure will decrease locally. The overdensity will therefore be squeezed by the environment, thus the density will further increase locally and the cooling will become even faster. This is a runaway instability creating again inhomogeneities and random motions (Field, 1965).

1.2.5 Magnetised medium

A crucial ingredient which is missing in the previously described formalism is the magnetic field. Observations of the hot interstellar medium based on the Zeeman and Faraday effects suggest that the interstellar magnetic field can be as high as 10 µG (Vallée, 2004). However, the magnetic field may be different inside superbubbles. The expanding outer shock is expected to sweep-up the preexisting field, which then accumulates in the shell, while the generation of turbulent hydromagnetic waves by supernovae and stellar winds could amplify the random component in the interior. Observations of HI shells (e.g. Heiles, 1989) show that the magnetic field is about a few microgauss to few tens of microgauss. However, this does not indicate the value in the interior, which is very challenging to probe observationally.

Tomisaka (1990) and Ferriere et al. (1991) were the first to propose a model of superbubble expanding in a magnetised interstellar medium. Solving a magnetohydrodynamic scheme, it was showed that the bubble would expand preferentially in the direction parallel to that of the field, for the field lines would be compressed in the shell and exert a pressure against its expansion in the perpendicular plane. Ferriere et al. (1991) also

noted that the radiative shell should be thickened by the magnetic field, whose pressure prevents the compression.

The compression of the magnetic field lines also induces an anisotropic transport of the electrons in the shell (charged particles would rather follow the field lines than cross them), which lowers the conductivity. This effect can be included phenomenologically by adding a scaling factor κ_0 to the conductivity C in Equation 1.10 (Shull and Saken, 1995). This is a very simplified treatment as the interplay between magnetic fields and thermal conduction is expected to be nonlinear: the magnetic field decreases the thermal conduction, the thermal conduction slows down the radiative shell, the shell compresses the magnetic field. As the internal density and temperature scale as $\kappa_0^{\pm 2/7}$, the bubble properties are only affected if the magnetic suppression is strong.

Since these early works, more and more realistic modelling of superbubbles have been developed. Several physical mechanisms influence the dynamics of superbubbles in non-trivial ways, often acting collectively via various instabilities. Even though analytic approaches are useful to understand the underlying mechanisms, realistic modelling must rely on numerical simulations.

1.2.6 Recent numerical simulations

There have been many efforts in the last decades put towards numerical simulations of superbubbles (Tomisaka, 1998; Korpi et al., 1999; Stil et al., 2009). We already briefly discussed the hydrodynamic simulation performed by Krause et al. (2013) to investigate how a superbubble is formed and evolves after the merging of three supernova remnants. The shell was shown to quickly develop a wavy shape due to the Vishniac instability, and to thicken up to a width about 10% of the radius of the superbubble. Rogers and Pittard (2013) investigated how three massive stars would carve a highly structured dense molecular cloud. They showed that the cloud would resist their feedback during the first million years, until the first supernovae explode, at which point the cloud would be quickly destroyed. An extensive numerical investigation of the most relevant physical ingredients (apart from magnetic fields) was then performed by Sharma et al. (2014). They concluded that the analytic solution obtained by Chevalier and Clegg (1985) for the internal wind profile could only be retrieved for very massive clusters, with more than 10^4 supernovae. Otherwise, supernova remnants cross the wind termination shock before becoming subsonic, which alters the thermodynamic properties of the inner regions. It was also shown, considering radiative cooling, that about 30% of the mechanical input is typically retained as thermal and shell kinetic energy. This is an interesting estimate which can be readily related to the parameter ξ introduced in the previous sections.

Yadav et al. (2017) and Vasiliev et al. (2017) performed three-dimensional hydrodynamic simulations of merging supernova remnants. Most of the results obtained in the one-dimensional model of Sharma et al. (2014) were confirmed. However, the radiative losses were found to reduce the efficiency of conversion of mechanical energy, in particular when the supernovae would explode at intervals larger than the cooling time. Indeed, in this case the remnants become radiative before merging, and most of the energy is lost during the coalescence of the individual shells. The computed efficiencies were of the order of a few percent. The expansion of the superbubble shell was also found to be slightly slower than predicted by the analytical theory, with a scaling $R \propto t^{0.56}$. Gentry et al. (2019) also pointed out, investigating a magnetohydrodynamic model, that the radiative shell would decrease the efficiency. However the amount of energy retained in the shell

was shown to strongly depend on the numerical resolution. Indeed, the finiteness of the grid was proved to artificially increase the conduction rate and convergence could not be reached. As previously discussed, thermal conduction and radiative cooling are non-trivial processes which strongly depend on hydrodynamic instabilities which are very difficult to resolve in numerical codes.

The magnetohydrodynamic model of Gentry et al. (2019) showed that the effect of the magnetic field is also non trivial. On one hand, the magnetic pressure exerted on the shell tends to reduce the growth of the bubble (see also van Marle et al., 2015). On the other hand, the magnetised fluid is less subject to instabilities (see also Ntormousi et al., 2017) and in particular its cooling time increases, which implies the radiative losses are less efficient. It was finally pointed out that shell instabilities, such as the Rayleigh-Taylor and Vishniac instabilities (e.g. Krause et al., 2013), greatly increase the surface of the interface between the interior of the bubble and the shell, thus enhancing the conduction flux, as was later comprehensively studied by El-Badry et al. (2019) (see Section 1.2.3). Since these instabilities can only be captured by 3D simulations, 1D models are only expected to provide upper bounds on the shell momentum.

Eventually, El-Badry et al. (2019) pointed out that the shocks produced by the expanding supernova remnants could left behind several inhomogeneities in the interior, although it is expected that instabilities and conduction would smooth them. In contrast with the simple analytic theory, realistic superbubbles are expected to be inhomogeneous, with substructures such as clumps too massive to be swept-up by the supernova blast waves, or filaments created by the mixing and interpenetration of the various phases of the interstellar medium (Kim et al., 2017).

The magnetohydrodynamic expansion of superbubble shells is not only important for the study of superbubbles, but it also determines the momentum imparted by superbubbles on the interstellar medium, which is a crucial parameter for the study of molecular clouds and star formation. The efficiency of conversion of the star mechanical energy to shell momentum varies by more than one order of magnitude from simulation to simulation, depending on which physical ingredients are included or even on the numerical resolution, for convergence is very difficult to achieve. In particular, an accurate modelling requires to resolve the small-scale instabilities which mix the cold and hot phases at the interface between the shell and the interior. There is still no successful numerical code capable of achieving this.

1.2.7 The fate of the bubble

The expansion of the superbubble can end in two different ways. If the luminosity of the cluster is not large enough, the radius of the shell will remain rather small until the end of the cluster life, and its momentum will be diluted in the surrounding interstellar medium. As the pressure decreases ($P \propto t^{-4/5}$) during the expansion of the shell, it may also become comparable to that of the interstellar medium at some point, in which case the bubble becomes *pressure-confined* (Koo and McKee, 1992a), similarly to a wind termination shock. If the external medium is magnetised, the bubble can also be confined by the magnetic pressure when it has not enough power anymore to work against the compressed field lines (Kamaya, 1998). On the other hand, if the superbubble achieves a size comparable to the height of the galactic disk before the death of the last star, it will not expand in a homogeneous medium anymore, but rather in a stratified interstellar medium which becomes more and more rarefied.

Koo and McKee (1992b) considered a power law ambient density profile $\rho \propto r^{-k_\rho}$ as well as a time-dependent luminosity $L \propto t^{\eta_{in}-1}$. The resulting scalings were modified in various ways. For instance, the adiabatic expansion of the external shock would read:

$$R_s \propto \left(\frac{(3-k_\rho)\xi L_*}{3\eta_{in}\rho_0} \right)^{1/(5-k_\rho)} t^{(2+\eta_{in})/(5-k_\rho)}, \tag{1.23}$$

and similar corrections were demonstrated for the density and temperature profiles. Various phases and bubble types were derived and classified, depending on e.g. the wind velocity, the importance of the radiative cooling in the shell and in the interior. An important conclusion which is readily seen from Equation 1.23 is that the expansion of the bubble is faster in a stratified medium, and the shell will *accelerate* if $k_\rho > 2$ (assuming a constant energy input $\eta_{in} = 1$). For luminous enough clusters, the stratification may even overcome the pressure exerted by a magnetic field parallel to the galactic disk (Tomisaka, 1990; Tomisaka, 1998).

When the size of the bubble becomes comparable to the galactic height, the variation of density along the galactic plane elongates the bubble since it is easier to expand in the direction of low density. The bubble becomes tubular and eventually breaks into the galactic halo (Mac Low et al., 1989). This provides a channel allowing enriched stellar material to flow into the halo, with critical consequences on the dynamics of the entire galaxy (Norman and Ikeuchi, 1989), in particular on star formation rates (Kim et al., 2017; Fielding et al., 2018).

1.3 Turbulence generation

It is expected that the material blown by the stars, when interacting with the surrounding medium, perturbs the plasma, producing large-scale random motions and magnetised waves. This can already occur in the core of compact stellar clusters, where individual winds collide and coalesce into a collective outflow. This was studied by e.g. Walder and Folini (2000) in a 2D hydrodynamic simulation. It was shown that at the interface between the colliding flows, various instabilities occur such as the Rayleigh-Taylor, the Vishniac or the thermal instabilities. The growth of unstable modes leads to mixing and turbulence motion. The medium becomes inhomogeneous, with the development of filaments and knots as well as strong velocity fluctuations, from subsonic to highly supersonic.

Because of the nonlinear nature of the fluid equations, these velocity fluctuations will interact and decay to smaller scales, producing a broad range of hydrodynamic waves described by a turbulence cascade up to the dissipation scale, the latter being typically the mean free path of the thermal particles in the plasma. The temperature gap at the interface between the interior and the shell is also expected to produce small-scale mixing. As the primary source of energy in the bubble is the mechanical input of the stars, it is customary to assume that a fixed fraction of this energy is diluted in turbulence over the bubble volume V_b, without specifying the microphysics. The average rate of turbulence generation is written as $S = \eta_T L_*/V_b$, where η_T is the conversion efficiency. The corresponding random magnetic field and mean velocity dispersion can be obtained from simple dimensional grounds assuming the equipartition of the turbulent energy between the hydrodynamic and magnetic waves as $\delta B^2/4\pi \sim \rho \delta u^2 \sim \left(\sqrt{\rho} S \lambda_m\right)^{2/3}$, where $\lambda_m \sim 1-10$ pc is the injection scale which it is natural to take as the average distance between the stars. For a young cluster of a few hundreds massive stars, i.e. luminosity about

10^{38} erg/s, and an efficiency $\eta \sim 10\%$, this provides $\delta u \sim v_A \sim 10 - 100$ km/s and $\delta B \sim 1 - 10$ µG.

The question of the turbulence generation inside molecular clouds is of prime importance for the study of star formation, as turbulence is believed to be a main factor triggering the collapse of local clumps in which newborn stars lit. Recent numerical simulations (Gallegos-Garcia et al., 2020) suggest that about 30% of the mechanical energy of the young massive star clusters goes into turbulent motions. Superbubble are therefore expected to be highly turbulent environments, storing hydromagnetic energy which dissipates within the hot interior.

The turbulence is described by its power spectrum $W(k)$, that is, how much energy is stored per wavenumber bands. The aforementioned simulations converged towards stationary power law wind-driven turbulence spectra with indices lying somewhere in between 1.5 - 2, compatible with the Kraichnan scaling ($W(k) \propto k^{-3/2}$), Kolmogorov's scaling ($W(k) \propto k^{-5/3}$) as well as the Burger's scaling ($W(k) \propto k^{-2}$). Accurate numerical simulations of hydromagnetic turbulence are still very challenging and the resulting power spectra often depend substantially on the adopted resolution (e.g. Offner and Arce, 2015). On the other hand, the kinematic signatures of random gas motions in superbubble interiors are difficult to observe. At the moment, there is to my knowledge no consensus on what turbulence regime should be expected within wind-blown interstellar bubbles.

Supernova remnants are expected to produce turbulent motions as well, in particular by means of plasma instabilities when they merge with the surrounding medium at the end of their expansion. While this has been quite extensively investigated in the context of the general interstellar medium outside superbubbles (e.g. Chamandy and Shukurov, 2020), less work have been done on supernova remnants expanding inside superbubbles. It is usually assumed that most of the energy of a remnant shell goes into turbulent motions when its velocity becomes comparable to the ambient sound speed. Because most of the energy has been radiated away during the snow-plow phase, this typically represents only 10% of the supernova energy for a supernova merging with the interstellar medium (Thornton et al., 1998; Tamburro et al., 2009). However, this value strongly depends on the ambient density. In low-density superbubbles, the supernova remnants become subsonic before becoming radiative and one could expect a strong enhancement of the turbulence generation. For instance, looking at the results obtained by Thornton et al. (1998), we observe that in a medium of density 0.01, about 30% of the supernova energy remains kinetic when the remnant velocity reaches the sound speed.

A major difference between supernovae and winds is that supernovae only inject energy in the ambient medium during a relatively short time. The turbulence is therefore expected to decay. The simulations performed by Krause et al. (2013) and Padoan et al. (2016) show that the energy input of supernova remnants retained in the bubble decays with a characteristic time around 1 Myr. The injection peak is about 20-40% of the input energy. This suggests that the energy input of the turbulence from supernovae can be phenomenologically written as $S = \eta_T E_{SN} \exp(-t/\tau)/\tau$, where $\eta_T \sim 30\%$ is in principle different from the conversion fraction of the wind energy, although of the same order of magnitude. While for winds the injection scale is usually assumed to be the typical distance between the stars, i.e. 1-10 pc, the supernova remnants are expected to inject turbulence on scales about the thickness of the postshock region, i.e. 50-100 pc (Padoan et al., 2016; Chamandy and Shukurov, 2020).

The interior of a superbubble can be a very clumpy medium, for dense knots cannot be swept-up by the expanding superbubble shell. These strong inhomogeneities are ex-

pected to increase the generation of turbulence by supernova remnants. When the forward shocks encounters a clump, it will produce a transmitted wave and a reflected one. If the supernova rate is high enough, this can result in a collection of stochastic shocks, that is, a strong supersonic hydrodynamic turbulence (Bykov, 1982; Parizot et al., 2004).

The spectrum of supernova-driven turbulence is still poorly constrained. Numerical simulations and observations are compatible with spectral indices from -1.5 to -2 (e.g. Korpi et al., 1998; Balsara et al., 2004; Padoan et al., 2016; López-Coto and Giacinti, 2018). In the simulations by Padoan et al. (2016), the magnetic field was not found to be amplified significantly by the supernova explosions, although the interacting supernovae were shown to produce a velocity spectrum scaling as k^{-2} in the inertial range. The hot interior of superbubbles is likely to be a non trivial collection of random motions and magnetised waves, which may not be describable by simple power law components.

1.4 Observations of superbubbles

Early bubble models were motivated by optical and UV observations of circumstellar environments (e.g. Mathews, 1967; Jenkins and Meloy, 1974). At the same time, large-scale structures were identified in the Large Magellanic Cloud and in the Milky Way, such as supershells (e.g. Heiles, 1979), "worms" (e.g. Heiles, 1984) and superbubbles (e.g. Cash et al., 1980). It was early realised that all these classes of objects with sizes ranging from stellar to galactic scales could have been formed by outflows produced by massive stars and stellar associations (Bruhweiler et al., 1980). Individual stars, in particular O-type, B-type and Wolf-Rayet stars, would blow *circumstellar bubbles* with radii of the order of a few pc. Compact stellar clusters, producing collective outflows, would create *interstellar bubbles* with radii around 10 pc. In star forming regions hosting several clusters or associations, these bubbles would coalesce into large-scale *superbubbles* with sizes about 100 pc. *Superbubbles* would then expand to create *supershells* extending on several hundreds of parsecs, and these would stretch perpendicularly to the galactic plane to eventually break out into the galactic halo, with *worms*-like shapes.

Since then, this scenario has been confirmed and many such objects have been discovered (see Chu, 2008, for a brief review). Telescopes such as FUSE (UV), XMM-Newton and Chandra (X-rays) allow to constrain the physical properties of the interiors and shells. Optical measurements probe the density, radius, and velocity of the shells. UV measurements allow to infer the properties of the massive stars, in particular the mass loss rate and the velocity of their winds. The X-ray spectra constrain the temperatures and chemical composition of the hot plasmas.

In the following I selected a few archetypal examples of bubbles and superbubbles observed in the Milky Way and in the Large Magellanic Cloud, in order to briefly describe their properties.

1.4.1 Circumstellar bubbles

Bubbles blown by individual massive stars are difficult to detect because they are delimited by weakly supersonic shells, which do not produce a strong density contrast with the background. Nevertheless, we do observe several of such bubbles, including for instance the Bubble nebula, S308, the Crescent nebula or the Thor's Helmet nebula shown in Figure 1.6.

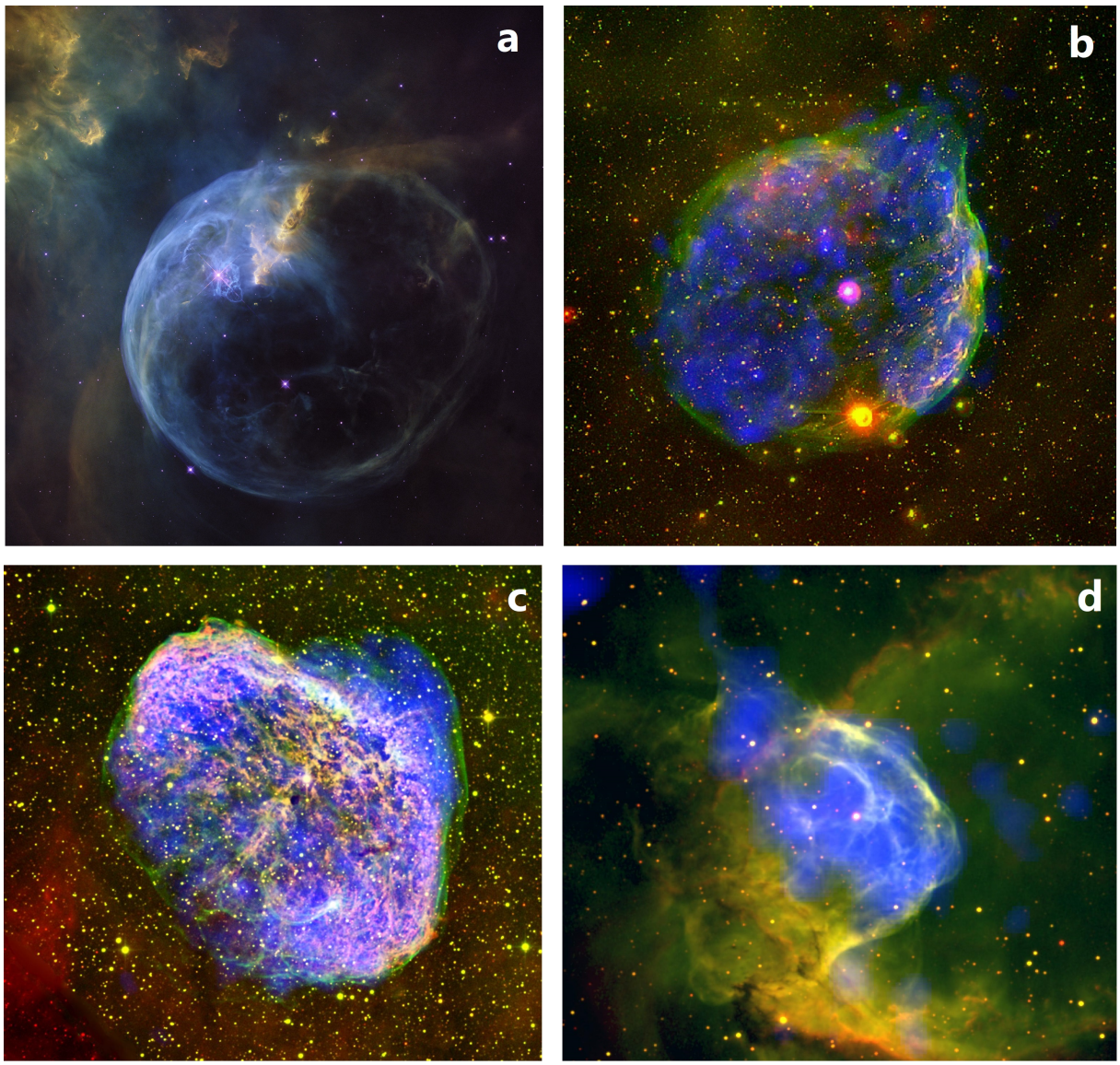

Figure 1.6: Composite images in optical lines and soft X-ray bands of three well-observed galactic circumstellar bubbles: the Bubble nebula (a), S308 (b), the Crescent nebula (NGC6888) (c), the Thor's Helmet nebula (d).
Credits: **Bubble nebula**: NASA, ESA, Hubble Heritage Team. **S308**: J. A. Toala and M. A. Guerrero (IAA-CSIC), Y.-H. Chu and R. A. Gruendl (UIUC), S. J. Arthur (CRyA - UNAM), R. C. Smith (NOAO/CTIO), S. L. Snowden (NASA/GSFC) and G. Ramos-Larios (IAM), ESA/XMM-Newton. **Crescent nebula**: J. A. Toalá, M. A. Guerrero, Y.-H. Chu et al. and ESA. **Thor's Helmet nebula**: J. A. Toala and M. A. Guerrero (IAA-CSIC), Y.-H. Chu (UIUC/ASIAA), R.A. Gruendl (UIUC), S. Mazlin, J. Harvey, D. Verschatse and R. Gilbert (SSRO-South) and ESA/XMM-Newton.

The Bubble nebula, discovered in 1787 by William Herschel, is viewed as a very neat spherical bubble with a diameter of 2.3 pc. Located at a distance of 2.7 kpc, it is ionised by the massive star BD+60°2522, which is about 4 Myr old, has a mass of $27M_\odot$ and blows a wind at 2000 km/s, losing $1.3\times10^{-6}M_\odot$ per year. The interstellar medium beyond the circumstellar shell is dense (about 100 cm^{-3}), and so is the shell. The star is seen off-centred in the Northern-East[7] This may be the sign that the bubble expands in an inhomogeneous medium, with smaller density in the south-west.

If the star is powerful enough to blow a bubble visible in optical wavelengths, no X-ray emission has been detected by the recent investigation of Toalá et al. (2020), which is at odd with the predictions of the standard bubble theory. It has been suggested that this bubble is in fact not a true wind-blown bubble, but rather a superposition of nested bow shocks which could be created if the star moves towards the northern rim in a stratified medium (Green et al., 2019). However, even if it is the case, the strong stellar wind interacting with the dense interstellar medium should emit X-rays, unless there is a strong extinction along the line of sight which prevents the radiation to reach us. Another possibility that has been suggested to explain the lack of X-ray emission is that the interface between the shell and the interior is so stable that there is a minimal conduction flux which induces an inefficient mass loading. The density of the interior would be so low that the X-ray emission would not be detectable. The Bubble nebula, although well-known and well studied, is still a very mysterious object.

The S308, a circumstellar bubble of diameter 18 pc located at 1.5 kpc and powered by the Wolf-Rayet star HD 50896, is observed in X-rays (Chu et al., 2003; Toalá et al., 2012), as shown in the upper right composite image of Figure 1.6. The diffuse X-ray emission at 0.1 - 1 keV is seen both in the thick ionised shell and interior (blue colour). It is well-confined within the bubble, even in the north-west blowout where it is well below the optical shell visible in [OIII](green) and Hα (red). The shell has a diameter of about 18 pc, in agreement with the theoretical scaling expected for a bubble blown by a rotating star of initial mass $40M_\odot$. The observed temperature of 10^6 K is however smaller than expected.

Two other bubbles powered by isolated Wolf-Rayet stars and observed in soft X-rays are the Crescent nebula (NGC 6888 Toalá et al., 2016) and the Thor's Helmet nebula (NGC 2359 Toalá et al., 2015), respectively located at 1.26 kpc and 3.67 kpc. They share rather similar properties, with complex morphologies within a few parsecs, interior densities about 0.5 cm^{-3} and temperature about $1-2\times10^6$ K. The Thor's Helmet nebula also displays a rather complex morphology with several blisters and a blow-out in the north-east. It presents a bow shock which indicates that it is a runaway star which left its parent stellar cluster and now moves in the interstellar medium with a supersonic proper motion. A unique feature of the Crescent nebula is its "caps" in the north-east and south-west rims, as well as its blow-out seen in the visible [OIII] line in the north-west. These are probably due to variations in the interstellar density. The winds of the massive star would sweep up the dense material in the north-east and south-west, while it would expand faster in the more dilute north-west region. These features are correlated with strong spatial variations of the X-ray emission, which displays three maxima in each of these regions. This could be due to various mixing efficiencies between the hot plasma and the wind material, or between the hot plasma and the external medium.

[7]Remember that in astrophysical pictures, the east in on the left and the west on the right.

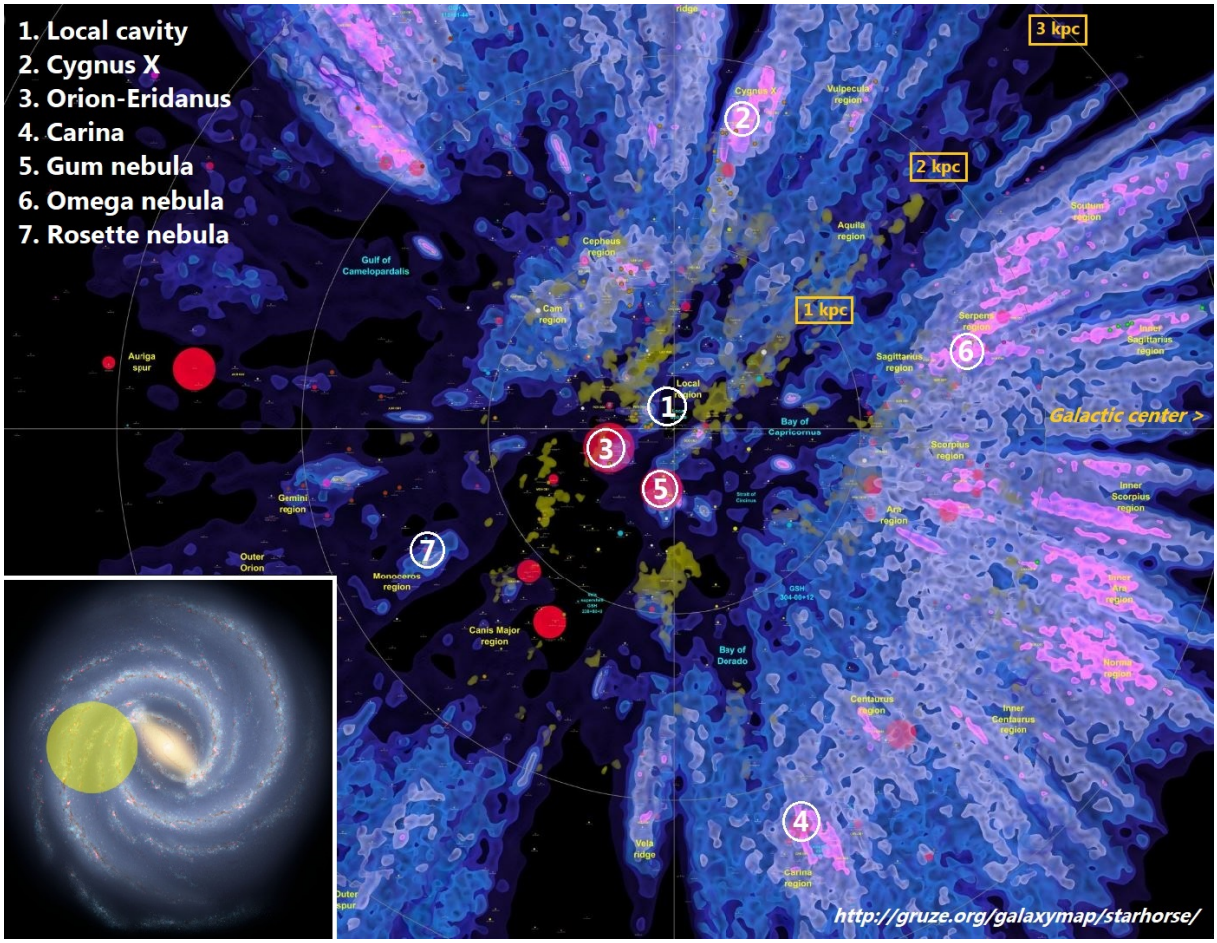

Figure 1.7: Position of well-observed superbubbles in the Orion arm. The orthographic map is K. Jardine's outstanding work (http://gruze.org/galaxymap/starhorse/).

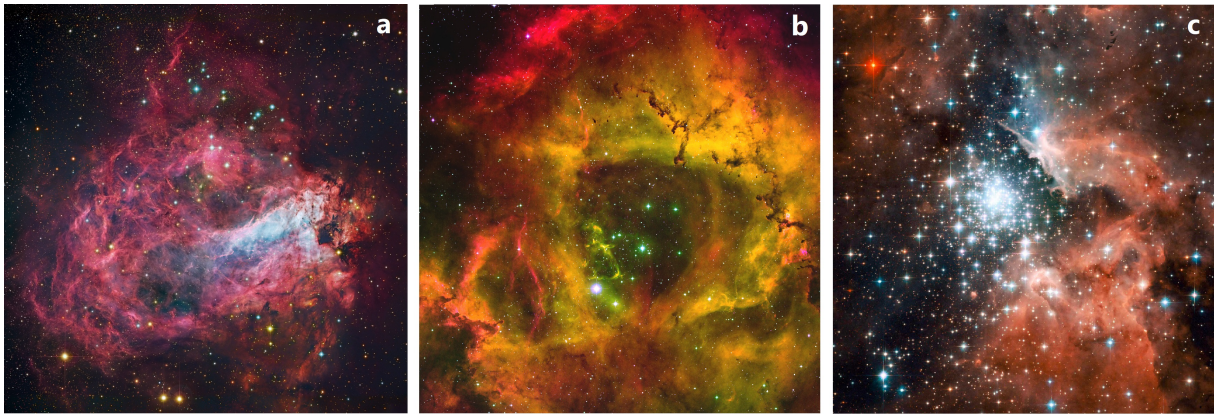

Figure 1.8: Interstellar bubbles. (a) Composite image of the Omega nebula (M17). (b) The Rosette nebula in false colours (SII in blue, [OIII] in green, Hα in red). (c) NGC3603 in three optical wavelengths: 435 nm (blue), 550 nm (green), 850 nm (red).
Credits: **M17**:Copyright 2013 Robert Gendler, Subaru Telescope (NAOJ), HST (composite image). **Rosette**: T. A. Rector/University of Alaska Anchorage, WIYN and NOIRLab/NSF/AURA. **NGC3603**: NASA, ESA, and the Hubble Heritage (STScI/AURA)-ESA/Hubble Collaboration.

1.4.2 Interstellar bubbles

After the brief introduction provided above on circumstellar bubbles blown by individual stars, let us now describe a few young interstellar bubbles, which are blown by star clusters of a few Myr in which no stars have exploded yet. Figure 1.7 provides the locations of most of the galactic objects which will now be discussed.

Omega nebula (M17)

The Omega nebula is a blister-like structure with a radius of 5.8 pc. It is powered by the small cluster NGC 6616, which contains 13 OB stars within a radius of 0.5 pc. It is at most 1 Myr old and its luminosity is estimate around 10^{37} erg/s (Dunne et al., 2003). This bubble is located on the edge of a massive molecular cloud, in a dense and magnetised medium. The shell has a high density of about 300 cm^{-3}. Magnetic fields are believed to inhibit heat conduction, which would explain why the theoretical scalings overpredict the X-ray luminosity by two orders of magnitude. On the other hand, if heat conduction is suppressed, then the bubble would be much hotter than what is observed (8.5×10^6 K). This suggests that the interface is subjected to strong instabilities, or that interstellar clumps which have not been swept-up by the expanding shell are cooling the interior.

Rosette nebula

This closed spherical cavity of radius 6.2 pc has been well described by Bruhweiler et al. (2010). It is carved by the open cluster NGC2244, which contains a few tens of OB stars which several of them can be seen as green point ([OIII]) sources in the picture shown in Figure 1.8. These stars have been formed about 2 Myr ago within the surrounding molecular cloud, a midly dense HII region of radius 17 pc and density about 15 cm^{-3}. The most massive star, which appears as a very bright green dot around the centre of the picture, is about $60 M_\odot$ and emits winds at 3150 km/s. The next most massive star weights about $50 M_\odot$ and is seen at the bottom of the cavity (see the chart in Bruhweiler et al., 2010). It emits winds with a comparable velocity. The strong outflows produced by the stars result in a soft diffuse X-ray emission (Townsley et al., 2003)

NGC 3603

This giant HII region located at 7 kpc in the Carina constellation hosts the very compact massive cluster HD 97950, which contains tens of young (about 1 Myr) massive stars within a few tenth of parsecs (Drissen et al., 1995). Three Wolf-Rayet stars have been detected. The brightest point source is actually a pair of Wolf-Rayet stars with tremendous masses of $116M_{\odot}$ and $89M_{\odot}$, which suggest initial masses of $148M_{\odot}$ and $106M_{\odot}$! Although the cluster is characterised by a high luminosity of 6.2×10^{38} erg/s, the surrounding interstellar bubble, detected in X-rays (Moffat et al., 2002; Townsley et al., 2011), is only a few parsecs wide.

1.4.3 Galactic superbubbles

The local cavities

It has been known for decades (e.g. Cox and Reynolds, 1987) that we live into a local cavity of dilute (< 0.01 cm^{-3}) hot ($> 10^6$ K) gas emitting a diffuse soft X-ray background on a hundred parsec scale. Lallement and collaborators (e.g. Lallement et al., 2003; Lallement et al., 2014; Puspitarini et al., 2014) provided a three-dimensional measurement of the gas distribution up to 1 kpc away from the solar system. It revealed that the local cavity is actually a tubular chimney, with a height of the order of 100-200 pc. On the galactic plane, the local cavity is surrounded by neighbouring rarefied regions, bounded by the Gould belt, the Orion clouds and the Vela region (see Figure 1.9 (a)). Among these nearby superbubbles are found the Orion superbubble, the Perseus superbubble, as well as several superbubbles blown by the unbound Scorpio-Centaurus OB association, including the Loop I bubble whose shell interacts directly with the local cavity. In the third quadrant of the map, a huge cavity is seen in direction to Canis Major, designated as the "superhole" GSH238+00+09. It is 500 by 1000 pc wide and is connected with the local cavity by a tunnel of about 150 pc long.

The age of the local cavity is estimated around 15 Myr and its origin remains unclear, in particular because it contains no OB associations. Breitschwerdt and de Avillez (2006) suggested that it resulted from several generations of supernova explosions in moving groups of massive stars, part of which would now be in the Pleiades or in the Scorpius-Centaurus association (see also Fuchs et al., 2009). The elongation of the bubble was successfully explained by the density and pressure gradients perpendicular to the galactic plane. Besides, Rayleigh-Taylor instabilities at the shell were found to launch clouds of gas travelling inwards, which is consistent with the measurements of the velocities of local clouds.

It has been suggested that all the local associations and cavities within a few hundreds parsec around the sun in fact originated from a common parent molecular cloud, which has been disrupted by an ancient superbubble possibly blown by the Cas-Tau association more than 50 Myr ago (Heiles, 2009, and references therein). The "Lindblad's ring", an ellipsoidal distribution of expanding gas of major axis 364 pc would correspond to the remnant shell of this extinct superbubble and all currently active nearby large-scale molecular clouds, bubbles and supershells such as the Orion-Eridanus superbubble, the North Polar Spur shell, the GSH238+00+09 superhole, etc. would have been formed after the cooling and collapse of this ancient shell, in which they are now expanding.

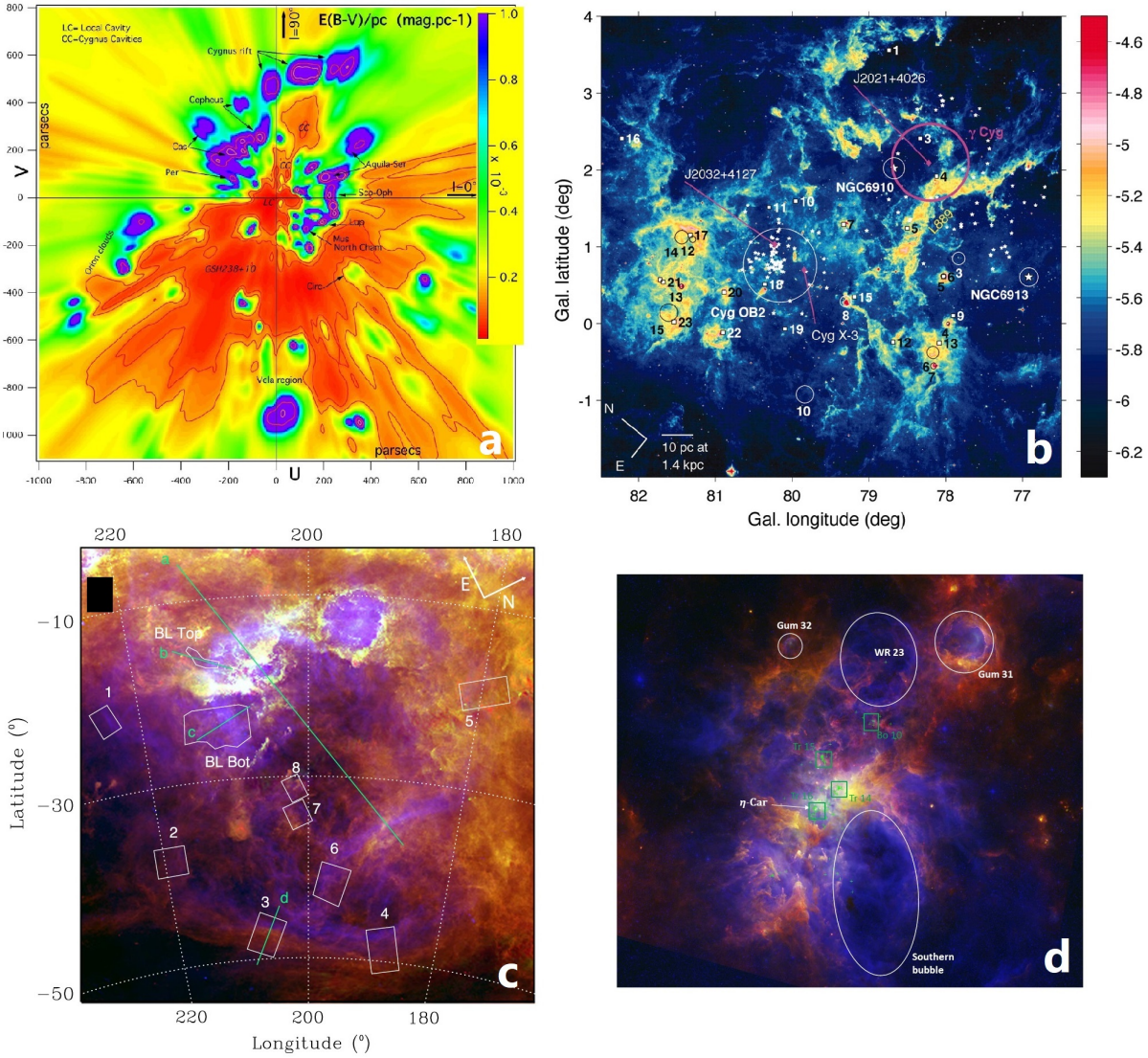

Figure 1.9: Galactic superbubbles. (a) Opacity distribution (increasing from red to violet) in the galactic plane, showing the nearby local cavities, including the local bubble within a radius of about 100 pc at the centre (adopted from Lallement et al. (2014)). (b) 8 µm intensity map of the Cygnus-X complex (adopted from Ackermann et al. (2011)). (c) Multi-wavelength image of the Orion-Eridanus superbubble: Hα in blue (ionised regions), WISE 12 µm band in green and Planck 353 GHz in red (dust) (adopted from Ochsendorf et al. (2015). (d) Composite optical/IR image of the Carina nebula: red optical in blue, Herschel 70 µm in green, Herschel 160 µm in red (adopted from Preibisch et al. (2012), apart from the annotations which I have added).

Orion-Eridanus

The Orion-Eridanus superbubble is one the most studied neighbouring cavities. It is characterised by a neutral shell delimiting a hot ionised cavity about 200 pc wide, carved by the Orion OB1 association which is part of the Orion nebula (Brown et al., 1995). This cluster is actually divided into four subgroups of various ages, from 2 Myr to 12 Myr (Bally, 2008) and several large-scale structures are observed in the surrounding, such as the Barnard's loop or the λ Ori region which have been described by Ochsendorf et al. (2015) (see Figure 1.9). The detailed stellar content of these clusters is not well-known. The integrated kinetic energy is estimated as 1.8×10^{52} erg, which, assuming an age of 10 Myr, gives a luminosity of about 6×10^{37} erg/s which is consistent with the number of 62 observed massive stars (Voss et al., 2010). The Orion-Eridanus region is actually likely to be a complex of nested bubbles expanding in an inhomogeneous and magnetised large-scale cavity. These small-scale shells have probably been blown in the course of continuous star formation in the past 10-15 Myr and are still actively forming stars while embedded clouds load mass in the interior. Joubaud et al. (2019) investigated the properties of the bubble using multi-wavelengths observations. They found a shell density of about 3-10 cm^{-3}. Planck polarisation data were also used by Soler et al. (2018) to infer the topography of the magnetic fields. This confirmed that the swept-up interstellar magnetic fields accumulate in the expanding shell with a rather ordered geometry following the shape of the shell. This analysis was refined by Joubaud et al. (2019) who inferred a magnetic field strength along the outer shell of about 10 µG.

Cygnus X region

The Cygnus X region is a star forming region located at about 1.5 kpc. Notably difficult to observe because of the foreground Cygnus "rift", a huge dark nebula, it is a complex of several OB clusters such as Cygnus OB1, OB2, OB9, NGC6910 or NGC6913. The massive stars have sculpted the parent molecular cloud on a hundred parsec scale, creating a intricate network of cavities and supershells (Uyaniker et al., 2001), which can be seen in the IR intensity map shown in Figure 1.9 (b).

Discovered by Cash et al. (1980) in X-rays, the Cygnus X "giant bubble" was one of the first observed, together with the Orion-Eridani superbubble and the Gum nebula. The primary source of energy is the young Cygnus OB2 association, which contains about 330 massive stars. The supernova remnant γ-Cygni as well as several pulsars detected in Cygnus-X suggest that it is several Myr old. The ages of the various clusters are correlated within a few Myr, which overall gives ages ranging from 4-5 Myr (Cygnus OB2) to 6-8 Myr (NGC6910) (Ackermann et al., 2011, and references therein).

The Cygnus X region has gained a lot of attention in the past decade since the detection of a hard excess of gamma-ray photons in extended regions around the main clusters (Ackermann et al., 2011; Abeysekara et al., 2021). It is still at the moment the only galactic complex of superbubbles seen in gamma-rays (another extended gamma-ray excess has been recently detected in the G25.0+0.0 region (Katsuta et al., 2017) but it is not clear whether it originates from a superbubble).

The Carina complex

Located at a distance of 2.3 kpc, the Carina complex is one of the most massive star forming region in the Milky Way. It extends over 40 pc and contains eight open clusters,

including Trumpler 16 which contains 46 O stars, among which is found the famous blue variable η-Carina, one of the brightest star of the southern sky, and WR 25, the brightest star of the Milky Way[8]. The ages of the clusters range from 1-2 Myr (Trumpler 14) to 5-8 Myr (Trumpler 15).

The morphology of the nebula has been well described by Preibisch et al. (2012). It appears as a multiphase web of cavities, pillars and filaments delimited by dense shells, which are best seen in infrared (see Figure 1.9 (d)). In the southern region extends an elliptical bubble of 33 pc length. Since there is no massive cluster identified in this region, its origin is unclear. It could be blown by the gas leaking from the central area, which would also explain its asymmetry. Several cavities are carved in the northern region, including the Gum 32 nebula surrounding a massive O star, the extended bubble surrounding the Wolf-Rayet star WR23 and the Gum 31 bubble powered by the young cluster NGC3324 in the north-west. These cavities are surrounded by large-scale structures such as the pillars seen in the south-east.

Townsley et al. (2011) investigated the soft diffuse X-ray emission of the Carina nebula. They inferred a plasma temperature of 4.5×10^6 K and an electron density of 0.14 cm^{-3}. It is likely that the interaction between the hot plasma and the surrounding dense structures significantly affects the dynamics of the cavities, for instance by enhancing the mass loading.

1.4.4 Superbubbles in the Large Magellanic Cloud

The investigation of galactic regions is made difficult by both the large extension of nearby objects and the extinction along the line of sight, in particular that of the X-ray emission. It is in fact easier to look at bubbles in the Large Magellanic Cloud. This small galaxy located at 50 kpc is seen almost face-on with little foreground extinction.

30 Doradus

The greatest complex observed in the Large Magellanic Cloud is the 30 Doradus region, known as the Tarentula nebula. As shown in Figure 1.10, it appears as a web of dense gas mostly seen in infrared surrounding ionised bubbles emitting diffuse X-rays (e.g. Townsley et al., 2006). The surrounding HII region extends on 100 pc and has a mean density of about 38 cm^{-3}. It contains a number of stellar clusters, the youngest ones being a few Myr old and the oldest ones about 7 Myr old. At the centre of the nebula lies for instance the R136 young dense star cluster, which contains some of the most massive stars ever observed (Crowther et al., 2010). The stellar content of 30 Doradus is rather well constrained (e.g. Doran et al., 2013). The total mechanical power has been estimated as 2.24×10^{39} erg/s.

Several superbubbles are seen in the nebula, including the well-known superbubble 30 Doradus C, blown by the OB association LH90 containing 26 O stars and 7 WR stars. Its diffuse X-ray emission is nearly spherical with a diameter of about 100 pc (Smith and Wang, 2004). The X-ray shell is confined within Hα filaments and there is probably a strong evaporation of the cool gas into the hot interior. A young supernova remnant is detected in 30 Doradus C, which indicates that it is already an evolved superbubble. Its age is estimated around 5 Myr.

[8] Although not visible by eye due to foreground extinction.

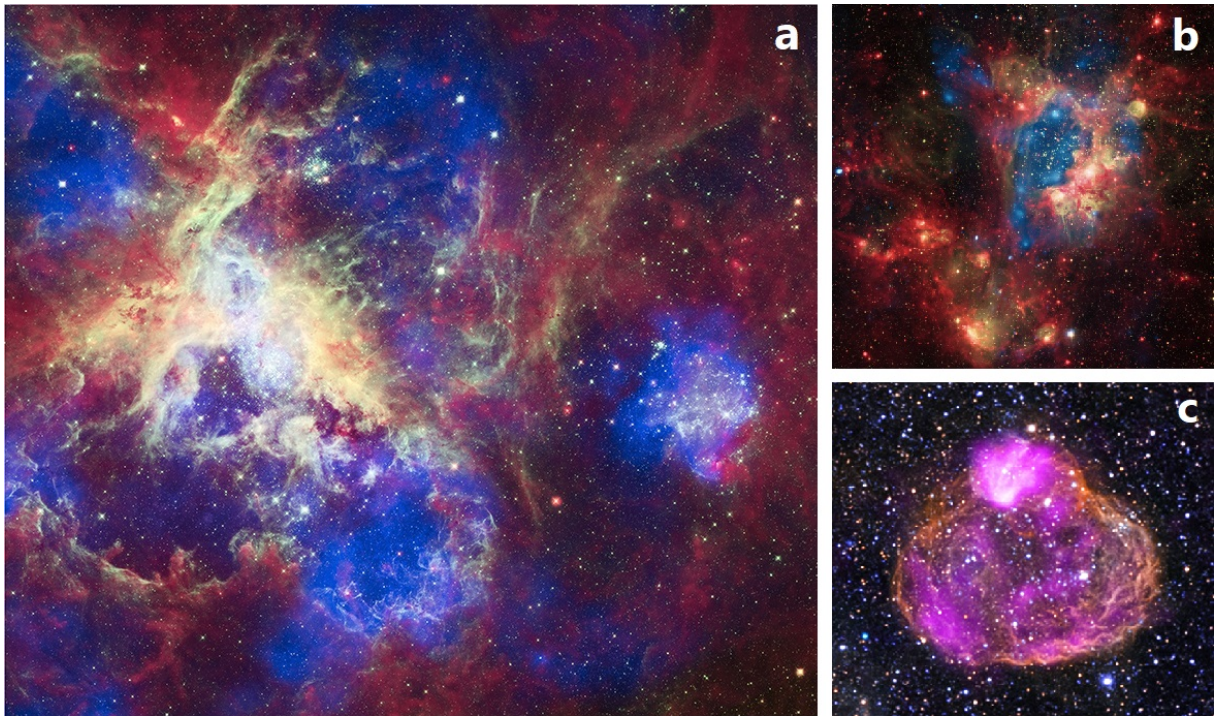

Figure 1.10: Multi-wavelength views of superbubbles located in the Large Magellanic Cloud. (a) The Tarentula nebula (30 Doradus), observed in optical (green), IR (red), X-rays (blue). (b) N44 in optical, IR and X-rays with same colours. (c) DEM L50 in optical (RGB), and X-rays (pink).
Credits: **30 Doradus**: X-ray: NASA/CXC/PSU/L. Townsley et al.; Optical: NASA/STScI; Infrared: NASA/JPL/PSU/L. Townsley et al. **NGC1929**: X-ray: NASA/CXC/U.Mich./S. Oey, IR: NASA/JPL, Optical: ESO/WFI/2.2-m. **DEML50**: X-ray: NASA/CXC/Univ of Michigan/A. E. Jaskot, Optical: NOAO/CTIO/MCELS.

Interestingly, a non thermal diffuse emission of hard X-rays (up to 20 keV) is detected in the whole shell of 30 Doradus C (Lopez et al., 2020), as well as a diffuse gamma-ray emission (Abramowski et al., 2015), which are evidence of efficient particle acceleration in the region.

Other superbubbles in the Large Magellanic Cloud

A number of other superbubbles are detected in the Large Magellanic Cloud (e.g. Chu and Mac Low, 1990), as shown in Figure 1.11 for illustration. All these bubbles are characterised by a diffuse X-ray emission.

The N180B and N11B are two small (respectively 11 and 7 pc) wind-blown bubbles within large HII regions containing several small clusters, large superbubbles and isolated bubbles around individual stars (Nazé et al., 2001).

The N44 (DEM L152) complex, of size similar to 30 Doradus, is divided in a set of four shells surrounding the large ionised superbubble shown in Figure 1.10 (b). This superbubble is powered by the star cluster NGC1929, which contains a few tens of massive stars formed 6 Myr ago. Last but not least, let us mention the bubble DEM L50, a slightly ellipsoidal bubble which is confused with a supernova remnant close to the northern edge (Jaskot et al., 2011). It is not clear if the remnant is part of the bubble or located farther away. This bubble is shown in Figure 1.10 (c).

Gupta et al. (2018) compiled the properties of the hot plasma inferred from the X-ray spectra measured in several superbubbles of the Large Magellanic Cloud and of the Milky Way. Figure 1.12 displays these data on a temperature-density diagram. All observed

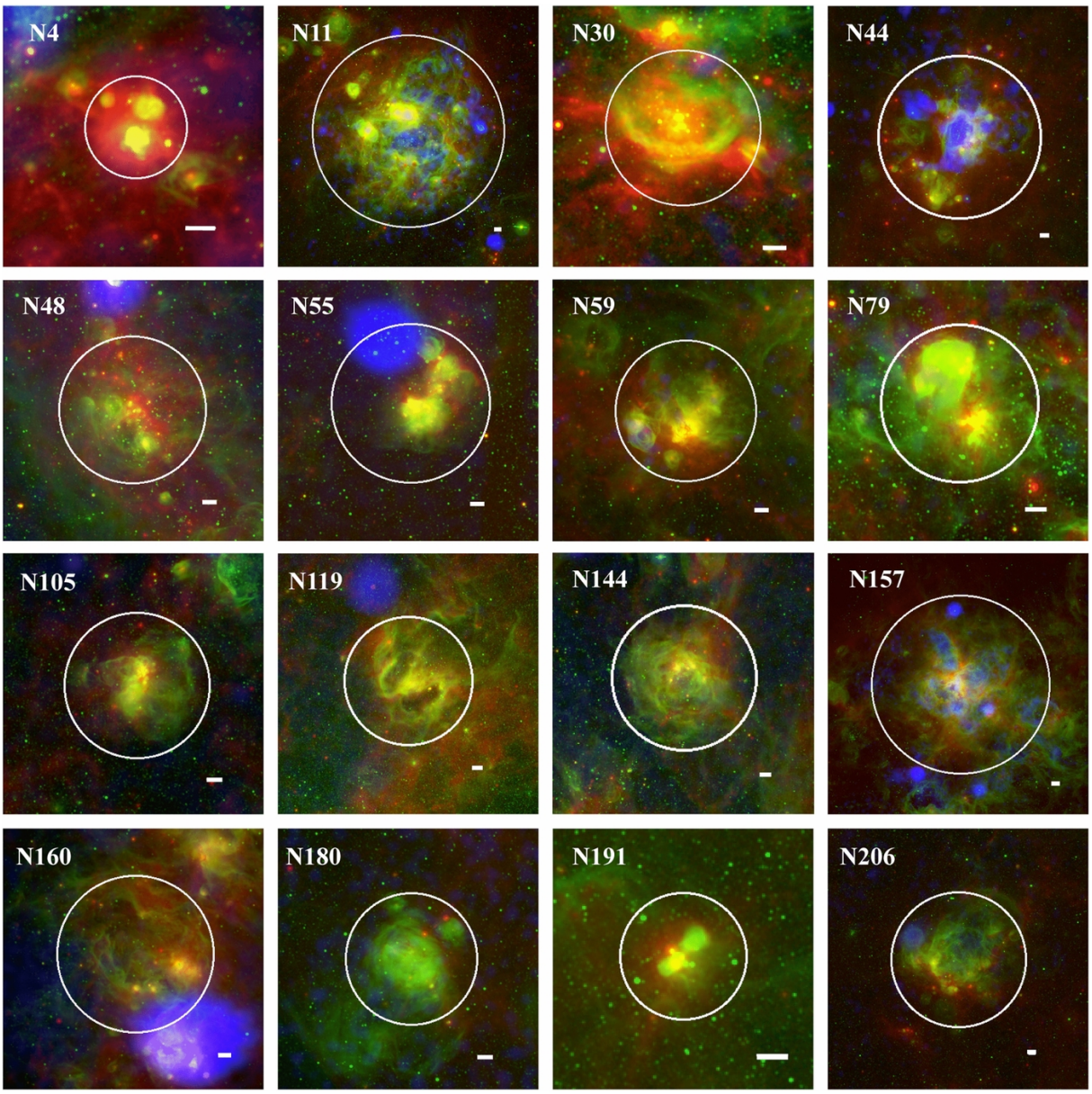

Figure 1.11: Multi-wavelength observations of superbubbles in the Large Magellanic Cloud (red: 24 µm, green: Hα, blue: X-rays). The white bar has a length of 1' ($\sim$ 14.5 pc). Figure adopted from Lopez et al. (2014).

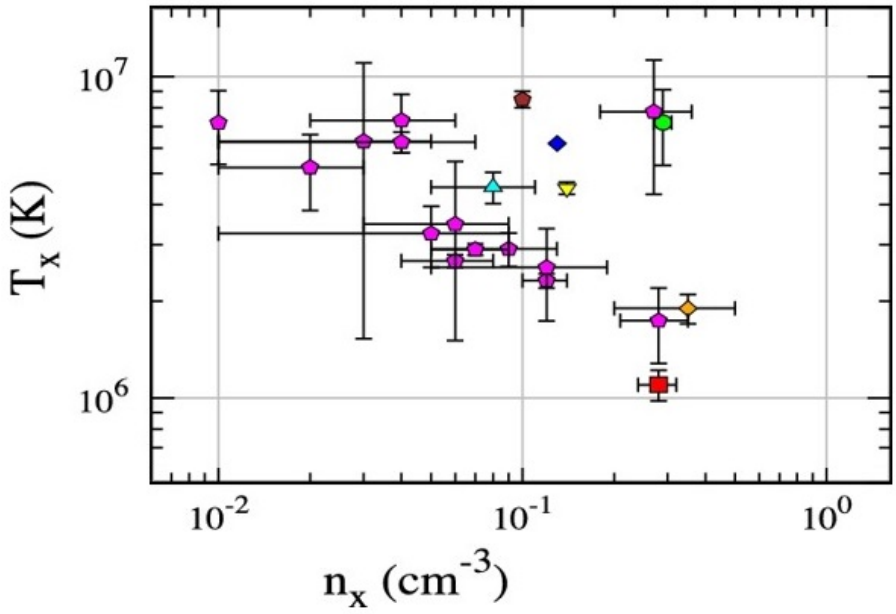

Figure 1.12: Number density and temperature of well-observed bubbles, obtained by fitting X-ray spectra. Red square: S308. Pink pentagon: Large Magellanic Cloud regions. Orange diamond: Orion. Yellow triangle: Carina. Blue triangle: 30 Doradus. Brown pentagon: Rosette. Blue diamond: NGC3606. Green circle: M17. The figure has been adopted from Gupta et al. (2018) (see the references therein).

superbubbles have very similar temperatures between 10^6 and 10^7 K and densities ranging from 0.01 and 0.4 cm^{-3}. This is consistent with the analytic theory which predicts a rather low dependency on the cluster luminosity. Besides, all these observed bubbles have similar ages ranging from a few Myr to about 10 Myr. The variance in density can be attributed to the variation of the external medium. However, most of these data are in quantitative disagreement with the analytic theory, which overpredicts almost systematically the temperature by one order of magnitude. Together with the observation that most known superbubbles are about 2 times smaller than expected, this has raised an important issue in the last decades known as the *superbubble energy crisis*.

1.5 Energy crisis

It was early realised that the observed superbubbles are much smaller than expected by the analytic theory. In the 90's, Saken et al. (1992) brought attention on the fact that the supershell surrounding the cluster OB1 in Cygnus, seen in infrared, has a dynamical age of a few 100 kyr, although the association is estimated to be about 5 Myr old. Similarly, Drissen et al. (1995) noted that the small wind bubble of radius about 1 pc seen in the galactic star forming region NGC 3603 would require a mechanical input of only a few 10^{36} erg/s to be blown within the expected 2.5 Myr age of the cluster HD 97950, located around the centre of the bubble within a radius of 0.15 pc and presumably at the origin of its formation. However this compact cluster contains three Wolf-Rayet stars as well as about 20 O stars, which provides an average luminosity about 30 to 50 times higher than what is theoretically needed. The Crescent nebula, taken as a show-case in the work by Garcia-Segura and Mac Low (1995), also could not fit the modelling, even including a r^{-2} density profile and relaxing the assumption of spherical symmetry. The energy input

required to fit the radius of this small ellipsoidal bubble was computed to be about ten times lower than the luminosity of the central Wolf-Rayet star. Do they appear as too high shell velocities and/or too large radii, such puzzling deviations from theory were further observed in a number of bubbles detected in the Large Magellanic Cloud, including e.g. DEM 152 (Oey and Massey, 1995), DEM 25, DEM 50, DEM 301 (Oey, 1996).

Early explanations suggested that the density of the external interstellar medium could have been greatly underestimated. However, the discrepancy could be reconciled only by assuming unrealistic densities, as was pointed out by Nazé et al. (2001) in the case of the two small wind-blown bubbles N180B and N11B located within large HII regions in the Large Magellanic Cloud. Again, a discrepancy of one to two orders of magnitude between the luminosity of the stellar clusters and the luminosity required to blow the bubbles to their current sizes was measured, despite a dense ($n_0 > 10$ cm^{-3}) external medium. An interstellar density of about 1000 cm^{-3} would be required to reconcile the observations with the theory. Besides, although density measurements rely on some assumptions to estimate the optical depth of the medium surrounding the bubble, an error as large as two orders of magnitude is unlikely. Finally, Oey (2009) pointed out that superbubbles evolve in very diverse environments, from dense molecular clouds ($n_0 \sim 100$ cm^{-3}) to diffuse interstellar regions ($n_0 \sim 0.1$ cm^{-3}), or even a stratification of phases if e.g. the bubble first expands in a dense cloud and then blows out in the standard interstellar medium. It could also be sometimes the case that a first, older, cluster sweeps up its surrounding dense medium, and only then other clusters blow a superbubble. The effect of the external density is therefore expected to greatly vary from superbubble to superbubble, such that it is not a good candidate to explain a nearly *systematic* discrepancy. In other words, the external density would require to be fine-tuned to account for the dynamics of a specific superbubble. The fact that HI environments can now be resolved and their density estimated with confidence (e.g. Oey et al., 2002) tends to disfavour this explanation.

The dynamical discrepancy was further aggravated by X-ray observations, which frequently measured a X-ray flux about one order of magnitude below that theoretically expected, even in simple wind-blown bubbles such as the Crescent nebula (Bochkarev, 1988). The internal temperature inferred from fits of the X-ray spectra was also frequently several times smaller than excepted. For instance, Cooper et al. (2004) observed the young superbubble DEM L192 in the Large Magellanic Cloud, which contains two stellar clusters expected to have imparted about 1.8×10^{52} erg in the bubble since their births. The temperature was obtained from the X-ray spectra and the internal thermal energy was inferred as $E_{th} \approx 9 \times 10^{50}$ erg, which only represents 5% of the energy input. From Hα and 21-cm line emission, the kinetic energy of the shell was estimated around 5×10^{51} erg, which represents 27% of the energy input. Thus, the observed properties of the bubble only account for one third of the energy budget. On the other hand, the cooling timescale of the hot gas was estimated around 200 Myr, which implies that the energy radiated away is completely negligible.

All these experimental facts converge towards the conclusion that only a small fraction of the cluster luminosity is converted into thermal energy and subsequent work on the shell. As reviewed by Oey (2009), only about 10% of the mechanical input is generally required to power the expansion of the shell and match the X-ray fluxes as well as the observed radii. The radiative losses are also systematically proved to be sub-dominant, if not completely negligible (e.g. Cooper et al., 2004). In a compilation of the properties of several well-observed superbubbles, I conclude that the original model by Weaver et al. (1977) can approximatively account for the observed radii provided that one corrects the

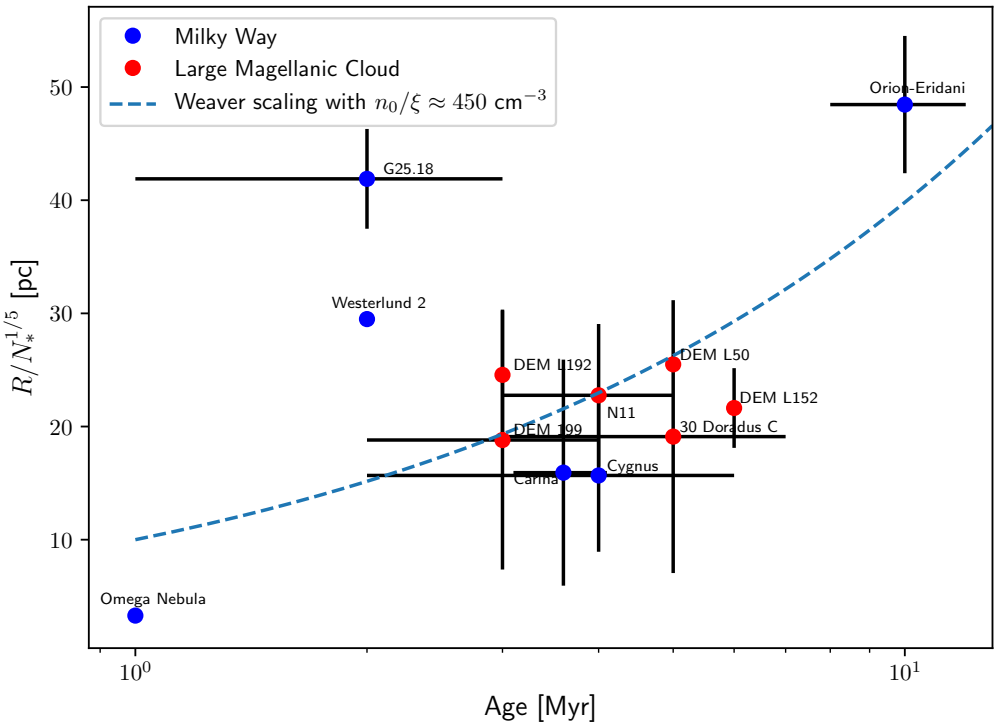

Figure 1.13: Sizes and ages of several observed clusters. The error bars reflect the variations found in the literature rather than the physical uncertainties. In particular, the number of massive stars in the G25 superbubble is only roughly estimated, and Westerlund 2 is poorly constrained. Data are found in Ackermann et al. (2011, and references therein) (Cygnus); Joubaud et al. (2019, and references therein),Voss et al. (2010) (Orion-Eridani); Lopez et al. (2020, and references therein) (30 Doradus C); Katsuta et al. (2017, and references therein) (G25); Maddox et al. (2009) (N11); Dunne et al. (2003) (Omega nebula); Smith (2006) and Smith and Brooks (2007) (η-Carina); Rauw et al. (2007) (Westerlund 2); Cooper et al. (2004) (DEM L192); Jaskot et al. (2011, and references therein) (DEM L152 and DEM L50); Dunne et al. (2001) and Massey et al. (1995) (DEM 199). See also the compilation in Ferrand and Marcowith (2010, and references therein).

cluster luminosity such that $n_0/\xi \sim 500$ cm^{-3} (e.g. $\xi \sim 2\%$ for $n_0 \sim 10$ cm^{-3}), as shown in Figure 1.13.

Where does the missing energy go? Several theoretical and numerical works have aimed to retrieve the energy balance of observed superbubbles without introducing artificial efficiencies. It was early suggested that the interstellar pressure beyond the superbubble could be underestimated. Oey and Garcia-Segura (2004) pointed out that the interstellar pressure could be similar to the pressure of the interior of the bubble, in particular in the Large Magellanic Cloud which is characterised by a high star formation rate. A simple one-dimensional model showed that the sizes of several superbubbles in the Large Magellanic Cloud could be satisfactorily recovered providing the external pressure was systematically increased by an order of magnitude. A large density could be due not only to efficient star formation, but also to the presence of magnetic fields.

Another explanation is that most of the stellar flows could be advected into the interstellar medium without doing work on the shell if the bubbles broke-out at some point in the shell. Harper-Clark and Murray (2009) formalised this hypothesis by introducing some "porosity" C_f, which represents the fraction of the surface covered by the shell, such

that the following loss term should be added in the energy balance:

$$L_{leak} \approx 6 \times 10^{37}\ (1 - C_f) \left(\frac{R_s}{100\ \mathrm{pc}}\right)^2 \left(\frac{n}{0.01\ \mathrm{cm^{-3}}}\right) \left(\frac{c_s}{100\ \mathrm{km/s}}\right)^3\ \mathrm{erg/s}\,. \tag{1.24}$$

Although instabilities are not found to break the shell in simulations (Pittard, 2013), holes could be carved in the shell if the bubble expands in a strongly inhomogeneous medium with e.g. dense clumps. There are indeed convincing clues that part of the gas may leak out of some superbubbles engulfed in complex regions such as Carina or 30 Doradus (e.g. Lopez et al., 2011). In this case, the hot gas might flow out, expand outside and cool, until a pressure equilibrium is reached. On the other hand, several superbubbles do not display any breaks, as pointed out by Cooper et al. (2004), who rather suggested that the lack of thermal energy could be due to the evaporation of dense interstellar clumps cooling the interior of the bubble. A related hypothesis is that interstellar dust could leak in the interior, be heated and radiate in infrared. The power lost by this channel can be estimated as (Rosen et al., 2014):

$$L_{dust} \leq 7 \times 10^{35} \left(\frac{n}{0.01\ \mathrm{cm^{-3}}}\right)^2 \frac{V}{10^6\ \mathrm{pc^3}} \left(\frac{T}{10^6\ \mathrm{K}}\right)^{3/2}\ \mathrm{erg/s}\,, \tag{1.25}$$

which is generally too low to account for two third of the energy. Moreover, the dust grains are expected to be sputtered with a typical timescale of 0.1 Myr in the hot interior, which is much smaller than the dynamical time of interstellar bubbles.

Another possibility is that the expansion is reduced by the time-dependency (or even the intermittency in extreme cases) of the cluster luminosity. This hypothesis has been investigated by means of 3D hydrodynamic simulations (Krause and Diehl, 2014). It was shown that the bubble blown by three massive stars was most of the time in a snow-plow phase rather than a pressure-driven expansion, which enhances the radiative losses in the shell. Besides, the supernova shocks were able to reach the edge of the bubble, imparting discrete impulses on the shell. Even though the small number of stars considered in this work can hardly be generalised to large clusters, it is important to bare in mind that supernova remnants may systematically reach the shell of typical superbubbles if the latter do not expand as rapidly as expected. One has to recall that the fact that supernovae merge with the interior of the bubble is a crucial hypothesis in the standard analytic bubble theory (Mac Low and McCray, 1988).

Finally, Rosen et al. (2014) showed that thermal conduction could efficiently remove energy from the interior of superbubbles, provided it is not inhibited by magnetic fields. As already mentioned, this process, coupled with shell instabilities as well as magnetic fields and turbulence, is difficult to resolve in numerical simulations and is not well constrained. Jaskot et al. (2011) pointed out a discrepancy between the small radii of N44 and DEM L50 and their high X-ray luminosity. While this cannot be accounted for by simply lowering the input energy, thermal conduction, besides driving the cooling of the bubble, also determines the evaporation from the shell. Efficient evaporation increases the density close to the inner edge and thus the X-ray emission.

The aforementioned hypotheses could well be all relevant. For instance, Jaskot et al. (2011) pointed out that the high X-ray fluxes observed in N44 and DEM L50 could not only be a clue of enhanced thermal conduction, but also a sign that supernova remnants interact with the superbubble shells. Alternatively, two bright knots in the southern region of N44 could be the source of an additional mass loading which cools the interior.

On the other hand, although several mechanisms can account for the missing energy up to about 10% each, it is still difficult to match all the observables, e.g. the density, the temperature, the X-ray spectra and brightness, the presence or absence of clumps and outflows etc. in a self-consistent model.

An alternative sink of energy which has gained considerable attention over the last years could be the acceleration of non-thermal particles. Butt and Bykov (2008) indeed pointed out that large-scale shocks and hydromagnetic turbulence could efficiently convert up to 30% of the energy into non-thermal particles, which would easily explain the lack of thermal energy. Besides, the random plasma motions also store a substantial fraction of the energy, as already discussed in Section 1.3. A non-thermal X-ray component was early detected in e.g. DEM L192 (Cooper et al., 2004), as well as in 30 Doradus C (Smith and Wang, 2004; Lopez et al., 2020), while gamma rays have been detected from the Cygnus cocoon (Ackermann et al., 2011; Abeysekara et al., 2021). These are hint of efficient non-thermal particle acceleration. Gupta et al. (2018) simulated the dynamics of a superbubble including the feedback of cosmic rays in a two-fluid model, where particles are accelerated at the wind termination shock. It was concluded that the observed radii and temperatures could be recovered providing the acceleration time of the particles is smaller than the dynamical time of the bubble, which is expected for realistic values of the diffusion coefficient.

1.6 Summary

What should be reminded from this rather lengthy review? If I were to summarise in a few sentences, I would say that we understand qualitatively the phenomena driving the dynamics of interstellar bubbles and superbubbles, from the collapse of dense molecular clouds to the break-out of the cavities, and all intermediate steps including star cluster formation, massive star evolution, supernova explosions, as well as the expansion of pressure-driven bubbles in admittedly complex interstellar media. Although most of the observations can be qualitatively discussed, we still lack a self-consistent predictive realistic modelling of stellar clusters and superbubbles, and important deviations between the measurements and the theoretical expectations are still not well understood.

Superbubbles are driven by a strong interplay between thermodynamics, fluid instabilities, thermal conduction, magnetic fields and non-thermal particles, which I attempted to depict in Figure 1.14. The primary mechanism driving the expansion of the bubbles is the conversion of the mechanical energy of the stars into internal energy, and then back into mechanical work in the shell. However stellar shocks also produce turbulence and non-thermal particles, while the properties of the hot plasma are affected by thermal conduction, cloud evaporation, dust heating etc. The pressurised and magnetised interstellar medium reacts on the shell, driving instabilities which again modify the internal mechanisms. All processes are intricate within several non trivial backreaction loops. Besides, realistic superbubbles are far from being spherically symmetric. Modern well-resolved observations reveal that some regions previously seen as "superbubbles" such as Orion-Eridani or Cygnus-X are in fact rather networks of cavities carved into their dense parent clouds associated with extended nebulae hosting several massive clusters and sub-clusters in hierarchical organisations. Even in a given cluster or association, massive stars do not lit exactly at the same time within a sub-parsec region, but they rather have ages and positions roughly correlated on a few Myr and few pc scales. Bubbles are then blown sequentially and merge successively from the smallest to the largest scales. All this is of

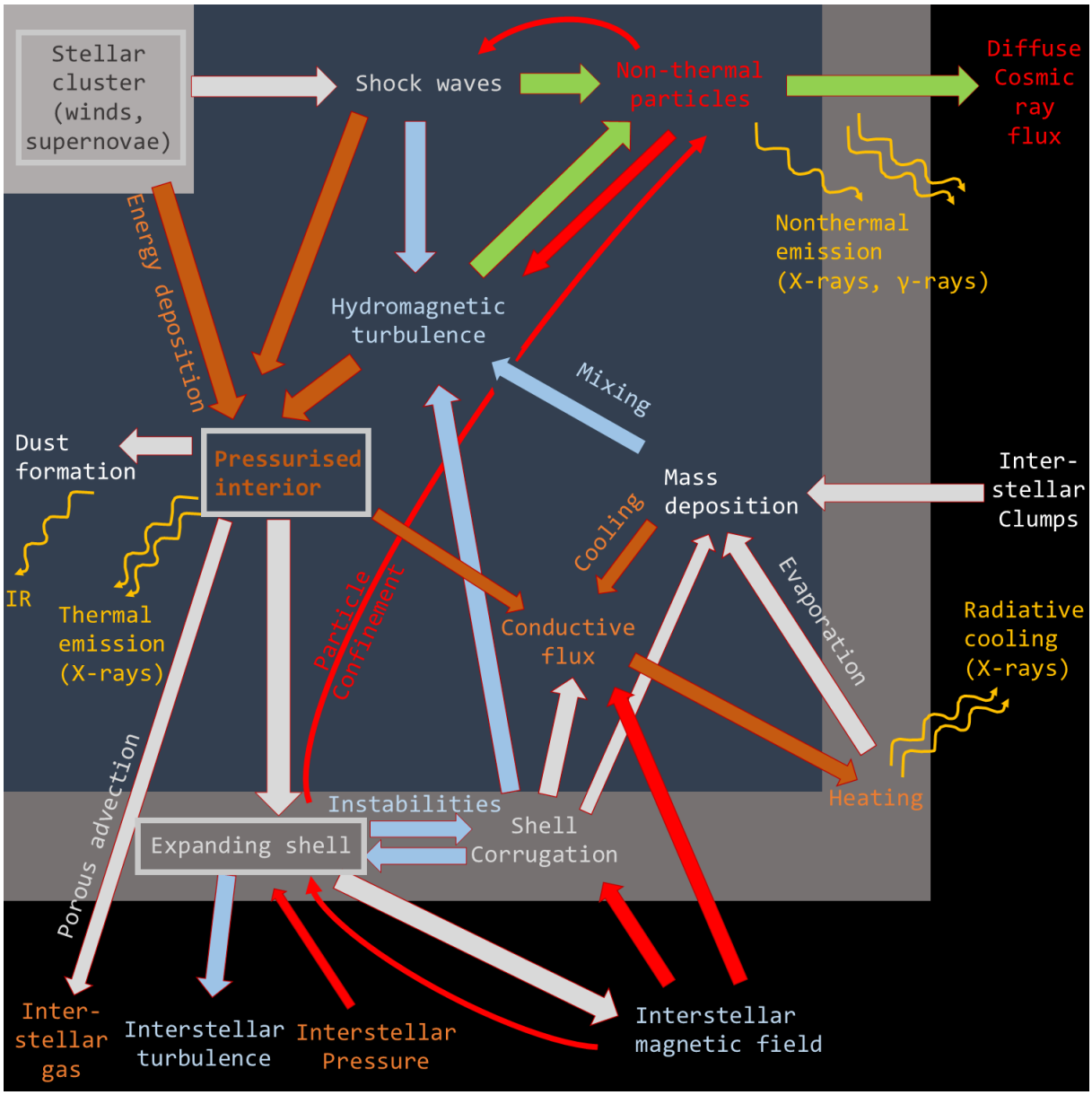

Figure 1.14: The physical processes driving the dynamics of superbubbles and their couplings.

course impossible to model analytically and very difficult to capture numerically. Given this complexity, it is eventually not that surprising that the models struggle to reproduce the observations. One could choose an optimistic point of view, noticing that a lot of progress have been done in the past decades. In particular, more and more interstellar bubbles are detected in soft X-rays in our galaxy as well as in the Magellanic clouds, and even in other galaxies such as NGC253 or IC10, and these observations are rather qualitatively understood. In particular we now have several tools to speculate about why most of the observed bubbles are colder and smaller than theoretically expected, although it is yet unclear which are the most relevant sinks of energy. It seems that the theoretical, numerical and observational works of the last decades converge towards the conclusion that the well-studied loss channels such as thermal conduction, dust heating, shell corrugation, are sub-dominant albeit non negligible. It is very possible that the sinks we are looking for will eventually appear to be energy reservoirs, for a substantial fraction (e.g. 60%) of the mechanical energy of the stars could be stored under the form of turbulent motions and non-thermal particles. Particle acceleration and diffusion in turbulence thus recently appeared as a natural way to resolve the superbubble energy crisis.

This chapter was far from being an exhaustive review on the subject of interstellar bubbles, for a complete development would make an entire book. My dear friend Clément W. warned me: "If you continue like that you'll have a list of references longer than the main text"; so I shall stop there this discussion.

References

Abbott, D. C. (Jan. 1979). "The domain of radiatively driven mass loss in the H-R diagram." In: *Mass Loss and Evolution of O-Type Stars*. Ed. by P. S. Conti and C. W. H. De Loore. Vol. 83, pp. 237–239.

Abeysekara, A. U. et al. (Mar. 2021). "HAWC observations of the acceleration of very-high-energy cosmic rays in the Cygnus Cocoon". In: *Nature Astronomy*. DOI: 10.1038/s41550-021-01318-y.

Abramowski, A. et al. (Jan. 2015). "The exceptionally powerful TeV γ-ray emitters in the Large Magellanic Cloud". In: *Science* 347.6220, pp. 406–412. DOI: 10.1126/science.1261313.

Ackermann, M. et al. (Nov. 2011). "A Cocoon of Freshly Accelerated Cosmic Rays Detected by Fermi in the Cygnus Superbubble". In: *Science* 334.6059, p. 1103. DOI: 10.1126/science.1210311.

Adams, S. M. et al. (July 2017). "The search for failed supernovae with the Large Binocular Telescope: confirmation of a disappearing star". In: MNRAS 468.4, pp. 4968–4981. DOI: 10.1093/mnras/stx816.

Avedisova, V. S. (Apr. 1972). "Formation of Nebulae by Wolf-Rayet Stars." In: Soviet Ast. 15, p. 708.

El-Badry, K. et al. (Dec. 2019). "Evolution of supernovae-driven superbubbles with conduction and cooling". In: MNRAS 490.2, pp. 1961–1990. DOI: 10.1093/mnras/stz2773.

Bally, J. (2008). "Overview of the Orion Complex". In: *Handbook of Star Forming Regions, Volume I*. Ed. by B. Reipurth. Vol. 4, p. 459.

Balsara, D. S. et al. (Dec. 2004). "Amplification of Interstellar Magnetic Fields by Supernova-driven Turbulence". In: ApJ 617.1, pp. 339–349. DOI: 10.1086/425297.

Blondin, J. M. et al. (June 1998). "Transition to the Radiative Phase in Supernova Remnants". In: ApJ 500.1, pp. 342–354. DOI: 10.1086/305708.

Bochkarev, N. G. (Apr. 1988). "X-ray emission from the ring nebula NGC6888". In: Nature 332.6164, pp. 518–520. DOI: 10.1038/332518a0.

Bozzetto, L. M. et al. (May 2017). "Statistical Analysis of Supernova Remnants in the Large Magellanic Cloud". In: ApJS 230.1, 2, p. 2. DOI: 10.3847/1538-4365/aa653c.

Breitschwerdt, D. and de Avillez, M. A. (June 2006). "The history and future of the Local and Loop I bubbles". In: A&A 452.1, pp. L1–L5. DOI: 10.1051/0004-6361:20064989.

Brown, A. G. A., Hartmann, D., and Burton, W. B. (Aug. 1995). "The Orion OB1 association. II. The Orion-Eridanus Bubble." In: A&A 300, p. 903.

Bruhweiler, F. C. et al. (May 1980). "Stellar winds, supernovae, and the origin of the H I supershells". In: ApJ 238, pp. L27–L30. DOI: 10.1086/183250.

Bruhweiler, F. C. et al. (Aug. 2010). "The Young Interstellar Bubble Within the Rosette Nebula". In: ApJ 719.2, pp. 1872–1883. DOI: 10.1088/0004-637X/719/2/1872.

Butt, Y. M. and Bykov, A. M. (Apr. 2008). "A Cosmic-Ray Resolution to the Superbubble Energy Crisis". In: ApJ 677.1, p. L21. DOI: 10.1086/587875.

Bykov, A. M. (June 1982). "Interstellar Turbulence and Shock Waves". In: *Soviet Astronomy Letters* 8, pp. 320–322.

Cantó, J., Raga, A. C., and Rodríguez, L. F. (June 2000). "The Hot, Diffuse Gas in a Dense Cluster of Massive Stars". In: ApJ 536.2, pp. 896–901. DOI: 10.1086/308983.

Cash, W. et al. (June 1980). "The X-ray superbubble in Cygnus." In: ApJ 238, pp. L71–L76. DOI: 10.1086/183261.

Castor, J., McCray, R., and Weaver, R. (Sept. 1975). "Interstellar bubbles." In: ApJ 200, pp. L107–L110. DOI: 10.1086/181908.

Chabrier, G. (July 2003). "Galactic Stellar and Substellar Initial Mass Function". In: PASP 115.809, pp. 763–795. DOI: 10.1086/376392.

Chamandy, L. and Shukurov, A. (July 2020). "Parameters of the Supernova-Driven Interstellar Turbulence". In: *Galaxies* 8.3, p. 56. DOI: 10.3390/galaxies8030056.

Chandrasekhar, S. (1961). *Hydrodynamic and hydromagnetic stability*.

Chevalier, R. A. (July 1982a). "Self-similar solutions for the interaction of stellar ejecta with an external medium." In: ApJ 258, pp. 790–797. DOI: 10.1086/160126.

Chevalier, R. A. (Aug. 1982b). "The radio and X-ray emission from type II supernovae." In: ApJ 259, pp. 302–310. DOI: 10.1086/160167.

Chevalier, R. A. and Clegg, A. W. (Sept. 1985). "Wind from a starburst galaxy nucleus". In: Nature 317.6032, pp. 44–45. DOI: 10.1038/317044a0.

Chu, Y.-H. (June 2008). "Bubbles and Superbubbles: Observations and Theory". In: *Massive Stars as Cosmic Engines*. Ed. by F. Bresolin, P. A. Crowther, and J. Puls. Vol. 250, pp. 341–354. DOI: 10.1017/S1743921308020681.

Chu, Y. et al. (Dec. 2003). "Hot Gas in the Circumstellar Bubble S308". In: *The Astrophysical Journal* 599.2, pp. 1189–1195. ISSN: 1538-4357. DOI: 10.1086/379607.

Chu, Y.-H. and Mac Low, M.-M. (Dec. 1990). "X-Rays from Superbubbles in the Large Magellanic Cloud". In: ApJ 365, p. 510. DOI: 10.1086/169505.

Clark, D. H. and Stephenson, F. R. (1977). *The historical supernovae*.

Clark, J. S. et al. (May 2005). "On the massive stellar population of the super star cluster Westerlund 1". In: A&A 434.3, pp. 949–969. DOI: 10.1051/0004-6361:20042413.

Cooper, R. L. et al. (Apr. 2004). "Energy Crisis in the Superbubble DEM L192 (N51D)". In: ApJ 605.2, pp. 751–758. DOI: 10.1086/382501.

Cowie, L. L. and McKee, C. F. (Jan. 1977). "The evaporation of spherical clouds in a hot gas. I. Classical and saturated mass loss rates." In: ApJ 211, pp. 135–146. DOI: 10.1086/154911.

Cox, D. P. and Reynolds, R. J. (Jan. 1987). "The local interstellar medium." In: ARA&A 25, pp. 303–344. DOI: 10.1146/annurev.aa.25.090187.001511.

Crowther, P. A. et al. (July 2010). "The R136 star cluster hosts several stars whose individual masses greatly exceed the accepted 150 $M_{\odot}$ stellar mass limit". In: *Monthly Notices of the Royal Astronomical Society* 408.2, pp. 731–751. ISSN: 0035-8711. DOI: 10.1111/j.1365-2966.2010.17167.x.

De Marchi, G. et al. (Sept. 2011). "Star Formation in 30 Doradus". In: ApJ 739.1, 27, p. 27. DOI: 10.1088/0004-637X/739/1/27.

Doran, E. I. et al. (Oct. 2013). "The VLT-FLAMES Tarantula Survey. XI. A census of the hot luminous stars and their feedback in 30 Doradus". In: A&A 558, A134, A134. DOI: 10.1051/0004-6361/201321824.

Drissen, L. et al. (Nov. 1995). "The Dense Galactic Starburst NGC 3603. I. HST/FOS Spectroscopy of Individual Stars in the Core and the source of Ionization and Kinetic Energy". In: AJ 110, p. 2235. DOI: 10.1086/117684.

Dunne, B. C., Points, S. D., and Chu, Y.-H. (Sept. 2001). "X-Rays from Superbubbles in the Large Magellanic Cloud. VI. A Sample of Thirteen Superbubbles". In: ApJS 136.1, pp. 119–135. DOI: 10.1086/321794.

Dunne, B. C. et al. (June 2003). "Diffuse X-Ray Emission from the Quiescent Superbubble M17, the Omega Nebula". In: ApJ 590.1, pp. 306–313. DOI: 10.1086/375010.

Ebinger, K. et al. (Jan. 2019). "PUSHing Core-collapse Supernovae to Explosions in Spherical Symmetry. II. Explodability and Remnant Properties". In: ApJ 870.1, 1, p. 1. DOI: 10.3847/1538-4357/aae7c9.

Ebinger, K. et al. (Jan. 2020). "PUSHing Core-collapse Supernovae to Explosions in Spherical Symmetry. IV. Explodability, Remnant Properties, and Nucleosynthesis Yields of Low-metallicity Stars". In: ApJ 888.2, 91, p. 91. DOI: 10.3847/1538-4357/ab5dcb.

Elmegreen, B. G. and Falgarone, E. (Nov. 1996). "A Fractal Origin for the Mass Spectrum of Interstellar Clouds". In: ApJ 471, p. 816. DOI: 10.1086/178009.

Falle, S. A. E. G. (Oct. 1975). "A numerical calculation of the effect of stellar winds on the interstellar medium." In: A&A 43.3, pp. 323–336.

Ferrand, G. and Marcowith, A. (Feb. 2010). "On the shape of the spectrum of cosmic rays accelerated inside superbubbles". In: A&A 510, A101, A101. DOI: 10.1051/0004-6361/200913520.

Ferrand, G. et al. (June 2019). "From Supernova to Supernova Remnant: The Three-dimensional Imprint of a Thermonuclear Explosion". In: ApJ 877.2, 136, p. 136. DOI: 10.3847/1538-4357/ab1a3d.

Ferrière, K., Gillard, W., and Jean, P. (May 2007). "Spatial distribution of interstellar gas in the innermost 3 kpc of our galaxy". In: A&A 467.2, pp. 611–627. DOI: 10.1051/0004-6361:20066992.

Ferriere, K. M., Mac Low, M.-M., and Zweibel, E. G. (July 1991). "Expansion of a Superbubble in a Uniform Magnetic Field". In: ApJ 375, p. 239. DOI: 10.1086/170185.

Field, G. B. (Aug. 1965). "Thermal Instability." In: ApJ 142, p. 531. DOI: 10.1086/148317.

Field, G. B., Blackman, E. G., and Keto, E. R. (Mar. 2008). "A model of cloud fragmentation". In: MNRAS 385.1, pp. 181–188. DOI: 10.1111/j.1365-2966.2007.12609.x.

Fielding, D., Quataert, E., and Martizzi, D. (Dec. 2018). "Clustered supernovae drive powerful galactic winds after superbubble breakout". In: MNRAS 481.3, pp. 3325–3347. DOI: 10.1093/mnras/sty2466.

Figer, D. F. (Dec. 2004). "Young Massive Clusters in the Galactic Center". In: *The Formation and Evolution of Massive Young Star Clusters*. Ed. by H. J. G. L. M. Lamers, L. J. Smith, and A. Nota. Vol. 322. Astronomical Society of the Pacific Conference Series, p. 49.

Fryer, C. L. (Sept. 1999). "Mass Limits For Black Hole Formation". In: ApJ 522.1, pp. 413–418. DOI: 10.1086/307647.

Fryer, C. L. (May 2003). "Black-hole formation from stellar collapse". In: *Classical and Quantum Gravity* 20.10, S73–S80. DOI: 10.1088/0264-9381/20/10/309.

Fuchs, B. et al. (Mar. 2009). "Origin of the Local Bubble". In: Space Sci. Rev. 143.1-4, pp. 437–448. DOI: 10.1007/s11214-008-9427-z.

Gallegos-Garcia, M. et al. (Aug. 2020). "Winds in Star Clusters Drive Kolmogorov Turbulence". In: ApJ 899.2, L30, p. L30. DOI: 10.3847/2041-8213/ababae.

Garcia-Segura, G. and Mac Low, M.-M. (Dec. 1995). "Wolf-Rayet Bubbles. I. Analytic Solutions". In: ApJ 455, p. 145. DOI: 10.1086/176563.

Gentry, E. S. et al. (Mar. 2019). "The momentum budget of clustered supernova feedback in a 3D, magnetized medium". In: MNRAS 483.3, pp. 3647–3658. DOI: 10.1093/mnras/sty3319.

Gofman, R. A., Gluck, N., and Soker, N. (2020). "Enhanced mass-loss rate evolution of stars with $\gtrsim$18 M$\odot$ and missing optically observed type II core-collapse supernovae". In: MNRAS 494.4, pp. 5230–5238. DOI: 10.1093/mnras/staa1085.

Green, D. A. (Aug. 2019). "A revised catalogue of 294 Galactic supernova remnants". In: *Journal of Astrophysics and Astronomy* 40.4, 36, p. 36. DOI: 10.1007/s12036-019-9601-6.

Green, D. A. and Stephenson, F. R. (2003). "Historical Supernovae". In: *Supernovae and Gamma-Ray Bursters*. Ed. by K. Weiler. Vol. 598, pp. 7–19. DOI: 10.1007/3-540-45863-8_2.

Green, S. et al. (May 2019). "Thermal emission from bow shocks. I. 2D hydrodynamic models of the Bubble Nebula". In: A&A 625, A4, A4. DOI: 10.1051/0004-6361/201834832.

Gupta, S. et al. (Jan. 2018). "Lack of thermal energy in superbubbles: hint of cosmic rays?" In: MNRAS 473.2, pp. 1537–1553. DOI: 10.1093/mnras/stx2427.

Gupta, S. et al. (Apr. 2020). "Realistic modelling of wind and supernovae shocks in star clusters: addressing ^{22}Ne/^{20}Ne and other problems in Galactic cosmic rays". In: MNRAS 493.3, pp. 3159–3177. DOI: 10.1093/mnras/staa286.

Harper-Clark, E. and Murray, N. (Mar. 2009). "One-Dimensional Dynamical Models of the Carina Nebula Bubble". In: ApJ 693.2, pp. 1696–1712. DOI: 10.1088/0004-637X/693/2/1696.

Heger, A. et al. (July 2003). "How Massive Single Stars End Their Life". In: ApJ 591.1, pp. 288–300. DOI: 10.1086/375341.

Heiles, C. (Apr. 1979). "H I shells and supershells". In: ApJ 229, pp. 533–537. DOI: 10.1086/156986.

Heiles, C. (Aug. 1984). "HI shells, supershells, shell-like objects, and "worms"." In: ApJS 55, pp. 585–595. DOI: 10.1086/190970.

Heiles, C. (Jan. 1989). "Magnetic Fields, Pressures, and Thermally Unstable Gas in Prominent H i Shells". In: ApJ 336, p. 808. DOI: 10.1086/167051.

Heiles, C. (Aug. 2009). "Our Local Superbubble and Local Bubble Environments". In: *The Local Bubble and Beyond II*. Ed. by R. K. Smith, S. L. Snowden, and K. D. Kuntz. Vol. 1156. American Institute of Physics Conference Series, pp. 199–207. DOI: 10.1063/1.3211814.

Herbst, W. and Miller, D. P. (Nov. 1982). "The age spread and initial mass function of NGC 3293: implications for the formation of clusters." In: AJ 87, pp. 1478–1490. DOI: 10.1086/113238.

Higdon, J. C. and Lingenfelter, R. E. (Aug. 2005). "OB Associations, Supernova-generated Superbubbles, and the Source of Cosmic Rays". In: ApJ 628.2, pp. 738–749. DOI: 10.1086/430814.

Janka, H.-T. (Nov. 2012). "Explosion Mechanisms of Core-Collapse Supernovae". In: *Annual Review of Nuclear and Particle Science* 62.1, pp. 407–451. DOI: 10.1146/annurev-nucl-102711-094901.

Jaskot, A. E. et al. (Feb. 2011). "Observational constraints on superbubble X-ray energy budgets". In: *The Astrophysical Journal* 729.1, p. 28. DOI: 10.1088/0004-637x/729/1/28.

Jenkins, E. B. and Meloy, D. A. (Nov. 1974). "A Survey with Copernicus of Interstellar O VI Absorption". In: ApJ 193, p. L121. DOI: 10.1086/181647.

Jiménez, S., Tenorio-Tagle, G., and Silich, S. (Sept. 2019). "The full evolution of supernova remnants in low- and high-density ambient media". In: MNRAS 488.1, pp. 978–990. DOI: 10.1093/mnras/stz1749.

Joubaud, T. et al. (Nov. 2019). "Gas shells and magnetic fields in the Orion-Eridanus superbubble". In: A&A 631, A52, A52. DOI: 10.1051/0004-6361/201936239.

Kamaya, H. (Feb. 1998). "Final Size of a Magnetized Superbubble". In: ApJ 493.2, pp. L95–L96. DOI: 10.1086/311145.

Katsuta, J., Uchiyama, Y., and Funk, S. (Apr. 2017). "Extended Gamma-Ray Emission from the G25.0+0.0 Region: A Star-forming Region Powered by the Newly Found OB Association?" In: *The Astrophysical Journal* 839.2, p. 129. DOI: 10.3847/1538-4357/aa6aa3.

Kim, C.-G., Ostriker, E. C., and Raileanu, R. (Jan. 2017). "Superbubbles in the Multiphase ISM and the Loading of Galactic Winds". In: ApJ 834.1, 25, p. 25. DOI: 10.3847/1538-4357/834/1/25.

Koo, B.-C. and McKee, C. F. (Mar. 1992a). "Dynamics of Wind Bubbles and Superbubbles. I. Slow Winds and Fast Winds". In: ApJ 388, p. 93. DOI: 10.1086/171132.

Koo, B.-C. and McKee, C. F. (Mar. 1992b). "Dynamics of Wind Bubbles and Superbubbles. II. Analytic Theory". In: ApJ 388, p. 103. DOI: 10.1086/171133.

Korpi, M. J. et al. (Oct. 1999). "Evolution of a superbubble in a turbulent, multi-phased and magnetized ISM". In: A&A 350, pp. 230–239.

Korpi, M. J., Brandenburg, A., and Tuominen, I. (July 1998). "Driving Galactic Turbulence by Supernova Explosions". In: *Studia Geophysica et Geodaetica* 42.3, pp. 410–418. ISSN: 1573-1626. DOI: 10.1023/A:1023381426082.

Krause, M. and Diehl, R. (Oct. 2014). "Dynamics and Energy Loss in Superbubbles". In: ApJ 794.2, L21, p. L21. DOI: 10.1088/2041-8205/794/2/L21.

Krause, M. et al. (Feb. 2013). "Feedback by massive stars and the emergence of superbubbles. I. Energy efficiency and Vishniac instabilities". In: A&A 550, A49, A49. DOI: 10.1051/0004-6361/201220060.

Krause, M. G. H. et al. (June 2020). "The Physics of Star Cluster Formation and Evolution". In: Space Sci. Rev. 216.4, 64, p. 64. DOI: 10.1007/s11214-020-00689-4.

Kroupa, P. (Jan. 2002). "The Initial Mass Function of Stars: Evidence for Uniformity in Variable Systems". In: *Science* 295.5552, pp. 82–91. DOI: 10.1126/science.1067524.

Kruijssen, J. M. D. (Nov. 2012). "On the fraction of star formation occurring in bound stellar clusters". In: MNRAS 426.4, pp. 3008–3040. DOI: 10.1111/j.1365-2966.2012.21923.x.

Krumholz, M. R., McKee, C. F., and Bland-Hawthorn, J. (Aug. 2019). "Star Clusters Across Cosmic Time". In: ARA&A 57, pp. 227–303. DOI: 10.1146/annurev-astro-091918-104430.

Lallement, R. et al. (Dec. 2003). "3D mapping of the dense interstellar gas around the Local Bubble". In: A&A 411, pp. 447–464. DOI: 10.1051/0004-6361:20031214.

Lallement, R. et al. (Jan. 2014). "3D maps of the local ISM from inversion of individual color excess measurements". In: A&A 561, A91, A91. DOI: 10.1051/0004-6361/201322032.

Lingenfelter, R. E. (Nov. 2018). "Cosmic rays from supernova remnants and superbubbles". In: *Advances in Space Research* 62.10, pp. 2750–2763. DOI: 10.1016/j.asr.2017.04.006.

Longmore, S. N. et al. (Jan. 2014). "The Formation and Early Evolution of Young Massive Clusters". In: *Protostars and Planets VI*. Ed. by H. Beuther et al., p. 291. DOI: 10.2458/azu_uapress_9780816531240-ch013.

López-Coto, R. and Giacinti, G. (Oct. 2018). "Constraining the properties of the magnetic turbulence in the Geminga region using HAWC γ-ray data". In: MNRAS 479.4, pp. 4526–4534. DOI: 10.1093/mnras/sty1821.

Lopez, L. A. et al. (Apr. 2011). "What Drives the Expansion of Giant H II Regions?: A Study of Stellar Feedback in 30 Doradus". In: ApJ 731.2, 91, p. 91. DOI: 10.1088/0004-637X/731/2/91.

Lopez, L. A. et al. (Nov. 2014). "The Role of Stellar Feedback in the Dynamics of H II Regions". In: ApJ 795.2, 121, p. 121. DOI: 10.1088/0004-637X/795/2/121.

Lopez, L. A. et al. (Apr. 2020). "Evidence of Particle Acceleration in the Superbubble 30 Doradus C with NuSTAR". In: ApJ 893.2, 144, p. 144. DOI: 10.3847/1538-4357/ab8232.

Mac Low, M.-M. and McCray, R. (Jan. 1988). "Superbubbles in Disk Galaxies". In: ApJ 324, p. 776. DOI: 10.1086/165936.

Mac Low, M.-M., McCray, R., and Norman, M. L. (Feb. 1989). "Superbubble Blowout Dynamics". In: ApJ 337, p. 141. DOI: 10.1086/167094.

Maddox, L. A. et al. (July 2009). "Nonthermal X-ray Emission in the N11 Superbubble in the Large Magellanic Cloud". In: ApJ 699.1, pp. 911–916. DOI: 10.1088/0004-637X/699/1/911.

Maggi, P. et al. (Jan. 2016). "The population of X-ray supernova remnants in the Large Magellanic Cloud". In: A&A 585, A162, A162. DOI: 10.1051/0004-6361/201526932.

Maggi, P. et al. (Nov. 2019). "The supernova remnant population of the Small Magellanic Cloud". In: A&A 631, A127, A127. DOI: 10.1051/0004-6361/201936583.

Marietta, E., Burrows, A., and Fryxell, B. (June 2000). "Type IA Supernova Explosions in Binary Systems: The Impact on the Secondary Star and Its Consequences". In: ApJS 128.2, pp. 615–650. DOI: 10.1086/313392.

Massey, P., Johnson, K. E., and Degioia-Eastwood, K. (Nov. 1995). "The Initial Mass Function and Massive Star Evolution in the OB Associations of the Northern Milky Way". In: ApJ 454, p. 151. DOI: 10.1086/176474.

Massey, P. et al. (Jan. 1989). "The Stellar Content of Two OB Associations in the LMC: LH 117 (NGC 2122) and LH 118". In: AJ 97, p. 107. DOI: 10.1086/114961.

Mathews, W. G. (Mar. 1967). "Dynamic Effects of Radiation Pressure in H II Regions". In: ApJ 147, p. 965. DOI: 10.1086/149087.

Mathieu, R. D. (Jan. 1986). "The dynamical evolution of young clusters and associations". In: *Highlights of Astronomy* 7, pp. 481–488.

Matsumoto, J. et al. (Dec. 2020). "2D numerical study for magnetic field dependence of neutrino-driven core-collapse supernova models". In: MNRAS 499.3, pp. 4174–4194. DOI: 10.1093/mnras/staa3095.

McCray, R. and Kafatos, M. (June 1987). "Supershells and Propagating Star Formation". In: ApJ 317, p. 190. DOI: 10.1086/165267.

McKee, C. F. and Ostriker, E. C. (Sept. 2007). "Theory of Star Formation". In: ARA&A 45.1, pp. 565–687. DOI: 10.1146/annurev.astro.45.051806.110602.

Moffat, A. F. J. et al. (July 2002). "Galactic Starburst NGC 3603 from X-Rays to Radio". In: ApJ 573.1, pp. 191–198. DOI: 10.1086/340491.

Molinari, S. et al. (Jan. 2014). "The Milky Way as a Star Formation Engine". In: *Protostars and Planets VI*. Ed. by H. Beuther et al., p. 125. DOI: 10.2458/azu_uapress_9780816531240-ch006.

Müller, B. (Aug. 2019). "A critical assessment of turbulence models for 1D core-collapse supernova simulations". In: MNRAS 487.4, pp. 5304–5323. DOI: 10.1093/mnras/stz1594.

Nagakura, H. et al. (Dec. 2019). "Towards an understanding of the resolution dependence of Core-Collapse Supernova simulations". In: MNRAS 490.4, pp. 4622–4637. DOI: 10.1093/mnras/stz2730.

Nazé, Y. et al. (Aug. 2001). "Interstellar Bubbles in Two Young H II Regions". In: AJ 122.2, pp. 921–937. DOI: 10.1086/322067.

Neustadt, J. M. M. et al. (Apr. 2021). "The search for failed supernovae with the Large Binocular Telescope: a new candidate and the failed SN fraction with 11 yr of data". In: *arXiv e-prints*, arXiv:2104.03318.

Norman, C. A. and Ikeuchi, S. (Oct. 1989). "The Disk-Halo Interaction: Superbubbles and the Structure of the Interstellar Medium". In: ApJ 345, p. 372. DOI: 10.1086/167912.

Ntormousi, E. et al. (Mar. 2017). "The role of magnetic fields in the structure and interaction of supershells". In: A&A 599, A94, A94. DOI: 10.1051/0004-6361/201629268.

Ochsendorf, B. B. et al. (Aug. 2015). "Nested Shells Reveal the Rejuvenation of the Orion-Eridanus Superbubble". In: ApJ 808.2, 111, p. 111. DOI: 10.1088/0004-637X/808/2/111.

Oey, M. S. (Aug. 1996). "The Dynamics of Superbubbles in the Large Magellanic Cloud". In: ApJ 467, p. 666. DOI: 10.1086/177642.

Oey, M. S. (Aug. 2009). "The Power Problem in Superbubbles". In: *The Local Bubble and Beyond II*. Ed. by R. K. Smith, S. L. Snowden, and K. D. Kuntz. Vol. 1156. American Institute of Physics Conference Series, pp. 295–304. DOI: 10.1063/1.3211829.

Oey, M. S. and Garcia-Segura, G. (Sept. 2004). "Ambient Interstellar Pressure and Superbubble Evolution". In: *The Astrophysical Journal* 613.1, pp. 302–311. DOI: 10.1086/421483.

Oey, M. S. and Massey, P. (Oct. 1995). "Triggered Star Formation and the Dynamics of a Superbubble in the LMC: The OB Association LH 47/48 in DEM 152". In: ApJ 452, p. 210. DOI: 10.1086/176292.

Oey, M. S. et al. (Jan. 2002). "The H I Environment of Three Superbubbles in the Large Magellanic Cloud". In: AJ 123.1, pp. 255–268. DOI: 10.1086/338092.

Offner, S. S. R. and Arce, H. G. (Oct. 2015). "Impact of Winds from Intermediate-mass Stars on Molecular Cloud Structure and Turbulence". In: ApJ 811.2, 146, p. 146. DOI: 10.1088/0004-637X/811/2/146.

Padoan, P. et al. (May 2016). "Supernova Driving. I. The Origin of Molecular Cloud Turbulence". In: ApJ 822.1, 11, p. 11. DOI: 10.3847/0004-637X/822/1/11.

Parizot, E. et al. (Sept. 2004). "Superbubbles and energetic particles in the Galaxy. I. Collective effects of particle acceleration". In: A&A 424, pp. 747–760. DOI: 10.1051/0004-6361:20041269.

Pauldrach, A., Puls, J., and Kudritzki, R. P. (Aug. 1986). "Radiation-driven winds of hot luminous stars. Improvements of the theory and first results." In: A&A 164, pp. 86–100.

Pittard, J. M. (Nov. 2013). "Self-sealing shells: blowouts and blisters on the surfaces of leaky wind-blown bubbles and supernova remnants". In: MNRAS 435.4, pp. 3600–3613. DOI: 10.1093/mnras/stt1552.

Portegies Zwart, S. F., McMillan, S. L. W., and Gieles, M. (Sept. 2010). "Young Massive Star Clusters". In: ARA&A 48, pp. 431–493. DOI: 10.1146/annurev-astro-081309-130834.

Powell, J. and Müller, B. (June 2020). "Three-dimensional core-collapse supernova simulations of massive and rotating progenitors". In: MNRAS 494.4, pp. 4665–4675. DOI: 10.1093/mnras/staa1048.

Prantzos, N. (Feb. 2012). "On the origin and composition of Galactic cosmic rays". In: A&A 538, A80, A80. DOI: 10.1051/0004-6361/201117448.

Preibisch, T. et al. (May 2012). "Herschel far-infrared observations of the Carina Nebula complex. I. Introduction and global cloud structure". In: A&A 541, A132, A132. DOI: 10.1051/0004-6361/201218851.

Puspitarini, L. et al. (June 2014). "Local ISM 3D distribution and soft X-ray background. Inferences on nearby hot gas and the North Polar Spur". In: A&A 566, A13, A13. DOI: 10.1051/0004-6361/201322942.

Rauw, G. et al. (2007). "Early-type stars in the core of the young open cluster Westerlund 2 ***". In: *A&A* 463.3, pp. 981–991. DOI: 10.1051/0004-6361:20066495.

Reynolds, T. M., Fraser, M., and Gilmore, G. (Nov. 2015). "Gone without a bang: an archival HST survey for disappearing massive stars". In: MNRAS 453.3, pp. 2885–2900. DOI: 10.1093/mnras/stv1809.

Rogers, H. and Pittard, J. M. (May 2013). "Feedback from winds and supernovae in massive stellar clusters - I. Hydrodynamics". In: MNRAS 431.2, pp. 1337–1351. DOI: 10.1093/mnras/stt255.

Rosen, A. L. et al. (Aug. 2014). "Gone with the wind: Where is the missing stellar wind energy from massive star clusters?" In: MNRAS 442.3, pp. 2701–2716. DOI: 10.1093/mnras/stu1037.

Saken, J. M. et al. (Oct. 1992). "An Infrared Supershell Surrounding the Cygnus OB1 Association". In: ApJ 397, p. 537. DOI: 10.1086/171810.

Salpeter, E. E. (Jan. 1955). "The Luminosity Function and Stellar Evolution." In: ApJ 121, p. 161. DOI: 10.1086/145971.

Sasaki, M. (Feb. 2020). "Supernova remnants in nearby galaxies". In: *Astronomische Nachrichten* 341.2, pp. 156–162. DOI: 10.1002/asna.202023772.

Scalzo, R. A., Ruiter, A. J., and Sim, S. A. (Dec. 2014). "The ejected mass distribution of Type Ia supernovae: a significant rate of non-Chandrasekhar-mass progenitors". In: MNRAS 445.3, pp. 2535–2544. DOI: 10.1093/mnras/stu1808.

Seo, J., Kang, H., and Ryu, D. (Apr. 2018). "The Contribution of Stellar Winds to Cosmic Ray Production". In: *Journal of Korean Astronomical Society* 51.2, pp. 37–48. DOI: 10.5303/JKAS.2018.51.2.37.

Sharma, P. et al. (Oct. 2014). "In a hot bubble: why does superbubble feedback work, but isolated supernovae do not?" In: MNRAS 443.4, pp. 3463–3476. DOI: 10.1093/mnras/stu1307.

Shull, J. M. and Saken, J. M. (May 1995). "Noncoeval Star Formation, Starbursts, and the Growth of Supershells in OB Associations". In: ApJ 444, p. 663. DOI: 10.1086/175638.

Smartt, S. J. (Apr. 2015). "Observational Constraints on the Progenitors of Core-Collapse Supernovae: The Case for Missing High-Mass Stars". In: PASA 32, e016, e016. DOI: 10.1017/pasa.2015.17.

Smith, D. A. and Wang, Q. D. (Aug. 2004). "Confronting the Superbubble Model with X-Ray Observations of 30 Doradus C". In: ApJ 611.2, pp. 881–891. DOI: 10.1086/422181.

Smith, N. (Apr. 2006). "A census of the Carina Nebula — I. Cumulative energy input from massive stars". In: *Monthly Notices of the Royal Astronomical Society* 367.2, pp. 763–772. ISSN: 0035-8711. DOI: 10.1111/j.1365-2966.2006.10007.x.

Smith, N. and Brooks, K. J. (July 2007). "A census of the Carina Nebula – II. Energy budget and global properties of the nebulosity". In: *Monthly Notices of the Royal Astronomical Society* 379.4, pp. 1279–1292. ISSN: 0035-8711. DOI: 10.1111/j.1365-2966.2007.12021.x.

Soler, J. D., Bracco, A., and Pon, A. (Feb. 2018). "The magnetic environment of the Orion-Eridanus superbubble as revealed by Planck". In: A&A 609, L3, p. L3. DOI: 10.1051/0004-6361/201732203.

Spitzer, L. (1962). *Physics of Fully Ionized Gases*.

Stil, J. et al. (Aug. 2009). "Three-dimensional Simulations of Magnetized Superbubbles: New Insights into the Importance of MHD Effects on Observed Quantities". In: ApJ 701.1, pp. 330–347. DOI: 10.1088/0004-637X/701/1/330.

Sukhbold, T. et al. (Apr. 2016). "Core-collapse Supernovae from 9 to 120 Solar Masses Based on Neutrino-powered Explosions". In: ApJ 821.1, 38, p. 38. DOI: 10.3847/0004-637X/821/1/38.

Tamburro, D. et al. (May 2009). "What is Driving the H I Velocity Dispersion?" In: AJ 137.5, pp. 4424–4435. DOI: 10.1088/0004-6256/137/5/4424.

Tang, S. and Wang, Q. D. (July 2005). "Supernova Blast Waves in Low-Density Hot Media: A Mechanism for Spatially Distributed Heating". In: ApJ 628.1, pp. 205–209. DOI: 10.1086/430875.

Tenorio-Tagle, G., Bodenheimer, P., and Rozyczka, M. (Aug. 1987). "Nonspherical supernova remnants. IV - Sequential explosions in OB associations". In: A&A 182.1, pp. 120–126.

Tenorio-Tagle, G. et al. (July 1991). "On the evolution of supernova remnants - II. Two-dimensional calculations of explosions inside pre-existing wind-driven bubbles." In: MNRAS 251, p. 318. DOI: 10.1093/mnras/251.2.318.

Thornton, K. et al. (June 1998). "Energy Input and Mass Redistribution by Supernovae in the Interstellar Medium". In: *The Astrophysical Journal* 500.1, pp. 95–119. DOI: 10.1086/305704.

Toalá, J. A. et al. (Aug. 2012). "X-Ray Emission from the Wolf-Rayet Bubble S 308". In: ApJ 755.1, 77, p. 77. DOI: 10.1088/0004-637X/755/1/77.

Toalá, J. A. et al. (Jan. 2015). "On the diffuse X-ray emission from the Wolf-Rayet bubble NGC 2359". In: MNRAS 446.1, pp. 1083–1089. DOI: 10.1093/mnras/stu2163.

Toalá, J. A. et al. (Mar. 2016). "X-ray emission from the Wolf-Rayet bubble NGC 6888 - II. XMM-Newton EPIC observations". In: MNRAS 456.4, pp. 4305–4314. DOI: 10.1093/mnras/stv2819.

Toalá, J. A. et al. (July 2020). "The Bubble Nebula NGC 7635 - testing the wind-blown bubble theory". In: MNRAS 495.3, pp. 3041–3051. DOI: 10.1093/mnras/staa752.

Tomisaka, K. (Sept. 1990). "Blowout of Superbubble in Galactic Magnetic Field". In: ApJ 361, p. L5. DOI: 10.1086/185814.

Tomisaka, K. (Aug. 1998). "Superbubbles in magnetized interstellar media: blowout or confinement?" In: MNRAS 298.3, pp. 797–810. DOI: 10.1046/j.1365-8711.1998.01654.x.

Townsley, L. K. et al. (Aug. 2003). "10 MK Gas in M17 and the Rosette Nebula: X-Ray Flows in Galactic H II Regions". In: ApJ 593.2, pp. 874–905. DOI: 10.1086/376692.

Townsley, L. K. et al. (Apr. 2006). "A Chandra ACIS Study of 30 Doradus. I. Superbubbles and Supernova Remnants". In: AJ 131.4, pp. 2140–2163. DOI: 10.1086/500532.

Townsley, L. K. et al. (May 2011). "An Introduction to the Chandra Carina Complex Project". In: ApJS 194.1, 1, p. 1. DOI: 10.1088/0067-0049/194/1/1.

Truelove, J. K. and McKee, C. F. (Feb. 1999). "Evolution of Nonradiative Supernova Remnants". In: ApJS 120.2, pp. 299–326. DOI: 10.1086/313176.

Uyaniker, B. et al. (May 2001). "The Cygnus superbubble revisited". In: A&A 371, pp. 675–697. DOI: 10.1051/0004-6361:20010387.

Vallée, J. P. (Sept. 2004). "Cosmic magnetic fields - as observed in the Universe, in galactic dynamos, and in the Milky Way". In: New A Rev. 48.10, pp. 763–841. DOI: 10.1016/j.newar.2004.03.017.

van Marle, A. J., Meliani, Z., and Marcowith, A. (Dec. 2015). "Shape and evolution of wind-blown bubbles of massive stars: on the effect of the interstellar magnetic field". In: A&A 584, A49, A49. DOI: 10.1051/0004-6361/201425230.

Vasiliev, E. O., Shchekinov, Y. A., and Nath, B. B. (July 2017). "Evolution of clustered supernovae". In: MNRAS 468.3, pp. 2757–2770. DOI: 10.1093/mnras/stx719.

Vázquez-Semadeni, E., González-Samaniego, A., and Colín, P. (May 2017). "Hierarchical star cluster assembly in globally collapsing molecular clouds". In: MNRAS 467.2, pp. 1313–1328. DOI: 10.1093/mnras/stw3229.

Vishniac, E. T. (Nov. 1983). "The dynamic and gravitational instabilities of spherical shocks". In: ApJ 274, pp. 152–167. DOI: 10.1086/161433.

Voss, R. et al. (Sept. 2010). "Probing the evolving massive star population in Orion with kinematic and radioactive tracers". In: A&A 520, A51, A51. DOI: 10.1051/0004-6361/201014408.

Walder, R. and Folini, D. (Oct. 2000). "On the Stability of Colliding Flows: Radiative Shocks, Thin Shells, and Supersonic Turbulence". In: Ap&SS 274, pp. 343–352. DOI: 10.1023/A:1026597318472.

Weaver, R. et al. (Dec. 1977). "Interstellar bubbles. II. Structure and evolution." In: ApJ 218, pp. 377–395. DOI: 10.1086/155692.

Woosley, S. E., Heger, A., and Weaver, T. A. (Nov. 2002). "The evolution and explosion of massive stars". In: *Reviews of Modern Physics* 74.4, pp. 1015–1071. DOI: 10.1103/RevModPhys.74.1015.

Woosley, S. E. and Weaver, T. A. (Nov. 1995). "The Evolution and Explosion of Massive Stars. II. Explosive Hydrodynamics and Nucleosynthesis". In: ApJS 101, p. 181. DOI: 10.1086/192237.

Yadav, N. et al. (Feb. 2017). "How multiple supernovae overlap to form superbubbles". In: MNRAS 465.2, pp. 1720–1740. DOI: 10.1093/mnras/stw2522.

Chapter 2

Cosmic rays in turbulence

Turbulence is ubiquitous in astrophysical plasmas. Be it generated by macroscopic outflows subject to viscous dissipation, or by small-scale excitation of waves, it appears in magnetised environments as a random ensemble of hydromagnetic perturbations on an extended range of scales, from typically 10^4 km to hundreds of parsecs.

Because they are charged particles, cosmic rays are affected by magnetic waves, and any theory of cosmic ray acceleration and propagation eventually relies on the description of the transport of particles in magnetised plasmas. This chapter summarises the main results of the standard "quasi-linear" theory of particle transport in turbulence, which will be later applied to superbubble environments.

2.1 Interstellar turbulence

2.1.1 Magnetohydrodynamic waves

Ideal magnetohydrodynamic fluids are fluids where all dissipative processes, viscous dissipation, electrical resistivity, thermal conductivity, or non-adiabatic heating or cooling are neglected. They are described by the following set of equations:

$$\text{Continuity equation :} \quad \partial_t \rho + \nabla \cdot (\rho \boldsymbol{u}) = 0 \,, \tag{2.1}$$

$$\text{Momentum equation :} \quad \partial_t \boldsymbol{u} + (\boldsymbol{u} \cdot \nabla)\, \boldsymbol{u} = \frac{1}{4\pi\rho} (\nabla \times \boldsymbol{B}) \times \boldsymbol{B} - \frac{\nabla P}{\rho} \,, \tag{2.2}$$

$$\text{Energy equation :} \quad \frac{\mathrm{d}}{\mathrm{d}t} \left(\frac{P}{\rho^\gamma} \right) = 0 \,, \tag{2.3}$$

$$\text{Induction equation :} \quad \partial_t \boldsymbol{B} = \nabla \times (\boldsymbol{u} \times \boldsymbol{B}) \,, \tag{2.4}$$

$$\text{Gauss law for magnetism :} \quad \nabla \cdot \boldsymbol{B} = 0 \,, \tag{2.5}$$

where $\boldsymbol{u}$ is the fluid velocity, ρ is the fluid density, $\boldsymbol{B}$ is the magnetic field frozen in the fluid, P is the external pressure exerted on the fluid, γ is the adiabatic index. The linearized version of these equations can be worked out to obtain the dispersion relation of the hydromagnetic waves:

$$\left(\omega^2 - k_\parallel^2 v_A^2\right) \left(\omega^4 - \omega^2 k^2 \left(v_A^2 + c_s^2\right) + k^2 k_\parallel^2 v_A^2 c_s^2\right) = 0 \,, \tag{2.6}$$

where $k_\parallel$ is the component of the wave vector projected along the mean magnetic field, $v_A = B/\sqrt{4\pi\rho}$ is the local Alfvén speed, c_s is the local sound speed such that $\nabla P = c_s \nabla \rho$.

Solving this equation leads to three types of waves with respective pulsations ω_A, ω_F and ω_S:

$$\omega_A = k_\parallel v_A \,, \tag{2.7}$$

$$\omega_{\substack{F\\S}} = \frac{k\sqrt{v_A^2 + c_s^2}}{\sqrt{2}} \left(1 \pm \sqrt{1 - \frac{4k_\parallel^2 c_s^2 v_A^2}{k^2 \left(v_A^2 + c_s^2\right)^2}}\right)^{1/2} . \tag{2.8}$$

Since $\omega_S < \omega_A < \omega_F$, these waves are respectively referred to as "slow" magnetoacoustic waves, "Alfvén" waves and "fast" magnetoacoustic waves. In the absence of magnetic field, the only wave remaining is the fast wave, which then corresponds to a standard sound wave. On the other hand, in an incompressible magnetised plasma ($\nabla\rho = 0$), the sound speed is infinite and we get $\omega_S = \omega_A$, $\omega_F = \infty$, meaning there exist only magnetic waves.

It can be shown from the linearised magnetohydrodynamic equations of incompressible fluids that Alfvén waves propagate a magnetic fluctuation $\boldsymbol{\delta B}$ in the direction of the background field and such that $\boldsymbol{\delta B}$ is perpendicular to the background field and the wave vector. On the other hand, slow waves propagate a perturbation perpendicular to the wave vector in the $(\boldsymbol{k}, \boldsymbol{B_0})$ plane, where $\boldsymbol{B_0}$ is the unperturbed magnetic field (Chandran, 2004).

When two hydromagnetic fluctuations propagating along a field line collide, the Lorentz force shears the wave packets in the plane perpendicular to the direction of propagation. As a result, the wavelength decreases: the perturbations decay to smaller scales, which induces a turbulence cascade.

2.1.2 Turbulence spectrum

Turbulent fluids are described by means of spectral tensors, which describe the spatio-temporal correlations between the observables. When dealing with magnetised turbulence, one is mainly interested into two quantities: the velocity of the fluid elements and the fluctuations of the magnetic field. Given the complexity of turbulent systems, it is illusory to believe one could track the details of their physical properties. Instead, a statistical description must be done. A static turbulent medium is then described by the average variations of the physical quantities on given lengths, which are mathematically written in terms of correlation tensors. For instance, the spectral tensor describing the spatial correlations between the magnetic field perturbations is defined as the Fourier coefficient of the spatial average of the correlations:

$$P_{ij}\left(\boldsymbol{k}\right) \equiv \frac{1}{(2\pi)^3} \int \langle b_i\left(\boldsymbol{x}\right) b_j\left(\boldsymbol{x} + \boldsymbol{l}\right)\rangle e^{-i\boldsymbol{k}\cdot\boldsymbol{l}} \mathrm{d}\boldsymbol{l} \,, \tag{2.9}$$

where the quantity in the brackets describes the spatial average. The time dependencies have been omitted as we consider static turbulence for simplicity (this is a reasonable assumption in many astrophysical environments). The magnetic energy spectrum directly follows from the spectral tensor as:

$$W_B\left(\boldsymbol{k}\right) = \frac{1}{2} \sum_i P_{ii}\left(\boldsymbol{k}\right) \,, \tag{2.10}$$

and similar quantities are defined for the velocity correlations and fluid kinetic energy. In the following we will mainly describe turbulence in terms of its differential energy spectrum $W(k)$, which contains both the hydrodynamic and magnetic components. Assuming

the equipartition of the energy between the velocity perturbations δu and the magnetic fluctuations δB provides the normalisation $\int \mathrm{d}k W(k) = \delta B^2/(4\pi) = \rho \delta u^2$. Unfortunately, deriving the spectrum of turbulence from a fundamental basis is a difficult task to achieve and it is customary to rather rely on phenomenological laws. The first theory of turbulence was developed by Kolmogorov in 1941 (see Kolmogorov and Tikhomirov, 1991) who explained on dimensional grounds that turbulence proceeds through a cascade of energy from large scales to small scales. Physically, these scales may correspond to e.g. the size of the eddies or the wavelength of the hydromagnetic waves. The energy is dissipated at the smallest scales, where viscous dissipation dominates. However, there usually exists a range of intermediate *inertial* scales where the viscosity as well as the large-scale injection processes are negligible. Let us denote the energy transfer rate at the scale $2\pi/k$ as $\Pi(k) \equiv \mathrm{d}E_k/\tau_k$, where $\mathrm{d}E_k = \int_k^{k+\mathrm{d}k} W(k)\mathrm{d}k$ is the energy contained in the scale $2\pi/k$ and τ_k is the time it takes for a structure of typical size $2\pi/k$ to be distorted by the turbulent motions. Because dissipation and injection are negligible in the inertial range, the energy transfer rate must be constant in order to ensure global energy conservation and we write: $\Pi(k) \equiv \epsilon$. This implies $E_k = \epsilon\tau_k$ and therefore $W(k) = \epsilon\partial_k\tau_k$. If the turbulence is not magnetised, the distortion time of the eddies is expected to be of the order of $(u_k k)^{-1}$, where u_k is the typical velocity across the eddy, such that $E_k \propto u_k^2$. We eventually find the well-known result:

$$W(k) = C_K \epsilon^{2/3} k^{-5/3}, \tag{2.11}$$

where C_K is a numerical constant. This is the so-called "universal" Kolmogorov phenomenology.

Magnetised turbulence is characterized by further parameters, magnetised waves, and cross-correlations between the velocity and the magnetic perturbations. Due to this additional complexity, there is no universality for inertial magnetohydrodynamic spectra. However, the turbulence is still expected to be described by a scale-free energy cascade, with a power law energy spectrum:

$$W(k) \propto k^{-q}. \tag{2.12}$$

Because of the lack of universality, several phenomenologies coexist, each of them providing a different value for the *spectral index* q. The first phenomenology of isotropic hydromagnetic turbulence was developed by Iroshnikov (1964) and Kraichnan (1965), who derived $q = 3/2$ in the limit of weak magnetic fluctuations, assuming that the rate of interaction between hydromagnetic waves was the inverse of the Alfvén time $(v_A k)^{-1}$. On the other hand, when magnetic fluctuations dominate over the mean magnetic field, it is not relevant to consider the Alfvén time anymore and it can be shown that the turbulence spectrum follows again a Kolmogorov-type spectrum with $q = 5/3$ (Marsch and Tu, 1990). Furthermore, in many astrophysical contexts anisotropies cannot be neglected. Weak anisotropic turbulence is described by $W(k) \propto k_\perp^{-2}$ (Galtier et al., 2000), while strong anisotropic turbulence follows the Goldreich-Sridhar phenomenology $W(k) \propto k_\perp^{-5/3}$ (Goldreich and Sridhar, 1995). More complex models have been developed since these pioneering works, however an extensive review of turbulence is not the purpose of this work.

2.1.3 Turbulence dynamics

The power law scalings described above correspond to the case where the turbulence is fully developed and stationary, which means that any correlation vanishes at large dis-

tances. In order to describe the time-dependent establishment of the turbulence cascade, a dynamical equation is needed. The simplest possible form of such equation for homogeneous isotropic turbulence is the following (Zhou and Matthaeus, 1990):

$$\partial_t W + \partial_k F = S\delta\left(k - k_0\right) , \tag{2.13}$$

where F is the energy flux from scale to scale and S is the source of turbulence at the injection scale k_0. This equation describes the local conservation of the flux through the neighbouring scales. A considerable simplification has been done by neglecting the non-local dynamical couplings between the whole range of scales. The turbulence was also assumed to be isotropic although it can be shown that anisotropies are expected to develop when the magnetic waves interact in either weak or strong turbulence.

As previously mentioned, in the inertial range of the turbulence, viscous dissipation does not play any role. The energy dissipates from the largest scale to the smallest scale because of the interactions between waves of similar wavelengths. The corresponding energy flux is phenomenologically written as $F \propto W(k)k/\tau_k$, where τ_k is the timescale of the interactions. The Kolmogorov phenomenology relates the interaction timescale with the eddy distortion ("turn-over") time $\tau_k = (u_k k)^{-1}$ where $u_k = \sqrt{2kW(k)/\rho}$ is the typical velocity at the scale $2\pi/k$. Kraichan phenomenology relates the interaction timescale with the inverse Alfvén time $\tau_A^{-1} = v_A k$ where $v_A = B_0/\sqrt{4\pi\rho}$ is the velocity of the magnetic waves (B_0 is the mean "background" field). The idea is that waves travelling rapidly will interact during a short time and therefore the energy transfer will not be efficient. A dimensional argument provides $\tau_k \propto v_A\rho/(W(k)k^2)$. In both Kolmogorov and Kraichnan phenomenologies, the interactions between the waves are nonlinear, and so is the transport equation of the turbulence:

$$\partial_t W + \partial_k \left(\frac{akB_0^3}{16\pi^2\sqrt{\rho}} \left(\frac{8\pi kW}{B_0^2} \right)^{\beta} \right) = S\delta(k - k_0) , \tag{2.14}$$

where $a \approx 1$ is a numerical constant determined from experiments or simulations (e.g. Verma et al. 1996, see also Norman and Ferrara 1996). $\beta = 3/2$ for the Kolmogorov phenomenology and $\beta = 2$ for the Kraichnan phenomenology. The stationary solution to this equation corresponds, by construction, to the standard power law scalings: $W_k \propto k^{-5/3}$ or $W_k \propto k^{-3/2}$. Another interesting scenario is the case where the magnetic fluctuations (denoted δB) dominate over the background field. The relevant velocity would be $v_k \sim \delta B_k/\sqrt{4\pi\rho}$, where δB_k is the amplitude of the magnetic waves of wavenumber k. The relevant interaction time would then scale as $\tau_k \propto \delta B_k\sqrt{\rho}/(W(k)k^2) \propto \sqrt{\rho/(W(k)k)}/k$. The latter is identical to the eddy turnover time of the Kolmogorov phenomenology (the eddies are analogous to the strong magnetic perturbations and the perturbations are distorted in a modified Alfvén time).

More sophisticated models of turbulence have been developped since the works of Kolmogorov and Kraichnan. For instance, a straighforward improvement is to describe the energy flux between the turbulent scales with Fick's law: $F \propto \nabla_k W$, that is, modelling the turbulence dynamics by a diffusion process. The transport equation becomes (Zhou and Matthaeus, 1990):

$$\partial_t W = \partial_k \left(C_D(k)k^2 \partial_k \left(\frac{W}{k^2} \right) \right) , \tag{2.15}$$

where $C_D(k) \propto k^2/\tau_k$ is the diffusion coefficient. This equation admits two stationary solutions depending on the boundary condition imposed at the smallest scales. If the

energy is assumed to vanish at the dissipation scale, the standard power law scalings are retrieved. On the other hand, if the dissipation is neglected, the solution is a flat spectrum. This last solution was not described by the first model given by Equation 2.13. Although it will not be useful in the present work, it has important applications elsewhere (e.g. Kraichnan and Montgomery, 1980).

2.2 Particle scattering on turbulence

Having briefly introduced the properties of turbulent plasmas, we now consider the transport of particles in a turbulent environment which consists in a random ensemble of hydromagnetic fluctuations.

2.2.1 Wave-particle interaction

The interaction between a charged particle and a magnetic fluctuation is dictated by the Lorentz force:

$$\frac{\mathrm{d}\boldsymbol{p}}{\mathrm{d}t} = Ze\left(\boldsymbol{E} + \frac{\boldsymbol{v}}{c} \times \boldsymbol{B}\right) , \tag{2.16}$$

where Ze is the charge of the particles and $\boldsymbol{p} = \gamma m \boldsymbol{v}$ is the particle momentum with γ the Lorentz factor and m the particle mass. The electric field accelerates the particles while the magnetic field exerts only a normal force which induces a gyromotion around the field lines, with gyroradius (or Larmor radius):

$$R_L = \frac{v \sin\theta}{\Omega_s} , \quad \Omega_s = \frac{qB}{\gamma m c} , \tag{2.17}$$

where $\cos\theta = \boldsymbol{v} \cdot \boldsymbol{B}/(vB) \equiv \mu$ is called the particle pitch-angle cosine and Ω_s is referred to as the synchrotron pulsation.

The interaction of an ensemble of particles with the plasma is described statistically. Instead of following the trajectories of each particle, we consider the dynamics of the *particle distribution function* f, which gives the density of particles in the $(\boldsymbol{x}, \boldsymbol{p})$ phase space. The number density and energy density of the particles are obtained by integration of f as:

$$n = \int \mathrm{d}^3\boldsymbol{p}\, f\left(\boldsymbol{x}, \boldsymbol{p}\right) , \tag{2.18}$$

$$E = \int \mathrm{d}^3\boldsymbol{p}\, \epsilon(p) f\left(\boldsymbol{x}, \boldsymbol{p}\right) , \tag{2.19}$$

where $\epsilon(p) = \sqrt{p^2 + m^2} - m$ is the kinetic energy of a particle of momentum p.

In a collisionless plasma, that is a plasma where the microscopic interactions are mediated by the electromagnetic fields rather than the Coulomb collisions, the evolution of the distribution function is dictated by the Liouville equation:

$$\partial_t f + \frac{\mathrm{d}\boldsymbol{x}}{\mathrm{d}t} \cdot \frac{\partial f}{\partial \boldsymbol{x}} + \frac{\mathrm{d}\boldsymbol{p}}{\mathrm{d}t} \cdot \frac{\partial f}{\partial \boldsymbol{p}} = 0 , \tag{2.20}$$

which states that the number of particles contained in a volume following the particle trajectories in phase space is conserved. The coupling between the plasma and the particles is hidden into the third term, which contains the Lorentz force.

2.2.2 The quasi-linear approximation

We now assume that the electromagnetic field is made of fluctuations over a background mean field, that is:

$$\boldsymbol{B} = \langle \boldsymbol{B} \rangle + \boldsymbol{b} = \langle \boldsymbol{B_0} \rangle + \boldsymbol{\delta B}\,, \tag{2.21}$$

$$\boldsymbol{E} = \boldsymbol{\delta E}\,, \tag{2.22}$$

where we have neglected the mean electric field, assuming that the conductivity of the medium is very high such that any large-scale fluctuation relaxes immediately. We further assume that there is no large-scale plasma motion, in which case the reference frame of the perturbations nearly coincides with the rest frame of the fluid. In the presence of background plasma motions, a change of reference frame must be performed, which is in particular responsible for the acceleration of particles at shock waves. This will be considered in the next chapter.

We further decompose the distribution function as the sum of a mean value and a fluctuation:

$$f = \langle f \rangle + f_1\,. \tag{2.23}$$

The Liouville equation can be averaged over an ensemble of waves to obtain (Berezinskii et al., 1990):

$$\partial_t \langle f \rangle + (\boldsymbol{v} \cdot \nabla) \langle f \rangle + \frac{Ze}{c} (\boldsymbol{v} \times \boldsymbol{B_0}) \cdot \frac{\partial \langle f \rangle}{\partial \boldsymbol{p}} = -Ze \langle \left(\boldsymbol{\delta E} + \frac{\boldsymbol{v}}{c} \times \boldsymbol{\delta B} \right) \cdot \frac{\partial f_1}{\partial \boldsymbol{p}} \rangle\,. \tag{2.24}$$

The right-hand side describes the collisions between the particles and the hydromagnetic waves. A similar equation is obtained for the fluctuation f_1, which depends on the mean field as well as its perturbations. At this point, it is usually assumed that the perturbations are small, such that they can be neglected in the computation of the fluctuating part of the distribution function f_1. Equivalently, this amounts to assume that, when computing f_1, the particles follow unperturbed trajectories, i.e. the trajectories dictated by the unperturbed magnetic field $\boldsymbol{B_0}$. This is the so-called *quasi-linear approximation* (QLT). It is a first-order theory valid in the limit of small perturbations, i.e. when $\delta B \ll B_0$. I shall comment later on the domain of validity of the approximation.

Within the quasi-linear theory, the fluctuating part of f can be formally written as:

$$f_1 = -\int_{-\infty}^{t} \mathrm{d}t' Ze \left(\boldsymbol{\delta E} + \frac{\boldsymbol{v}}{c} \times \boldsymbol{\delta B} \right) \cdot \frac{\partial \langle f \rangle}{\partial \boldsymbol{p}}\,, \tag{2.25}$$

where, according to the quasi-linear approximation, the integration must be performed over the unperturbed trajectories. The right-hand side of the Boltzmann equation is thus found to describe a diffusion in momentum space, of the form:

$$\boldsymbol{C} \cdot \frac{\partial}{\partial \boldsymbol{p}} \left(\int \mathrm{d}t' \boldsymbol{C} \cdot \frac{\partial \langle f \rangle}{\partial \boldsymbol{p}} \right)\,. \tag{2.26}$$

2.2.3 Pitch-angle scattering and momentum diffusion

Tedious algebra must be performed to properly work out Equation 2.24. Here I only transcribe some of the intermediate steps, which hopefully provide a physical understanding of the wave-particle interaction. First, one must write the Fourier transform of the

electromagnetic fluctuations:

$$\boldsymbol{\delta E} = \sum_{\alpha} \int \mathrm{d}^3\boldsymbol{k}\, e^{-\mathrm{i}\omega_\alpha(\boldsymbol{k})t+\mathrm{i}\boldsymbol{k}\cdot\boldsymbol{x}} \boldsymbol{\delta E_\alpha}\left(\boldsymbol{k}\right), \tag{2.27}$$

$$\boldsymbol{\delta B} = \sum_{\alpha} \int \mathrm{d}^3\boldsymbol{k}\, e^{-\mathrm{i}\omega_\alpha(\boldsymbol{k})t+\mathrm{i}\boldsymbol{k}\cdot\boldsymbol{x}} \boldsymbol{\delta B_\alpha}\left(\boldsymbol{k}\right). \tag{2.28}$$

The sum runs over the different modes of the hydromagnetic waves, such as the Afvén and magnetoacoustic waves discussed in Section 2.1.1. Then, it is usually assumed that the gyrofrequency of the particles is so large compared to the timescale of the particle-wave interaction that the particle distribution function is gyrotropic. The two remaining variables in momentum space are taken as the cylindrical coordinates (p, μ), where μ is the particle pitch-angle cosine.

Working out Equation 2.24 in the limit of large gyrofrequency $k_\perp v_\perp/\Omega_s \ll 1$ leads to an equation of the following form:

$$\partial_t f_0 + \boldsymbol{v}\cdot\nabla f_0 = \pi Z^2 e^2 \sum_{\alpha} \int \mathrm{d}^3\boldsymbol{k} \sum_{s} \delta\left(\omega_\alpha\left(\boldsymbol{k}\right) - k_\parallel \mu v - s\Omega_s\right) I_{\alpha,s}(\boldsymbol{k},\omega_\alpha)\mathcal{D}^2_{p,\mu}[f_0]\,, \tag{2.29}$$

where f_0 denotes the gyroaveraged mean distribution and $\mathcal{D}^2_{p,\mu}$ is a second order differential operator in momentum space, containing the derivatives ∂_p, ∂_μ, ∂_p^2, ∂_μ^2, $\partial_p\partial_\mu$. The delta function has emerged from the computation of the following time integral:

$$\Re \int \mathrm{d}t e^{-\mathrm{i}\left(k_\parallel v\mu + s\Omega_s - \omega_\alpha(\boldsymbol{k})\right)t} = \pi\delta\left(\omega_\alpha\left(\boldsymbol{k}\right) - k_\parallel\mu v - s\Omega_s\right). \tag{2.30}$$

This delta function shows that the interactions between the particles and the electromagnetic fluctuations are actually resonant. Particles only scatter on the waves under the following condition:

$$\omega_\alpha\left(\boldsymbol{k}\right) - k_\parallel \mu v = s\Omega_s\,, \quad s \in \mathbb{Z}\,, \tag{2.31}$$

which is called the gyroresonance condition. It states that a particle interacts with a wave only if the frequency of the wave measured in the reference frame moving with the particle along the background regular magnetic field line is a multiple of the frequency of gyration around the field line. This ensures that the effect of the Lorentz force cumulates during the rotation of the particle. If the resonance condition is not fulfilled, the Lorentz force is averaged during the particle rotation and the net force experienced by the particle vanishes, thus there is no effective interaction. Furthermore, the amplitude of the interaction $I_{\alpha,s}$ depends on the Bessel functions J_s, J_{s+1} and J_{s-1}, all evaluated at $k_\perp v_\perp/\Omega_s$. In the limit of large gyrofrequency, the only non-negligible harmonics will therefore be $s = 0, \pm 1$.

The second interesting feature of Equation 2.29 is the presence of a second-order differential operator. Second-order derivatives, in particular $\partial_{\mu\mu}$ and ∂_{pp}, give rise to diffusion terms, respectively in pitch-angle and momentum.

The physical picture of the wave-particle interactions is therefore understood as follows: when a particle propagates in a turbulent ensemble of hydromagnetic waves, it interacts with the waves whose wave numbers resonate with the parallel component of the particle velocity. This interaction results in two phenomena: the pitch-angle of the particle is slightly tilted, and the momentum of the particle is either increased of decreased, depending on the direction of propagation of the particle with respect to that

of the wave. Since the waves form an ensemble of random fluctuations, the pitch-angle and the momentum of a particle becomes random variables, such that the particle follows a random wandering in the (p, μ) space. When one considers a large amount of particles through their distribution function, an effective diffusion emerges. The diffusion coefficients can be computed from the time correlations between the random variables, e.g.:

$$D_{\mu\mu}(\mu) = \int_0^\infty \mathrm{d}t \, \langle \dot{\mu}(t)\dot{\mu}(0)\rangle \, , \quad D_{pp}(p) = \int_0^\infty \mathrm{d}t \, \langle \dot{p}(t)\dot{p}(0)\rangle \, , \tag{2.32}$$

where the average is performed over the ensemble of waves. It can generally be assumed that the diffusion in pitch-angle is much faster than the diffusion in momentum. Indeed, since both phenomena have the same physical origin, they occur at the same rate, which is the scattering rate of particles on hydromagnetic waves. When a particle encounters a magnetic perturbation $(\boldsymbol{\delta B}, \boldsymbol{\delta E})$, the pitch-angle deflection $\Delta\theta$ is due to the magnetic field while the energy gain is due to the electric field. From the Lorentz force and the induction equation, we have $\delta E \sim v_A \delta B/c$ where v_A is the Alfvén velocity. This provides $\Delta\theta \sim qv\delta B/pc$ and $\Delta p \sim qv_A\delta B/c$, thus $\Delta p/p \sim (v_A/v)\Delta\theta \ll \Delta\theta$. The variables p and μ are therefore decorrelated such that the non diagonal terms of the momentum diffusion tensor can be neglected and we are left with a transport equation of the following form:

$$\partial_t f_0 + \boldsymbol{v}\cdot\nabla f_0 = \partial_\mu D_{\mu\mu}\partial_\mu f_0 + \frac{1}{p^2}\partial_p\left(p^2 D_{pp}\partial_p f_0\right) \, , \tag{2.33}$$

which describes the isotropisation and stochastic acceleration of a distribution of charged particles propagating in a plasma.

2.2.4 The diffusion approximation

Assuming for simplicity that the mean magnetic field is directed along the x-axis, the gyroaveraged transport equation simplifies to:

$$\partial_t f_0 + \mu v\partial_x f_0 = \partial_\mu D_{\mu\mu}\partial_\mu f_0 + \frac{1}{p^2}\partial_p\left(p^2 D_{pp}\partial_p f_0\right) \, . \tag{2.34}$$

The pitch-angle scattering term induces an anisotropy in momentum space, such that f_0 can be decomposed as:

$$f_0(x,\mu,p,t) = \bar{f}_0(x,p,t) + f_1(x,\mu,p,t) \, , \qquad \bar{f}_0(x,p,t) \equiv \frac{1}{2}\int_{-1}^{1}\mathrm{d}\mu \, f(x,\mu,p,t) \, . \tag{2.35}$$

Assuming that the anisotropic part of f_0 is small, and that the distribution function evolves on time and momentum scales much larger than the scattering time, the integration of Equation 2.34 from -1 to μ and from -1 to 1 gives to lowest order:

$$\frac{\mu^2-1}{2}v\partial_x\bar{f}_0 = D_{\mu\mu}\partial_\mu f_1 \, , \tag{2.36}$$

$$2\partial_t\bar{f}_0 - v\partial_x\int_{-1}^{1}\mathrm{d}\mu\,\frac{\mu^2-1}{2}\partial_\mu f_1 = \frac{1}{p^2}\partial_p\left(p^2\left[\int_{-1}^{1}\mathrm{d}\mu D_{pp}\right]\partial_p f_0\right) \, , \tag{2.37}$$

where we used $D_{\mu\mu}(\pm 1) = 0$, as particles moving along the magnetic field are not deflected. The first equation shows how the anisotropy induced by the variation of the particle pitch-angles produces a net flux of particles in space. The distribution function then obeys a diffusion equation in space:

$$\partial_t \bar{f}_0 = \partial_x D_\parallel \partial_x \bar{f}_0 + \partial_p \left(p^2 \bar{D_{pp}} \partial_p f_0 \right) , \tag{2.38}$$

where:

$$D_\parallel \equiv \frac{v^2}{8} \int_{-1}^{1} \mathrm{d}\mu \, \frac{(\mu^2 - 1)^2}{D_{\mu\mu}} , \quad \bar{D_{pp}} \equiv \frac{1}{2} \int_{-1}^{1} \mathrm{d}\mu D_{pp} . \tag{2.39}$$

The spatial diffusion parallel to the mean magnetic field is understood as follows. When a particle experiences many scatterings, it has a chance to reverse its direction of propagation with respect to the background field lines. The spatial variables thus become random variables and give rise to a diffusive behaviour. The more effective the pitch-angle scattering (i.e. the larger $D_{\mu\mu}$), the more frequent the particles change direction, the less effective the spatial diffusion along the field lines (i.e. the smaller $D_\parallel$).

The hypothesis that the background field is one-dimensional can also be relaxed. In realistic astrophysical plasmas, the background field is usually rather a large-scale random field and the quasi-linear approximation is only valid locally. The large-scale fluctuations induce a wandering of the field lines in space, which, together with other processes discussed below, produces an additional diffusion of the particles perpendicularly to the average direction of the background field, with a diffusion coefficient $D_\perp$. The generalization of Equation 2.38 to the three-dimensional case leads to:

$$\partial_t f = \nabla \cdot (D \cdot \nabla f) + \frac{1}{p^2} \partial_p p^2 D_{pp} \partial_p f , \tag{2.40}$$

where f is the isotropic and gyrotropic part of the distribution function averaged over the magnetic fluctuations, and D is the diffusion tensor which contains in particular the component parallel to the local magnetic field $D_\parallel$ and the components perpendicular to the local magnetic field $D_\perp$. In general, the perpendicular diffusion is expected to be a much less efficient process unless the turbulence is very strong. Finally D_{pp} is the momentum diffusion coefficient averaged over the pitch-angle.

The spatial and momentum diffusion coefficients can be estimated as follows. The rate at which scatterings occur is $\nu \approx v/\lambda$, where λ is the mean free path of the particles in the turbulent plasma. Assuming isotropy, the parallel spatial diffusion coefficient is $D_\parallel \approx \lambda^2 \nu / 3$. On the other hand, at each scattering particles gain an energy $\Delta p \approx p v_A / v$. Thus the momentum diffusion coefficient is $D_{pp} \approx p^2 (v_A/v)^2 \nu / 3$, and we obtain the well-known relation:

$$D_\parallel D_{pp} \approx p^2 v_A^2 / 9 . \tag{2.41}$$

To obtain a similar relation for the perpendicular diffusion coefficient is a nontrivial task. Numerical simulations (e.g. Casse et al., 2001) show that the expressions obtained in the context of quasilinear theory are very inaccurate, underestimating the perpendicular transport of the particles. Nonlinear effects beyond the quasi-linear approximation, in particular the perturbation of the trajectories of the guiding centres in the turbulent plasma, enhance the perpendicular diffusion.

2.2.5 Perpendicular diffusion

Although a computation from first principles is possible in the framework of quasi-linear theory, a simple heuristic argument can be invoked to investigate the process of particle diffusion perpendicularly to the mean magnetic field (Bieber and Matthaeus, 1997). This very general phenomenological approach is *a priori* not restricted to the regime of weak turbulence. The starting point is the Taylor-Green-Kubo formula, which relates the diffusion coefficients to the velocity correlations:

$$D_{\parallel} = \int_0^{\infty} \mathrm{d}t \, \langle v_{\parallel}(t) v_{\parallel}(0) \rangle \,, \quad D_{\perp} = \int_0^{\infty} \mathrm{d}t \, \langle v_{\perp}(t) v_{\perp}(0) \rangle \,. \tag{2.42}$$

We now assume that any trajectory is randomised after a given time, such that the predictability of the particle helical motion is exponentially suppressed:

$$\langle v_{\parallel}(t) v_{\parallel}(0) \rangle \propto v^2 e^{-\nu_{\parallel} t} \,, \tag{2.43}$$

$$\langle v_{\perp}(t) v_{\perp}(0) \rangle \propto v^2 \cos(\Omega_s t) \, e^{-\nu_{\perp} t} \,, \tag{2.44}$$

where the cosine accounts for the periodic variation of the perpendicular velocity due to the Larmor gyration. The integrals 2.42 provide:

$$D_{\parallel} = \frac{v^2}{3\nu_{\parallel}} \,, \tag{2.45}$$

$$D_{\perp} = \frac{v R_L}{3} \frac{\epsilon}{1+\epsilon^2} \,, \quad \epsilon \equiv \Omega_s / \nu_{\perp} \,. \tag{2.46}$$

The rates $\nu_{\parallel}$ and $\nu_{\perp}$ are determined by any possible physical processes which stochastically affect the trajectories of the particles, such that the scattering of the pitch-angles or the stochastic wandering of the magnetic field lines. In the framework of quasi-linear theory, it is natural to assume that the only process which affects the trajectories are the resonant interactions with the magnetic waves, which provides $\nu_{\perp} = \nu_{\parallel}$ ($\propto D_{\mu\mu}$). Under this assumption, one gets immediately:

$$D_{\perp} = \frac{D_{\parallel}}{1 + \left(\lambda_{\parallel}/R_L\right)^2} \,, \quad \lambda_{\parallel} = 3 D_{\parallel} / v \,, \tag{2.47}$$

which is a well-known result of quasi-linear theory. In general, $\lambda_{\parallel} \gg R_L$ and one gets $D_{\perp} D_{\parallel} = D_{bohm}^2$, where $D_{bohm} = R_L v/3$ is the Bohm diffusion coefficient, which, as we shall see in the next section, corresponds to the limit case where particles are efficiently isotropised in one gyration.

However, the above scaling for the transverse diffusion coefficient is in poor agreement with numerical simulations (e.g. Casse et al., 2001). Not only it greatly underestimates the perpendicular transport, but the law $D_{\perp} D_{\parallel} = D_{Bohm}^2$ is actually never retrieved, even when low turbulence levels, $\delta B \ll B_0$, are considered. In fact, simulations suggest the opposite scaling $D_{\perp} \propto D_{\parallel}$.

It was early realised that quasi-linear theory could not properly encompass perpendicular diffusion, for it neglects the wandering of the magnetic field lines. Indeed, the trajectories of the particles are driven by the total field $B_0 + \delta B$, and the fluctuations δB are only correlated on short scales. The total field lines are bent in such a way that any information on the geometry beyond the *correlation length* is lost. This implies in turn that the particles will "forget" their initial trajectories after one *correlation time*, which

is the time it takes for a particle to travel one correlation length. Many efforts have been done since the 60's to account for the wandering of the field lines. I shall restrict the discussion to a very simple argument which reproduces at least qualitatively the numerical results.

From the Lorentz force, we know that $v_\perp \sim \delta B/B v_\parallel$, where δB is the fluctuation in the direction perpendicular to the total field B. This implies that the mean displacement perpendicular to the local field line reads $\langle \delta x_\perp^2 \rangle \sim (\delta B/B)^2 \langle \delta s^2 \rangle$, where s is the curvilinear coordinate (following the mean field lines along the local "parallel" axis) and $x_\perp$ the coordinate perpendicular to the field lines. Due to pitch-angle scattering, the motion parallel to the local field lines is diffusive, and we get the relation between the perpendicular displacement and the parallel diffusion coefficient as: $\langle \delta x_\perp^2 \rangle \sim 2(\delta B/B)^2 D_\parallel t$. Note that the displacement now increases with $D_\parallel$. In the previous computation, the particles were deflected at each scattering and the perpendicular transport would be faster for a high scattering rate. In contrast, the perpendicular transport driven by field line wandering is faster if the particles can freely follow the bent field lines, i.e. when the scattering does not slow down their propagation.

We now speculate that the perpendicular velocity decorrelates when $\langle \delta x_\perp^2 \rangle^{1/2} \propto (B/\delta B) R_L$. This is motivated by the observation that in strong turbulence $B \sim \delta B$, the trajectories are expected to be randomised within one gyration, while the correlation length should increase for lower levels of turbulence. Of course, other scalings could have been chosen (see e.g. the heuristic arguments in Yan and Lazarian, 2008), and we restrict the discussion to this simple case for illustration. This scaling implies that the perpendicular correlation time t_c is determined by: $R_L^2 \propto (\delta B/B)^4 D_\parallel t_c$, and the decorrelation rate $\nu_\perp = t_c^{-1}$ follows as:

$$\nu_\perp \propto (\delta B/B)^4 D_\parallel / R_L^2 \,, \tag{2.48}$$

such that we obtain:

$$D_\perp \approx \left(\frac{\delta B}{B} \right)^4 D_\parallel \,, \tag{2.49}$$

where the numerical factor has been adjusted in order to recover $D_\perp = D_\parallel$ in the strong turbulence regime $\delta B \approx B \, (\ll B_0)$. This is in relatively good agreement with the numerical solution of e.g. Giacalone and Jokipii (1999) or Casse et al. (2001). In the latter it was found that the scaling $D_\perp = (\delta B/B)^{4.3} D_\parallel$ would provide a successful fit to the simulation, which was confirmed by more recent results (e.g. Xu and Yan, 2013), although state-of-the art simulations seem to tend towards $D_\perp \approx (\delta B/B)^{3.5} D_\parallel$ (Mertsch, 2020, and references therein).

The above argument is restricted to the case where the scattering of the particles is fast. As summarised in Chandran (2000), there exist in fact a variety of other regimes of perpendicular transport, depending on the scattering rate, the coherence length of the mean magnetic field, or the level of turbulence (e.g. Rechester and Rosenbluth, 1978; Kirk et al., 1996). For instance, if the decorrelation rate is higher than the scattering rate, the motion of the particles along the field lines is not diffusive anymore within a perpendicular correlation time, but rather ballistic ($\langle \delta s^2 \rangle^{1/2} \sim v_\parallel t$). In this case the perpendicular diffusion of the particles is purely driven by the random walk of the field lines and $D_\perp$ is independent of the momentum in the relativistic limit.

2.2.6 Calculation of the diffusion coefficients

Let us now consider a compressible cold plasma $c_s \ll v_A$. There exist two types of hydromagnetic waves which can efficiently scatter particles: Alfvén waves and fast magnetosonic waves. Alfvén waves are anisotropic waves: their dispersion relation $\omega_\alpha(\boldsymbol{k}) = \pm k_\parallel v_A$ shows that they propagate preferentially along the magnetic field. The ± 1 factor describes two counterpropagating waves. On the other hand, magnetosonic waves, with dispersion relation $\omega_\alpha(\boldsymbol{k}) = \pm k v_A$, are isotropic. However, their component perpendicular to the background field is strongly damped. Although it may well be the case that transverse compressible modes are actually the main scattering centres (Yan and Lazarian, 2002), we shall restrict our analysis to the perturbations propagating along the background field.

Under this assumption it can be shown that the Boltzmann equation 2.29 takes the form, in the limit $v_A \ll v$ (Berezinskii et al., 1990):

$$\partial_t f_0 + \boldsymbol{v}\cdot\nabla f_0 = \frac{\pi^2 Z^2 e^2}{p^2}\left(\frac{v_A}{c}\right)^2 \sum_\alpha \left(\partial_p\left(p^2 \frac{(1-\mu^2)W_\alpha\left(k_{res}\right)}{v|\mu|}\partial_p f_0\right) + \partial_\mu\left(\left(\frac{v}{v_A}\right)^2 \frac{(1-\mu^2)W_\alpha\left(k_{res}\right)}{v|\mu|}\right)\partial_\mu f_0\right) , \quad (2.50)$$

where:

$$k_{res} \approx \Omega_s/(|\mu|v) . \quad (2.51)$$

We identify the pitch-angle and momentum diffusion coefficients as:

$$D_{\mu\mu} = \frac{\pi^2 Z^2 e^2}{p^2 c^2} v \frac{(1-\mu^2)}{|\mu|} W\left(k_{res}\right) , \quad (2.52)$$

$$D_{pp} = \frac{\pi^2 Z^2 e^2}{v}\left(\frac{v_A}{c}\right)^2 \frac{(1-\mu^2)}{|\mu|} W\left(k_{res}\right) , \quad (2.53)$$

where W is the total energy spectrum of the hydromagnetic waves: $W = \sum_\alpha W_\alpha$. Note that we retrieve the relation $D_{pp} = (v_A/v)^2 p^2 D_{\mu\mu}$, which was expected from the Lorentz force ($\Delta p \sim p(v_A/v)\Delta\theta$).

Because of the $1/\mu$ dependency, the diffusion coefficients may diverge if the turbulence spectrum decreases too rapidly as function of the wave-number. This is a consequence of the so-called 90° scattering problem. It is an artefact of the quasi-linear theory: particles propagating in the plane perpendicular to the background field will never be deflected, unless the effect of the magnetic perturbations is taken into account in the computation of their trajectories. If the particles are not deflected, their mean-free path is infinite and so is the spatial diffusion coefficient.

Let us now compute the pitch-angle averaged diffusion coefficients using Equation 2.39 and changing variable from μ to k:

$$D_\parallel = \frac{B_0^2 v}{4\pi^2}\int_{\Omega_s/v}^{\infty} \frac{\mathrm{d}k}{k^3}\frac{\left(1-\left(\Omega_s/(kv)\right)^2\right)}{W\left(k\right)} , \quad (2.54)$$

$$\bar{D_{pp}} = \frac{\pi^2 Z^2 e^2}{v}\left(\frac{v_A}{c}\right)^2 \int_{\Omega_s/v}^{\infty} \frac{\mathrm{d}k}{k}\left(1-\left(\frac{\Omega_s}{kv}\right)^2\right) W\left(k\right) . \quad (2.55)$$

These integrals show that the particles can only interact with waves at scales $k > \Omega_s/v$. They also enlight two limitations of quasi-linear theory. First, at high energies such that

the Larmor radius is always larger than the largest turbulence scale, i.e. $\Omega_s/v < k_{min}$, the theory fails because particles cannot interact over their whole pitch-angle range. Second, at low energies such that the Larmor radius is always smaller than the smallest turbulence scale, i.e. $\Omega_s/v > k_{max}$, particles move along the background field lines without any possibility to interact resonantly with the turbulent waves. Both cases could only be treated under a relaxation of the resonance condition. The intermediate regime, in which quasi-linear theory is expected to be valid to describe particle interactions in weak turbulence, is called the resonant scattering regime. Note that in the astrophysical environments which will be considered in this work, the dissipation scale is roughly the mean free path of the thermal particles, that is about 10^9 cm, while the injection scale is typically 10-100 pc, which corresponds to the Larmor radius of 10-100 PeV particles in a magnetic field of 1 µG.

Let us now assume that the turbulence is generated by an external source injecting a power S at the injection scale, as described by Equation 2.14. The stationary solution is a power law energy spectrum normalised as:

$$W(k) = \frac{\eta B_0^2}{8\pi k_0}\left(\frac{k}{k_0}\right)^{-q}, \quad \eta \equiv \left(\frac{16\pi^2\sqrt{\rho}S}{a k_0 B_0^3}\right)^{q-1}, \tag{2.56}$$

where q is the spectral index of the turbulence. The diffusion coefficients eventually read:

$$\begin{aligned} D_{\parallel} &= \frac{4v k_0^{1-q}}{3\pi\eta\alpha(q)}\left(\frac{pc}{ZeB_0}\right)^{2-q}, \qquad \alpha = (8+q(q-6))/3\,, \\ \bar{D_{pp}} &= \frac{\pi\eta p^2 v_A^2}{12\beta(q)v}\left(\frac{pc}{ZeB_0}\right)^{q-2} k_0^{q-1}\,, \qquad \beta = q(q+2)/3\,, \\ D_{\parallel}\bar{D_{pp}} &= \frac{p^2 v_A^2}{9\alpha(q)\beta(q)}\,. \end{aligned} \tag{2.57}$$

One interesting case is that of a flat turbulence energy spectrum: $W(k) \propto k^{-1}$. In this case $D_{\mu\mu} \sim \Omega_s/3$, which means that the particles are isotropised within one gyration. It implies the well-known *Bohm diffusion* regime for the spatial diffusion coefficient: $D_{\parallel} \sim v^2/(3\Omega_s)$, which is expected in highly turbulent media where the isotropisation of the particles is very efficient. Indeed, if particles are isotropised within one gyration, their mean free path is the Larmor radius v/Ω_s and the interaction time is Ω_s^{-1}. Assuming that the diffusion is isotropic, this provides the diffusion coefficient as $D_{\parallel} \sim v^2/(3\Omega_s)$. Finally, we retrieve the well-known result of quasi-linear theory $D_{\parallel}\bar{D_{pp}} = p^2 v_A^2/9$. Such strong diffusion regime is expected in particular when the turbulence is excited by the particles themselves, e.g. around strong shocks (see Section 2.4.2).

Even though all our results have been obtained assuming that the wavenumbers of the perturbations are aligned with the background field, this hypothesis can be relaxed. General analytical expressions of the diffusion coefficients can be directly derived from the general Boltzmann equation (see e.g. Schlickeiser, 2002). It is however customary to assume that the magnetic fluctuations have some symmetries, which simplify the results. Such symmetries include the slab turbulence model, where it is assumed that the correlations between the magnetic perturbations only propagate along the direction parallel to the background magnetic field, or the isotropic model, where it is assumed that the correlations between the fluctuations are statistically isotropised[1].

[1]This does not mean that the magnetic field is isotropic or that there is no preferred direction for the propagation of the perturbations, but rather that the deformations of the fluctuating field propagate in all directions.

2.2.7 Beyond the quasi-linear approximation

The quasi-linear approximation provides a simple framework to describe the transport of particles in weak turbulence. Surprisingly, it has been found to provide reliable estimates of the parallel diffusion coefficient in a one-dimensional turbulence, even at the edge of its domain of validity, namely $\delta B \approx B_0$ (see Mertsch, 2020, for a recent review of the numerical investigations performed over the last 20 years). However, it has two major defects. First, we already identified the possibility of getting a diverging diffusion coefficient. This issue arises because particles moving exactly perpendicularly to the background field lines are not deflected in the direction of the parallel axis. In particular, QLT fails to describe the transport of particles in isotropic turbulence (Tautz et al., 2006a). Second, QLT systematically underestimates the perpendicular diffusion coefficient and fails to reproduce the numerical results, even qualitatively. This arises because the particles are assumed to follow the unperturbed one-dimensional field lines, disregarding the stochastic bending of the (turbulent) field lines.

In order to solve these issues, one must consider theories beyond the quasi-linear regime. Several extensions have been developed in the past 50 years (see Shalchi, 2009, for a review). When the hypothesis that particles propagate along the unperturbed field lines is relaxed, the parallel velocity becomes a stochastic variable even in between scattering events, for particles follow bent field lines. The projected position of a particle onto the direction of the unperturbed field (x) becomes a random variable, which can for instance be assumed to follow a Gaussian statistics:

$$f(x) = \frac{1}{\sqrt{2\pi}\sigma_z} e^{-\frac{(z-\langle z \rangle)^2}{2\sigma_z^2}} , \tag{2.58}$$

where $\langle z \rangle = v\mu t$ is the position that would be expected if the particle motion were driven by the unperturbed field, and $\sigma_z = \langle \Delta v_\parallel \rangle^{1/2} t$ is the deviation due to the uncertainty on the parallel velocity $\Delta v_\parallel$. This is the basis of the *guiding centre theory*.

The stochasticity of the parallel velocity in between scattering events is a general outcome of nonlinear theories of particle propagation in turbulence. Recalling that the quasi-linear resonance condition reads $k_{res} \approx \Omega / v_\parallel$, introducing an uncertainty on $v_\parallel$ would allow more wavenumbers to resonate with the particle. This is a general outcome of nonlinear theories: the resonance function (denoted $\mathcal{R}$) is not a delta-function anymore and the Boltzmann equation 2.29 takes the form:

$$\partial_t f_0 + \boldsymbol{v} \cdot \nabla f_0 = \pi Z^2 e^2 \sum_\alpha \int \mathrm{d}^3 \boldsymbol{k} \sum_s \mathcal{R} \left(\omega_\alpha (\boldsymbol{k}) - k_\parallel \mu v - s\Omega_s \right) I_{\alpha,s}(\boldsymbol{k}, \omega_\alpha) \mathcal{D}^2_{p,\mu}[f_0] \, . \tag{2.59}$$

For instance, the resonance function is a Gaussian in the guiding centre theory. Physically, one should recall that the resonant character of the wave-particle interactions had emerged from the fact that the wave must be in phase with the particle gyration in order for the Lorentz force to not cancel on average. If the particle trajectories are allowed to depart from the standard picture of the combination of a gyration and a translation along the background field, the resonance condition is relaxed and the resonant function broadens. This naturally solves the 90° scattering issue and provides more reliable predictions for the diffusion coefficients, in particular in two-dimensional and three-dimensional geometries (e.g. Tautz et al., 2006a; Tautz et al., 2006b; Yan and Lazarian, 2008)

2.3 Stochastic particle reacceleration

The diffusion in momentum space arising from the term $1/p^2 \partial_p p^2 D_{pp} f$ in the transport equation (2.40) gives rise to particle acceleration. This process is similar to the first model of acceleration suggested by Fermi (1949). In his seminal argument, the particles were assumed to scatter on randomly distributed cosmic magnetic fields, which are analogous to an ensemble of random magnetic waves. In both cases, the acceleration time scales as $(v_A/c)^2$, where v_A is the velocity of the scattering centres. It is therefore a second order process, sometimes referred to as the *second order Fermi mechanism* (*acceleration in turbulence* or *stochastic particle (re)acceleration* are equivalent designations). As early noted, this is a rather inefficient mechanism, for the velocity of the scattering centres is usually much smaller than the speed of light. Furthermore, the thermal particles having a mean free path of the order of the dissipation scale of the turbulence, they cannot resonate with inertial perturbations. It is found difficult to accelerate ("inject") a thermal distribution, hence the term *re*acceleration. Furthermore, the stochastic reacceleration of particles in turbulence cannot account in itself for the observed cosmic ray flux. However, it may still modulate a distribution of pre-accelerated particles.

Let us assume that there exists a putative accelerator injecting continuously a spectrum of non-thermal particles $Q(p)$ in a turbulent environment. The transport equation reads:

$$\partial_t f = \nabla \cdot (D \cdot \nabla f) + \frac{1}{p^2} \partial_p p^2 D_{pp} \partial_p f + Q(p)\,. \tag{2.60}$$

Averaging this equation over the volume of the environment, one gets:

$$\partial_t f = -\frac{f}{\tau_{esc}} + \frac{1}{p^2} \partial_p p^2 D_{pp} \partial_p f + Q(p)\,, \tag{2.61}$$

where τ_{esc} is the characteristic escape time from the region. Let us assume, as suggested by Equation 2.57, $D_{pp} = p^2/\tau_{acc}$, with $\tau_{acc} \propto p^{2-q}$, and $\tau_{esc} \propto p^{q-2}$. A simple solution to Equation 2.61 can be derived in the case where τ_{esc} is independent of energy. This corresponds to $q = 2$, i.e. τ_{acc} is also independent of energy. This steep turbulence spectrum is expected in presence of supersonic random motions, that is when the medium is characterised by an ensemble of shocks (Bykov and Toptygin, 1985; Bykov, 1988). One can show that in this case the stationary fundamental solution of Equation 2.61, obtained for a monochromatic injection $Q(p) = \delta(p - p_0)$), is a power law: $f(p) \propto (p/p_0)^{-\beta}/p_0$, where:

$$\beta = \frac{3}{2} + \frac{3}{2}\left(1 + \frac{4}{9}\frac{\tau_{acc}}{\tau_{esc}}\right)^{1/2}\,. \tag{2.62}$$

In the case where the stochastic acceleration is very efficient, $\tau_{acc} \ll \tau_{esc}$, one finds the asymptotic index $\beta \to 3$ that is, a hard cosmic ray spectrum. If on the contrary the escape dominates, the spectrum can be arbitrarily steep. A flat spectrum ($\beta = 4$) is obtained if $\tau_{acc} = 4\tau_{esc}$. If in addition one assumes that the putative accelerator injects a power law $Q(p) = p^{-\alpha}$, the stationary solution of Equation 2.61 is obtained as the convolution between the fundamental solution and the source:

$$f(p) \propto \int_{p_0}^{p} \frac{\mathrm{d}p'}{p'} \left(\frac{p}{p'}\right)^{-\beta} p'^{-\alpha} = \frac{p_0^{-\alpha}}{\beta - \alpha}\left(\left(\frac{p}{p_0}\right)^{-\alpha} - \left(\frac{p}{p_0}\right)^{-\beta}\right)\,, \tag{2.63}$$

where we assumed $\beta \neq \alpha$. If $\beta \ll \alpha$, then $f(p) \propto p^{-\beta}$: the stochastic reacceleration dominates, while if $\beta \gg \alpha$, $f(p) \propto p^{-\alpha}$: the reacceleration is not efficient.

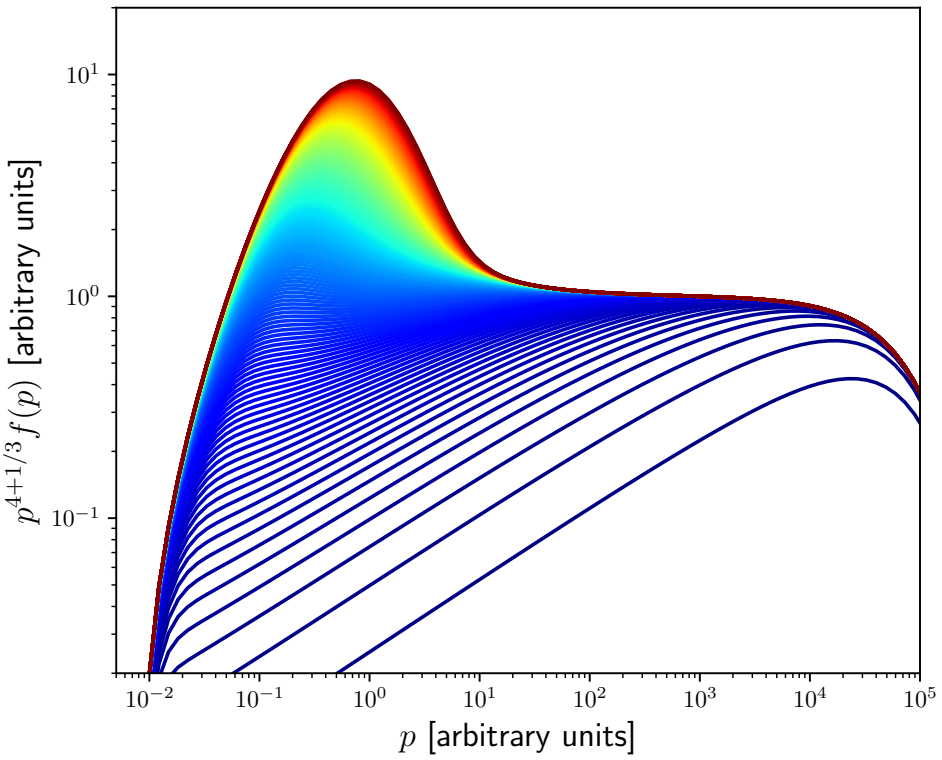

Figure 2.1: Typical evolution of the distribution function in a turbulent medium, for a stationary injection $Q(p) \propto p^{-4} \exp(-p/10^4)$. The colour scale runs from early times (blue) to late times (red).

Let us now assume that the spectral index of the turbulence is $q = 5/3$ (Kolmogorov turbulence). Figure 2.1 shows the time-dependent numerical solution of Equation 2.61, assuming a power law injection supplemented with an exponential cutoff $Q(p) \propto p^{-4} \exp(-p/10^4)$. We set $\tau_{acc}/\tau_{esc} = 10$ at $p = 1$. One observes how the injected distribution is progressively modulated as the time is increased. The distribution steepens at high energies because of the escape and it hardens at low energies because of the stochastic acceleration. The stationary solution displays a typical transition from a hard regime (which is not fitted by a power law), to a soft power law driven by the escape of the particles, $f = \tau_{esc} Q \propto p^{4+2-q}$. The "bumpy" shape can be understood in terms of the slope β, which should now be considered momentum-dependent. At low momenta, $\tau_{acc} \ll \tau_{esc}$ and the spectrum is hard. At high momenta, $\tau_{acc} \gg \tau_{esc}$ which implies $\beta \to \infty$; the fundamental solution of Equation 2.61 $p^{-\beta}$ nearly becomes a delta function such that the convolution 2.63 is dominated by the source term. Eventually, the bump is expected to flatten when $\beta = 4$.

2.4 The particle feedback on the waves

The previous sections have been dedicated to show how the waves change the dynamics of a distribution of charged particles. Two important processes have emerged. First, the waves deflect the particles, scatter them efficiently in such a way that any anisotropy is rapidly relaxed. Second, the waves impart a net acceleration on the distribution of particles. Up to now, it was implicitly assumed that these effects would not have any impact on the distribution of the waves, that is, the turbulence spectrum. In astrophysical plasmas, this

is generally not the case, for the energy contained in the non-thermal particles is often similar to the energy of the turbulence. By conservation of energy, if the waves accelerate the particles, as seen in the previous section, it means that the turbulence must *lose* energy. By conservation of momentum, if the waves isotropise an anisotropic distribution of particles, as seen in Section 2.2.3, it means that the turbulence must *gain* energy. The first process, scarcely considered, is a non-thermal damping of the waves. It will be later proved relevant in the turbulent interiors of superbubbles. The second process, which is of great importance e.g. for particle acceleration at shocks, is a *streaming instability* which excites hydromagnetic waves.

Let us derive the growth and damping rates of both processes from first principles. The following procedure is detailed in e.g. Melrose (1968), Melrose and Wentzel (1970), Wentzel (1974), and Skilling (1975). We start by considering again the transport equation of the distribution function before pitch-angle averaging, which is obtained from the Boltzmann equation under the assumption that the waves propagate along the background field lines at velocity v_A (Berezinskii et al., 1990):

$$\frac{\mathrm{d}f}{\mathrm{d}t} = \frac{1}{p^2}\left(\partial_p\left(p^2 D_{pp}\partial_p f + \frac{v}{v_A} p D_{pp}\partial_\mu f\right) + \frac{v}{v_A}\partial_\mu\left(pD_{pp}\partial_p f + \frac{v}{v_A}D_{pp}\partial_\mu f\right)\right) , \tag{2.64}$$

which reduces to Equation 2.33 when f is close to isotropy, for in this case the cross derivatives do not survive the pitch-angle averaging, as expected since p and μ would be decorrelated. However, we are now interested in the integrated variation of energy, not restricting to the isotropic part of the distribution function at late times.

The variation of the total energy carried by the particles reads:

$$\frac{\mathrm{d}E_c}{\mathrm{d}t} = 2\pi \int \mathrm{d}p p^2 \epsilon(p) \int_{-1}^{1} \mathrm{d}\mu \frac{\mathrm{d}f}{\mathrm{d}t} . \tag{2.65}$$

Since the momentum diffusion coefficient $D_{pp} \propto 1-\mu^2$, which comes from the fact that particles propagating along the field lines are not deflected by the waves, the second term $\partial_\mu(...)$ in Equation 2.64 vanishes when integrated on the pitch-angle. The remaining integral reads:

$$\frac{\mathrm{d}E_c}{\mathrm{d}t} = 4\pi \int \mathrm{d}p \epsilon(p) \int_{0}^{1} \mathrm{d}\mu \partial_p \left(p^2 D_{pp}\partial_p f + \frac{v^2}{v_A} p \frac{\mu^2-1}{2}\frac{D_{pp}}{D_{\mu\mu}}\partial_x f\right) , \tag{2.66}$$

where we have used the diffusion approximation to express $\partial_\mu f$ as function of $\partial_x f$ at the lowest order in the anisotropy, according to Equation 2.36. We now integrate by parts and use $D_{pp} = (v_A/v)^2 p^2 D_{\mu\mu}$ (Equation 2.52) to perform the pitch-angle integration of the second term:

$$\frac{\mathrm{d}E_c}{\mathrm{d}t} = 2\pi \int \mathrm{d}p \partial_p (v p^2 \bar{D_{pp}}) f + v_A \frac{4\pi}{3} \int \mathrm{d}p p^3 v \partial_x f . \tag{2.67}$$

The quantity $\partial_p(vp^2\bar{D_{pp}})$ is the mean energy transferred per unit time from the waves to the particles via the stochastic acceleration in momentum space (see also Thornbury and Drury, 2014). In the second term, we recognise the total pressure of the particles. Using Equation 2.54, we write the momentum diffusion coefficient in integral form, and we eventually change variable in the second term from p to $k = ZeB_0/pc$ to get:

$$\frac{\mathrm{d}E_c}{\mathrm{d}t} = \int \frac{\mathrm{d}k}{k} W(k) \left(4\pi^3 Z^2 e^2 \left(\frac{v_A}{c}\right)^2 \int_{\frac{ZeB_0}{kc}} \mathrm{d}p\, pf + \frac{4\pi}{3}\frac{v_A}{W(k)}\left[p^4 v \partial_x f\right]_{p=\frac{ZeB_0}{kc}}\right) . \tag{2.68}$$

Since the energy must be balanced between the waves and the particles, the variation of energy carried by the particles must appear in the dynamical equation of the turbulence (2.14), which for simplicity we write here assuming a Kolmogorov phenomenology ($C \approx 0.8$):

$$\partial_t W + \partial_k \left(\frac{C k^{5/2} W^{3/2}}{\sqrt{\rho}} \right) = -\Gamma W + 2\sigma W + S\delta(k - k_0)\,, \tag{2.69}$$

with the damping rates identified as:

$$\Gamma(k) = \frac{8\pi^3 Z^2 e^2}{k} \left(\frac{v_A}{c} \right)^2 \int_{\frac{ZeB_0}{kc}} \mathrm{d}p\, p f\,, \tag{2.70}$$

$$\sigma(k) = -\frac{4\pi}{3k} \frac{v_A}{W(k)} \left[p^4 v \frac{\boldsymbol{B_0}}{B_0} \cdot \nabla f \right]_{p=\frac{ZeB_0}{kc}}\,. \tag{2.71}$$

The damping rate Γ is identical to that written in e.g. Eilek (1979), Miller and Roberts (1995), Miller et al. (1996), and Brunetti et al. (2004). It differs from the expression appearing in the works of e.g. Ptuskin et al. (2006) by a factor 2π due to the choice of normalisation of Equation 2.69. The growth rate σ is identical to that written in e.g. Schwartz and Skilling (1978), up to a factor 2 which is due to the fact that we have defined W as the total differential turbulent energy, including the hydrodynamic energy (and assuming equipartition).

Finally, the total energy variation of the turbulence reads:

$$\partial_t E_{turb} = -\int \mathrm{d}k \Gamma(k) W(k) - 2 v_A \frac{\boldsymbol{B_0}}{B_0} \cdot \nabla p_c\,, \tag{2.72}$$

where we identified the pressure of the particles $p_c = (4\pi/3) \int \mathrm{d}p p^3 v f$.

The streaming instability corresponds to the transfer of momentum between an anisotropic distribution of particles and the distribution of hydromagnetic waves. The presence of a gradient of charged particles induces a current, which induces magnetic perturbations if it propagates in the direction of the mean magnetic field.

2.4.1 Non-thermal wave damping

Since the damping term Γ scales as $(v_A/c)^2$, it is customary to neglect it. However, this may violate the energy balance if the particles carry an energy of the order of that of the turbulence. Ptuskin and collaborators (Ptuskin et al., 2003; Ptuskin et al., 2005; Ptuskin et al., 2006; Ptuskin et al., 2017) revived the interest for this feedback. In particular, they showed that it may have a significant impact on the transport of low energy particles in the interstellar medium.

In order to investigate the influence of the damping term, let us compute the stationary solution of Equation 2.69 in the absence of streaming instability ($\sigma = 0$):

$$W(k) = k^{-5/3} \left(\frac{\sqrt{\rho} S}{C} \right)^{2/3} \left(1 - \frac{2\pi^2}{5} \left(\frac{ZeB_0}{\rho^2 C^2 S} \right)^{1/3} \int_{ZeB_0/k} \mathrm{d}p' f(p') p'^{8/3} \right)^2\,. \tag{2.73}$$

The feedback of the particles on the turbulence is non trivial. Not only it reduces the density of the magnetic waves, but it may even terminate the turbulence cascade at

large scales. Indeed, it may happen that for high enough cosmic ray energy densities the quantity in the parenthesis in Equation 2.73 vanishes below a given scale, possibly larger than the dissipation scale. Low energy particles will then not be able to resonate with the magnetised waves anymore, and their momentum diffusion coefficient will vanish, while the quasi-linear spatial diffusion coefficient will diverge. This was already pointed out by e.g. Ptuskin et al. (2006) in the context of cosmic ray diffusion in the interstellar medium.

Noticing that at $k \to \infty$ the integral in the right-hand side of Equation 2.73 is nearly the energy density of the cosmic rays, the waves will be suppressed at scales $k > k_*$ if the energy density of the particles satisfies the following approximate condition:

$$e_{CR} \gtrsim 3c \left(\frac{\rho^2 S}{k_*} \right)^{1/3} . \tag{2.74}$$

For standard astrophysical plasmas, the smallest turbulence scale is of the order of the Larmor radius of the thermal particles, which is about 10^9 cm. Assuming that the ambient density is $\rho = m_p$ cm^{-3} and the source of the turbulence is $S = 10^{40}$erg s^{-1}/(400 kpc^3), which corresponds to one percent of the power injected by supernova remnants in the galaxy, the smallest turbulent scales will begin to be suppressed if the energy of the particles exceeds $1-10$ eV/cm^3. Indeed, Ptuskin et al. (2006) concluded that the feedback of the particles on the turbulence spectrum of the interstellar medium should be important below GeV energies.

2.4.2 Streaming instability

The streaming instability arises if for some reason a sustained inhomogeneity appears in the distribution function. In this case, the pressure gradient of charged particles induces a current, which amplifies the Alfvén waves propagating in the same direction. This is expected in a number of situations, in particular in presence of super-Alvénic large-scale motions in the fluid which would advect the particles. For instance, this is thought to be the case in the upstream region of a strong shock. If the advection time dominates over the diffusion time, the waves are not able to isotropise the particles.

In presence of large-scale super-Alfvénic motions, one writes the dynamical equation of the waves excited by the streaming instability as:

$$\partial_t W + \boldsymbol{u} \cdot \nabla W = -\frac{8\pi}{3k} v_A \left[p^4 v \frac{\boldsymbol{B_0}}{B_0} \cdot \nabla f \right]_{p=ZeB_0/kc} , \tag{2.75}$$

where the second term of the left-hand side describes the advection of the waves by a flow of velocity $\boldsymbol{u}$. Let us simplify the problem by considering a one-dimensional homogeneous stationary flow. We further assume that the distribution function is a power law: $f = p^{-\beta} f_0(x)$, and we restrict ourselves to the relativistic regime $v \approx c$. The solution to Equation 2.75 reads:

$$\partial_x W = \frac{8\pi}{3k} \frac{v_A}{u} c \, (ZeB_0/kc)^{4-\beta} \, \partial_x f_0 \, . \tag{2.76}$$

The turbulence spectrum therefore scales as $W(k) \propto k^{\beta-5}$. As we shall see in the next chapter, the acceleration of particles around strong shocks produces both a gradient upstream of the shock and a power law spectrum with index $\beta = 4$. In this case, waves are efficiently excited along a flat power spectrum $W(k) \propto 1/k$, which corresponds to the Bohm scaling discussed in Section 2.2.6.

Considering the variation of the total energy of the turbulence, and assuming that the distribution of particles vanishes far away from the region of interest, we further get (Bell, 1978; Amato and Blasi, 2006):

$$\left(\frac{\delta B}{B_0}\right)^2 = 1 + \frac{2u}{v_A}\frac{p_c}{\rho u^2} = 1 + 2\frac{u}{v_A}\xi_c\,, \tag{2.77}$$

where $\xi_c = p_c/(\rho u^2)$ is the acceleration efficiency in the large-scale flow. Assuming for instance $\xi_c = 0.1$ and $u/v_A = 10^3$, we get $\delta B \approx 14 B_0$. The streaming instability generally amplifies the waves so efficiently that the quasi-linear theory breaks down. The nonlinear amplification of the magnetic field and its saturation are beyond the reach of simple analytic computations. Finally, it is worth stressing out that in the framework of quasi-linear theory, we did not account for the modification of the dispersion relation of the Alfvén waves due to cosmic ray streaming. Indeed, for a complete treatment the pressure gradient should be introduced at the level of the fluid equations. The modification of the dispersion relation of the hydromagnetic waves in particular unlocks *non-resonant interactions*, which further excite waves and amplify magnetic fields (Bell (2004), see also Bykov et al. (2013) for a review).

The streaming instability is a crucial ingredient of particle acceleration at shocks, for it confines the particles near the shock and increases the shock crossing rate. Enhanced confinement near sources is another important process to describe the propagation of cosmic rays in the galaxy. This has been recently investigated by e.g. Nava et al. (2016) and Brahimi et al. (2020).

2.5 Summary

I have described the transport of particles in weakly turbulent environments within the framework of quasi-linear theory, which assumes that particles gyrate around the unperturbed magnetic field lines. The distribution function of the particles is disturbed by repeated interactions with stochastic hydromagnetic perturbations, which first rapidly isotropise the distribution, second give rise to a spatial diffusion, and third slowly reaccelerate the particles. Useful formulae were obtained in the simple case of the one-dimensional ("slab") Alfvénic turbulence and the perpendicular transport has been discussed using heuristic arguments beyond the quasi-linear theory, for the latter fails to provide a reliable description of the transverse diffusion. The dynamics of the turbulence has further been investigated, in particular considering the backreaction of the particles which both excite and damp the waves, depending on the energy carried by the particle and the spatial inhomogeneity of their distribution. The discussion was admittedly restricted, for the subject of particle transport in turbulence is a broad topic with applications from plasma physics to astrophysics. More comprehensive discussions, e.g. on more complicated turbulence symmetries, damping processes, nonlinearities, applications to specific environments etc. can be found in the books by Berezinskii et al. (1990), Longair (1994), Kirk et al. (1994), Schlickeiser (2002), and Shalchi (2009).

References

Amato, E. and Blasi, P. (Sept. 2006). "Non-linear particle acceleration at non-relativistic shock waves in the presence of self-generated turbulence". In: MNRAS 371.3, pp. 1251–1258. DOI: 10.1111/j.1365-2966.2006.10739.x.

Bell, A. R. (Jan. 1978). "The acceleration of cosmic rays in shock fronts - I." In: MNRAS 182, pp. 147–156. DOI: 10.1093/mnras/182.2.147.

Bell, A. R. (Sept. 2004). "Turbulent amplification of magnetic field and diffusive shock acceleration of cosmic rays". In: MNRAS 353.2, pp. 550–558. DOI: 10.1111/j.1365-2966.2004.08097.x.

Berezinskii, V. S. et al. (1990). *Astrophysics of cosmic rays*.

Bieber, J. W. and Matthaeus, W. H. (Aug. 1997). "Perpendicular Diffusion and Drift at Intermediate Cosmic-Ray Energies". In: ApJ 485.2, pp. 655–659. DOI: 10.1086/304464.

Brahimi, L., Marcowith, A., and Ptuskin, V. S. (2020). "Nonlinear diffusion of cosmic rays escaping from supernova remnants: Cold partially neutral atomic and molecular phases". In: A&A 633, A72. DOI: 10.1051/0004-6361/201936166.

Brunetti, G. et al. (June 2004). "Alfvénic reacceleration of relativistic particles in galaxy clusters: MHD waves, leptons and hadrons". In: MNRAS 350.4, pp. 1174–1194. ISSN: 0035-8711. DOI: 10.1111/j.1365-2966.2004.07727.x.

Bykov, A. M. (Feb. 1988). "A Model for the Generation of Interstellar Turbulence". In: *Soviet Astronomy Letters* 14, p. 60.

Bykov, A. M., Gladilin, P. E., and Osipov, S. M. (Mar. 2013). "Non-linear model of particle acceleration at colliding shock flows". In: MNRAS 429.3, pp. 2755–2762. DOI: 10.1093/mnras/sts553.

Bykov, A. M. and Toptygin, I. N. (Mar. 1985). "Shock Generation of Turbulence and Cosmic-Ray Diffusion in the Interstellar Medium". In: *Soviet Astronomy Letters* 11, pp. 75–77.

Casse, F., Lemoine, M., and Pelletier, G. (Nov. 2001). "Transport of cosmic rays in chaotic magnetic fields". In: Phys. Rev. D 65.2. ISSN: 1089-4918. DOI: 10.1103/physrevd.65.023002.

Chandran, B. D. G. (Jan. 2000). "Confinement and Isotropization of Galactic Cosmic Rays by Molecular-Cloud Magnetic Mirrors When Turbulent Scattering Is Weak". In: *The Astrophysical Journal* 529.1, pp. 513–535. DOI: 10.1086/308232.

Chandran, B. D. (2004). "A Review of the Theory of Incompressible MHD Turbulence". In: Ap&SS 292.1-4, pp. 17–28. ISSN: 0004-640X. DOI: 10.1023/b:astr.0000044997.79246.d7.

Eilek, J. A. (June 1979). "Particle reacceleration in radio galaxies." In: ApJ 230, pp. 373–385. DOI: 10.1086/157093.

Fermi, E. (Apr. 1949). "On the Origin of the Cosmic Radiation". In: *Physical Review* 75.8, pp. 1169–1174. DOI: 10.1103/PhysRev.75.1169.

Galtier, S. et al. (June 2000). "A weak turbulence theory for incompressible magnetohydrodynamics". In: *Journal of Plasma Physics* 63.5, pp. 447–488. DOI: 10.1017/S0022377899008284.

Giacalone, J. and Jokipii, J. R. (July 1999). "The Transport of Cosmic Rays across a Turbulent Magnetic Field". In: ApJ 520.1, pp. 204–214. DOI: 10.1086/307452.

Goldreich, P. and Sridhar, S. (Jan. 1995). "Toward a Theory of Interstellar Turbulence. II. Strong Alfvenic Turbulence". In: ApJ 438, p. 763. DOI: 10.1086/175121.

Iroshnikov, P. S. (Feb. 1964). "Turbulence of a Conducting Fluid in a Strong Magnetic Field". In: Soviet Ast. 7, p. 566.

Kirk, J. G., Duffy, P., and Gallant, Y. A. (Oct. 1996). "Stochastic particle acceleration at shocks in the presence of braided magnetic fields." In: A&A 314, pp. 1010–1016.

Plasma Astrophysics (Jan. 1994).

Kolmogorov, A. and Tikhomirov, V. (1991). *Selected Works I: Mathematics and Mechanics*. Vol. 25. Mathematics and its Applications. Springer Netherlands. ISBN: 9789401130301.

Kraichnan, R. H. and Montgomery, D. (May 1980). "Review article: Two-dimensional turbulence". In: *Reports on Progress in Physics* 43.5, pp. 547–619. DOI: 10.1088/0034-4885/43/5/001.

Kraichnan, R. H. (1965). "Inertial-Range Spectrum of Hydromagnetic Turbulence". In: *The Physics of Fluids* 8.7, pp. 1385–1387. DOI: 10.1063/1.1761412.

Longair, M. S. (1994). *High Energy Astrophysics*. 2nd ed. Vol. 2. Cambridge University Press. DOI: 10.1017/CBO9781139170505.

Marsch, E. and Tu, C. .-.-Y. (Aug. 1990). "Spectral and spatial evolution of compressible turbulence in the inner solar wind". In: J. Geophys. Res. 95.A8, pp. 11945–11956. DOI: 10.1029/JA095iA08p11945.

Melrose, D. B. (Oct. 1968). "The Emission and Absorption of Waves by Charged Particles in Magnetized Plasmas". In: Ap&SS 2.2, pp. 171–235. DOI: 10.1007/BF00651567.

Melrose, D. B. and Wentzel, D. G. (Aug. 1970). "Interaction Between Cosmic-Ray Electrons and Cosmic-Ray Protons". In: ApJ 161, p. 457. DOI: 10.1086/150552.

Mertsch, P. (Aug. 2020). "Test particle simulations of cosmic rays". In: Ap&SS 365.8, 135, p. 135. DOI: 10.1007/s10509-020-03832-3.

Miller, J. A., Larosa, T. N., and Moore, R. L. (Apr. 1996). "Stochastic Electron Acceleration by Cascading Fast Mode Waves in Impulsive Solar Flares". In: ApJ 461, p. 445. DOI: 10.1086/177072.

Miller, J. A. and Roberts, D. A. (Oct. 1995). "Stochastic Proton Acceleration by Cascading Alfven Waves in Impulsive Solar Flares". In: ApJ 452, p. 912. DOI: 10.1086/176359.

Nava, L. et al. (Oct. 2016). "Non-linear diffusion of cosmic rays escaping from supernova remnants - I. The effect of neutrals". In: MNRAS 461.4, pp. 3552–3562. DOI: 10.1093/mnras/stw1592.

Norman, C. A. and Ferrara, A. (Aug. 1996). "The Turbulent Interstellar Medium: Generalizing to a Scale-dependent Phase Continuum". In: ApJ 467, p. 280. ISSN: 1538-4357. DOI: 10.1086/177603.

Ptuskin, V. S., Zirakashvili, V. N., and Seo, E. C. (Apr. 2017). "Diffusion of cosmic rays in a model with interstellar turbulence damping due to interaction with energetic particles". In: *Bulletin of the Russian Academy of Sciences: Physics* 81.4, pp. 437–438. ISSN: 1934-9432. DOI: 10.3103/S1062873817040359.

Ptuskin, V. S. et al. (July 2003). "Dissipation of Hydromagnetic Waves on Energetic Particles: Impact on Interstellar Turbulence and Cosmic Ray Transport". In: *International Cosmic Ray Conference*. Vol. 4. International Cosmic Ray Conference, p. 1929.

Ptuskin, V. et al. (2005). "Propagation model for cosmic ray species in the Galaxy". In: *Advances in Space Research* 35.1. Mars International Reference Atmosphere, Living With a Star and Fundamental Physics, pp. 162–166. ISSN: 0273-1177. DOI: https://doi.org/10.1016/j.asr.2003.08.051.

Ptuskin, V. S. et al. (May 2006). "Dissipation of Magnetohydrodynamic Waves on Energetic Particles: Impact on Interstellar Turbulence and Cosmic-Ray Transport". In: ApJ 642.2, pp. 902–916. DOI: 10.1086/501117.

Rechester, A. B. and Rosenbluth, M. N. (Jan. 1978). "Electron heat transport in a tokamak with destroyed magnetic surfaces". In: Phys. Rev. Lett. 40.1, pp. 38–41. DOI: 10.1103/PhysRevLett.40.38.

Schlickeiser, R. (2002). *Cosmic Ray Astrophysics*.

Schwartz, S. J. and Skilling, J. (Nov. 1978). "The Escape of Cosmic Rays from Supernova Remnants". In: A&A 70, p. 607.

Shalchi, A. (2009). *Nonlinear Cosmic Ray Diffusion Theories*. Vol. 362. DOI: 10.1007/978-3-642-00309-7.

Skilling, J. (Nov. 1975). "Cosmic Ray Streaming - III. Self-consistent solutions". In: MNRAS 173.2, pp. 255–269. ISSN: 0035-8711. DOI: 10.1093/mnras/173.2.255.

Tautz, R. C., Shalchi, A., and Schlickeiser, R. (May 2006a). "Comparison between test-particle simulations and test-particle theories for cosmic ray transport: I. Magnetostatic turbulence". In: *Journal of Physics G: Nuclear and Particle Physics* 32.6, pp. 809–833. DOI: 10.1088/0954-3899/32/6/006.

Tautz, R. C., Shalchi, A., and Schlickeiser, R. (June 2006b). "Comparison between test-particle simulations and test-particle theories for cosmic ray transport: II. Plasma wave turbulence". In: *Journal of Physics G: Nuclear and Particle Physics* 32.7, pp. 1045–1059. DOI: 10.1088/0954-3899/32/7/013.

Thornbury, A. and Drury, L. O. (June 2014). "Power requirements for cosmic ray propagation models involving re-acceleration and a comment on second-order Fermi acceleration theory". In: MNRAS 442.4, pp. 3010–3012. ISSN: 0035-8711. DOI: 10.1093/mnras/stu1080.

Verma, M. K. et al. (1996). "A numerical study of the nonlinear cascade of energy in magnetohydrodynamic turbulence". In: *Journal of Geophysical Research: Space Physics* 101.A10, pp. 21619–21625. DOI: https://doi.org/10.1029/96JA01773.

Wentzel, D. G. (1974). "Cosmic-Ray Propagation in the Galaxy: Collective Effects". In: *Annual Review of* A&A 12.1, pp. 71–96. DOI: 10.1146/annurev.aa.12.090174.000443.

Xu, S. and Yan, H. (Dec. 2013). "Cosmic-Ray Parallel and Perpendicular Transport in Turbulent Magnetic Fields". In: ApJ 779.2, 140, p. 140. DOI: 10.1088/0004-637X/779/2/140.

Yan, H. and Lazarian, A. (Dec. 2002). "Scattering of Cosmic Rays by Magnetohydrodynamic Interstellar Turbulence". In: Phys. Rev. Lett. 89.28. ISSN: 1079-7114. DOI: 10.1103/physrevlett.89.281102.

Yan, H. and Lazarian, A. (Feb. 2008). "Cosmic-Ray Propagation: Nonlinear Diffusion Parallel and Perpendicular to Mean Magnetic Field". In: ApJ 673.2, pp. 942–953. DOI: 10.1086/524771.

Zhou, Y. and Matthaeus, W. H. (1990). "Models of inertial range spectra of interplanetary magnetohydrodynamic turbulence". In: J. Geophys. Res. 95.A9, pp. 14881–14892. DOI: https://doi.org/10.1029/JA095iA09p14881.

Chapter 3

Particle acceleration at shock fronts

While the previous chapter was dedicated to the description of the transport of charged particles in a turbulent plasma at rest, we shall now consider the effect of large-scale plasma motions, and in particular the acceleration of the particles in hydrodynamic shocks. This is currently thought to be the primary mechanism of cosmic ray production.

3.1 Interstellar shocks

It has been mentioned in Section 2.1.1 that in the absence of magnetic fields, perturbations propagate in a fluid as sound waves with velocity $c_s = \sqrt{\mathrm{d}P/\mathrm{d}\rho}$, where P and ρ are respectively the pressure and the density of the fluid. For an adiabatic gas, the sound speed can be equivalently written as function of the temperature T: $c_s = \sqrt{\gamma kT/(0.6 m_p)}$, where $\gamma \approx 5/3$ is the adiabatic index ($P \propto \rho^\gamma$) and k is the Boltzmann constant. This provides the useful estimate $c_s \approx 100\sqrt{T/10^6\mathrm{K}}$ km/s (all the estimates given in the following are obtained assuming a typical superbubble environment, with a density $n = 0.01$ cm^{-3} and $T = 10^6$ K, according to Equations 1.11).

For an adiabatic gas one computes $c_s \propto \rho^{1/3}$, meaning that fluid perturbations evolve in a nonlinear way. Indeed, a density perturbation modifies the local sound speed in such a way that the maximum of the oscillation propagates faster than the minimum, leading to a steepening of the wave. If the initial perturbation is strong enough, it may eventually collapse onto a vertical front, inducing a sharp transition in the flow which is called a shock. This happens when an object moves at a supersonic velocity in the fluid, for in this case the perturbations have by definition no time to propagate and collapse immediately onto a shock front. The fluctuations accumulate behind the front, raising the density. In the stationary regime, there is therefore a density gap between the "upstream" region, where the density is low and the motion supersonic, and the "downstream" region, where the density is high and the motion subsonic. By mass (resp. energy) conservation, this implies that there is a similar gap in the velocity (resp. pressure) profiles. By solving the stationary fluid equations, one shows that the fluid is homogeneous everywhere except at the location of the shock front. The transition itself cannot be described by the fluid equations, for its width is of the order of the mean free path of the thermal particles from which the plasma is made. Assuming a magnetic field of 1 µG, the particle mean free path, driven by the electromagnetic interactions, is of the order of 10^{10} cm, which is much smaller than the extent of the astrophysical systems we consider. The transition is therefore mathematically treated as a discontinuity and by abuse of language, it will be sometimes referred to as the "shock discontinuity" or "shock jump".

The conservation equations integrated around the discontinuity provide the *compression ratio* (or *compression factor*) of the shock jump, $r \equiv \rho_2/\rho_0 = u_0/u_2$ as function of the upstream (supersonic) velocity u_0, where the index "0" (resp. "2") refers to upstream (resp. downstream) variables. Providing one defines the *Mach number* $\mathcal{M} \equiv u_0/c_{s,0}$, with $c_{s,0}$ the sound speed far away upstream of the shock, one gets, in the case of a one-dimensional[1] non radiative [2] and non relativistic[3] shock:

$$r = \frac{(\gamma+1)\mathcal{M}^2}{(\gamma-1)\mathcal{M}^2+2}\,, \tag{3.1}$$

$$\frac{P_2}{P_0} = \frac{2\gamma\mathcal{M}^2+1-\gamma}{1+\gamma}\,. \tag{3.2}$$

An interesting case is the strong shock limit $\mathcal{M} \gg 1$. Assuming $\gamma = 5/3$, one gets $r \to 4$ and $P_2 \sim 3/4\rho u_0^2$. The upstream flow has a negligible thermodynamic pressure (i.e. it is cold). In the downstream region on the other hand, the dissipation of the particles convert $3/4$ of the ram pressure into thermal pressure, that is, heat. The thermal energy downstream of a strong shock is in fact in equipartition with the kinetic energy. In other words, the work done by the supersonic object on the upstream fluid is converted equivalently into thermal and kinetic energy downstream. *In fine*, a non-radiative shock is a very efficient entropy factory.

Astrophysical plasmas being magnetised, one should in fact solve the equations of the magnetohydrodynamics in order to derive the jump conditions. For a one-dimensional "parallel shock", i.e. when the magnetic field is aligned with the direction of the outflow, the compression factor and pressure jump are identical to the hydrodynamic case, for the strength of the magnetic field is not modified when the fluid is compressed in the direction of the field. On the other hand in a "perpendicular shock", i.e. when the magnetic field is parallel to the plane of the shock, the magnetic field is compressed in the downstream region ($B_2 = rB_0$ by the flux freezing theorem) and the jump condition becomes slightly more complicated. In the following, we will only consider parallel shocks as these are believed to be the most efficient accelerators of particles (e.g. Caprioli and Spitkovsky, 2014a).

The astrophysical shocks which will be of interest for this work are the stellar wind termination shocks and the supernova blast waves. These have been briefly described in Chapter 1. Wind termination shocks are created by the supersonic outflows of the stars, be they isolated or embedded inside clusters. As seen in Section 1.2.1, the Mach number of a collective wind termination shock surrounding a stellar cluster depends on the size of the region of energy deposition, such that these shocks can be either weak or strong. On the other hand, supernova shocks are time-dependent. As they expand,

[1] If the radius of a spherical shock is large compared to the diffusion length of the non-thermal particles diffusing around the discontinuity, the curvature is expected to have a negligible impact on the acceleration of the particles. On the other hand, particles with Larmor radius of the order of the shock radius do feel the curvature, which will be shown to have important consequences regarding the maximum energy reached in supernova remnant and wind termination shocks.

[2] Old supernova remnants expanding in the interstellar medium are radiative shocks of importance for the field of High Energy Astrophysics, however it was shown in Section 1.2.2 that supernovae do not become radiative inside superbubbles. Furthermore, the acceleration is expected to be much more efficient in the non radiative phases.

[3] Relativistic shocks are crucial in some aspects of High Energy Astrophysics, in particular for the study of pulsars – which may be embedded inside superbubbles. However this work will be restricted to wind termination shocks and supernova blast waves, which are assumed to be the main hadronic accelerators.

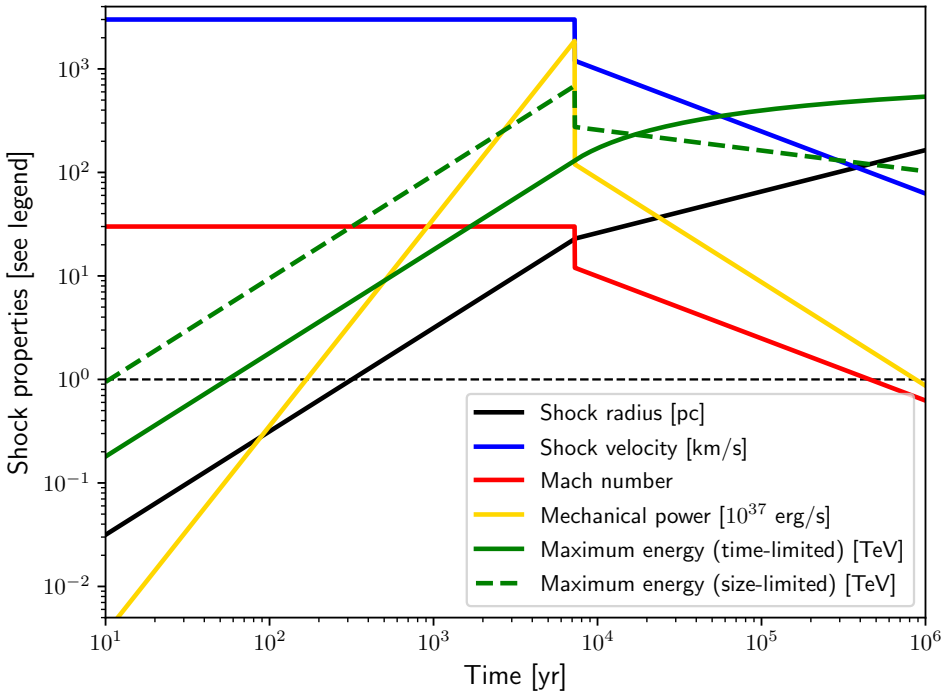

Figure 3.1: Time evolution of the shock radius R, velocity V and mechanical power $2\pi R^2 \rho V^3$, as well as the maximum energy attainable by the particles (see Section 3.5) estimated in a simple model of supernova evolution, assuming an explosion energy of 10^{51} erg and an initial ejecta velocity of 3000 km/s, while the ambient number density is 10^{-2} cm^{-3}.

they sweep-up the ambient matter which accumulates in the downstream region and slows down the blast wave. The main phases of the evolution, described in Section 1.1.4, are summarised in Figure 3.1. Although it is a simplified model (e.g. the velocity is assumed to be constant in the free expansion phase, which is not the case in reality (Chevalier, 1982)), it provides reliable estimates. The adiabatic phase starts after about 7 kyr (for a low density of 0.01 cm^{-3}) and the shock remains strong ($\mathcal{M} > 10$) up to an age of 10 kyr (corresponding to a radius of 25 pc), while the blast wave becomes subsonic at about 400 kyr (corresponding to a radius of 120 pc), at which time the shock disperses.

3.2 Thermal leakage injection

Having described the basic properties of shocks embedded inside superbubbles, we now consider the transport of particles around these inhomogeneities. The present section discusses the *thermal leakage injection recipe*, which is a phenomenological description of the microphysics driving the injection of thermal particles in the shock acceleration mechanism. This recipe was originally introduced to describe nonlinear shocks, that is, taking into account the pressure of the accelerated particles onto the flow profile. Although it is not customary to discuss this phenomenology in an introduction to shock acceleration, I believe it is useful to get an intuition on how particles are injected in the accelerator before considering the acceleration process in itself. One should however keep in mind that it is a simplistic model.

Let us consider a shock propagating in the interior of a superbubble at a constant velocity V (or equivalently by change of reference frame, a stationary shock sustained

by an upstream supersonic outflow). The surrounding medium consists in a magnetised turbulent plasma made of low energy particles. It is usually assumed that these particles are in thermal equilibrium, i.e. distributed according to the Maxwell-Boltzmann distribution. As the shock sweeps up the medium, low energy "thermal" particles cross the front from the upstream region to the downstream region. Most of these particles are then advected downstream and leave the shocked region. However, in the turbulent downstream medium, the particles also diffuse (as discussed in the previous section, part of the upstream bulk motion is converted into a downstream random motion). In consequence, particles with high enough energy have a non zero probability to cross the shock back from the downstream region to the upstream region. This may happen only if the mean free path of the particles in the turbulent plasma is larger than the thickness of the shock. As discussed in the previous section, the astrophysical shocks which we consider are collisionless, such that the shock thickness is typically of the order of the Larmor radius of the thermal particles. It is worth recalling at this point that the Maxwell-Boltzmann distribution reads, in momentum:

$$f_{th}(p) = n\pi^{-3/2}p_{th}^{-3}e^{-(p/p_{th})^2}\,, \quad p_{th} = \sqrt{2m_pkT}\,, \tag{3.3}$$

where n is the density of thermal particles, m_p the proton mass, k the Boltzmann constant and T the temperature of the medium. If we assume that the thermal distribution is isotropic, p_{th} is the most probable momentum carried by the thermal particles. It is therefore natural to estimate the thickness of the shock as about $p_{th}/(qB)$. Particles will be able to cross the shock from the downstream to the upstream if their Larmor radius is somewhat larger than the shock thickness, i.e. $p \gtrsim \xi p_{th}$, where $\xi = \mathcal{O}(1)$. In other words, while the bulk of thermal particles determines the shock thickness, particles in the tail beyond the injection momentum are able to cross the discontinuity and return into the upstream region after having been swept-up. This is the starting step of the acceleration process, which is called the *thermal leakage recipe* (Blasi et al., 2005) as particles with high enough energy "leak" from the downstream thermal distribution to the upstream, being "injected" into the accelerator in the sense that they will be able to experience several cycles around the shock before being definitively advected downstream. As we shall see below, particles are slightly accelerated each time they cross the shock. By this mechanism, thermal particles are injected into a non-thermal distribution.

Since the Maxwell-Boltzmann distribution is exponentially suppressed beyond the thermal momentum p_{th}, we consider that all freshly injected particles (i.e. particles which return upstream of the shock for the first time) have an *injection momentum* $p_0 \equiv \xi p_{th}$, which amounts to neglect the high energy tail of the thermal distribution. Let us assume that the shock has accelerated a non-thermal distribution of particles with an efficiency η, meaning that a density ηn_2 of thermal particles has been accelerated, where n_2 is the number density downstream of the shock. Let us further assume that the distribution of accelerated particles follows a power law of spectral index $s > 3$. This implies $\eta n = 4\pi/(s-3)p_0^3 f(p_0)$. Eventually we impose the continuity between the thermal and non-thermal distributions at the injection momentum in order to get the following expression for the injection fraction:

$$\eta = \frac{4}{(s-3)\sqrt{\pi}}\xi^3 e^{-\xi^2}\,. \tag{3.4}$$

The function 3.4 is plotted in Figure 3.2 for $s = 4$. In order to have an efficiency $\eta \approx 10^{-3} - 10\%$, ξ must be around 2.5 - 4 (i.e. $p_0 \approx 10 - 50$ MeV/c for a shock velocity

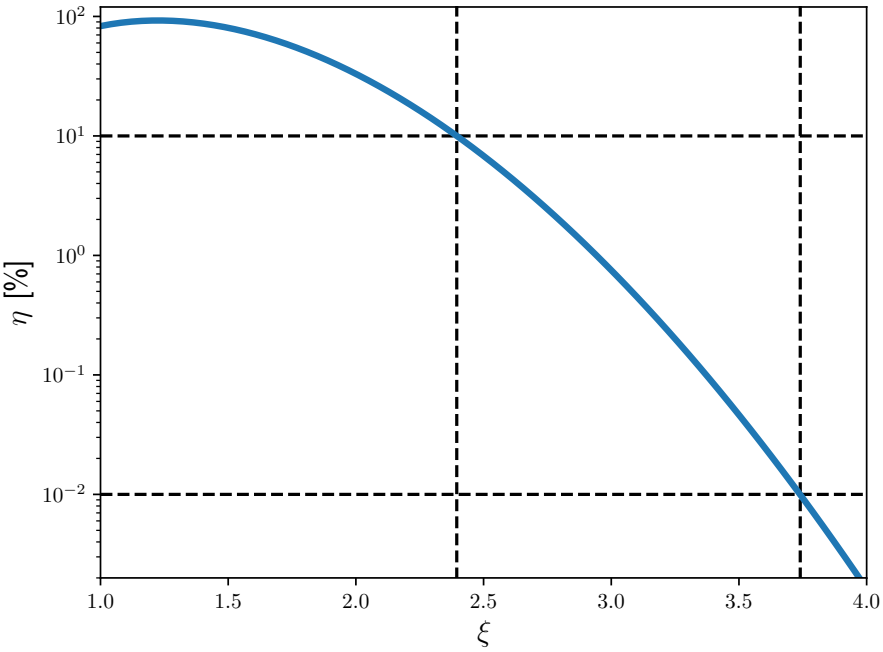

Figure 3.2: Injection efficiency as function of the injection parameter according to the thermal leakage phenomenology.

of a few thousand km/s). This is consistent with the interpretation of the injection mechanism, which requires $\xi \sim \mathcal{O}(1)$.

Finally, one can derive the flux of particles injected at a shock, denoted Q, which corresponds to the number of particles injected in the accelerator per unit volume per unit momentum per unit time. This quantity should be such that the flux of thermal particles is injected into the non-thermal distribution at an efficiency η, i.e. $\int \mathrm{d}^3p\, Q \equiv \eta n_0 u_0$. According to the previous discussion, the particles are injected at a specific momentum p_0, and at the location of the shock ($x = 0$) since they become non-thermal as soon as they cross the shock from the downstream back to the upstream. These constraints provide, for a strong shock:

$$Q(x,p) = \eta \frac{n_0 u_0}{4\pi p_0^2} \delta(x)\delta(p-p_0)\,. \tag{3.5}$$

Although the thermal leakage injection recipe provides a satisfactory intuition, it is admittedly based on rather dubious assumptions. In particular, one may object that the "thermal" particles will not arrange themselves alongside a Maxwell-Boltzmann distribution near the shock, for their diffusion is balanced by the advection. Nevertheless, this approach is broadly consistent with results coming from sophisticated numerical simulations of shocks (Caprioli and Spitkovsky, 2014a).

3.3 Energy gain

It was realised in the end of the 70's that shock waves could accelerate particles efficiently (Axford et al., 1977; Krymskii, 1977; Bell, 1978a; Blandford and Ostriker, 1978). The main assumption at the basis of the so-called *diffusive shock acceleration* mechanism is that the turbulence efficiently isotropises the particles both in the upstream and downstream regions, by repeated scatterings on the turbulent hydromagnetic waves (see

Section 2.2.3). Since the velocity of the plasma flow is different in each region, the isotropisation is realised with respect to two different frames. Particles crossing the shock discontinuity therefore experience a Lorentz boost from one frame to another. The plasma being magnetised, this change of frame induces the interaction with an electric field and the particles are slightly accelerated. Eventually, because they are efficiently isotropised, they have a chance to diffuse back into the shock from the downstream region to the upstream region. In this way, they may experience a large number of cycles and gain a lot of energy before being advected far away in the downstream flow.

Let us consider a particle of initial kinetic energy E_1. The energy gained after one crossing from upstream to downstream, and then from downstream back to upstream, is computed according to special relativity as:

$$\begin{aligned} E_2' &= \Gamma_s E_1 (1 - \beta \cos\theta_1) \,, \\ E_1' &= \Gamma_s E_2 (1 + \beta \cos\theta_2) \,, \end{aligned} \tag{3.6}$$

where $\beta = (u_1 - u_2)/c$, $\Gamma_s = (1-\beta^2)^{-1/2}$, E_1' and E_2' are respectively the energy of the particle after it has crossed the shock from upstream to downstream and downstream to upstream, E_2 is the energy of the particle after it has crossed the shock the first time from upstream to downstream, and θ_1, θ_2 are the incidence angles of the particle when it crosses the shock. During one upstream-downstream-upstream cycle, a particle of initial energy E therefore gains the following energy:

$$\Delta E(\theta_1, \theta_2) = (\cos\theta_2 - \cos\theta_1)\, \beta E \,, \tag{3.7}$$

where the second order terms in β have been neglected as the shock is assumed to be non-relativistic. The average energy gain is the average of ΔE weighted by the probability that a particle crosses the shock with an angle $\theta_{1,2}$. The latter is proportional to $\cos\theta_{1,2}$, the projection of the particle velocity along the shock normal, if $\pi/2 < \theta_1 < \pi$ (for a particle crossing from upstream to downstream) and $0 < \theta_2 < \pi/2$ (for a particle crossing from downstream to upstream). Assuming that the particle distribution is isotropised, the average energy gain per cycle eventually reads:

$$\Delta E = \frac{\beta E}{A} \int_0^{\pi/2} \mathrm{d}\theta_2 \int_{\pi/2}^{\pi} \mathrm{d}\theta_1 \, (\cos\theta_2 - \cos\theta_1) \cos\theta_1 \sin\theta_1 \cos\theta_2 \sin\theta_2 \,, \tag{3.8}$$

with A a normalisation factor given by:

$$A = \left| \int_0^{\pi/2} \mathrm{d}\theta_2 \int_{\pi/2}^{\pi} \mathrm{d}\theta_1 \cos\theta_1 \sin\theta_1 \cos\theta_2 \sin\theta_2 \right| . \tag{3.9}$$

This provides $\Delta E = 4\beta E/3$. The gain in energy is systematic and proportional to E, in contrast with the stochastic acceleration mechanism discussed in Section 2.3, which was a second-order diffusive process. In consequence, this process of diffusive shock acceleration is often referred to as the *first order Fermi mechanism*.

3.4 Particle spectrum

At each cycle, particles have a non zero probability to be advected downstream and never cross the shock back. To reach high energies, particles need to experience many cycles

before escaping. Even though it is possible to accelerate particles up to high energies, it is expected that there will be less and less particles in higher and higher energy bands. The computation of the energy spectrum is done on a statistical basis. Assuming again that the distribution of the particles is isotropic upstream and that the particles have a velocity close to the speed of light, the flux of particles crossing the shock from upstream to downstream is $n_{cr}c/2\int_{\pi/2}^{\pi}\mathrm{d}\theta_2\cos\theta_2\sin\theta_2 = n_0c/4$, where n_{cr} is the density of non-thermal particles. On the other hand, the flux of particles advected downtream is $n_{cr}u_2$. The escape probability per cycle is simply the ratio of both fluxes:

$$P_{esc} = 4u_2/c\,. \tag{3.10}$$

The number of particles which will do more than N cycles before escaping is then:

$$n(\geq N) = n_{cr}\left(1-P_{esc}\right)^N\,, \tag{3.11}$$

while the energy gained after N cycles reads, according to the previous discussion:

$$E(N) = (1+4\beta/3)^N E_0\,, \tag{3.12}$$

which allows to switch variable from N to E:

$$n(\geq E) = n_0\left(E/E_0\right)^{\frac{\ln(1-P_{esc})}{\ln(1+4\beta/3)}} \approx n_0\left(E/E_0\right)^{\frac{3}{1-r}}\,, \tag{3.13}$$

where the last relation holds in the limit of a non relativistic shock. The differential energy spectrum follows by differentiation:

$$n(E) \propto \left(E/E_0\right)^{\frac{2+r}{1-r}}\,. \tag{3.14}$$

The diffusive shock acceleration mechanism therefore accelerates particles with a power law spectrum. The spectral index depends on the strength of the shock. For strong shocks, $r=4$ and $n(E)\propto E^{-2}$ is a universal solution. It should be stressed again that this simple mechanism provides a rather satisfactory explanation of both the universality of the energy spectrum of cosmic rays observed near Earth and its slope, once the propagation effects from the source to the Earth have been taken into account.

3.5 Maximum energy

The above derivation gives no clue about the maximum energy achievable by the particles. Although the number density of the particles was found to be smaller and smaller in spectral bands of higher and higher energy, there was no limitation on the number of cycles that a particle could experience. In reality, such limitations do exist.

A first limitation is related to the size of the system. Indeed, a shock wave is not an infinite plane and particles with upstream diffusion length larger than the radius of the shock will escape the accelerator as the shock will never be able to catch them back. Assuming Bohm's scaling for the diffusion coefficient, which is expected to arise due to the streaming instability downstream (see Section 2.4.2), the diffusion length upstream of the shock reads $L_D = r_L c/(3u_0)$, which provides the following estimate of the maximum energy:

$$E_{max,size} = 0.3\ \mathrm{PeV}\,\frac{u_0}{3000\ \mathrm{km/s}}\,\frac{ZB}{1\ \mu\mathrm{G}}\,\frac{R_s}{10\ \mathrm{pc}}\,. \tag{3.15}$$

This is basically the Hillas criterion (Equation 0.1) corrected by a factor $u_0/c \sim 0.01$.

Another limitation is related to the finite lifetime of the accelerator. This is for instance the case when one considers supernova blast waves (Lagage and Cesarsky, 1983). On average, particles travel one diffusion length downstream and upstream of the shock during one cycle. Thus, assuming again Bohm's diffusion regime, it takes a time $\Delta t \approx r_L(1+r)/(3u_0)$ to perform one cycle around a shock of compression ratio r. The acceleration rate of relativistic particles is therefore $\mathrm{d}E/\mathrm{d}t \approx \Delta E/\Delta t = 4qBu_0^2(r-1)/((1+r)r)$, and the maximum energy which can be reached within a time t in a strong shock ($r = 4$) follows by integration:

$$\begin{aligned} E_{max,time,t<t_{ST}} &= 0.2 \text{ PeV} \frac{ZB}{1 \text{ µG}} \left(\frac{u_0}{3000 \text{ km/s}}\right)^2 \frac{t}{10 \text{ kyr}}, \\ E_{max,time,t>t_{ST}} &= 0.2 \text{ PeV} \frac{ZB}{1 \text{ µG}} \left(\frac{u_0}{3000 \text{ km/s}}\right)^2 \frac{t_{st}}{10 \text{ kyr}} \left(6 - 5\left(\frac{t_{ST}}{t}\right)^{1/5}\right), \end{aligned} \tag{3.16}$$

where for simplicity we assumed a constant velocity $u_0 = V_e$ in the free expansion phase and a power law deceleration $u_0 = V_e(t/t_{ST})^{-3/5}$ in the adiabatic phase. t_{ST}, whose expression was given in Equation 1.17, is the time at which the evolution transitions from an ejecta-dominated expansion to an adiabatic expansion.

A supernova shock being time-dependent, so is the maximum energy achievable by the particles. The latter is plotted in green in Figure 3.1 for a magnetic field of 1 µG. The size limitation is the less stringent criterion in the free expansion phase, while it becomes the main limitation after about 20 kyr (again, in a low density medium). However at this age the mechanical power of the supernova, shown in yellow in Figure 3.1, becomes much smaller than its peak value at the end of the free expansion phase. Thus the maximum energy is overall mostly driven by the finite age of the system, and the acceleration is most efficient at the end of the free expansion phase, during a few thousand years. The maximum energy is typically of the order of 10-100 TeV, and PeV bands can only be reached if the magnetic field is strongly amplified. Because of the streaming instability, it is however very possible that magnetic fields as high as several hundred µG could rise around the shock, as suggested by X-ray and γ-ray observations (e.g. Völk et al., 2005; Parizot et al., 2006; Caprioli, 2011), even though the amplification could be less efficient in low-density environments such as in the interior of superbubbles (e.g. Vink, 2012). The amplification of the magnetic field due to the streaming instability also strongly impacts the time evolution of the maximum energy (Marcowith et al., 2018; Gaggero et al., 2018). Depending on the properties of the ambient medium, other limitations may come from particle losses (Marcowith et al., 2018).

3.6 Diffusive shock acceleration from first principles

3.6.1 Transport equation in the presence of large-scale motions

Although the physical argument described in Sections 3.3 and 3.4 provides a simple derivation of the power law spectrum of particles accelerated in shocks, it is not suitable to model finite geometries, include time-dependent effects, nonlinearities, account for particle reacceleration etc. To do so, one should carefully analyse the dynamics of the particles distribution function using again the transport equation. In Section 2.2.4, the transport

equation was obtained after averaging over the magnetic fluctuations as:

$$\partial_t f + \frac{1}{2}\int_{-1}^{1} \mathrm{d}\mu\, \boldsymbol{v}\cdot\nabla f = \nabla\cdot(D\cdot\nabla f) + \frac{1}{p^2}\partial_p D_{pp}\partial_p f\,, \tag{3.17}$$

where the second term in the left-hand side would vanish in the absence of large-scale motions. Let us now consider the more general case where there do exist large-scale motions in the plasma characterised by a velocity $\boldsymbol{u}(\boldsymbol{x})$. The left-hand side of Equation 3.17 expresses the variation of the distribution function along the particle trajectories measured in the frame of the observer, i.e. $f = f(\boldsymbol{x}_o, \boldsymbol{p}_o)$ where $\boldsymbol{x}_o$ and $\boldsymbol{p}_o$ are measured with respect to the observer. On the other hand, the collision terms in the right-hand side have been previously obtained using the diffusion approximation, which is only valid in the rest frame of the scattering centres where the repeated scatterings are expected to efficiently isotropise the particles. One should therefore write $f = f(\boldsymbol{x}_s, \boldsymbol{p}_s)$ in the right-hand side, where $\boldsymbol{x}_s$ and $\boldsymbol{p}_s$ are measured with respect to the scattering centres advected by the plasma. Equation 3.17, although valid in a plasma at rest, therefore becomes inconsistent in the presence of large-scale motions.

An astute way to solve this inconsistency is to redefine $f \equiv f(\boldsymbol{x}_o, \boldsymbol{p}_s)$ as the distribution function of particles with position $\boldsymbol{x}_o$ measured in the frame of the observer and momentum $\boldsymbol{p}_s$ measured in the rest frame of the scattering centres. The spatial diffusion term in Equation 3.17 comes exclusively from the pitch-angle diffusion $\partial_\mu D_{\mu\mu}\partial_\mu$, which is an operator in momentum space, hence does not depend on the frame relative to which the position $\boldsymbol{x}$ is measured. The same remark holds trivially for the momentum diffusion operator. Thus, the right-hand side of Equation 3.17 is invariant under the transformation $\boldsymbol{x}_s \to \boldsymbol{x}_o$.

The only term which is modified is the second term in the left-hand side. Let us assume that the scattering centres move at a velocity $\boldsymbol{u}(\boldsymbol{x}_o)$ with respect to the observer. We can perform the change of variable in momentum from the frame of the observed to the frame of the scattering centres to get (the computation is detailed in e.g. Kirk et al., 1994):

$$\frac{1}{2}\int_{-1}^{1} \mathrm{d}\mu\, \boldsymbol{v}\cdot\nabla f = \boldsymbol{u}\cdot\nabla f(\boldsymbol{x}_0, p_s) - \frac{p_s}{3}\left(\nabla\cdot\boldsymbol{u}\right)\partial_{p_s} f(\boldsymbol{x}_0, p_s)\,, \tag{3.18}$$

where we have once again used that f is nearly isotropic in the frame of the scattering centres. Dropping the indices referring to the frames and the explicit dependencies, the transport equation is finally obtained as (Parker, 1965; Drury, 1983):

$$\partial_t f + \boldsymbol{u}\cdot\nabla f - \frac{p}{3}\left(\nabla\cdot\boldsymbol{u}\right)\partial_p f = \nabla\cdot(D\cdot\nabla f) + \frac{1}{p^2}\partial_p D_{pp}\partial_p f\,, \tag{3.19}$$

where f is the isotropic and gyrotropic part of the averaged distribution function in the mixed phase space $\{\boldsymbol{x}_o, \boldsymbol{p}_s\}$. The second term in the left-hand side accounts for the advection of the particles with the plasma motion. The third term in the left-hand side accounts for the compression of the distribution at plasma inhomogeneities. In principle, the velocity $\boldsymbol{u}$ is the velocity of the scattering centres, although it is customary to assume that it is equal to the velocity of the background plasma, for hydromagnetic waves are expected to be advected with the large-scale flow. Let us finally recall that the first term in the right-hand side of Equation 3.19 accounts for the effective spatial diffusion due to the scattering of the pitch-angles on magnetic fluctuations, while the second term in the right-hand side accounts for the stochastic reacceleration.

3.6.2 Infinite plane parallel stationary shock

For simplicity, let us consider a one-dimensional parallel shock with $\boldsymbol{u} \parallel \boldsymbol{B} \parallel \boldsymbol{e_x}$, and let us disregard the stochastic acceleration. The transport equation 3.19 becomes:

$$\partial_t f + u\partial_x f - \frac{p}{3}\partial_x u \partial_p f = \partial_x D_{\parallel}\partial_x f + Q_1 \delta(x)\delta(p-p_0)\,, \quad Q_1 \equiv \eta \frac{n_0 u_0}{4\pi p_0^2}\,, \tag{3.20}$$

where we further added the injection term discussed in Section 3.2 (Equation 3.5). In the stationary regime, integrating once either in the downstream region $x > 0$ or in the upstream region $x < 0$ provides $uf = D_{\parallel}\partial_x f + constant$, which implies $\partial_x f|_{x>0} = 0$ in order for the distribution to not diverge as $x \to \infty$, while in the upstream region we get $f = f_\infty + (f_1 - f_\infty)e^{ux/D_{\parallel}}$, where f_1 is the distribution function at the shock and f_∞ is the boundary condition far upstream of the shock. Finally the integration around the shock provides:

$$f_1 - f_\infty + \frac{p}{s}\partial_p f_1 = \frac{Q_1}{u_0}\delta(p-p_0)\,, \quad s \equiv 3r/(r-1)\,, \tag{3.21}$$

which can be integrated first around p_0 to get $f_1(p_0) = \eta s n_0/(4\pi p_0^3)$ and then from p_0 to p to obtain:

$$f_1(p) = s\left(\frac{p}{p_0}\right)^{-s}\left(\frac{\eta n_0}{4\pi p_0^3} + \int_{p_0}^{p}\frac{\mathrm{d}p'}{p'}\left(\frac{p'}{p_0}\right)^{s} f_\infty(p')\right)\,. \tag{3.22}$$

The first term is the standard power law solution which was phenomenologically derived in Section 3.4. The distribution function in energy is related to the one in momentum by $f(E)\mathrm{d}E = 4\pi p^2 f(p)\mathrm{d}p$, therefore $f(p) \propto p^{-s}$ implies $f(E) \propto p^{2-s}/v$. In the relativistic regime we retrieve the spectral index derived in Equation 3.14 as $2 - s = (2+r)/(1-r)$.

The integral term in Equation 3.22 appears as a convolution between the power law solution $f_G(p,p') \equiv s(p/p')^{-s}/(u_0 p')$ and a source function $S(p') \equiv u_0 f_\infty(p')$. This could have been equivalently derived using the Green function formalism, for $f_G(p,p')$ is precisely the kernel of Equation 3.20. This is a useful formalism to keep in mind, because it allows one to find the *reacceleration* of a pre-existing distribution of particles. For instance, galactic cosmic rays which diffuse after having escaped from their first sources may encounter other interstellar shocks and be reaccelerated (Bell, 1978b; White, 1985; Cristofari and Blasi, 2019; Bresci et al., 2019).

Let us assume that the pre-existing particles are distributed along a power law spectrum: $f_\infty(p) = \mathcal{A}(p/p_0)^{-\beta}$. The reaccelerated spectrum can be computed analytically as:

$$\begin{aligned} f_1(p) &= s\left(\frac{p}{p_0}\right)^{-s}\left(\frac{\eta n_0}{4\pi p_0^3} + \frac{\mathcal{A}}{s-\beta}\left(\left(\frac{p}{p_0}\right)^{s-\beta} - 1\right)\right)\,, \quad s \neq \beta\,, \\ f_1(p) &= s\left(\frac{p}{p_0}\right)^{-s}\left(\frac{\eta n_0}{4\pi p_0^3} + \mathcal{A}\ln(p/p_0)\right)\,, \quad s = \beta\,. \end{aligned} \tag{3.23}$$

If the spectrum of pre-existing particles (also called "seeds") is steeper than the spectrum of freshly accelerated particles ($\beta \gg s$), then the standard power law solution is retrieved, for in this case most of the pre-existing particles carry small momenta. On the other hand, if $\beta \ll s$, the high energy seeds dominate over the ones which have been reaccelerated from low energy bands, and the final distribution function is a combination between the spectrum of the freshly accelerated particles (of spectral slope s) and the seed spectrum (of spectral slope β). In the special case where the slope of the seeds is equal to the

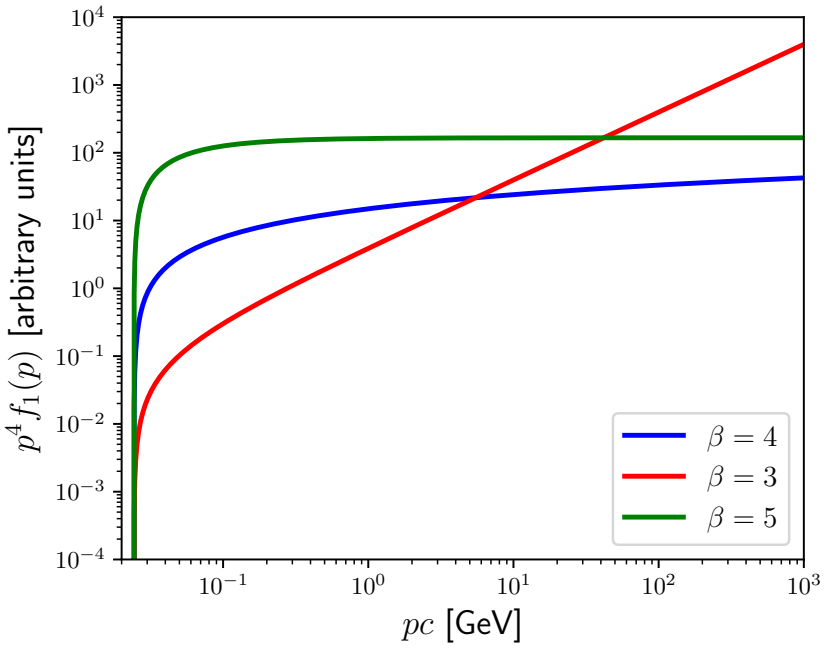

Figure 3.3: Reacceleration of a flat ($\beta = 4$), hard ($\beta = 3$) and steep ($\beta = 5$) distribution of seeds. The acceleration efficiency is small enough for the normalisation of the seeds to dominate over that of the freshly injected particles.

slope of the freshly injected particles, the seeds only impart a logarithmic modulation. For illustration, Figure 3.3 shows the spectrum resulting from the reacceleration of a flat ($\beta = 4$), hard ($\beta = 3$) and steep ($\beta = 5$) distribution of seeds.

3.6.3 Generalisations

Although the above results are restricted to the case of an infinite plane parallel non-relativistic shock in the steady-state regime, these assumptions can be relaxed. Indeed, the transport equation 3.19 being very general, it allows to consider a number of physical refinements. Instead of considering a one-dimensional shock, one could for instance write the transport equation in spherical symmetry. This would allow to compute the acceleration of cosmic rays in the collective wind termination shock driven by a stellar cluster, as recently studied by Morlino et al. (2021). It is shown that the geometry effects modulate the standard power law solution by an exponential cut-off, which implies that a maximum energy naturally arises, with a scaling qualitatively similar to Equation 3.15. Time-dependent effects can also be accounted for (e.g. Prishchep and Ptuskin, 1981). In particular it is possible to compute the acceleration time, which is the time it takes for a particle to be accelerated up to a given energy, by performing the Laplace transform of the time-dependent transport equation. One obtains (Drury, 1983):

$$t_{acc}(p) = \frac{3}{u_0 - u_2} \int_{p_0}^{p} \frac{\mathrm{d}p'}{p'} \left(\frac{D_0(p')}{u_0} + \frac{D_2(p')}{u_2} \right) . \tag{3.24}$$

Assuming Bohm's diffusion regime $D(p) = vr_L/3$, one gets, in the relativistic limit, $t_{acc}(p) \approx \frac{(r+1)r}{(r-1)u_0^2} \frac{pc}{qB}$, such that the maximum energy achievable in a strong shock of age t is $E = 3qBu_0^2 t/20$, which reproduces exactly Equation 3.16 in the case of a time-independent flow velocity.

The transport equation formalism also allows to consider various magnetic field geometries, for instance oblique and perpendicular shocks (e.g. Jokipii, 1987) even though simulations suggest that the acceleration efficiency is much lower than in the case of a parallel magnetic field (Caprioli and Spitkovsky, 2014a).

Eventually, the transport equation is suitable for simple numerical resolutions (e.g. Drury, 1991; Kang and Ryu, 2011), which are much faster than heavy particle-in-cell or hybrid simulations, although the latter are crucial to probe the validity of the assumptions, for instance regarding the mechanism of injection, the diffusion coefficient (Caprioli and Spitkovsky, 2014c), nonlinear effects such as the amplification of the magnetic field (Caprioli and Spitkovsky, 2014b) or the feedback of the particles on the flow (Caprioli et al., 2020).

3.7 Nonlinear diffusive shock acceleration

The energy density carried by the freshly accelerated particles can be obtained by integrating Equation 3.22:

$$e_{cr} = \frac{\eta n_0 s p_0^s}{p_0^3} \int \mathrm{d}p\, p^{2-s} \epsilon(p) \approx 4\eta n_0 p_0 c \ln\left(\frac{p_{max}}{m_p c}\right) \approx 100 \eta \rho_0 u_0 c\,, \tag{3.25}$$

where we assumed $s = 4$ and we discarded the non-relativistic energy bands for simplicity. The last equality has been obtained using $p_0 = \xi p_{th}$, $\gamma P_0 \mathcal{M}^2 = \rho_0 u_0^2$, $P = \rho k T$, as well as Equation 3.1, and assuming $p_{max} \sim 1$ PeV. One concludes that the shock will transfer *all* its kinetic energy to the particles whenever $\eta > 0.01 u_0/c \approx 10^{-4}$. This is of course non physical: the back-reaction of the particles onto the fluid must be taken into account. Indeed, the pressure of the particles should be introduced in the hydrodynamic equations, which is expected to modify the flow profile, which in turn modifies the particle spectrum. The problem becomes nonlinear and the solution can sometimes greatly differ from that obtained in the so-called *test-particle* approximation, where it is assumed that the particles do not affect the fluid.

3.7.1 Wave and fluid equations

Not only the pressure of the particles is expected to modify the flow profile, but it also excites hydromagnetic waves by means of the streaming instability which has been evoked in Section 2.4.2. Allowing for possible inhomogeneities in the flow ($u = u(x)$), it can indeed be shown that the magnetic pressure $p_B = \rho v_A^2/2$ obeys (Caprioli et al., 2009):

$$2(u(x) - v_A(x)) \frac{\mathrm{d}p_B}{\mathrm{d}x} = v_A(x) \frac{\mathrm{d}p_{cr}}{\mathrm{d}x} - 3 p_B(x) \frac{\mathrm{d}(u - v_A)}{\mathrm{d}x}\,, \tag{3.26}$$

which is basically the integral version of Equation 2.76, where the discrepancy between the rest frame of the fluid and that of the scattering centres has been taken into account, and where the last term cannot be discarded if the flow is inhomogeneous. As discussed in Section 2.4.2, the excitation of the Alfvén waves is due to the gradient of the cosmic ray pressure, $p_{cr}(x) = 4\pi/3 \int \mathrm{d}p p^3 v f(x,p)$.

The solution of Equation 3.26 reads, at the second order in v_A/u (Caprioli, 2012):

$$p_B(x) = \frac{2}{25} \frac{\left(1 - U(x)^{5/4}\right)^2}{U(x)^{3/2}} \rho_0 u_0^2\,, \tag{3.27}$$

where $U \equiv u/u_0$. Formally, this equation has been derived for a shock characterized by very large Mach and Alfvénic numbers, $\mathcal{M}^2 \gg 1$ and $\mathcal{M}_A^2 \gg 1$ (where $\mathcal{M}_A = u/v_A$).

Let us now consider the hydrodynamic equations. The fluid dynamics of the shock transition is governed by the mass and momentum conservation laws:

$$\rho_0 u_0 = \rho(x) u(x)\,, \tag{3.28}$$

$$\rho_0 u_0^2 + p_{g,0} + p_{cr,0} = \rho(x) u(x)^2 + p_g(x) + p_{cr}(x) + p_B(x)\,, \tag{3.29}$$

where p_g is the pressure of the gas and the index "0" refers to quantities evaluated far upstream. It is convenient to divide the momentum equation by $\rho_0 u_0^2$ and introduce normalised pressures ($P_g = p_g/\rho_0 u_0^2$, etc.) to obtain:

$$1 + P_{g,0} + P_{cr,0} = U(x) + P_g(x) + P_{cr}(x) + P_B(x)\,. \tag{3.30}$$

Assuming an adiabatic equation of state for the gas in the upstream region with adiabatic index γ we can further write:

$$P_g(x) = \frac{U^{-\gamma}(x)}{\gamma M_0^2}\,. \tag{3.31}$$

Because the distribution of particles is expected to depend on x, at least in the upstream region for, in the absence of seeds, it must vanish at upstream infinity, the velocity and pressure of the flow are expected to be inhomogeneous.

3.7.2 Kinetic equation

In an inhomogeneous flow, the compression ratio of the shock must be redefined more precisely. We define the total compression factor $R_{tot} = u_0/u_2$ and the compression factor at the *subshock* (the discontinuity itself) $R_{sub} = u_1/u_2$, where the indices $i = 0,\ 1,\ 2$ refer to quantities at upstream infinity, immediately upstream of the shock, and immediately downstream of the (sub)shock, respectively.

The transport equation 3.20 was obtained under the assumption that the rest frame of the scattering centres and that of the flow coincide. This is not a valid approximation anymore when Alfvén waves are excited by the pressure gradient of cosmic rays. This implies that upstream of the shock the fluid velocity u that appears in Equation 3.20 should be substituted by the velocity of the scattering centres, $u - v_A$. On the other hand, at equilibrium, the particle distribution function downstream of the shock is expected to be spatially uniform. There is no pressure gradient and therefore streaming instability does not operate there. Moreover, if the magnetic turbulence is isotropised after the passage through the shock, the effective Alfvén speed vanishes and scattering centres move away from the shock at the fluid speed u_2.

In the presence of strong field amplification the substitution $u \to u - v_A$ upstream of the shock may impact significantly onto the spectrum of accelerated particles, as first noticed in Zirakashvili and Ptuskin (2008) and Caprioli (2012)[4].

The solution of the modified transport equation can be found as before by integrating it first between $x = 0^-$ and $x = 0^+$ and then between $x = -\infty$ and $x = 0^-$. With the

[4]In fact, a non vanishing values of the Alfvén speed might also be present downstream, due to the *inertia* of waves excited upstream and compressed by the shock (Caprioli et al., 2020). Such an effect, not considered here, would further increase the impact that the drift of scattering centres has on the spectrum of cosmic rays accelerated at the shock.

boundary condition $f_\infty = 0$, i.e. assuming that there are no seeds upstream of the shock[5], the following differential equation is obtained:

$$\frac{p}{3}(u_2 - u_p)\frac{\mathrm{d}f_1}{\mathrm{d}p} = \left(u_p + \frac{p}{3}\frac{\mathrm{d}u_p}{\mathrm{d}p}\right) f_1 - Q_1\delta(p - p_0)\,, \tag{3.32}$$

where we introduced the quantity u_p defined as (Blasi, 2002):

$$u_p(p) \equiv u_1 - v_{A,1} - \frac{1}{f_1(p)}\int_{-\infty}^{0} \mathrm{d}x\,\mathrm{d}_x\left(u - v_A\right) f(x,p)\,, \tag{3.33}$$

which represents the characteristic velocity of scattering centres experienced upstream of the shock by particles of momentum p. Eventually, the particle distribution function at the position of the shock is assumed to match the thermal distribution at the injection momentum p_0, as discussed in Section 3.2, which provides the following boundary condition:

$$f_1(p_0) = \frac{n_0 R_{tot}}{\pi^{3/2} p_0^3}\xi^3 e^{-\xi^2}\,. \tag{3.34}$$

3.7.3 Method of solution

The nonlinear system closed by Equations 3.30, 3.32 together with the boundary condition in momentum 3.34 can be solved within an iterative procedure (Caprioli et al., 2010). A simplified treatment has however been proved to provide a very accurate approximation which is extensively used in the literature (e.g. Blasi, 2002; Amato et al., 2008, and references therein). Let us introduce a distance $x_p(p)$ upstream of the shock defined in this way: particles accelerated to a momentum p can probe a region ahead of the shock up to a distance $x_p(p)$. This can be expressed mathematically as:

$$f(x,p) = f_1(p)\vartheta[x - x_p(p)]\,, \tag{3.35}$$

as first pointed out by Eichler (1979).

After adopting this assumption, the expression for the cosmic ray pressure at a given position simplifies significantly and can be written as:

$$p_c(x_p) \approx \frac{4\pi}{3}\int_p^\infty \mathrm{d}p' p'^3 v(p') f_1(p')\,. \tag{3.36}$$

Moreover, Equation 3.33 becomes:

$$U_p(p) \approx U(x_p) - V_A(x_p) = \left(\frac{7}{5}U(x_p) - \frac{2}{5}U(x_p)^{-1/4}\right)\,. \tag{3.37}$$

Solving this equation gives $U(x_p)$ as function of p. For the sake of clarity, we make this dependency explicit by renaming $U(x_p)$ as $\zeta(p)$. Equation 3.37 is rewritten as:

$$U_p(p) \approx \left(\frac{7}{5}\zeta(p) - \frac{2}{5}\zeta(p)^{-1/4}\right)\,. \tag{3.38}$$

Plugging this expression into Equation 3.32 gives, after some algebra:

$$\frac{p}{3}\frac{\mathrm{d}f_1}{\mathrm{d}p}\left(\frac{1}{R_{tot}} - \frac{7}{5}\zeta + \frac{2}{5}\zeta^{-1/4}\right) = \frac{f_1}{5}\left(7\zeta - 2\zeta^{-1/4} + \frac{p}{6}\left(14 + \zeta^{-5/4}\right)\zeta'(p)\right)\,. \tag{3.39}$$

[5]This assumption will be relaxed in Section 5.3.

The fluid and magnetic pressure terms evaluated at $x = x_p$ are functions of $U(x_p)$ only, while the cosmic ray pressure term at x_p is function of $U(x_p)$ and p. Evaluating the momentum equation at x_p, we therefore get an equation which only depends on $\zeta(p)$ and p. After differentiating this equation with respect to p, we get:

$$\zeta'(p)\left[\frac{27}{25} - \frac{\zeta^{-\gamma-1}}{M_0^2} + \frac{\zeta^{-5/4}}{25} - \frac{3\zeta^{-5/2}}{25}\right] = \frac{4\pi}{3\rho_0 u_0^2} p^3 v(p) f_1(p)\,. \tag{3.40}$$

Two boundary conditions are needed to solve Equation 3.39 together with Equation 3.40. Equation 3.34 provides the boundary condition for the distribution function. Then, we start with an initial guess value of U_1, which provides an initial value for ζ, as $\zeta(p_0) \approx U_1$. The total compression factor is computed from the Rankine-Hugoniot condition at the subshock, with the dynamical effect of the magnetic field properly implemented to satisfy Maxwell's equations at the subshock (Caprioli et al., 2009):

$$\begin{aligned} R_{tot}^{\gamma+1} &= \frac{M_0^2 R_{sub}^{\gamma}}{2}\left(\frac{\gamma + 1 - R_{sub}(\gamma-1)}{1+\Lambda_B}\right)\,, \\ \Lambda_B &= \frac{2}{25}\left(1 - U_1^{5/4}\right)^2 U_1^{\gamma-3/2}\gamma M_0^2\left(1 + R_{sub}\left(\frac{2}{\gamma} - 1\right)\right)\,. \end{aligned} \tag{3.41}$$

The fluid and effective compression factors are further related by:

$$\begin{aligned} R_{sub} &= R_{tot} U_1\,, \\ S_{sub} &= R_{sub}\left(1 - \frac{2}{5}\left(U_1^{-1/4} - U_1\right)\right)\,. \end{aligned} \tag{3.42}$$

Now that two initial values have been obtained for the functions f and ζ, together with the properties of the subshock, Equations 3.40 and 3.39 can be solved together numerically as follows. Equation 3.40 gives $\zeta'(p)$ and $\zeta(p+dp)$ as function of $f_1(p)$ and $\zeta(p)$. Equation 3.39 gives $f_1(p+dp)$ as function of $f_1(p)$, $\zeta(p)$ and $\zeta'(p)$. We can therefore reconstruct the full solutions f_1 and ζ for a given guess value of U_1. The physical value of U_1 is the one for which $\zeta(p_{max}) = 1$, as the flow profile should not be modified at large distances from the shock.

3.7.4 Numerical solution

The downstream distribution of particles accelerated in a nonlinear shock is shown in Figure 3.4, where it is assumed that the shock expands in a typical superbubble environment. A cut-off has been introduced at 1 PeV, meaning that all particles accelerated beyond this threshold are considered to escape far upstream and are discarded. As the injection parameter ξ approaches unity, the injection is more and more efficient, thus the particles carry more and more energy and their back-reaction on the flow is stronger and stronger. The table given on the right of Figure 3.4 provides the main properties of the flow and non-thermal distribution. One notices that the compression factor far away from the shock, R_{tot}, is different from the compression factor at the discontinuity, R_{sub}, which shows that the upstream flow is inhomogeneous. The pressure of the particles decelerate the flow within one diffusion length upstream of the shock. This decrease of velocity is referred to as the *shock precursor*. Particles of low momentum stay close to the shock, thus experience a small compression ratio, especially when Alfvén waves are efficiently excited in the region. In other words, low energy particles feel a weak shock and are not

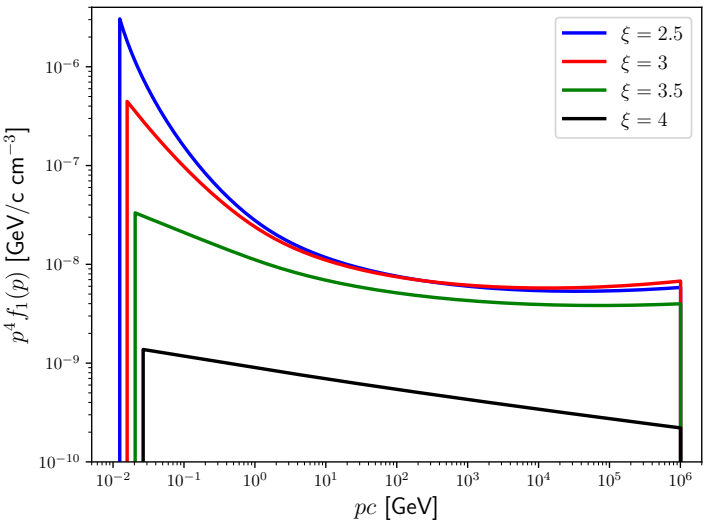

ξ	2.5	3	3.5	4
R_{tot}	4.6	4.7	4.5	4.0
R_{sub}	3.0	3.4	3.9	4.0
S_{sub}	2.1	2.7	3.5	4.0
F_e	40%	36%	20%	0.025%
F_a	49%	39%	23%	1.8%

Figure 3.4: Left: Downstream distribution of non-thermal particles at a nonlinear shock characterised by a Mach number $\mathcal{M} = 30$ expanding in a medium of number density 0.01 cm^{-3} and temperature 10^6 K. Right: Total compression factor $R_{tot} = u_0/u_2$, compression factor at the subshock $R_{sub} = u_1/u_2$, effective compression factor at the subshock $S_{sub} = (u_1 - v_{A,1})/u_2$, escape energy flux of cosmic rays upstream of the shock and advected energy flux downstream of the shock in units of the shock mechanical power $1/2\rho_0 u_0^3$. Four values of the injection parameter ξ ($p_0 = \xi p_{th}$) are probed.

accelerated efficiently. On the other hand, the effective compression ratio experienced by high energy particles diffusing far away from the shock becomes higher than 4, and therefore these particles are very efficiently accelerated. At the end of the day, the spectrum of the accelerated particles appears to be very steep in the low energy bands, while it is slightly harder than the test-particle expectation in the high energy bands, which results in a *concave* spectrum rather than a power law.

Because modified shocks usually produce spectra harder than p^{-4} at high energies, a non negligible amount of energy carried by escaping particles leaks upstream of the flow. The escape flux F_e normalised to the kinetic energy of the shock can be computed using the conservation of the energy between the downstream region and upstream infinity (Blasi et al., 2005):

$$F_e = 1 - \frac{1}{R_{tot}^2} + \frac{2}{M_0^2(\gamma - 1)} - \frac{2}{R_{tot}}\frac{\gamma}{\gamma - 1}P_{g,2} - \frac{2}{R_{tot}}\frac{\gamma_c}{\gamma_c - 1}P_{cr,2}\,, \tag{3.43}$$

$$P_{g,2} = U_1 - \frac{1}{R_{tot}} + \frac{1}{\gamma M_0^2}U_1^{-\gamma} + \frac{2}{25U_1^{3/2}}\left(1 - U_1^{5/4}\right)^2\,, \tag{3.44}$$

where $\gamma_c = 1 + p_{cr}/e_{cr}$ is the adiabatic index of the particles and $U_1 = R_{sub}/R_{tot}$ is the flow velocity immediately upstream of the shock normalised to the upstream velocity. The magnetic pressure does not appear in the first equation because we assumed that the hydromagnetic waves were efficiently isotropised downstream, and that there were no streaming instability at upstream infinity. On the other hand it appears in the second equation because the Alfvén waves are excited immediately upstream of the shock.

The nonlinear feedback of the particles on the flow always ensures that even for very high injection efficiencies (e.g. $\eta \sim 10\%$), only a fraction of the shock pressure will be transferred into cosmic rays. The model of acceleration is now self-consistent, in the sense

that it ensures energy conservation between the flow and the particles, in contrast with the test-particle computation which, as shown earlier, could easily violate the energy balance.

3.7.5 Non-resonant field amplification

Nonlinear shocks producing hard spectra in the high energy bands, the escape flux is non-negligible. Escaping cosmic rays induce a current $j_{cr} = e\rho_0 u_0^3 F_e/(p_0 c) \ln(p_{max}/p_0)$ (Schure et al., 2012) in the upstream region. By the condition of quasi-neutrality, a return current is induced in the plasma in the opposite direction. This current destabilises any small perturbation perpendicular to the current, which will grow at a rate $\gamma = \sqrt{kB_0 j_{cr}/(\rho c)}$ (Schure et al., 2012). In a one-dimensional parallel shock, this mechanism will amplify magnetic perturbations in the direction perpendicular to the magnetic field and preferentially of small wavelengths. This is called the *non-resonant streaming instability* (Bell, 2004), for it does not rely on the resonant interactions between the waves and the particles but is generated instead by the particles whose Larmor radii are larger than the largest turbulence scale, such that they stream nearly freely. The destabilising current could also be induced by high energy seeds (Caprioli et al., 2018).

Because the amplification of the magnetic field is due to particles which are not affected by the turbulence, the magnetic pressure is not expected to follow the exponential suppression of the cosmic ray pressure upstream of the shock, the latter being due to the diffusion of the particles. Instead, one can assume, in first approximation, that a fraction of the shock ram pressure is converted into magnetic pressure (Schure et al., 2012), independently of the position in the upstream region, such that we can write:

$$P_B \approx \frac{u_0}{c} \frac{F_e}{\ln(p_{max}/p_0)}\,, \tag{3.45}$$

where $F_e \approx 1 - 50\%$ is the normalised escape flux of cosmic rays. This typically provides $P_B \approx 10^{-5} - 10^{-3}$.

Under this approximation, the non-resonant streaming instability only affects the jump condition 3.41. Indeed, a homogeneous magnetic pressure is not expected to modify the dynamics of the upstream flow and Equation 3.40 becomes:

$$\zeta'(p)\left[1 - \frac{\zeta^{-\gamma-1}}{M_0^2}\right] = \frac{4\pi}{3\rho_0 u_0^2} p^3 v(p) f_1(p)\,. \tag{3.46}$$

We also make the simplifying assumption that the non-resonant streaming instability only amplifies perpendicular perturbations, which does not affect the effective velocity felt by the diffusing cosmic rays. Then one can assume that the velocity of the scattering centres matches that of the flow, such that Equation 3.39 reduces to:

$$\frac{p}{3}\frac{\mathrm{d}f_1}{\mathrm{d}p}\left(\frac{1}{R_{tot}} - \zeta\right) = f_1\left(\zeta + \frac{p}{3}\zeta'(p)\right)\,. \tag{3.47}$$

The result of the nonlinear resolution of these coupled equations is shown in Figure 3.5. For expected values of the normalised magnetic pressure, $P_B = 10^{-5} - 10^{-3}$, corresponding to an amplified magnetic field $B = 1 - 10$ µG (in a low-density medium), we do not witness strong deviations from the solution without field amplification (black curve in Figure 3.5). A concave spectrum is retrieved for high injection efficiencies (small values of the parameter ξ) and a power law of spectral index close to 4 for low injection efficiencies

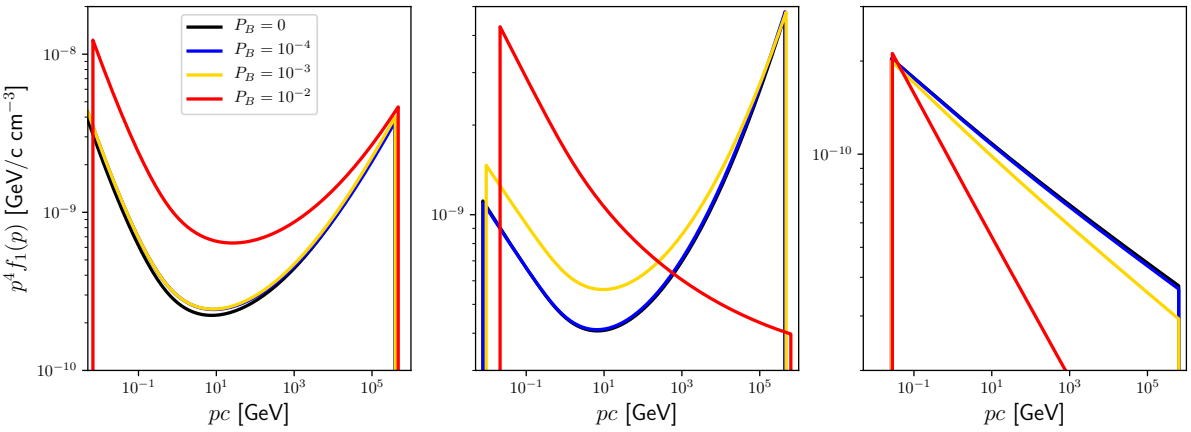

Figure 3.5: Nonlinear diffusive shock acceleration with non-resonant field amplification, for a Mach number of 30 and three different values of the injection parameter: $\xi = 3$ (left panel), $\xi = 3.5$ (middle panel), $\xi = 4$ (right panel).

($\xi > 4$). For high amplification efficiencies, e.g. 10% ($B = 30$ µG), and low injection efficiencies, the spectrum resembles a steep power law (about $p^{-4.1} - p^{-4.4}$). Indeed, the magnetic pressure jump decreases the compression ratio of the shock up to $r \approx 3$ for $P_B = 10\%$, and to even lower values if for some reason the amplification is more efficient, up to the point where the magnetic pressure becomes of the order of the ram pressure, in which case the shock is smoothed out.

Although realistic values of the amplification efficiency do not lead to a strong modification of the spectral shape of the accelerated particles, one should remember that a large magnetic field is required in order to efficiently confine the particles around the shock, which is a necessary condition to reach high energies bands. According to Equation 3.16, PeV bands could be reached at the end of the free expansion phase if the magnetic field is raised to 10 µG, which can be expected if the injection efficiency is high (e.g. $\xi = 3$), for in this case the spectrum is very concave and the escape flux induces a strong current in the upstream region.

3.8 Summary

The fundamentals of the diffusive shock acceleration mechanism have been briefly reviewed. Charged particles gain energy in fluid inhomogeneities, and in particular when they cross a shock discontinuity. Because the medium is turbulent around the shock, the particles are able to diffuse back and forth and cross the shock several times. The energy gain of each particle being balanced by the probability to escape, the particles end up being distributed along a power law of spectral index $s = 3r/(r-1)$, where r is the compression ratio of the shock. The maximum achievable energy is limited in particular by the finite size and finite age of the system. Only if the level of turbulence is very high particles may reach PeV energy bands, for in this case they are quickly scattered back into the shock after each crossing. High levels of turbulence are indeed expected if a strong field amplification takes place in the upstream flow, which could originate from the non-resonant streaming instability triggered by the escaping particles. Indeed, when the backreaction of the cosmic ray pressure onto the flow is accounted for, concave spectra are typically obtained with a hard component at high energies, which implies that most

of the non-thermal energy is carried away by the escaping particles.

The transport equation of the particles in presence of large-scale motions together with the global conservation of mass, momentum and energy provide a suitable framework to perform semi-analytical computations in a variety of configurations. In particular, once the solution for a monoenergetic injection of particles is found, the reacceleration of pre-existing ("seed") particles can be computed as a convolution between the fundamental solution and the seed distribution. This will be very useful to compute the reacceleration of particles confined inside superbubbles.

References

Amato, E., Blasi, P., and Gabici, S. (Mar. 2008). "Kinetic approaches to particle acceleration at cosmic ray modified shocks". In: MNRAS 385.4, pp. 1946–1958. ISSN: 0035-8711. DOI: 10.1111/j.1365-2966.2008.12876.x.

Axford, W. I., Leer, E., and Skadron, G. (Jan. 1977). "The Acceleration of Cosmic Rays by Shock Waves". In: *International Cosmic Ray Conference*. Vol. 11. International Cosmic Ray Conference, p. 132.

Bell, A. R. (Jan. 1978a). "The acceleration of cosmic rays in shock fronts - I." In: MNRAS 182, pp. 147–156. DOI: 10.1093/mnras/182.2.147.

Bell, A. R. (Feb. 1978b). "The acceleration of cosmic rays in shock fronts - II." In: MNRAS 182, pp. 443–455. DOI: 10.1093/mnras/182.3.443.

Bell, A. R. (Sept. 2004). "Turbulent amplification of magnetic field and diffusive shock acceleration of cosmic rays". In: MNRAS 353.2, pp. 550–558. DOI: 10.1111/j.1365-2966.2004.08097.x.

Blandford, R. D. and Ostriker, J. P. (Apr. 1978). "Particle acceleration by astrophysical shocks." In: ApJ 221, pp. L29–L32. DOI: 10.1086/182658.

Blasi, P., Gabici, S., and Vannoni, G. (Aug. 2005). "On the role of injection in kinetic approaches to non-linear particle acceleration at non-relativistic shock waves". In: MNRAS 361.3, pp. 907–918. DOI: 10.1111/j.1365-2966.2005.09227.x.

Blasi, P. (Feb. 2002). "A semi-analytical approach to non-linear shock acceleration". In: *Astroparticle Physics* 16.4, pp. 429–439. DOI: 10.1016/S0927-6505(01)00127-X.

Bresci, V. et al. (Sept. 2019). "Effects of re-acceleration and source grammage on secondary cosmic rays spectra". In: MNRAS 488.2, pp. 2068–2078. DOI: 10.1093/mnras/stz1806.

Caprioli, D. and Spitkovsky, A. (Mar. 2014a). "Simulations of Ion Acceleration at Non-relativistic Shocks. I. Acceleration Efficiency". In: ApJ 783.2, 91, p. 91. DOI: 10.1088/0004-637X/783/2/91.

Caprioli, D. and Spitkovsky, A. (Oct. 2014b). "Simulations of Ion Acceleration at Non-relativistic Shocks. II. Magnetic Field Amplification". In: ApJ 794.1, 46, p. 46. DOI: 10.1088/0004-637X/794/1/46.

Caprioli, D. and Spitkovsky, A. (Oct. 2014c). "Simulations of Ion Acceleration at Non-relativistic Shocks. III. Particle Diffusion". In: ApJ 794.1, 47, p. 47. DOI: 10.1088/0004-637X/794/1/47.

Caprioli, D. et al. (May 2009). "Dynamical feedback of self-generated magnetic fields in cosmic ray modified shocks". In: MNRAS 395.2, pp. 895–906. DOI: 10.1111/j.1365-2966.2009.14570.x.

Caprioli, D. et al. (Sept. 2010). "Comparison of different methods for non-linear diffusive shock acceleration". In: MNRAS 407.3, pp. 1773–1783. DOI: 10.1111/j.1365-2966.2010.17013.x.

Caprioli, D. (May 2011). "Understanding hadronic gamma-ray emission from supernova remnants". In: J. Cosmology Astropart. Phys. 2011.5, 026, p. 026. DOI: 10.1088/1475-7516/2011/05/026.

Caprioli, D. (July 2012). "Cosmic-ray acceleration in supernova remnants: non-linear theory revised". In: J. Cosmology Astropart. Phys. 2012.7, 038, p. 038. DOI: 10.1088/1475-7516/2012/07/038.

Caprioli, D., Haggerty, C. C., and Blasi, P. (Dec. 2020). "Kinetic Simulations of Cosmic-Ray-modified Shocks. II. Particle Spectra". In: ApJ 905.1, 2, p. 2. DOI: 10.3847/1538-4357/abbe05.

Caprioli, D., Zhang, H., and Spitkovsky, A. (June 2018). "Diffusive shock re-acceleration". In: *Journal of Plasma Physics* 84.3, 715840301, p. 715840301. DOI: 10.1017/S0022377818000478.

Chevalier, R. A. (July 1982). "Self-similar solutions for the interaction of stellar ejecta with an external medium." In: ApJ 258, pp. 790–797. DOI: 10.1086/160126.

Cristofari, P. and Blasi, P. (Oct. 2019). "Gamma-rays from reaccelerated particles at supernova remnant shocks". In: MNRAS 489.1, pp. 108–115. DOI: 10.1093/mnras/stz2126.

Drury, L. O. (July 1991). "Time-dependent diffusive acceleration of test particles at shocks". In: MNRAS 251, pp. 340–350. DOI: 10.1093/mnras/251.2.340.

Drury, L. O. (Aug. 1983). "An introduction to the theory of diffusive shock acceleration of energetic particles in tenuous plasmas". In: *Reports on Progress in Physics* 46.8, pp. 973–1027. DOI: 10.1088/0034-4885/46/8/002.

Eichler, D. (Apr. 1979). "Particle acceleration in collisionless shocks: regulated injection and high efficiency." In: ApJ 229, pp. 419–423. DOI: 10.1086/156969.

Gaggero, D. et al. (Apr. 2018). "Time evolution of gamma rays from supernova remnants". In: MNRAS 475.4, pp. 5237–5245. DOI: 10.1093/mnras/sty140.

Jokipii, J. R. (Feb. 1987). "Rate of Energy Gain and Maximum Energy in Diffusive Shock Acceleration". In: ApJ 313, p. 842. DOI: 10.1086/165022.

Kang, H. and Ryu, D. (June 2011). "Re-acceleration of Non-thermal Particles at Weak Cosmological Shock Waves". In: ApJ 734.1, 18, p. 18. DOI: 10.1088/0004-637X/734/1/18.

Plasma Astrophysics (Jan. 1994).

Krymskii, G. F. (June 1977). "A regular mechanism for the acceleration of charged particles on the front of a shock wave". In: *Akademiia Nauk SSSR Doklady* 234, pp. 1306–1308.

Lagage, P. O. and Cesarsky, C. J. (Sept. 1983). "The maximum energy of cosmic rays accelerated by supernova shocks." In: A&A 125, pp. 249–257.

Marcowith, A. et al. (Oct. 2018). "Core-collapse supernovae as cosmic ray sources". In: MNRAS 479.4, pp. 4470–4485. DOI: 10.1093/mnras/sty1743.

Morlino, G. et al. (Mar. 2021). "Particle acceleration in winds of star clusters". In: MNRAS. DOI: 10.1093/mnras/stab690.

Parizot, E. et al. (July 2006). "Observational constraints on energetic particle diffusion in young supernovae remnants: amplified magnetic field and maximum energy". In: A&A 453.2, pp. 387–395. DOI: 10.1051/0004-6361:20064985.

Parker, E. N. (Jan. 1965). "The passage of energetic charged particles through interplanetary space". In: Planet. Space Sci. 13.1, pp. 9–49. DOI: 10.1016/0032-0633(65)90131-5.

Prishchep, V. L. and Ptuskin, V. S. (Aug. 1981). "Fast-Particle Acceleration at a Spherical Shock Front". In: Soviet Ast. 25, p. 446.

Schure, K. M. et al. (Nov. 2012). "Diffusive Shock Acceleration and Magnetic Field Amplification". In: Space Sci. Rev. 173.1-4, pp. 491–519. DOI: 10.1007/s11214-012-9871-7.

Vink, J. (Dec. 2012). "Supernova remnants: the X-ray perspective". In: A&A Rev. 20, 49, p. 49. DOI: 10.1007/s00159-011-0049-1.

Völk, H. J., Berezhko, E. G., and Ksenofontov, L. T. (Apr. 2005). "Magnetic field amplification in Tycho and other shell-type supernova remnants". In: A&A 433.1, pp. 229–240. DOI: 10.1051/0004-6361:20042015.

White, R. L. (Feb. 1985). "Synchrotron emission from chaotic stellar winds." In: ApJ 289, pp. 698–708. DOI: 10.1086/162933.

Zirakashvili, V. N. and Ptuskin, V. S. (Dec. 2008). "The influence of the Alfvénic drift on the shape of cosmic ray spectra in SNRs". In: *American Institute of Physics Conference Series*. Ed. by F. A. Aharonian, W. Hofmann, and F. Rieger. Vol. 1085. American Institute of Physics Conference Series, pp. 336–339. DOI: 10.1063/1.3076675.

Chapter 4

Particle acceleration at colliding shocks

4.1 Motivation

As discussed in Chapter 1, most massive stars are expected to live inside clusters originating from a common molecular cloud. Stellar clusters may contain hundreds of stars within a sphere of relatively small radius. Assuming that a supernova blast wave expands at 3000 km/s, the forward shock will reach the boundary of a cluster of radius R_* after typically $R_*/(3\ \mathrm{pc})$ kyr. If two stars explode within that time interval, a collision between the shocks can be expected to occur inside the cluster. The average time interval between two supernova explosions is of the order of 35 Myr/N_*, where N_* is the initial number of massive stars in the cluster. It is therefore expected that in average about $R_*N_*/(100\ \mathrm{pc})\%$ of the supernovae will collide. For a typical compact cluster, $R_*N_* \sim 1000$ pc, which provides a fraction of 10%. This fraction can further rise in loose clusters, where the mean distance between the stars may reach several tens of parsecs. The supernovae exploding inside a compact cluster will also systematically collide with the collective termination shock surrounding the cluster. Although this is not expected to enhance the maximum achievable energy, for the latter will always be limited by the size of the shocks at the time of collision, which is of the order of the size of the cluster (10 pc), it may change the spectral shape in non-trivial ways.

Colliding shocks are furthermore not restricted to star clusters, but are expected in a great variety of astrophysical contexts, spanning from the interplanetary medium (e.g. shocks in the solar wind, Colburn and Sonett, 1966), to jets of gamma ray bursts and active galactic nuclei (Kobayashi et al., 1997; Spada et al., 2001).

In a seminal paper, Lieu and Axford (1990) concluded that the spectrum of particles accelerated at colliding shocks should follow very closely the standard prediction for diffusive shock acceleration at a single shock, i.e. a power law $f(p) \propto p^{-4}$ (see Chapter 3). In more recent times, a number of authors reconsidered the problem of particle acceleration at colliding shocks and claimed that some important differences might appear with respect to the standard p^{-4} scenario. In particular, Bykov et al. (2013) developed a semi-analytic and nonlinear model to describe the acceleration of particles at a couple of colliding shocks, where the pressure of cosmic rays onto the structure of the shocks was also taken into account. To simplify the problem, Bykov et al. (2013) assumed the two shocks to be very close to each other, and solved the steady-state (time independent) transport equation for accelerated particles. The resulting spectrum of accelerated particles was found to be very hard, scaling as p^{-3}. The model was then used to make predictions on the gamma-ray and neutrino emission from colliding winds in compact

stellar clusters (Bykov et al., 2015) and in bow shock wind nebulae (Bykov et al., 2019).

Wang et al. (2017) and Wang et al. (2019) developed a Monte Carlo code to study the acceleration of particles at a pair of colliding shocks. They considered both the case of converging shocks (Wang et al., 2017) and that of a faster shock catching up with a slower one (Wang et al., 2019). In both cases, they concluded that spectral features such as breaks may appear in the spectrum of accelerated particles.

Finally, Siemieniec-Ozieblo and Ostrowski (2000) considered the case of particle acceleration in converging flows of plasma, where a pair of standing shocks may appear. They considered the case of accretion of matter onto cosmological structures, and concluded again that the resulting spectrum of accelerated particles is a hard power law.

The aforementioned analytical or semi-analytical works have all been derived in the stationary regime. In contrast, here we investigate the acceleration of particles in a time-dependent collision. The situation is described in Section 4.2. We tackle the problem both numerically (Section 4.3) and analytically (Section 4.4), and demonstrate that under certain conditions an analytic self-similar solution can be found asymptotically. A pair of standing shocks in a converging flow of matter is eventually discussed in Section 4.6. This chapter is a reproduction, with minor modifications, of the analysis published in Vieu et al. (2020).

4.2 Physical setup

4.2.1 Model

We consider a system of two infinite and plane shocks initially separated by a distance $2L$. The two shock surfaces are parallel to each other, and move along the same direction (defined as the x axis) at a velocity V and $-V$, respectively. The origin of the x axis is defined in such a way that the positions of the shocks at a given time t are $x_s = \pm(L - Vt)$. In other words, the system is symmetric with respect to $x = 0$, and the shocks will collide at a time $t_{\rm coll} = L/V$. The initial setup of the problem is shown in Figure 4.1, where one can see that while the upstream medium between the shocks is at rest, the downstream medium moves in the same direction of the shock with a speed equal to $3/4V$. Here, we have assumed strong shocks with compression ratio $r = 4$. The generalisation of the analysis to weak shocks is straightforward.

We now model the acceleration of particles at the system of two shocks in the test-particle limit, i.e. assuming that the pressure of the accelerated particles does not affect the shock structure. We also assume a spatially homogeneous and steady diffusion coefficient of cosmic rays both upstream and downstream of the shock, and we neglect energy losses.

Under these simplifying assumptions, the evolution of the particle distribution function $f(x, p, t)$ is determined by the cosmic ray transport equation 3.20:

$$\partial_t f + u\partial_x f = \partial_x \left(\kappa \partial_x f\right) + \frac{1}{3}(\partial_x u) p \partial_p f + Q_i \delta(x \pm x_s)\delta(p - p_i)\,, \tag{4.1}$$

where u is the plasma velocity, κ the particle diffusion coefficient, and Q_i the injection at the shocks of particles of momentum p_i. Finally, $\delta(x \pm x_s) = \delta(x + x_s) + \delta(x - x_s)$, where $\pm x_s$ are the positions of the shocks.

We rescale Equation 4.1 with the following space dilatation:

$$X \equiv x/(L - Vt)\,, \tag{4.2}$$

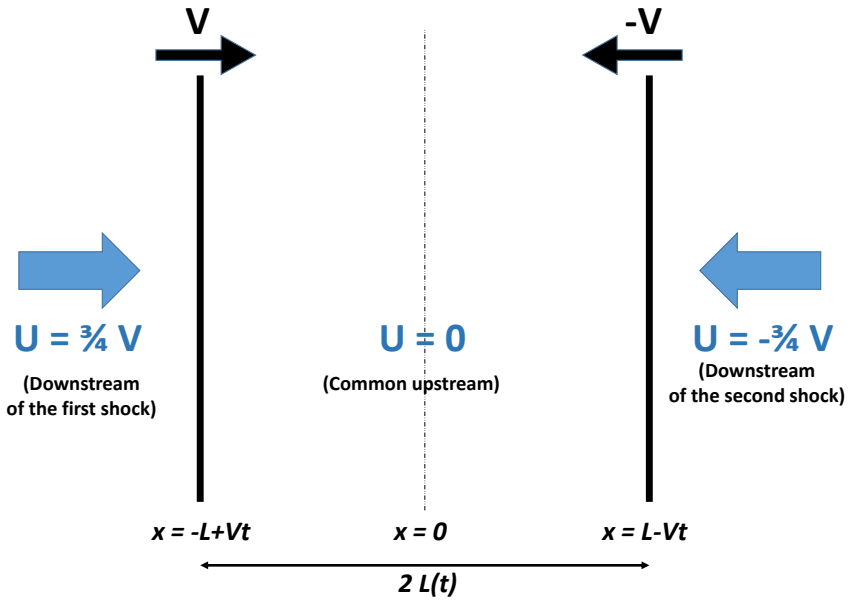

Figure 4.1: Setup of the problem.

such that in the new rest frame the two shocks stand at a fixed position $X = \pm 1$. We also define the following dimensionless quantities:

$$\begin{aligned} U &\equiv u/V\,, \quad K \equiv \kappa/(LV)\,, \quad P \equiv p/p_i\,, \\ \tilde{t} &\equiv Vt/L\,, \quad T \equiv -\ln\left(1-\tilde{t}\right)\,, \end{aligned} \tag{4.3}$$

in order to obtain the following dilated dimensionless transport equation:

$$\partial_T f + (X+U)\partial_X f = \partial_X\left(e^T K \partial_X f\right) + \frac{\partial_X U}{3} P \partial_P f + Q\,, \tag{4.4}$$

where $Q = \delta(X \pm 1)\delta(P-1)$ (the injection density $Q_i/V/p_i$ has been absorbed in f). The additional term $X\partial_X$ comes from a fictitious velocity due to the fact that we are gradually zooming in the space coordinate as time flows. The factor e^T in front of the diffusion coefficient accounts for the increase of the diffusion length over separation length ratio: as in the new rest frame the separation length remains constant in time, the diffusion length should effectively vary in time.

As we have two length scales, the diffusion length and the separation distance, it is not possible to absorb both by a redefinition of the spatial coordinate, which is why the diffusion coefficient still appears in the dimensionless transport equation 4.4. However, provided that we assume some shape for the diffusion coefficient K as function of momentum,

$$K = K_0 \psi(P)\,, \tag{4.5}$$

we can translate the time as:

$$\hat{T} \equiv T + \ln K_0 = -\ln\left(\frac{1-\tilde{t}}{K_0}\right)\,, \tag{4.6}$$

in order to get rid of at least K_0 in the transport equation:

$$\partial_{\hat{T}} f + (X+U)\partial_X f = \partial_X\left(e^{\hat{T}} \psi(P) \partial_X f\right) + \frac{\partial_X U}{3} P \partial_P f + Q\,, \tag{4.7}$$

at the price of a shifted initial time:

$$\hat{T}_0 = \ln K_0 \ . \tag{4.8}$$

As K is the ratio between the diffusion length and the initial distance between the shocks (see Equation 4.3), K_0 is a parameter describing how far away are the shocks from each other at the beginning of the process. The parameter K_0 will be used for quantitative comparisons between the acceleration of particles at two converging shocks and at a single shock. In particular, the case $K_0 = 0$ corresponds to two shocks at an infinite distance that would behave as two isolated shocks. More importantly, the introduction of the parameter K_0 also shows that the result of Equation 4.7 will only depend on the normalisation of the diffusion coefficient through the ratio between diffusion length and initial shock distance.

4.2.2 Timescales

The characteristic diffusion length of particles of momentum p at a single shock is given by $l_d(p) = \kappa(p)/V$ (e.g. Drury, 1991). This means that particles of momentum p fill a region of size l_d upstream of the shock. Therefore, when the distance between the shocks $2(L - Vt)$ equals twice the diffusion distance $2l_d(p)$, particles of momentum p start to be affected by both shocks. This happens at a critical time:

$$t_c(E) = t_{\rm coll} - \kappa(p)/V^2 \ , \tag{4.9}$$

where $t_{\rm coll} = L/V$ is the time at which the collision occurs.

The acceleration time of particles of energy E at a single shock is (e.g. Drury, 1991):

$$t_{\rm acc} = \xi\kappa(p)/V^2 \ , \tag{4.10}$$

where ξ is a dimensionless parameter to be determined later, depending on model assumptions. For a single shock in the test-particle regime, after a time $t_{\rm acc}(p)$, the spectrum of accelerated particles is a power law up to particle momentum p.

At this point, we can define a momentum-dependent dimensionless parameter $r_{\rm eq}$ as:

$$r_{\rm eq}(p) \equiv \frac{t_c}{t_{\rm acc}} = \frac{1}{\xi}\left(\frac{LV}{\kappa(p)} - 1\right) = \frac{1}{\xi}\left(\frac{1}{K} - 1\right) \ . \tag{4.11}$$

The case $r_{\rm eq}(E) \ll 1$ corresponds to $t_c \ll t_{\rm acc}$, i.e., to a situation where the two shocks become very close to each other before they had time to accelerate particles up to a momentum p. On the other hand, $r_{\rm eq}(p) \gg 1$ implies that particles can be accelerated at a single shock up to a momentum p well before both of the shocks begin to contribute to the acceleration of particles of that energy.

The case $r_{\rm eq}(p_{\rm eq}) = 1$ defines a characteristic momentum $p_{\rm eq}$ and gives:

$$\kappa(p_{\rm eq}) = \frac{LV}{\xi + 1} \ , \tag{4.12}$$

or, using Equation 4.9:

$$t_c^{\rm eq} = \frac{\xi}{1+\xi} t_{\rm coll} \ . \tag{4.13}$$

The physical meaning of $t_c^{\rm eq}$ is the following: for times earlier than $t_c^{\rm eq}$ the two shocks accelerate particles as two isolated systems, while after $t_c^{\rm eq}$ the two shocks behave as a single particle accelerator.

Let us now determine the value of the parameter ξ. The acceleration time at a single shock is defined as (Equation 3.24, Drury, 1983):

$$t_{\rm acc} = \frac{3}{u_1 - u_2} \int_{p_0}^{p} \frac{{\rm d}p'}{p'} \left(\frac{\kappa_1(p')}{u_1} + \frac{\kappa_2(p')}{u_2} \right) \ . \tag{4.14}$$

For strong shocks $u_2 = u_1/4 = V/4$. We further assume that κ_1 and κ_2 are spatially uniform and obey the Bohm scaling $\kappa_{1,2} \propto p$. Moreover, we set $\kappa_2 = \alpha \times \kappa_1$. It is generally believed that, due to magnetic field compression and generation of magnetic turbulence downstream of the shock, $\alpha < 1$. Then, one can easily see that $\xi = 4(1 + 4\alpha)$ and that for $0 < \alpha < 1$ one gets:

$$t_c^{\rm eq} = 0.8...0.95 \times t_{\rm coll} \, , \tag{4.15}$$

meaning that only during the late phase of the collision process accelerated particles are affected by both shocks simultaneously. This also implies that, as pointed out by Lieu and Axford (1990), the maximum particle energy attainable at such systems will most likely not change dramatically with respect to that expected at a single shock. For example, assuming Bohm diffusion ($\kappa = \kappa_0 p$) the maximum momentum will be $p_{\rm max} \gtrsim p_{\rm eq} \sim LV/(1+\xi)/\kappa_0$, which is similar to the maximum momentum achievable in a single shock of age $t_{\rm coll} = L/V$.

Therefore, as we will confirm in the following, the spectrum resulting from the acceleration of particles at a pair of converging shocks will not change significantly as long as low momenta (i.e. much smaller than $p_{\rm eq}$) are considered. However, the shape of the spectral cutoff could be affected. Therefore, the study presented here can have a significant impact on the interpretation of the cutoffs observed in the non-thermal spectra of astrophysical sources. The study of spectral cutoffs is of paramount importance in order to constrain the physical properties of astrophysical accelerators (Romoli et al., 2017).

4.3 Numerical solution

In this section we present a numerical solution of Equation 4.7, which provides the spatial distribution and the spectrum of accelerated particles at the system of two converging shocks.

4.3.1 Methods

Since the system of approaching shocks considered here is symmetric with respect to $x = 0$, we only solve the transport equation for the half space $x < 0$, imposing that the derivative of the particle density distribution vanishes at $x = 0$ and that the function itself vanishes at $x \to -\infty$. In order to account for the whole space from $-\infty$ to 0, we further change variable in Equation 4.7, defining $Z \equiv \exp(X + 1)$ such that Z goes from 0 to e, with the shock at $Z = 1$. We finally change the momentum variable for $Y = \ln P$. The transformed transport equation reads:

$$\partial_{\hat{T}} f + WZ\partial_Z f = \tilde{K} Z^2 \partial_Z^2 f + \delta(Z-1) \left(\frac{\Delta U}{3} \partial_Y f + \delta(Y) \right) \ , \tag{4.16}$$

where $\tilde{K} = \psi(P) e^{\hat{T}}$, $W = (\ln Z - 1 + U - \psi)$ and $\Delta U = U_2 - U_1$.

Our numerical scheme follows that presented in Drury (1991): the spatial variable is treated using a Crank-Nicholson method, while the momentum transfer at the shock is updated at each time step, starting from the injection momentum $P = 1$. The shock is treated as a step function, and the matching condition is used at the discontinuity.

In order to define the problem, the only parameter to be specified is the shifted initial time $\hat{T}_0 = \ln K_0$. It should be stressed that a smaller value of K_0 translates into an higher maximum energy. This can be understood in two different equivalent ways: *i)* if the initial time is smaller there is more time to accelerate particles before the shock collision happens; *ii)* Bohm diffusion implies $r_{\rm eq} \propto 1/K_0$, so that a small K_0 results in $r_{\rm eq} \gg 1$ and the considerations made in Section 4.2.2 apply. However, as $L \propto 1/K_0$, the smaller K_0 the bigger the initial physical distance between the shocks, hence one needs a finer spatial resolution to solve the problem with small values of K_0, which increases the computation time. Eventually we found $K_0 = 0.003$ to be a satisfying compromise between the required accuracy and computation time. Then several resolutions in space, momentum and time have been tested to ensure that the solution is reliable. In particular, several spatial grids have been tested with consistent results. The fastest and most accurate spatial grid was found to be an inhomogeneous resolution, with higher precision around the shock, and an exponential decrease of the resolution to minus infinity. We further tested our numerical recipe in the context of single shock acceleration to compare with the time-dependent solution obtained by Drury (1991). We found a good agreement within a typical 5% discrepancy imputable to the resolution in energy. In particular, the spectral index at low energies in Figure 4.3 is 3.9 and not 4. We checked that increasing the energy resolution leads to a convergence towards 4. Using a higher energy resolution however requires to decrease the spatial resolution, which is crucial when a second shock is introduced: a compromise had to be found to keep a low value for the parameter K_0 which, as previously discussed, is crucial for particles to have time to be accelerated before the collision occurs.

4.3.2 Results

Figure 4.2 eventually shows the solution of Equation 4.16. The spatial distribution of accelerated particles is plotted for three different particle momenta, corresponding to $r_{\rm eq} \gg 1$ (top panel), $r_{\rm eq} \gtrsim 1$ (middle panel), and $r_{\rm eq} \sim 1$ (bottom panel). The sharp features in the curves indicate the position of the shock waves.

At small momenta ($r_{\rm eq} \gg 1$, top panel) and small times, one recovers the solution for particle acceleration at single shocks, characterised by an exponential decay of f upstream of the shocks. Then, as time increases, the gradient of the particle distribution ahead of each shock gradually decreases because of the influence of the other shock. When the two shocks are very close, a sharp peak at the position of each shock also appears. This happens when the value of f at $x = 0$ is no longer negligible, i.e., when the number of particles coming from the other shock exceeds the number of particles injected there.

The origin of the bump visible downstream of the shocks at late times (top panel in Figure 4.2) can be better understood by rewriting the transport equation (Equation 4.7) in terms of the time variable $\tau \equiv e^{\hat{T}} - 1$:

$$\partial_\tau f + \frac{1}{1+\tau}(X+U)\partial_X f = \partial_X\left(\psi \partial_X f\right) + \frac{1}{1+\tau}\left[\frac{\partial_X U}{3} P \partial_P f + \delta(X \pm 1)\delta(P-1)\right], \quad (4.17)$$

which is a diffusion (first term on the right) advection (second term on the left) equation, with an effective injection represented by the second term on the right. As time passes,

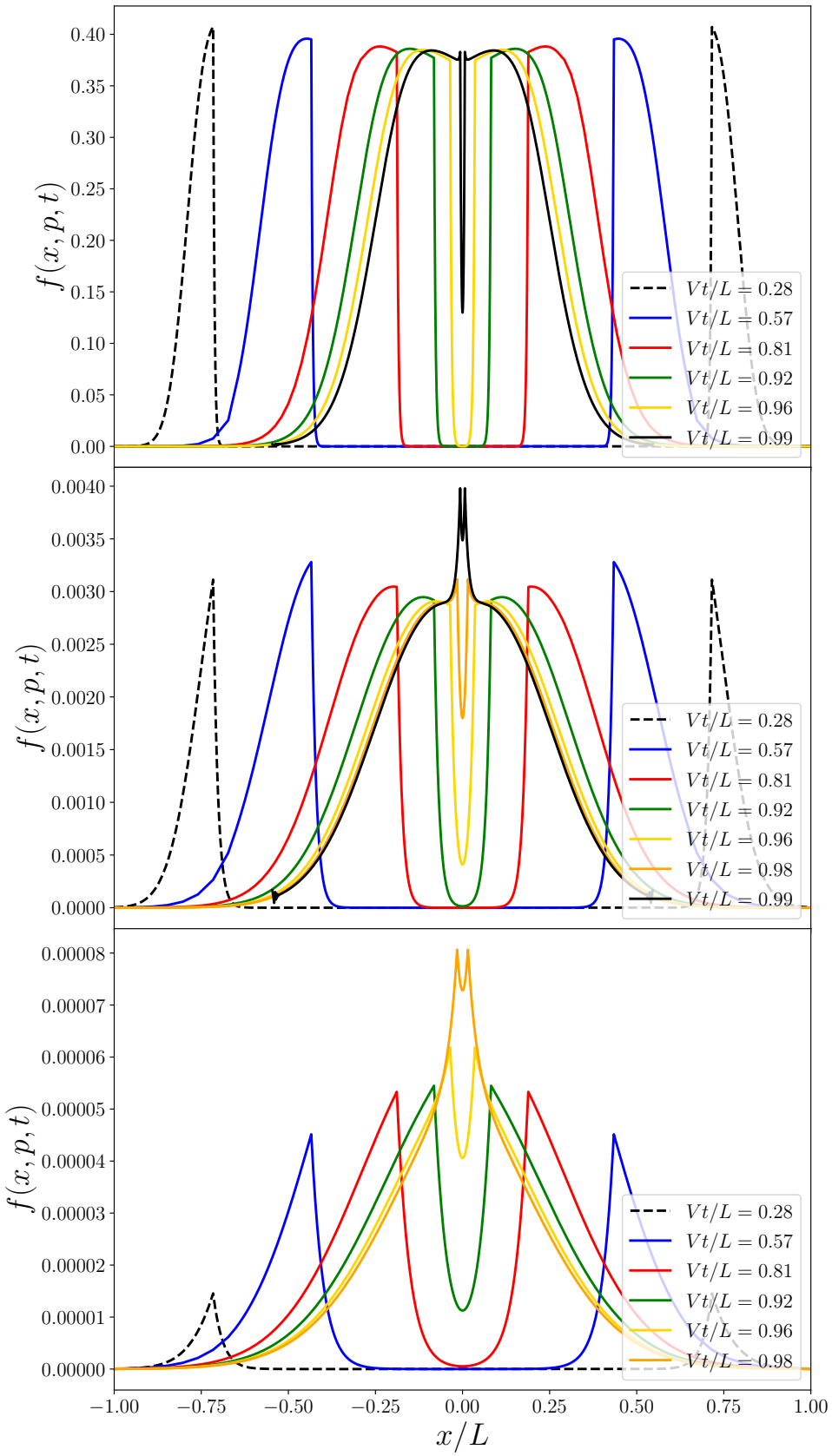

Figure 4.2: Spatial distribution of accelerated particles (arbitrary dimensionless units) for three different particle momenta, as given by the dimensionless parameter r_{eq} (Equation 4.11). From top to bottom: $r_{\mathrm{eq}} = 13$, $r_{\mathrm{eq}} = 3.7$, $r_{\mathrm{eq}} = 1.3$.

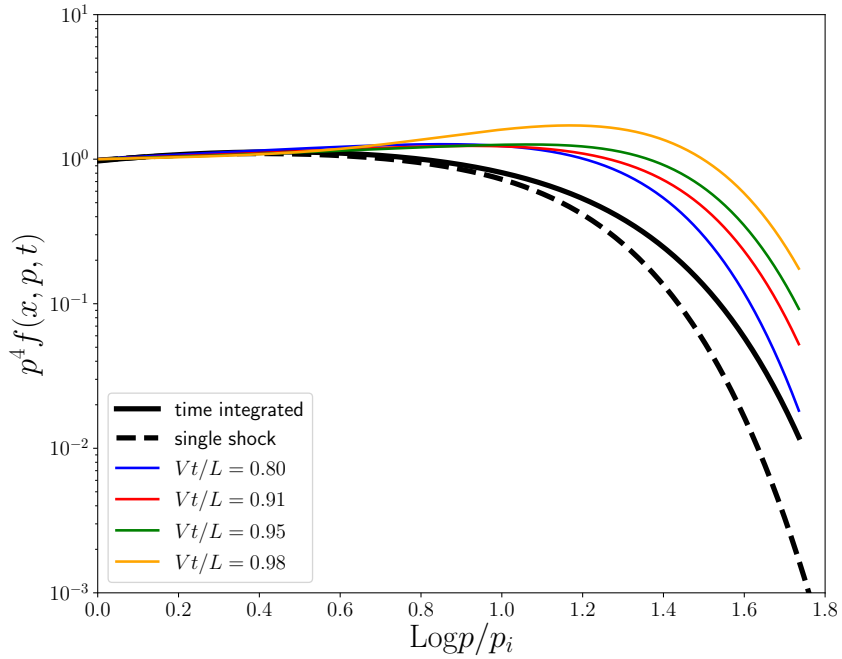

Figure 4.3: Spectra of accelerated particles at the shock location are shown with coloured thin lines for different times. The black solid line represents the spectrum of particles integrated over the entire volume at the time of shock collision (or, equivalently, the total spectrum of particles accelerated during the entire lifetime of the system). This is compared with the same quantity one would obtain for a single shock (dashed line).

the advection and injection at all momenta are less and less efficient, as the corresponding terms in the Equation scale as $1/(1+\tau)$. The reduced injection induces a suppression in the value of f at the shock, and the reduced advection makes particles less capable to reach large distances in the downstream region. This creates a "bump".

For high momenta ($r_{\rm eq} \sim 1$, bottom panel in Figure 4.2), the shocks become very close to each other before being able to accelerate a significant number of particles, and this explains the increase in time of the maximum of f. The double-peak feature visible at very late times has the same origin as in the top panel. The intermediate case $r_{\rm eq} \gtrsim 1$ is shown in the middle panel.

Figure 4.3 shows the particle spectra obtained at the shocks positions for different times, compared to the solution for a single shock. For small times and momenta, one recovers the canonical spectral index close to 4. However, at energies such that the diffusion length equals half the distance between the shocks, each shock begins to be fed by the other, such that there are more energetic particles around it: this is why, at times close to the collision, one sees a bump in the spectrum at high energies. The bump is averaged out when computing the time-integrated spectrum over the entire lifetime of the system (black solid line in Figure 4.3) but the shape of the cut-off is broader than what expected for particle acceleration at a single shock (black dashed line in Figure 4.3).

Apart from this shape modification at the high energy end of the time-integrated spectrum, we did not find any break in the spectrum, which remains very close to the canonical p^{-4} power law for all particle energies significantly smaller than the cutoff.

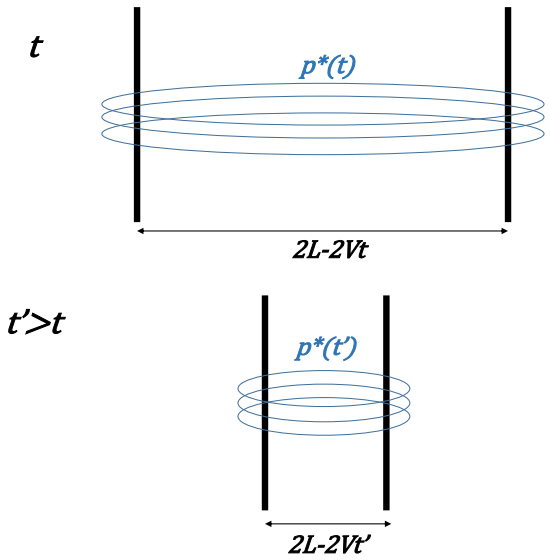

Figure 4.4: The cartoon shows the two shocks at different times. The thin blue lines represent the diffusion length of particles of a given momentum. One can see that particles of a given momentum $p^*(t)$ at a given time t behave like particles of lower momentum $p^*(t')$ at a later time t'.

4.4 Analytic approach

In this section we develop an approximate, analytic and self-similar model to describe the acceleration of particles at converging shocks. Here the analysis is restricted to the case of Bohm diffusion, $\kappa \propto p$. The generalisation to a generic turbulence spectrum is straightforward and can be found in Vieu et al. (2020) (Appendix A2).

4.4.1 The self-similarity hypothesis

Let us consider particle momenta that satisfy the condition $r_{\rm eq}(p) > 1$, where the parameter $r_{\rm eq}$, which was introduced in Section 4.2.2, takes values larger than unity when particles of energy p are accelerated at each one of the converging shocks before being affected by the presence of the other shock. In other words, particles reach a momentum p at each shock after an acceleration time $t_{\rm acc}(p)$ shorter than the time $t_c(p)$ when they begin to be affected by the presence of the other shock.

The top panel of the cartoon in Figure 4.4 represents the converging shock system at a given time t. By imposing $t_c(p) \sim t$ one can derive a momentum $p_*(t)$ such that particles of that energy begin at a time t to be affected by both shocks. The bottom panel of Figure 4.4 shows the system at a later time $t' > t$. This cartoon illustrates that particles of momentum $p_*(t')$ will be, at time t', in the very same situation as particles of larger momentum $p_*(t)$ at the earlier time t. Assuming Bohm diffusion, the two momenta are connected by the relation:

$$p_*(t') = \frac{L - Vt'}{L - Vt} p_*(t)\,. \tag{4.18}$$

The relation between momenta p_* at different times (Equation 4.18) is identical to that connecting the coordinate x of a point as seen from the new reference frame introduced

by Equation 4.2. Indeed, for a fixed value of the new spatial coordinate X the scaling is:

$$x(t') = \frac{L - Vt'}{L - Vt} x(t) \ . \tag{4.19}$$

This motivated us to search for a self-similar (scale invariant) solution of the acceleration problem, that mathematically translates into the requirement:

$$f(x, p, t) = \lambda^\alpha f(\lambda x, \lambda p, t_0) \ , \quad \lambda = \frac{L - Vt_0}{L - Vt} \ . \tag{4.20}$$

The property of self-similarity is further expected from the fact that the problem is characterised by a single parameter, K_0, as shown in Section 4.2. Indeed, this parameter contains both the time scale and the length scale, such that one should be able to replace the time evolution by a scale dilatation. Equation 4.20 can alternatively be understood as a generalisation of the condition of stationarity for a system of standing shocks. Indeed, in the limit $V = 0$, one retrieves $f(x, p, t) = f(x, p, t_0)$.

In order to determine the value of the parameter α it is convenient to compute the time derivative of $f(x, p, t)$ as given by Equation 4.20:

$$\partial_t f(x, p, t) = \frac{V}{L - Vt} \left(\alpha f\left(x, p, t\right) + x \partial_x f\left(x, p, t\right) + p \partial_p f\left(x, p, t\right) \right) \ . \tag{4.21}$$

We know that at any time, for any $p < p_*(t)$, i.e. for all particles that are not able to cross the upstream region separating the shocks, the solution should be the one obtained in the case of a single shock acceleration, which is time invariant and spatially constant in a region downstream of the shock of length $\ll Vt/4$. Under these circumstances Equation 4.21 reduces to:

$$\alpha f + p \partial_p f = 0 \ , \tag{4.22}$$

which shows that in order to recover the solution $f \sim p^{-4}$ for particles accelerated at a single shock the value of the parameter α must be equal to 4.

The numerical approach described in Section 4.3 allows to test the hypothesis of self-similarity. Figure 4.5 shows the results of our numerical computation for the particle distribution function f plotted at different times, with particle momenta and space coordinates rescaled as in Equations 4.18 and 4.19, and multiplied by λ^α (see Equation 4.20). For the highest resolution numerical calculation that we performed we found that the best match is obtained by setting $\alpha = 3.9$. The small discrepancy with respect to the analytic prediction ($\alpha = 4$) is most likely due to the numerical accuracy of our approach.

Figure 4.5 validates the hypothesis of scale invariance upstream. Indeed, all rescaled solutions collapse onto the same curve. The discrepancy downstream shows that the self-similarity hypothesis only holds at a finite distance from the shock. Indeed, as time increases, particles are advected further and further away, as it is the case for the acceleration at a single shock. The extension of the downstream tail is always time-dependent.

To be more quantitative, we plot in Figure 4.6 the distribution in the plane (x, t) of the following quantity:

$$\left| \lambda^\alpha f\left(\lambda x, \lambda p, t\right) - f\left(x, p, t_f\right) \right| / f\left(x, p, t_f\right) \ , \tag{4.23}$$

at four different momenta p, where $\lambda = (L - Vt)/(L - Vt_f)$. The quantity defined in Equation 4.23 measures the error between the distribution function obtained at time

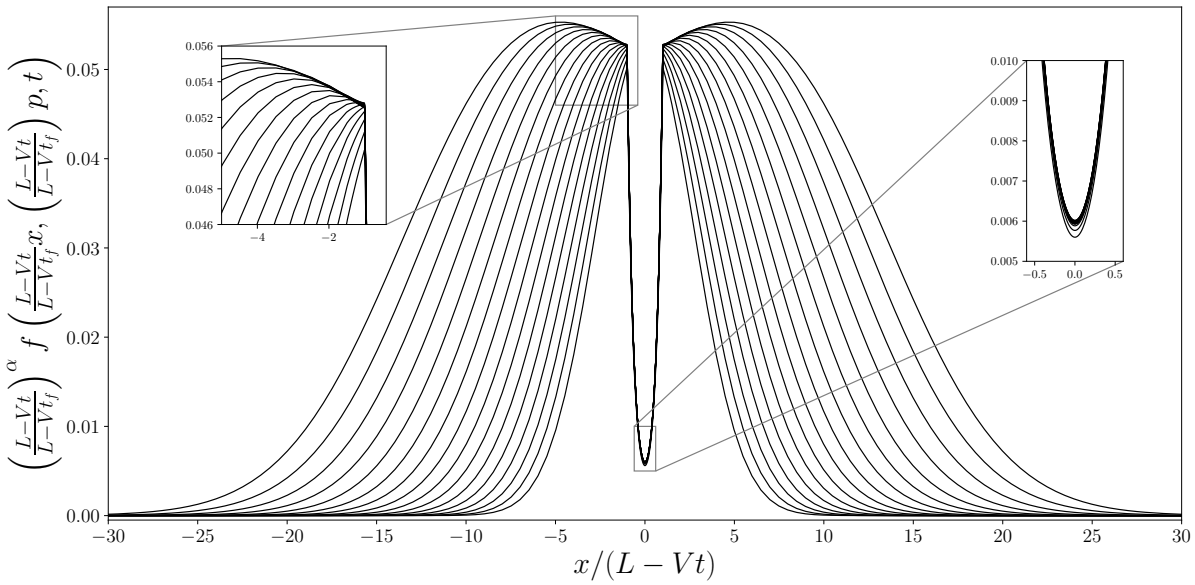

Figure 4.5: Spatial distribution of accelerated particles in rescaled coordinates (see text). Curves refer to different times between $Vt_i/L = 0.9$ and $Vt_f/L = 0.98$, and for a momentum at t_i equal to $p/p_i = 10$. The best match between solutions at different times is found for values of α gradually approaching $\sim$4 as we increase the resolution of the numerical scheme.

t_f after rescaling the solution at earlier time t by means of Equation 4.20, and the one directly computed numerically at time t_f. We show the result for $t_f = 0.98$, i.e. very close to the collision ($t_f = 1$). Figure 4.6 shows that the self-similarity hypothesis holds well upstream of the shock, as well as in a close region downstream. The agreement between the self-similar and the numerical solution is good whenever the energy-dependent criterion $r_{\rm eq} > 1$ is fulfilled (blue regions in the map).

At low times, the distance between the shocks is large, thus the rescaled momenta λp are high. In the case where the acceleration time is larger than the time considered, i.e. $r_{\rm eq} < 1$, the self-similar solution is not achieved (yellow regions in the map). In the limit of instantaneous acceleration (which would be analogous to assuming stationarity in the case of single shock acceleration), the self-similarity is expected to hold at any time for any momenta. In other words, the self-similar solution cannot account for the cutoff of the spectrum, while it is otherwise a very good approximation.

4.4.2 Time-dependent shock velocity

Although we derived it under simplifying assumptions, the hypothesis of self-similarity is very general and can account for a large variety of phenomena. One trivial generalisation consists in relaxing the assumption that the shocks propagate at a constant velocity. This could account for the deceleration of supernova remnant shocks. In this case, our previous rescaling arguments are still expected to be valid, except that $L - Vt$ should be replaced by $L - \int_0^t {\rm d}t' V(t')$. Here and in the following, to simplify notations we define:

$$\langle V \rangle_t \equiv \frac{1}{t} \int_0^t {\rm d}t' V(t') \,. \tag{4.24}$$

In particular, the rescaling factor λ is generalised to:

$$\lambda = (L - \langle V \rangle_{t_0} t_0)/(L - \langle V \rangle_t t) \,. \tag{4.25}$$

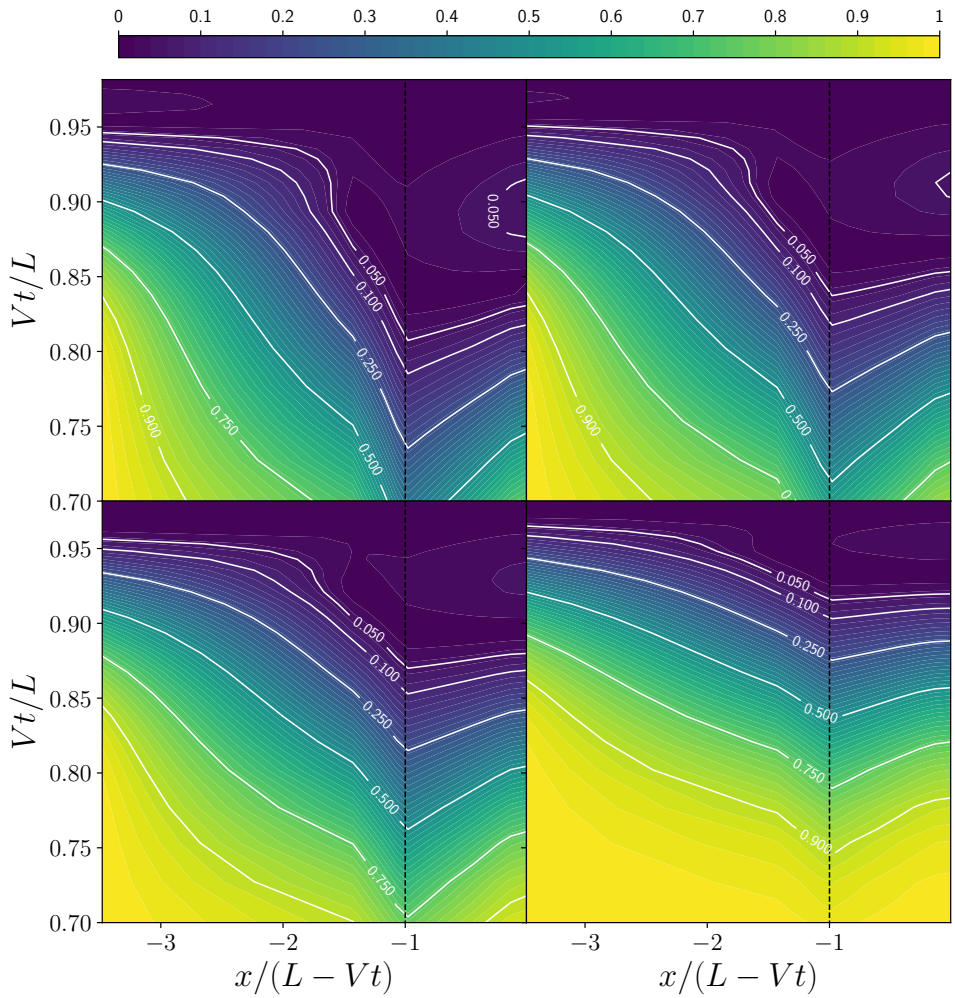

Figure 4.6: The colour scale refers to the value of the quantity defined in Equation 4.23, i.e. the discrepancy between the self-similar solution and the numerical one at a time $t_f = 0.98$ (see text for more details). The self-similar solution is computed rescaling the solution at an earlier normalised time Vt/L. The four panels (from top left to bottom right) refer to momenta equal to $p/p_i = 16,\ 19,\ 25,\ 40$ at the normalised time $Vt/L = 0.7$.

Other generalisations can be found in Vieu et al. (2020), in particular the extension to an arbitrary turbulence spectrum.

4.4.3 The self-similar transport equation

We can now substitute the rescaled solution for the particle distribution function f (Equation 4.20, with $\alpha = 4$) into the transport equation (Equation 4.1). We obtain the following *stationary*[1] differential equation:

$$4f + (X+U)\partial_X f - \tilde{K}\partial_X^2 f = \left(\frac{\partial_X U}{3} - 1\right) P\partial_P f + \tilde{Q}\delta(X \pm 1)\delta(P-1)\ , \qquad (4.26)$$

[1]The strength of the self-similarity hypothesis precisely lies in the fact that it allows a dynamical equation (with a term $\partial_t f$) to be written as a stationary equation with time-dependent parameters. The stationary equation can then be solved at any time to obtain the time-dependent solution.

where $X = x/(L - Vt)$, $P = p/p_i$, $\tilde{K} = \frac{K(P)L}{L-Vt}$, $\tilde{Q} = \left(\frac{L-Vt}{L-Vt_0}\right)^4 \frac{Q}{V}$. Note that the only physical parameter is the normalised diffusion coefficient $\tilde{K}$, so that the high energy limit is equivalent to $\tilde{t} \to 1$. This reflects the idea of self-similarity: at times close to the collision, particles of any energies cross both shocks within one diffusion length, as was the case earlier for particles of high energy only.

Assuming a power law for the distribution function $f \sim P^{-4\beta}$, Equation 4.26 reduces upstream (in between the shocks, $U = 0$) to:

$$4(1-\beta)f + X\partial_X f - \tilde{K}\partial_X^2 f = 0 \ . \tag{4.27}$$

The solution at the location of one shock (e.g. $X \to -1^+$) is expressed in terms of hypergeometric functions. Interestingly, these hypergeometric functions are divergent at small momenta or small times ($\tilde{K} \ll 1$) unless $\beta = 1$. We therefore retrieve the standard P^{-4} spectrum in this limit, as expected.

At a generic momentum, evaluating Equation 4.27 in $X = 0$ gives:

$$\beta = 1 - \frac{\partial_X^2 f|_0}{f_0}\frac{\tilde{K}}{4} < 1 \ . \tag{4.28}$$

The spectrum is therefore expected to be harder at high momenta (or equivalently late times), because both shocks contribute to the acceleration process. This is in agreement with the results of the numerical solution (see Figure 4.3): at high momenta, before the cut-off, the spectrum hardens. In order to derive a precise value for β, one needs to find $\partial_X^2 f|_0$, i.e. to solve Equation 4.26. Let us define $\xi \equiv 4(1-\beta)$ to simplify the notation. Equation 4.26 becomes:

$$\xi f + (X+U)\partial_X f - \tilde{K}\partial_X^2 f = -\frac{4\beta}{3}\partial_X U f \, , \tag{4.29}$$

where the injection has been omitted as we aim at probing high energy bands, the low energy solution being known asymptotically as the single shock power law. The solutions upstream ($U = 0$) and downstream ($U \neq 0$) read respectively, in the high energy limit $\tilde{K} \gg 1$:

$$f_u \sim f_0 \left(1 + \xi\frac{X^2}{2\tilde{K}}\right) \ , \tag{4.30}$$

$$f_d \sim \mathcal{C}_1 \left(1 + \frac{\xi(U+X)^2}{2\tilde{K}}\right) + \mathcal{C}_2 \frac{(U+X)}{\sqrt{\tilde{K}}} \frac{\Gamma\left(\frac{1+\xi}{2}\right)}{\Gamma\left(\frac{\xi}{2}\right)} \, , \tag{4.31}$$

where $\mathcal{C}_{1,2}$ are integration constants and Γ is the Euler gamma function. The asymptotic difference of the derivatives around the shock at $X = -1$ can then be computed as:

$$-\left[\partial_X f_u - \partial_X f_d\right]_{X=-1} \sim \frac{\xi f_0}{\tilde{K}} U + \frac{\mathcal{C}_2 \Gamma\left(\frac{\xi+1}{2}\right)}{\sqrt{\tilde{K}}\Gamma\left(\xi/2\right)} \ , \tag{4.32}$$

where we have imposed the continuity of f around the shock to express the constant $\mathcal{C}_1$ as function of $\mathcal{C}_2$ and f_0. Then, by integrating Equation 4.29 around the shock we get at first order in $1/\tilde{K}$:

$$\frac{\xi f_0}{\tilde{K}} U + \frac{\mathcal{C}_2' \Gamma\left(\frac{\xi+1}{2}\right)}{\sqrt{\tilde{K}}\Gamma\left(\xi/2\right)} \sim \frac{4U}{3\tilde{K}}\beta f_{-1} \sim \frac{4U}{3\tilde{K}}\beta f_0 \ , \tag{4.33}$$

which is valid for any (big) $\tilde{K}$, hence each order should vanish independently and we obtain $\beta = 3/4$, i.e. $f(p) \propto P^{-3}$, similarly to what was found by Bykov et al. (2013) in the steady-state description of converging shocks. At a given time, the system of colliding shocks produces a spectrum asymptotically flat $f(p) \propto P^{-4}$ at low momenta (because the low energy particles do not cross the upstream region), and an asymptotically hard spectrum at high momenta (because the high energy particles are accelerated by both shocks). The transition between both regimes typically occurs at $\tilde{K} \sim 1$, i.e. at the (time-dependent) momentum such that the diffusion length equals the (time-dependent) distance between the shocks.

In fact, a p^{-3} spectrum is never recovered in our numerical results due to the finite lifetime of the system. As a result, a cut-off appears in the spectrum before the asymptotic solution $f \sim p^{-3}$ can be established. This will be investigated further in Section 4.4.5.

The result obtained above can even be generalised to non symmetric situations (flows with different velocities). Indeed, it is always possible to move into the reference frame where the shock velocities are opposite (such that the self-similarity hypothesis can be used), at the price of a non zero plasma velocity upstream. However, one can show using a reasoning similar to that detailed above that the plasma velocity does not change the result in the limit of $\tilde{K} \gg 1$. This is physically expected: in this regime, particles are not much affected by the upstream flow.

Interestingly, a backward collision between two shocks (i.e. two shocks moving in the same direction with different speeds) have recently been investigated using a Monte-Carlo simulation by Wang et al. (2019), and a hardening of the cosmic ray spectrum was reported at high energies, in agreement with our findings. Conversely, our conclusions differ from an earlier claim from the same authors (Wang et al., 2017) that a collision between two shock fronts may induce a steepening in the spectrum of accelerated particles. This difference is likely due to the rather dubious setup considered in Wang et al. (2017).

4.4.4 Maximum energy

When a relativistic particle crosses a strong shock propagating at velocity V, its momentum is increased by $\Delta p = pV/(2c)$ (see Section 3.3). In a system of colliding shocks, the typical time between two crossings is the downstream diffusion time plus the minimum between the upstream diffusion time and the time it takes to travel from one shock to the other. However if the latter is much smaller than the former, then it is negligible compared to the downstream diffusion time. We have therefore three regimes: *(i)* large distance between the shocks, which implies that the particles wait two diffusion times between crossing the shocks; *(ii)* the distance between the shocks is of the order of two diffusion lengths; *(iii)* the distance between the shocks is negligible. We therefore obtain:

$$\Delta t \propto \frac{\xi\kappa}{V^2}\frac{\Delta p}{p}\,, \tag{4.34}$$

where the proportionality constant is 1 for case *(i)* and *(ii)* and 1/2 for case *(iii)*, and where ξ is a model-dependent number as defined in Equation 4.10. Assuming Bohm diffusion and constant shock velocities we can separate variables and integrate to get:

$$\begin{aligned} P_m &= \mathcal{I}(t)\,, \qquad \text{for cases } (i),\ (ii),\\ P_m &= P_c + \int_{t_c}^{t} \frac{2V}{LK_0\xi}\mathrm{d}t' = 2\mathcal{I}(t) - P_c\,, \qquad \text{for case } (iii), \end{aligned} \tag{4.35}$$

where t_c is the time at which $P_m = P_c = (\lambda K_0)^{-1}$, i.e. $t = t_c$ is the time of the transition from regime *(ii)* to regime *(iii)*. $\mathcal{I}(t)$ is defined by:

$$\mathcal{I}(t) \equiv 1 + \frac{1}{LK_0\xi}(t - t_0)V \sim \frac{1}{LK_0\xi}(t - t_0)V \ , \tag{4.36}$$

where we assumed $K_0 \ll 1$. This implies that t_c is solution of:

$$\frac{L - Vt_c}{(t_c - t_0)V} = \frac{L - Vt_0}{L\xi} \sim 0 \ , \tag{4.37}$$

where we assumed $\xi \gg 1$. Hence $t_c \sim L/V$ and we actually almost never see regime *(iii)*, such that one can set $P_m(t) \sim \mathcal{I}(t)$ at any time.

4.4.5 Time integrated spectrum of cosmic rays accelerated at converging shocks

In this section we seek an analytic expression of the time-integrated spectrum of cosmic rays accelerated at converging shocks. We propose the following approximate expression to describe the spectrum of accelerated particles at the shock position:

$$f \propto P^{-4}\left(1 + \frac{P}{P_c(t)}\right)\exp\left(\frac{-P}{P_m(t)}\right) \ , \tag{4.38}$$

where $P_c(t) = (\lambda K_0)^{-1}$ is the particle momentum such that $\tilde{K}(P_c) = 1$ (for particles of momentum P_c the diffusion length is equal to the distance between the two shocks). The expression above captures all of the features of the solution: the p^{-4} spectrum at low energies, the hardening to p^{-3} at high energies, and the cutoff at the maximum momentum $P_m(t)$ derived in the previous section.

We now integrate the instantaneous spectrum (Equation 4.38) over the entire time history of the accelerator. Performing the change of variable $w \equiv 1 - \lambda^{-1}$ leads to our final result:

$$S(p_0, p) = \frac{\mathcal{A}}{p_0}\left(\frac{p}{p_0}\right)^{-4}\int_0^1 \mathrm{d}w \left(1 + \frac{K(p)}{1 - w}\right)\exp\left(\frac{-K(p)}{K(p_0) + \frac{w}{\xi}}\right) \ , \tag{4.39}$$

where $K(p) = K_0 p/p_0$ and $\mathcal{A}$ is a normalisation constant. Plotting the function described in Equation 4.39 from a low initial momentum $p_0 \sim 1$ GeV, we retrieve a p^{-4} spectrum without any noticeable feature, in agreement with the numerical solution obtained in Section 4.3.2. This is because the ratio P_m/P_c, which drives the appearance of non-universal features at the end of the spectrum, increases too slowly. Otherwise stated, particles begin to be affected by both shocks only at the very end of the process. The spectrum for the case of two shocks moving at a constant speed is represented as a blue line in Fig. 4.7.

In fact, in a more realistic situation, the colliding shocks might not move at a constant speed, but rather decelerate. This is an interesting situation to be investigated because in this case particles would feel the effect of both shocks for a longer time. Assuming a self-similar evolution $V(t) = V_0\left(\frac{t}{t_0}\right)^{-\nu}$, the integrated spectrum can be computed as

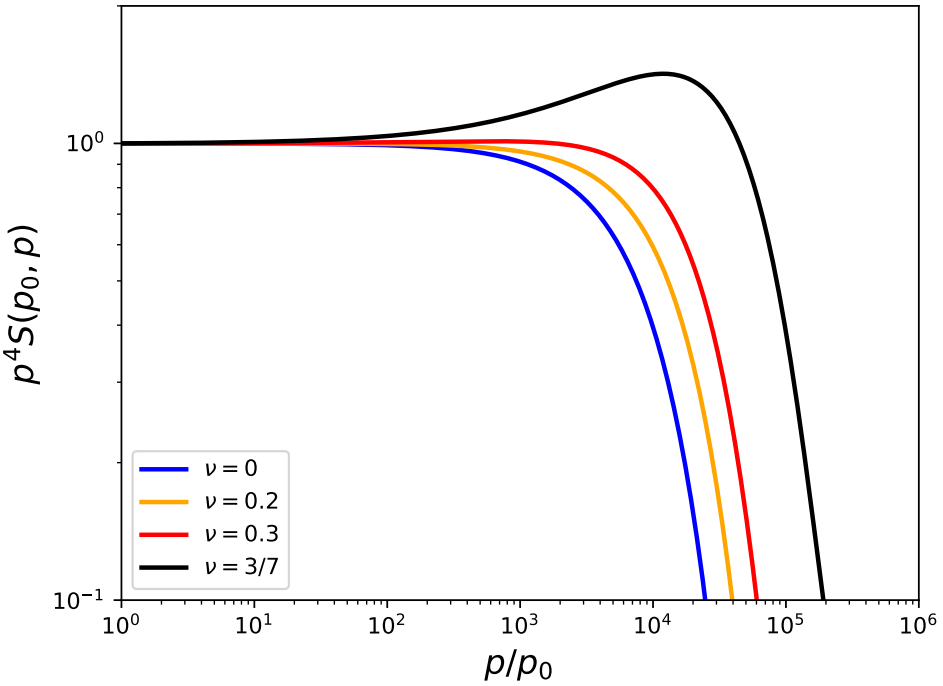

Figure 4.7: Time-integrated spectra of accelerated particles for $p_0 = 1$ GeV with $V(t) \propto t^{-\nu}$, for various values of ν, assuming Bohm diffusion. $K_0 = 10^{-6}$ ($\kappa_0 \sim 10^{20}$ cm^2/s at $p_0 = 1$ GeV (Bykov et al., 2013)), $\xi = 20$.

(Vieu et al., 2020):

$$S(p_0,p) = \frac{\mathcal{A}}{p_0}\left(\frac{p}{p_0}\right)^{-4}\int_0^1 \mathrm{d}w \left(1+\left(\frac{K(p)}{1-w}\right)\right) \times \exp\left(\frac{-\xi K(p)(1-2\nu)}{\xi K(p_0)(1-2\nu)+\chi^{\frac{\nu}{1-\nu}}((1-\nu)w)^{\frac{1-2\nu}{1-\nu}}-\chi}\right)\left(\frac{w\chi}{\chi+(1-\nu)w}\right)^{\frac{\nu}{1-\nu}}. \quad (4.40)$$

It is clear from Equation 4.40 that the exponent ν is the key parameter to see the peculiar features of the system of converging shocks. Indeed, higher values of ν give a bigger weight to values of w close to one, thanks to the last factor, and w close to one means late times.

Time-integrated spectra for various values of ν are shown in Figure 4.7. The value $\nu = 3/7$ is the scaling for a Type I supernova remnant in the free expansion phase according to Chevalier 1982. It is evident that the position of the spectral cutoff shifts to larger energies when ν increases, and above a certain value a small bump appears in the spectrum.

4.5 Spectrum of cosmic rays reaccelerated by converging supernovae shocks

Time-dependent colliding shocks do not provide strikingly unusual features on cosmic ray spectra, because particles do not have time to be accelerated up to the relevant energies before the end of the process. However, a more significant effect can be expected in the case of the reacceleration of pre-existing cosmic rays by colliding shocks, because then particles of high energies already exist at the beginning of the process.

In order to see how the system of converging shocks reaccelerates particles, we assume that at the time of the creation of the converging shocks, pre-existing cosmic rays have a standard p^{-4} spectrum with a maximum energy higher than the energy that could be reached by acceleration at the pair of colliding shocks (e.g. cosmic rays confined in a superbubble whose strong turbulence and intermittent supernovae explosions keep reaccelerating them up to PeV energies (Ferrand and Marcowith, 2010)). Results can be easily generalised to the case of a spectrum of preexisting particles different than p^{-4}.

Realising that Equation 4.40 is, up to a normalisation constant, the Green function of a system of self-similar converging shocks with time-dependent velocity, the reaccelerated spectrum can be computed according to:

$$f(p) = \int_{p_i}^{p} \mathrm{d}p_0 \left(\frac{p_0}{p_i}\right)^{-4} S(p_0, p) \ , \tag{4.41}$$

provided the normalisation constant of Equation 4.40 is adjusted numerically to impose the conservation of particles (i.e. $\int \mathrm{d}p\, S(p_0, p) = 1$). This convolution is similar to that derived in Section 3.6.2 in the case of the reacceleration by a single shock.

We set the injection $p_i = 10$ MeV and $K_0 = 10^{-6}$. The parameter ξ is set to 20 as expected assuming a homogeneous diffusion coefficient. The spectrum obtained from the reacceleration by colliding shocks (also including a fresh acceleration component) is plotted in red in the top panel of Figure 4.8, while the blue line shows for comparison the reacceleration by two isolated shocks which would last the same time as the collision time of the converging shocks. The bottom panel displays the corresponding spectral indices.

The system of colliding shocks pushes the particles of low energies (0.1 - 1 GeV) towards intermediate energies (10 - 100 GeV), up to the maximum energy which can be reached in the reacceleration process (limited by the finite acceleration time inherent to the time-dependency of the system of converging shocks). This leads to a well-known spectral hardening (Melrose and Pope, 1993; Cristofari and Blasi, 2019).

The maximum energy of the first bump (around 100 GeV) is due to the finite acceleration time of the system of colliding flows: freshly injected particles as well as low-energy preexisting particles are only accelerated up to the maximum energy derived in Section 4.4.4. Preexisting particles which already had the maximum energy will remain in the same energy band.

The second hardening starting around 10 TeV is due to the collective effect of the two shocks, which redistribute the high-energy particles in order to tend towards the asymptotic solution $f(p) \sim p^{-3}$. However, this asymptotic solution is not reached in our example, because the maximum energy of preexisting cosmic rays has been set to 10 PeV. Confining particles of higher energies is difficult to achieve in galactic astrophysical systems.

The resulting particle distribution is similar to the recently modelled spectrum of cosmic ray leptons escaping from the bow shock pulsar wind nebula of the millisecond pulsar PSR 0437–4715 (Bykov et al., 2019). This system is thought to be a site of efficient particle reacceleration in the colliding shock flow zone between the pulsar termination shock and the bow shock.

Although we show that reacceleration effects may be observable at high energies in physical systems where converging shocks appear, we point out that an important hypothesis must be made: that is, preexisting particles need to remain confined between the two converging shocks until their collision. This is not the case if, for instance, the colliding shocks have a much smaller spatial extension than the confining system. As the issue

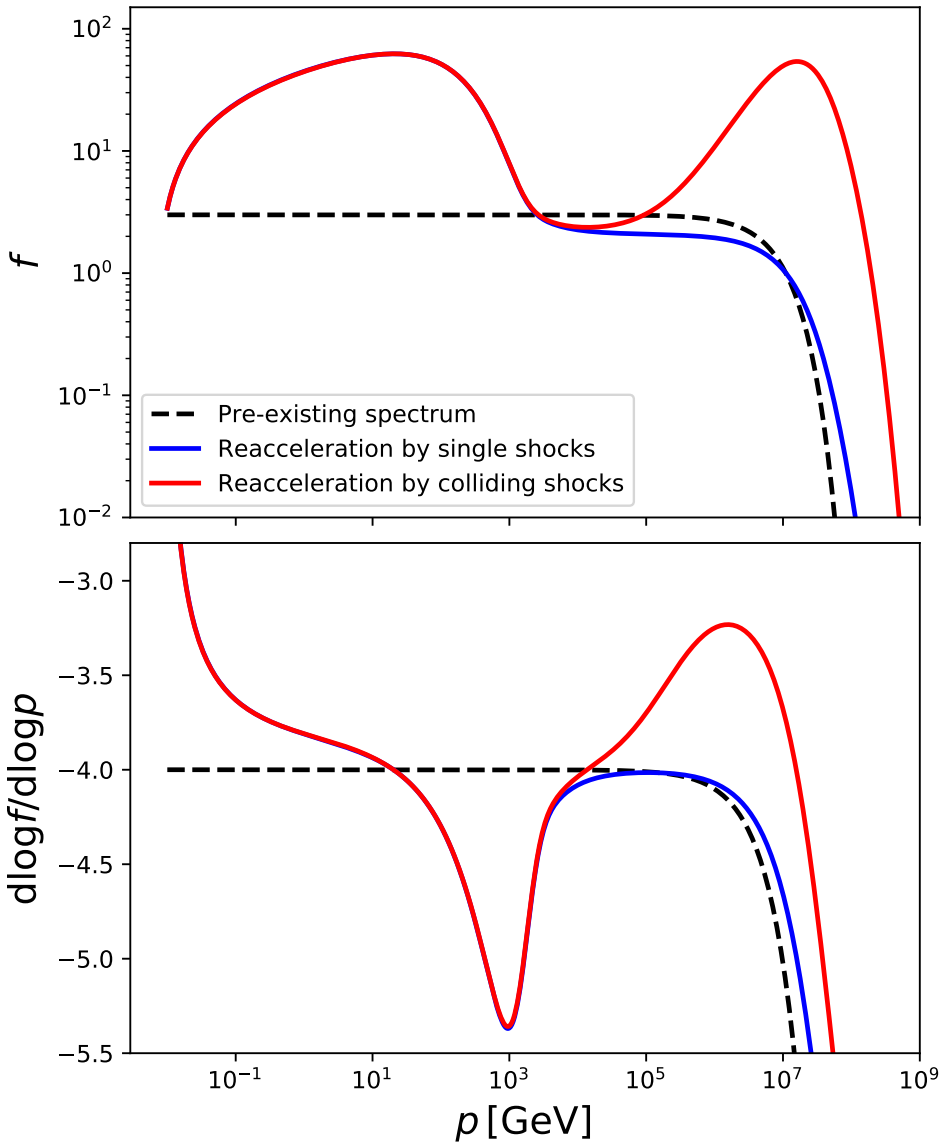

Figure 4.8: Spectrum reaccelerated by colliding shocks in comparison with reacceleration by single shocks.

of the confinement introduces a new scale in the problem, another quantitative analysis must be performed. Qualitatively, one expects that beyond the maximum energies that the second accelerator can confine, the preexisting spectrum $f(p) \sim p^{-4}$ should be recovered, while below this limit our results would still be valid. Whether this would erase the hard component at high energies or not depends on the properties of the accelerators. For supernovae expanding within superbubbles, there is a typical discrepancy of one order of magnitude between the maximum energy confined in the system and the maximum energy achieved due to the finite acceleration time (see the green curves in Figure 3.1). A slight hardening could be expected in this energy band, providing the high energy particles do not escape the region before their first acceleration and the subsequent reacceleration by colliding shocks.

4.6 Colliding winds

Let us eventually highlight a mathematical analogy between the self-similar transport Equation 4.26 and the transport equation describing a system of stationary standing shocks. We consider a converging *flow* where matter moves along the x axis with a velocity $\pm u_1$. At the positions $x = \pm x_s$ matter will flow across two stationary shocks. Such a configuration was considered by Siemieniec-Ozieblo and Ostrowski (2000) to describe the accretion of matter onto cosmological sheets, such as the local Supercluster plane. It could also describe in an approximate manner the region of collision of two stellar winds (see e.g. Reimer et al., 2006).

In the downstream region between the two shocks Siemieniec-Ozieblo and Ostrowski (2000) considered a linear profile for the velocity, $u_2(x) = -u_1 x/(4x_s)$. Following Reimer et al. (2006) we also add, between the two shocks, a sink term for particles. This might be due to an advective motion of the shocked plasma along a direction orthogonal to the x axis (see Reimer et al., 2006; Grimaldo et al., 2019, for further details). For simplicity, we assume the sink term to be proportional to the particle number density. Under these conditions the stationary transport equation for accelerated particles between the two shocks can be written in a way which is very similar to Equation 4.26:

$$4\frac{f}{\theta} - X\partial_X f - \partial_X[K\partial_X f] = -\frac{P}{3}\partial_P f + \tilde{Q}\delta(X \pm 1)\delta(P-1)\,, \tag{4.42}$$

where $X = x/x_s$, $K = 4\kappa/(x_s u_1)$, $\tilde{Q} = 4Q/(u_1 p_i)$, $\theta = \tau u_1/x_s$. Here, θ accounts for particle escape, τ being an energy independent escape time.

Assuming a homogeneous diffusion coefficient and a power law spectrum $P\partial_P f = -4\beta f$, the above equation can be solved to give the particle distribution function in the downstream region:

$$f_d = {}_1F_1\left(\frac{2\beta}{3} - \frac{2}{\theta}; \frac{1}{2}; -\frac{X^2}{2K}\right) f_0 \sim f_0\left(1 + \left(\frac{2}{\theta} - \frac{2\beta}{3}\right)\frac{X^2}{K}\right)\,, \tag{4.43}$$

where ${}_1F_1$ indicates the confluent hypergeometric function of the first kind.

Upstream, the velocity profile being constant, one retrieves the standard exponential suppression:

$$f_u = f_s \exp\left(\frac{4}{K}(X+1)\right)\,. \tag{4.44}$$

Finally, flux conservation at each shock surface provides, for $K \gg 1$ (high energy limit):

$$-4\beta = -3\left(1 + \frac{1}{\theta}\right)\,, \tag{4.45}$$

which shows that the solution $f(p) \propto p^{-3}$ is the hardest possible spectrum one can get, recovered only in the limiting case of infinite escape time. The solutions obtained by Siemieniec-Ozieblo and Ostrowski (2000) and Bykov et al. (2013) belong to this category. For finite values of θ the spectrum is always steeper than p^{-3}, and the spectral slope increases monotonically as θ decreases.

The escape time may depend on the particle energy, for instance if it is diffusive. In this case, the exponent given by Equation 4.45 is only an approximation of the local slope of the spectrum for a given ratio of the escape time over the advection time x_s/u_1. This is very similar to the solution derived in Section 2.3 for the stochastic acceleration

in small-scale turbulence (Fermi II). A realistic spectrum of particles accelerated around standing shocks is therefore qualitatively expected to display three components. In low energy bands particles diffuse around single shocks and should be distributed along a standard p^{-4} spectrum. At intermediate energies such that $4\kappa > x_s u_1$, i.e. the diffusion length is larger than the distance between the shocks, and $\tau > 3x_s/u_1$, i.e. the escape time is larger than the time it takes to diffuse from one shock to the other, the spectrum is expected to harden, although it is not likely that the asymptotic p^{-3} solution will be achieved. Indeed, as the momentum is further increased, the escape time will decrease and the spectrum will steepen, eventually displaying a bump beyond which the escape is expected to induce an exponential suppression as $\theta \ll 1$. This is very similar to the result that we obtained in the case of converging shocks, where the hardening was limited by the collision time. In standing shocks, although the hardening is limited by the geometry, the escape time is analogous to the collision time. Note that the crucial parameter is always the distance between the shocks, x_s. A more careful analysis of the situation is left for future work.

4.7 Summary

In an attempt to solve analytically the time-dependent problem of particle acceleration in a system of colliding shocks, we found that the spectrum of accelerated particles follows quite closely the canonical p^{-4} prediction of diffusive shock acceleration at a single shock, except at the highest particle energies, where a hardening appears, originating a bumpy feature just before the exponential cutoff. However we showed that this hardening is only asymptotic and not realised when the time-dependency of the collision is properly accounted for. Indeed the finite time available before the shock collision does not allow the formation of the asymptotic p^{-3} solution provided by earlier claims. We also recall that the maximum energy is not expected to increase by more than a factor of two compared to the case of acceleration at a single shock (see also Lieu and Axford, 1990).

Nevertheless the mathematical formalism developed in this chapter is very general and the approach can be used to solve a variety of connected problems. We have shown in particular how it applies in a system of standing shocks in converging flows (e.g. wind-wind collisions), accounting for the escape of the particles in between the shocks. When no escape is allowed, one recovers the asymptotic solution $f \propto p^{-3}$, in agreement with Bykov et al. (2013). This is the hardest possible solution of the problem. If the escape is independent of the energy of the particles, for instance if it is due to a perpendicular advection in large-scale flows, the resulting particle spectra are power laws in energy, with a slope that depends on how effectively particles can escape the acceleration region. In the case where the escape is energy-dependent, the spectrum is qualitatively expected to display a bump at intermediate energies and to be exponentially suppressed at high energies.

We have further used our formalism to investigate the effect of the reacceleration of preexisting cosmic rays by a system of two shocks. We found that under certain conditions non-universal spectral features can appear in the cutoff region. The analysis of particle reacceleration by multiple shocks is the purpose of the next chapter.

References

Bykov, A. M., Gladilin, P. E., and Osipov, S. M. (Mar. 2013). "Non-linear model of particle acceleration at colliding shock flows". In: MNRAS 429.3, pp. 2755–2762. DOI: 10.1093/mnras/sts553.

Bykov, A. M. et al. (Oct. 2015). "Ultrahard spectra of PeV neutrinos from supernovae in compact star clusters". In: MNRAS 453.1, pp. 113–121. DOI: 10.1093/mnras/stv1606.

Bykov, A. M. et al. (2019). "GeV-TeV Cosmic Ray Leptons in the Solar System from the Bow Shock Wind Nebula of the Nearest Millisecond Pulsar J0437-4715". In: *Astrophys. J.* 876.1, p. L8. DOI: 10.3847/2041-8213/ab1922.

Chevalier, R. A. (July 1982). "Self-similar solutions for the interaction of stellar ejecta with an external medium." In: ApJ 258, pp. 790–797. DOI: 10.1086/160126.

Colburn, D. S. and Sonett, C. P. (June 1966). "Discontinuities in the Solar Wind". In: Space Sci. Rev. 5.4, pp. 439–506. DOI: 10.1007/BF00240575.

Cristofari, P. and Blasi, P. (Oct. 2019). "Gamma-rays from reaccelerated particles at supernova remnant shocks". In: MNRAS 489.1, pp. 108–115. DOI: 10.1093/mnras/stz2126.

Drury, L. O. (July 1991). "Time-dependent diffusive acceleration of test particles at shocks". In: MNRAS 251, pp. 340–350. DOI: 10.1093/mnras/251.2.340.

Drury, L. O. (Aug. 1983). "An introduction to the theory of diffusive shock acceleration of energetic particles in tenuous plasmas". In: *Reports on Progress in Physics* 46.8, pp. 973–1027. DOI: 10.1088/0034-4885/46/8/002.

Ferrand, G. and Marcowith, A. (Feb. 2010). "On the shape of the spectrum of cosmic rays accelerated inside superbubbles". In: A&A 510, A101, A101. DOI: 10.1051/0004-6361/200913520.

Grimaldo, E. et al. (Jan. 2019). "Proton Acceleration in Colliding Stellar Wind Binaries". In: *The Astrophysical Journal* 871.1, p. 55. DOI: 10.3847/1538-4357/aaf6ee.

Kobayashi, S., Piran, T., and Sari, R. (Nov. 1997). "Can Internal Shocks Produce the Variability in Gamma-Ray Bursts?" In: ApJ 490, p. 92. DOI: 10.1086/512791.

Lieu, R. and Axford, I. W. (1990). "Cosmic Ray Acceleration in Colliding Shock Fronts". In: *International Cosmic Ray Conference* 4, p. 105.

Melrose, D. B. and Pope, M. H. (Jan. 1993). "Diffusive Shock Acceleration by Multiple Shocks". In: *Proceedings of the Astronomical Society of Australia* 10.3, p. 222.

Reimer, A., Pohl, M., and Reimer, O. (June 2006). "Nonthermal High-Energy Emission from Colliding Winds of Massive Stars". In: *The Astrophysical Journal* 644.2, pp. 1118–1144. DOI: 10.1086/503598.

Romoli, C., Taylor, A., and Aharonian, F. (2017). "Cut-off characterisation of energy spectra of bright fermi sources: Current instrument limits and future possibilities". In: *Astroparticle Physics* 88, pp. 38–45. ISSN: 0927-6505. DOI: https://doi.org/10.1016/j.astropartphys.2016.12.007.

Siemieniec-Ozieblo, G. and Ostrowski, M. (Mar. 2000). "On energy spectra of UHE cosmic rays accelerated in supergalactic accretion flows". In: A&A 355, pp. 51–55.

Spada, M. et al. (Aug. 2001). "Internal shocks in the jets of radio-loud quasars". In: MNRAS 325.4, pp. 1559–1570. DOI: 10.1046/j.1365-8711.2001.04557.x.

Vieu, T., Gabici, S., and Tatischeff, V. (May 2020). "Particle acceleration at colliding shock waves". In: MNRAS 494.3, pp. 3166–3176. DOI: 10.1093/mnras/staa799.

Wang, X. et al. (2017). "Particle Acceleration in Two Converging Shocks". In: *The Astrophysical Journal* 842.2, p. 74. DOI: 10.3847/1538-4357/aa750f.

Wang, X. et al. (Oct. 2019). "Particle Acceleration at the Pileup Collision of the Twin Shock". In: *The Astrophysical Journal* 885.1, p. 66. DOI: 10.3847/1538-4357/ab4655.

Chapter 5

Particle acceleration by multiple shocks

This chapter investigates the acceleration of cosmic rays in presence of multiple shocks. Multiple shock acceleration is thought to take place for instance in chaotic winds (White, 1985), accretion disks (Spruit, 1988; Achterberg, 1990), galaxy clusters (Kang, 2021) and superbubbles. In the latter, young clusters are indeed expected to inject a consequent amount of energy in large-scale hydrodynamic flows confined in relatively compact bubbles, which will produce an ensemble of stochastic shocks. Then, supernovae are expected to explode at nearly regular intervals and collectively reaccelerate the particles confined in old superbubbles. These two aspects will be reviewed in Sections 5.1 and 5.2, respectively. Although most of the previous works analysed the test-particle case, we show that the acceleration is generally so efficient that the backreaction of the particles onto the shocks must be taken into account. A nonlinear model is therefore developed in Section 5.3 and then applied to various situations.

5.1 Particle acceleration in supersonic turbulence

The theory of particle transport in a plasma characterised by a strong supersonic turbulence, i.e. a stochastic distribution of shock fronts on top of smooth perturbations, was developed by Bykov and Toptygin (Bykov and Toptygin, 1990; Bykov and Toptygin, 1993) using nonperturbative averaging methods (see also Achterberg, 1990). We define κ the local diffusion coefficient of the particles which scatter on the small-scale turbulence between the shocks, u the root mean square velocity of the stochastic shocks, L the mean distance between the fronts, which is also identified as the largest turbulence scale. For traditional regimes of small-scale turbulence (e.g. Kolmogorov or Kraichnan), the diffusion coefficient is expected to be an increasing function of the momentum of the particles, as shown in Section 2.2.6. Denoting p_* such that $\kappa(p_*)/u = L$, particles with $p < p_*$ will be accelerated around individual fronts while particles with $p > p_*$ will experience an ensemble of shock fronts within one diffusion length, such that the shocks will be viewed as perturbations. The characteristic momentum p_* can also be understood using timescales: if the acceleration time at shocks κ/u^2 (see the discussion in Section 3.5 and Equation 3.24) is much smaller than the advection time L/u, the particle distribution function is expected to peak around the shocks, with a spatially intermittent structure.

5.1.1 High momenta

Let us first consider the case $\kappa/u \gg L$. Because high energy particles experience the ensemble of stochastic shocks as small-scale perturbations, the transport equation takes the following simple form for a spatially isotropic distribution function (Achterberg, 1990; Bykov and Toptygin, 2001):

$$\partial_t f = \nabla \cdot (D \cdot \nabla f) + \frac{1}{p^2} \partial_p p^2 D_{pp} \partial_p f \,, \quad D_{pp} = \frac{u^2 p^2}{9\kappa} \,. \tag{5.1}$$

This equation is nothing but Equation 2.60, the transport equation in small-scale turbulence in the absence of large-scale motions. The interplay between the energy gained at shock fronts and the propagation in the rarefaction regions in between the fronts leads to a diffusion in momentum space analogous to the stochastic acceleration (Fermi II) process discussed in Section 2.3. If the particles diffuse on scales larger than the mean distance between two shocks, their distribution function is expected to be nearly spatially uniform and can be averaged to get Equation 2.61, which I reproduce there:

$$\partial_t f = -\frac{f}{\tau_{esc}} + \frac{1}{p^2} \partial_p p^2 D_{pp} \partial_p f \,, \tag{5.2}$$

where τ_{esc} is the typical time it takes for a particle to escape the region. A major difference between a strong hydrodynamic supersonic turbulence in contrast with the magnetised turbulence considered in Chapter 2 is that the mean free path Λ of high energy particles is a constant equal to the mean distance between the stochastic fronts (which is the correlation length of the supersonic turbulence). This implies that the diffusion coefficient of relativistic particles, $\kappa \sim \Lambda c$, is independent of momentum, and the stochastic acceleration time $\tau_{acc} \equiv p^2/D_{pp} = \frac{9\kappa}{u^2}$ as well. As derived in Section 2.3, the stationary solution to Equation 5.2 is a simple power law, $f(p) \propto p^{-\beta}$, with $\beta = 3/2 + 3/2\,(1 + 4\tau_{acc}/(9\tau_{esc}))^{1/2}$.

5.1.2 Low momenta

In the low momentum regime $\kappa/u \ll L$, the particles experience strong inhomogeneities. The distribution function is expected to be spatially intermittent, peaking near the shocks, and the problem cannot be tackled within a perturbative approach.

In the regions between the shock fronts, the particles diffuse on small-scale hydromagnetic waves, are advected by large-scale motions and accelerated in flow inhomogeneities. The relevant transport equation was derived in Section 3.6.1 (Equation 3.19) as:

$$\partial_t f + \boldsymbol{u} \cdot \nabla f - \frac{p}{3} (\nabla \cdot \boldsymbol{u}) \, \partial_p f = \nabla \cdot (D \cdot \nabla f) + \frac{1}{p^2} D_{pp} \partial_p f \,. \tag{5.3}$$

One diffusion length away from any shock fronts, the distribution function is nearly homogeneous: $f \approx \bar{f}$, where $\bar{f}$ denotes the average of f over all scales from the diffusion length to the distance separating the fronts. On the other hand, close to the shocks the distribution function is obtained by integrating the transport equation around the discontinuity with the boundary condition $f_\infty = \bar{f}$ far away from the front. This amounts to *reaccelerate* the distribution function as was solved in Section 3.6.2 (Equation 3.22). Defining for convenience the reacceleration operator as:

$$\mathcal{R}[\bar{f}](p) = s \int^p \frac{\mathrm{d}p'}{p'} \left(\frac{p}{p'}\right)^{-s} \bar{f}(p') \,, \quad s = \frac{3r}{r-1} \,, \tag{5.4}$$

the distribution function around the stochastic shocks can be approximated as (see the discussion at the beginning of Section 3.6.2):

$$f(z,p) = \begin{cases} \bar{f}(p) + \left(\mathcal{R}[\bar{f}](p) - \bar{f}(p)\right) e^{\frac{\Delta u}{\kappa} z} & \text{upstream}\,, \\ \mathcal{R}[\bar{f}](p) & \text{downstream}\,. \end{cases} \tag{5.5}$$

Let us now average the above equations over the intermediate scales (larger than the diffusion length but smaller than the distance between the fronts), in order to get a consistent equation describing the transport of the low-energy particles around the shocks. Denoting Δ the intermediate scales, the average quantities are computed as:

$$\bar{X} = \frac{1}{\Delta} \sum_i \int_{z_i - \Delta/2}^{z_i + \Delta/2} \mathrm{d}z\, X\,, \tag{5.6}$$

where the sum runs over all shock fronts located at positions z_i. The quantity X can stand for the velocity field, the distribution function, the diffusion coefficient etc. The result of the averaging procedure is computed as (Bykov and Toptygin, 1990):

$$\partial_t \bar{f} + \bar{\boldsymbol{u}} \cdot \nabla \bar{f} = \nabla \cdot \left(\bar{D} \cdot \nabla \bar{f}\right) + \frac{p}{3} \left(\nabla \cdot \bar{\boldsymbol{u}}\right) \partial_p \bar{f} + \sum_i \frac{\Delta u_i}{3\Delta} \hat{L} \bar{f}\,, \tag{5.7}$$

where we have introduced the "stochastic reacceleration operator" $\hat{L}$ defined as:

$$\hat{L}\bar{f} \equiv \frac{1}{3p^2} \partial_p p^{3-s} \int^p \mathrm{d}p' p'^s \partial_p \bar{f}\,. \tag{5.8}$$

This operator emerges naturally from the integration by parts of the reacceleration operator $\mathcal{R}$. In the above, we assumed for simplicity that the velocity jump were the same at all shocks and we disregarded the stochastic acceleration in small-scale turbulence since it is much less efficient than the first order acceleration process around shocks.

Now that we have averaged the transport equation around the local discontinuities, the next and last step is to average it further over the largest turbulence scale. Assuming that the stochastic acceleration of the particles in the velocity perturbations is weak, the averaging can be done perturbatively. A careful analysis provides the following result (Bykov and Toptygin, 1990; Bykov and Toptygin, 1993):

$$\partial_t \langle \bar{f} \rangle + \frac{\langle \bar{f} \rangle}{\tau_{esc}} = \left(\frac{1}{\tau_{sh}} + B \left(1 + 2 \frac{p}{3} \partial_p \right) \right) \hat{L} \langle \bar{f} \rangle + A \hat{L}^2 \langle \bar{f} \rangle + \frac{1}{p^2} \partial_p p^4 D \partial_p \langle \bar{f} \rangle\,, \tag{5.9}$$

where the transport coefficients τ_{esc}, A, B and D, defined in Bykov and Toptygin (1990), are computed as function of the properties of the supersonic turbulence. In particular the correlations between the random velocities determine the escape time τ_{esc} as well as the hydrodynamic momentum diffusion coefficient D, the correlations between the shock fronts determine the "reacceleration coefficient" A, and the correlations between the compression and rarefactions of the flow determine the "compression coefficient" B. Eventually $\tau_{sh} = L/u$ is the characteristic "reacceleration time", i.e. the time interval between two shock reaccelerations. Equation 5.9, which I shall refer to as the *Bykov-Toptygin transport equation*, therefore describes the reacceleration around shocks, the decompression in between reaccelerations, as well as the stochastic reacceleration (Fermi II) in large-scale turbulence which, as seen in the previous subsection, drives the transport of high energy particles. The integro-differential form of Equation 5.9 reveals the non-perturbative

character of the transport of low energy particles in strong turbulence. Eventually the transport coefficients can be renormalised in order to consistently describe the strong turbulence regime (Bykov and Toptygin, 1993).

Assuming that the first order acceleration around shocks is much more efficient than the stochastic acceleration, it can be shown that the Bykov-Toptygin transport equation admits the time-dependent solution $\langle \bar{f} \rangle \propto p^{-3}$ for $p \ll p_t = p_0 \exp(t/((s-3)\tau_{sh}))$ and $\langle \bar{f} \rangle \propto p^{-s}$ for $p \gg p_t$ (Bykov and Fleishman, 1992; Bykov, 1999). This provides the stationary solution $f(p) \propto p^{-3}$. In this limit case the model is in fact very similar to that of Klepach et al. (2000), who considered the transport of cosmic rays in stochastic winds (see their Equations 17-19). However Bykov (2001) showed that the shock reacceleration process is so efficient that the energy of the particles becomes comparable to the energy of the large-scale motions after a few "reacceleration times". This calls for a nonlinear treatment of the problem. By considering the damping of the large-scale turbulence induced by cosmic ray acceleration, Bykov (2001) recovered a standard p^{-4} spectrum at late times. Although this is a simple way to achieve a self-consistent model, one should keep in mind that turbulence damping is only an approximate description of the backreaction of the particles on the fluid. In particular, it does not account for the spatial inhomogeneities which are expected to develop upstream of nonlinear shocks under the form of precursors (see Section 3.7). We have seen that these precursors may drastically change the acceleration mechanism and produce non-universal concave spectra. Bykov and Toptygin (1993) mentioned that the effect of precursors could be rendered phenomenologically (see the end of their Section 7.2) although I am not aware of any work applying it to an astrophysical environment. Finally, one must realise that the derivation of the Bykov-Toptygin transport equation 5.9 relied on the Green function formalism, which is only applicable if the superposition principle holds. This is restricted to the linear regime. Extending the above formalism to incorporate a nonlinear reacceleration operator is far from being straightforward.

5.1.3 Supersonic turbulence in superbubbles

Eventually, the model by Bykov, Fleishman and Toptygin can be applied to a variety of realistic environments. Bykov (2001) (see also Bykov, 1997) considered the acceleration of cosmic rays in young superbubbles. It is argued that in the first few million years, the stellar feedback produces a strong supersonic turbulence in the bubble interior, in particular because of shock interactions: when two strong shock waves collide, they cascade into weaker shocks. These secondary shocks are the constituent of the supersonic turbulence, with a mean separation of a few parsecs and velocities of the order of 1000 km/s. Under these circumstances, a change in the acceleration regime is expected to occur at the characteristic momentum p_* such that $\kappa(p_*) \approx 10^{26} - 10^{27}$ cm^2/s, i.e.:

$$p_* \sim \left(\frac{10^{26} - 10^{27} \text{ cm}^2/\text{s}}{\kappa_{\text{GeV}}} \right)^{\frac{1}{2-q}} \text{ GeV} , \tag{5.10}$$

where κ_{GeV} is the diffusion coefficient at 1 GeV and q the spectral index of the turbulence. Using Equation 2.57, one can estimate the diffusion coefficient in the small-scale

turbulence as:

$$\kappa_{\rm GeV} = 10^{27}\,\eta^{-1}\left(\frac{L}{10\ {\rm pc}}\right)^{2/3}\left(\frac{B_0}{10\ \mu{\rm G}}\right)^{-1/3}\ {\rm cm}^2/{\rm s}\quad \text{for } q = 5/3\,, \tag{5.11}$$

$$\kappa_{\rm GeV} = 4\times10^{21}\,\eta^{-1}\left(\frac{B_0}{10\ \mu{\rm G}}\right)^{-1}\ {\rm cm}^2/{\rm s}\qquad \text{for } q = 1\,, \tag{5.12}$$

where $\eta \sim (\delta B_0/B_0)^2 \sim 1$ is the turbulence level. This provides $p_* \approx 1$ GeV for Kolmogorov turbulence, an estimate similar to that obtained in Bykov et al. (2020). On the other hand, assuming a Bohm diffusion regime possibly provides a transition momentum as high as $0.1 - 1$ PeV. Bykov (2001) pointed out that this could explain the "knee" in the diffuse cosmic ray spectrum observed near Earth. The spectral index at momenta $p > p_*$ is driven by the ratio of the stochastic acceleration time and the escape time, $\tau_{acc}/\tau_{esc} = 9\kappa/(u^2\tau_{esc}) = 54\kappa^2/(u^2R^2)$, where R is the radius of the superbubble. From the estimate derived above in the case of Bohm diffusion and assuming that after a few million years a superbubble has a typical radius of about 50 pc (see Equation 1.7), we eventually get $\tau_{acc}/\tau_{esc} \approx 4$ and thus $f(p > p_*) \propto p^{-\beta}$ with $\beta = 4 - 5$. This means that one would indeed expect a steepening at the break energy with a slope in qualitative agreement with the observations, even though the model is not very predictive for the final result strongly depends on the properties of the magnetic fields, the large-scale flows and the geometry of the superbubble (which depends in particular on the mechanical power of the cluster). It is also crucial to keep in mind that this spectral break relies on the assumption that the mean free path is constant above the break energy, which is only expected if the medium is spanned by an ensemble of stochastic shocks. A simple energetic argument comparing the mechanical power of the stars and supernovae with the turbulent energy density shows that after a few million years, the mechanical input is diluted within the (expanding) superbubble to the point where the root mean square velocity of the perturbations is subsonic. In this case, even particles of the highest energies will diffuse on smooth perturbations with an energy-dependent mean free path, in such a way that the ratio of the stochastic acceleration time over the escape time will increase rapidly as function of the energy. In this case, the stochastic reacceleration will be exponentially suppressed and one should expect a spectrum similar to that displayed in Figure 2.1, with a "Fermi II bump" at low energies and a power law at high energies due to the diffusive shock acceleration at winds and supernovae (Ferrand and Marcowith, 2010).

5.2 Successive shocks

In the previous section the acceleration of particles in an ensemble of *coexisting* shocks has been discussed. In this case, the distribution of shocks was *spatially* intermittent. An analogous acceleration mechanism is provided by a distribution of *successive* shocks, i.e. a distribution of shocks which is *temporally* intermittent. This is expected to happen inside superbubbles, where the supernovae will successively sweep-up the medium surrounding the stellar cluster on a scale of a few tens of parsecs. The escape time of GeV particles from such region is typically 1 Myr, providing a substantial fraction of the mechanical power of the stars is transferred into turbulence which confines the cosmic rays. In typical clusters containing a few hundred massive stars, it is very likely that GeV-TeV energy bands will be reaccelerated by a few shocks before escaping the central region.

In the low-energy limit, the solution for the reacceleration in temporally intermittent shocks is expected to match that in spatially intermittent shocks discussed in Section 5.1.2: $f(p) \propto p^{-3}$. It was indeed already shown by Bell (1978) that multiple shock acceleration produces hard spectra and the asymptotic solution reached after many shocks was later derived by Melrose and Pope (1993), properly accounting for the adiabatic decompression of the medium between two shocks. When considering successive linear shocks, the reacceleration operator defined by Equation 5.4 can be used at a macroscopic level. We further assume that besides reaccelerating the preexisting distribution of particles produced by the previous shocks, each new shock accelerates particles from the thermal bath. The distribution downstream of the ith shock therefore reads, according to Equation 3.22:

$$f^{(i)}_{downstream}(p) = s \left(\frac{p}{p_0}\right)^{-s} \left(\frac{\eta n_0}{4\pi p_0^3} + \int_{p_0}^{p} \frac{\mathrm{d}p'}{p'} \left(\frac{p'}{p_0}\right)^{s} f^{(i-1)}(p')\right) . \tag{5.13}$$

We assume that no cosmic rays preexist before the first shock, i.e. $f^{(0)}(p) = 0$, and that the shocks are all identical and characterised by a compression factor r such that the spectral index in Equation 5.13 is $s = 3r/(r-1)$. We further assume that the shocks do not coexist. This implies that the downstream medium is decompressed between each shock. By virtue of the Liouville's theorem, this spatial decompression must be accompanied by a decompression in momentum space $p \to r^{1/3}p$, and the distribution function of the particles reads, after decompression, $f_{decompressed}(p) = f_{downstream}(r^{1/3}p)$. We therefore get the distribution function after the passage and fading of the ith shock as:

$$f^{(i)}(p) = s \left(\frac{r^{1/3}p}{p_0}\right)^{-s} \left(\frac{\eta n_0}{4\pi p_0^3} + \int_{p_0}^{r^{1/3}p} \frac{\mathrm{d}p'}{p'} \left(\frac{p'}{p_0}\right)^{s} f^{(i-1)}(p')\right) . \tag{5.14}$$

By iteration, it is straightforward to prove that the solution to this recursive relation reads:

$$f^{(N)}(p) = \frac{\eta n_0}{4\pi p_0^3} \left(\frac{p}{p_0}\right)^{-s} \sum_{i=1}^{N} \frac{s^i r^{-is/3}}{(i-1)!} \left[\ln\left(r^{i/3}p/p_0\right)\right]^{i-1} , \tag{5.15}$$

and one concludes that the distribution of particles hardens as the shocks sweep up the medium. The sum describes the contribution of all ith fresh injections which are then reaccelerated $N+1-i$ times, where N is the total number of shocks. The asymptotic distribution $f^{(\infty)}$ obtained after the passage of a large number of shocks can be obtained by defining a function Φ as:

$$\Phi \equiv \frac{\eta n_0}{4\pi p_0^3} + \int_{p_0}^{r^{1/3}p} \frac{\mathrm{d}p'}{p'} \left(\frac{p'}{p_0}\right)^{s} f^{(\infty)}(p') , \tag{5.16}$$

and then realising that in the limit $i \to \infty$, Equation 5.14 is equivalent to the following differential equation:

$$p\, \partial_p \Phi\big|_p = s r^{-s/3} \Phi\left(r^{1/3}p\right) , \tag{5.17}$$

which has a universal power law solution $\Phi(p) \propto p^{s-3}$. This implies that $f^{(\infty)}(p) \propto p^{-3}$ is the asymptotic solution which does not depend on the compression ratio of the successive shocks. This universal hardening was early realised by White (1985), Achterberg (1990), and Melrose and Pope (1993). It is analogous to the low-energy stationary solution derived in Section 5.1.2 in the case of coexisting shocks.

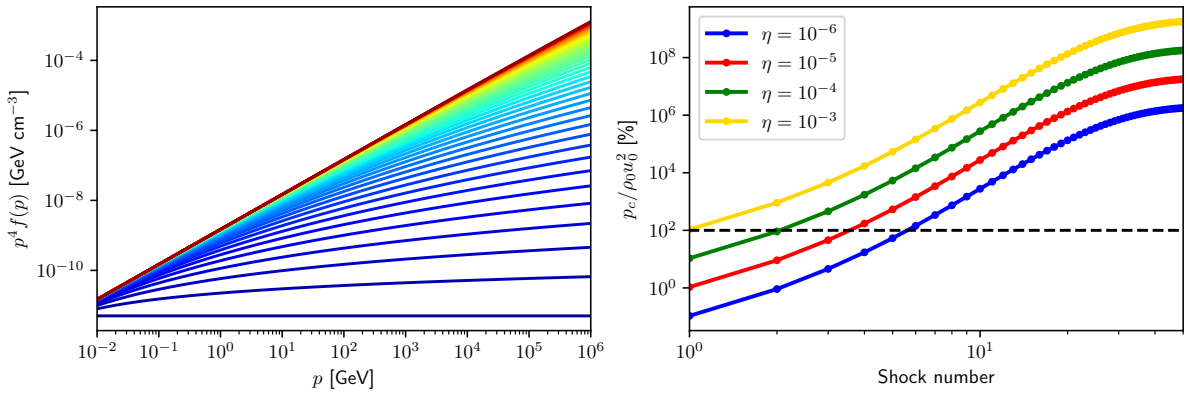

Figure 5.1: Left: Reaccelerated distribution after the passage of successive strong shocks (first shocks in blue, last shocks in red). Right: Evolution of the cosmic ray pressure normalised to the shock ram pressure.

The left panel of Figure 5.1 shows the reaccelerated distributions $f^{(N)}$ for $N = 1...50$. The first acceleration (blue curve at the bottom) is the standard p^{-4} power law solution at strong shocks. The curve immediately above the first one shows the expected logarithmic modulation of the p^{-4} solution, which was already derived analytically in Equation 3.23. Then the spectrum hardens as the shocks succeed each other and eventually converges toward the asymptotic p^{-3} solution.

The right panel of Figure 5.1 displays the evolution of the cosmic ray pressure as the shocks succeed each other. The pressure is shown to rise very rapidly. It saturates after a few tens of shocks, in which case an equilibrium between the fresh injection of particles and the adiabatic decompression is set, corresponding to the asymptotic solution $f^{(\infty)}(p) \propto p^{-3}$.

As anticipated in Equation 3.25, in the test-particle regime the very first shock would already transfer all its pressure to the (compressed) cosmic rays for an injection parameter $\eta = 10^{-4}$. Even assuming very small efficiencies, the energy balance will always be violated after a few reaccelerations, as underlined by Bykov and Toptygin (2001) in the analogous case of coexisting shocks. It is clear that the shocks cannot eventually transfer a million times their energy into cosmic rays! The test-particle solution is only valid in systems where particles are only reaccelerated by a few weak shocks, such as galaxy clusters, as recently analysed by Kang (2021). Other situations, such as the reacceleration in superbubbles, call for a nonlinear treatment of the problem.

5.3 A nonlinear model of shock reacceleration

The remainder of this chapter is a reproduction, with minor modifications and addenda, of Vieu et al. (2021a) (see also Vieu et al., 2021b).

Since the pioneer work of Eichler (1979), Blandford (1980), and Drury and Voelk (1981), there have been many attempts to model nonlinear particle acceleration at shocks, including two-fluid models (e.g. Malkov and Voelk, 1996), semi-analytical solutions (Blasi, 2002; Caprioli et al., 2009), numerical resolutions (e.g. Kang and Ryu, 2011), hydrodynamic simulations (e.g. Caprioli and Spitkovsky, 2014). It is now understood that the backreaction of the accelerated particles creates a precursor in the gas upstream of the shock, as discussed in Section 3.7. The compression factor at the subshock decreases

while the total compression factor increases, in such a way that the cosmic ray spectrum develops a concave shape instead of the power law predicted by the linear theory.

As far as I know, the only studies which addressed the question of the nonlinear *reacceleration* of seeds were performed by Blasi (2004), where it was shown that the flow profile can be indeed strongly affected by the seeds, Ferrand et al. (2008), where the problem was briefly investigated numerically, Kang and Ryu (2011) in the context of weak cosmological shock waves, and Caprioli et al. (2018) who emphasised the possibility to excite turbulence by means of the non-resonant streaming instability induced by the seeds.

In the remainder of this chapter, we therefore aim at computing, in the nonlinear regime, the acceleration of particles by successive shocks. The present section is dedicated to a description of an updated version of the semi-analytical model of Blasi (2004), including the more recent developments describing injection, streaming instability and Alfvénic drift. Then the reacceleration of preexisting seeds is discussed in Section 5.4. Particle acceleration by an ensemble of successive shocks is eventually tackled in Section 5.5.

5.3.1 Kinetic equation

We consider an infinite and plane shock propagating along the x axis (from right to left) into a region filled by a population of non-thermal seed particles whose distribution function is spatially homogeneous far upstream and denoted by $f_\infty(p)$. In the following, the indices *0*, *1* and *2* refer respectively to quantities evaluated at upstream infinity ($x \to -\infty$), immediately upstream of the shock and immediately downstream of the shock. The formalism presented in Section 3.7 can be easily extended to account for the preexisting particles. The transport equation integrated around the shock (Equation 3.32) is generalised to:

$$\frac{p}{3}\left(u_2 - u_p\right)\frac{\mathrm{d}f_1}{\mathrm{d}p} = \left(u_p + \frac{p}{3}\frac{\mathrm{d}u_p}{\mathrm{d}p}\right) f_1 - u_0 f_\infty - Q_1 \delta(x)\delta(p - p_0)\,, \tag{5.18}$$

where we introduced the quantity u_p defined as (Blasi, 2002):

$$u_p(p) \equiv u_1 - v_{A,1} - \frac{1}{f_1(p)}\int_{-\infty}^{0} \mathrm{d}x\, \mathrm{d}_x\left(u - v_A\right) f(x,p)\,. \tag{5.19}$$

Let us recall that when seed particles are neglected, u_p represents the characteristic velocity of scattering centres experienced upstream of the shock by particles of momentum p. When seeds are taken into account, the physical meaning of u_p is not as straightforward. Yet, it remains a useful mathematical quantity to carry out further computations.

In the following we will assume that seed particles with momentum smaller than the injection momentum p_0 are thermalised once they cross the shock, such that they do not participate in the injection process. The injection term is then determined by the thermal leakage injection recipe discussed in Section 3.2 (Equation 3.5). In particular, the injection term can be equivalently supplemented by the following boundary condition in momentum:

$$f_1(p_0) = \frac{n_0 R_{tot}}{\pi^{3/2} p_0^3}\xi^3 e^{-\xi^2}\,, \tag{5.20}$$

which states that the distribution of accelerated particles matches the distribution of the thermal particles at the injection momentum. We recall that n_0 is the plasma density

at upstream infinity, $R_{tot} = u_0/u_2$ is the ratio of the velocity at upstream infinity over the velocity immediately downstream of the (sub)shock, and $\xi = 2.5 - 4$ is the injection parameter of the protons such that $p_0 = \xi p_{th}$, with $p_{th} = \sqrt{2 m_p k T_2}$ the downstream thermal momentum, where T_2 is the downstream temperature. In the following we further define the effective compression factor at the subshock $S_{sub} \equiv (u_1 - v_{A,1})/u_2$, with $v_{A,1}$ the Alfvén speed immediately upstream of the shock which is introduced to account for the streaming instability due to the pressure gradient of the upstream distribution of particles.

5.3.2 Fluid equations

Let us recall the hydrodynamic equations derived in Section 3.7.1. The properties of the shock transition are governed by the mass and momentum conservation laws. The latter is written in terms of the normalised pressures ($P_g = p_g/\rho_0 u_0^2$, etc.) as (Caprioli, 2012):

$$1 + P_{g,0} + P_{c,0} = U(x) + P_g(x) + P_c(x) + P_B(x)\,, \tag{5.21}$$

$$P_g(x) = \frac{U^{-\gamma}(x)}{\gamma M_0^2}\,, \quad P_B(x) = \frac{2}{25}\frac{\left(1 - U(x)^{5/4}\right)^2}{U(x)^{3/2}}\,, \tag{5.22}$$

where $U(x) \equiv u(x)/u_0$. The expression for the gas pressure is obtained assuming an adiabatic equation of state in the upstream region, with adiabatic index γ, while the magnetic pressure is derived from the transport equation of the hydromagnetic waves (3.26), assuming that the waves are excited by resonant scatterings[1]. Finally, let us recall that the normalised cosmic ray pressure is related to the particle distribution function $f(x,p)$ as $P_c(x) = 4\pi/(3\rho_0 u_0^2)\int_{p_0}^{\infty} \mathrm{d}p p^3 v(p) f(x,p)$, where one should keep in mind that $f(x,p)$ is the total distribution function, including the seed particles.

5.3.3 Method of solution

The solution of the problem is obtained following the approximate procedure described in Section 3.7.3, introducing the distance $x_p(p)$ such that particles of momentum p only probe a distance $x_p(p)$ upstream of the shock (recall that in the test-particle regime, the solution reads $f = f_\infty + (f_1 - f_\infty)e^{-ux/D_\parallel}$):

$$f(x,p) = [f_1(p) - f_\infty(p)]\,\vartheta[x - x_p(p)] + f_\infty(p)\,. \tag{5.23}$$

After adopting this assumption, the expression for the cosmic ray pressure at a given position simplifies significantly and can be written as:

$$P_c(x_p) \approx \frac{4\pi}{3\rho_0 u_0^2}\left\{\int_{p_0}^{p} \mathrm{d}p' p'^3 v(p') f_\infty(p') + \int_{p}^{\infty} \mathrm{d}p' p'^3 v(p') f_1(p')\right\}\,. \tag{5.24}$$

This expression differs from that stated in Blasi (2004), which I reproduce here:

$$P_c(x_p) \approx P_{c,0} U_p^{-\gamma_c} + \frac{4\pi}{3\rho_0 u_0^2}\int_{p}^{\infty} \mathrm{d}p' p'^3 v(p') f_1(p')\,, \tag{5.25}$$

[1]The growth rate of the resonant streaming instability only depends on the gradient of the non-thermal particles, thus is not affected by the presence of seeds at upstream infinity. The current of reaccelerated seeds may however excite non-resonant modes (Caprioli et al., 2018), which is beyond the scope of this analysis.

with γ_c the adiabatic index of the cosmic rays. Our prescription describes the adiabatic compression of the seed particles in a more accurate way since it ensures that the low energy seeds are not counted twice. Indeed, evaluating Equation 5.25 at $p = p_0$, i.e. very close to the shock (for particles of small momenta only probe a negligible distance upstream of the shock), one gets $P_{c,1} \approx P_{c,0} U_{p,0}^{-\gamma_c} + P_{c,1}$, which is not correct in the presence of seeds ($P_{c,0} \neq 0$).

Under the approximation 5.23, Equation 5.19 becomes:

$$U_p(p) \approx \left(\frac{7}{5}\zeta(p) - \frac{2}{5}\zeta(p)^{-1/4}\right)\left(1 - \frac{f_\infty(p)}{f_1(p)}\right) + \frac{f_\infty(p)}{f_1(p)}\,, \tag{5.26}$$

where we have defined $\zeta(p) \equiv U(x_p)$ for clarity. Equations 3.39, 3.40 are eventually generalised to:

$$\frac{p}{3}\frac{\mathrm{d}f_1}{\mathrm{d}p}\left(\frac{1}{R_{tot}} - \frac{7}{5}\zeta + \frac{2}{5}\zeta^{-1/4}\right) = \frac{f_1 - f_\infty}{5}\left(7\zeta - 2\zeta^{-1/4} + \frac{p}{6}\left(14 + \zeta^{-5/4}\right)\zeta'(p)\right)\,, \tag{5.27}$$

$$\zeta'(p)\left[\frac{27}{25} - \frac{\zeta^{-\gamma-1}}{M_0^2} + \frac{\zeta^{-5/4}}{25} - \frac{3\zeta^{-5/2}}{25}\right] = \frac{4\pi}{3\rho_0 u_0^2} p^3 v(p)\left[f_1(p) - f_\infty(p)\right]\,. \tag{5.28}$$

Finally, the Rankine-Hugoniot conditions 3.41 are not affected by the seeds for the total distribution of particles is continuous across the shock discontinuity. The system of Equations 5.27 is solved as in Section 3.7.3: starting from a guess value of $\zeta(p_0) \approx U_1$, the total compression factor R_{tot} is computed from the jump condition at the subshock and then Equations 5.27, 5.28 are solved together iteratively with the boundary condition 5.20. We eventually find f_1 and ζ for a given value of U_1 and the computation is repeated until a value of U_1 matching the boundary condition $\zeta(p_{max}) = 1$ is found[2]. The maximum momentum p_{max} is left as a free parameter, set by hand with a cutoff ($f(p) \equiv 0$ for $p > p_{max}$). The three main parameters of the model are therefore the shock Mach number at upstream infinity $\mathcal{M}_0$, the injection parameter ξ which determines the injection efficiency as well as the injection momentum, and the maximum momentum p_{max}.

5.3.4 Adiabatic decompression and escape flux

Similarly to the test-particle case, the particles bound to the fluid are compressed by a factor R_{tot} after the passage of a shock. When successive reaccelerations occur, the decompression of the particles must be computed in between each shock, otherwise one could obtain arbitrarily hard spectra at low energy. As discussed in Section 5.2, one gets, by Liouville's theorem: $f_{decompressed}(p) = f_1(R_{rot}^{1/3} p)$ (Melrose and Pope, 1993). As pointed out by Ferrand et al. (2008), in doing numerical resolutions the steps of the momentum grid in logarithmic scale should be chosen as exact fractions of the momentum shift $\log(R_{tot})/3$, otherwise numerical errors are expected. In nonlinear shocks, this requirement cannot be fulfilled a priori since the total compression is unknown. We therefore correct the pressure after decompression by a renormalisation factor to ensure that an adiabatic change takes place: $P_{c,decompressed} = R_{tot}^{-\gamma_c} P_{c,1}$, where γ_c is the adiabatic index of the cosmic rays and $P_{c,1}$ the cosmic ray pressure at the shock. The renormalisation factor is always close to unity in our computation. In the following, the decompressed distribution of cosmic rays remaining after the passage of a shock will be referred to as the "postshock" distribution.

[2] In practice we start with a coarse grid of values for U_1 before refining the solution using a dichotomy up to an arbitrary precision ($|\zeta(p_{max}) - 1| < 10^{-5}$ in the following).

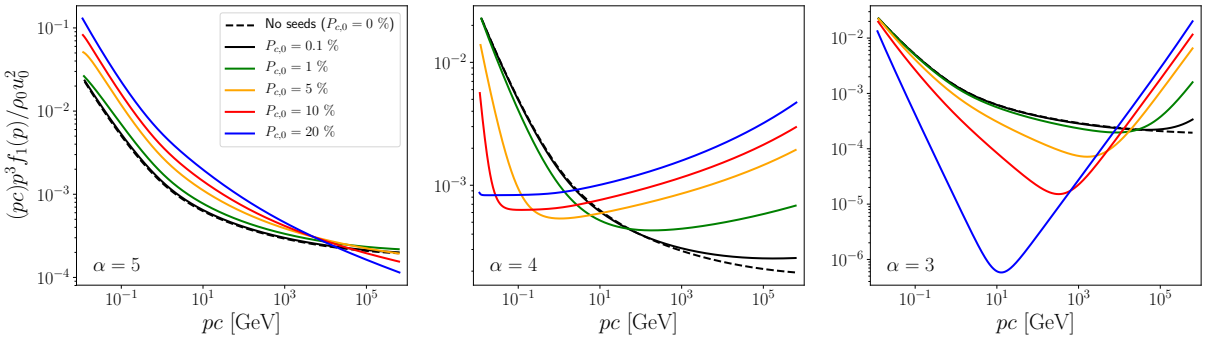

Figure 5.2: Spectra after reacceleration and decompression of seeds with spectral index $\alpha = 5$ (top), $\alpha = 4$ (middle), $\alpha = 3$ (bottom).

In order to probe the energetics and in particular the efficiency of the acceleration, it is useful to introduce the flux of particles escaping at the maximum momentum upstream (or equivalently the cosmic ray flux at a finite "free escape boundary" upstream of the shock (Caprioli et al., 2009). This is indeed mandatory to ensure the conservation of the energy in a stationary plane infinite shock producing hard spectra in the high energy bands. As in Section 3.7.4, the escape term F_e normalised to $\rho_0 u_0^3/2$ is introduced phenomenologically in the equation of energy conservation as:

$$\begin{aligned} F_e &= 1 - \frac{1}{R_{tot}^2} + \frac{2}{M_0^2(\gamma-1)} - \frac{2}{R_{tot}}\frac{\gamma}{\gamma-1}P_{g,2} + \frac{2}{R_{tot}}\frac{\gamma_c}{\gamma_c-1}\left(P_{c,0} - \frac{P_{cr,2}}{R_{tot}}\right), \\ P_{g,2} &= U_1 - \frac{1}{R_{tot}} + \frac{1}{\gamma M_0^2}U_1^{-\gamma} + \frac{2}{25U_1^{3/2}}\left(1 - U_1^{5/4}\right)^2, \end{aligned} \tag{5.29}$$

where the additional term $P_{c,0}$ compared to Equation 3.43 arises due to the pressure of the seeds at upstream infinity.

5.4 Reacceleration of seed particles

In this section we investigate the effect of the nonlinearities on the reacceleration of preexisting seeds. We set the shock Mach number $M_0 = 20$ ($u_0 = 3320$ km/s), the density far upstream $n_0 = 0.01$ cm^{-3}, the temperature $T_0 = 10^6$ K, the adiabatic index of the gas $\gamma = 5/3$ and the injection parameter $\xi = 3$. The spectrum of the seeds is assumed to be a power law of index α. Figure 5.2 shows the spectra resulting from the acceleration of seeds with spectral indices 3 (hard), 4 (flat) and 5 (steep).

In the absence of seeds, the spectrum typically steepens up to 1 TeV and then hardens in the high energy bands, as discussed in Section 3.7.4. For seed spectra steeper than p^{-4}, the energy of the seeds is initially located around the injection momentum and there is not much difference between the reacceleration of these seeds and the acceleration of particles from the thermal bath, as can be seen in the left panel of Figure 5.2. In contrast, if the spectral index of the seeds is flat ($\alpha = 4$), the plasma flow is much more modified compared to the case where seeds are not present. As the compression factor of the subshock decreases, the injection of particles from the thermal pool becomes inefficient. On the other hand, high energy seeds feel the total compression factor and can thus be efficiently reaccelerated, which hardens the spectra at high energies. This results in hard spectra over almost all energy bands, as can be seen in the middle panel

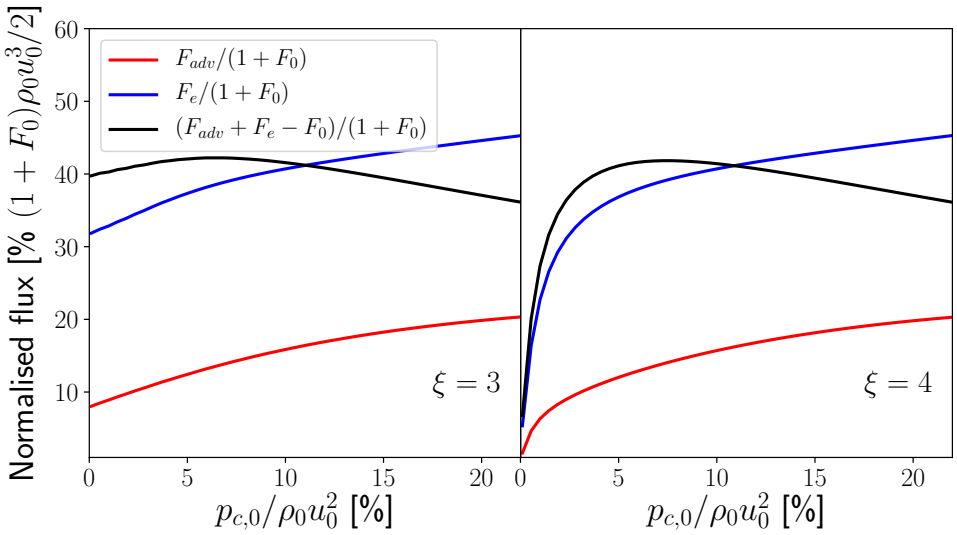

Figure 5.3: Flux advected downstream F_{adv}, escape flux upstream F_e, net flux gain $F_{adv} + F_e - F_0$, all normalised to the upstream incoming flux (ram hydrodynamical flux $\rho u_0^3/2$ plus flux of preexisting particles F_0), as function of the pressure of the seeds at upstream infinity, for an injection parameter $\xi = 3$ (left) and $\xi = 4$ (right).

of Figure 5.2. Finally, if the spectrum of the seeds is harder than p^{-4}, the reacceleration becomes inefficient at high energies such that the high energy end of the spectrum is close to that of the seeds. On the other hand, the freshly injected particles are not efficiently accelerated at the subshock, which leads to extremely steep spectra at low energies. This results in very concave spectra, which are basically the superposition of an injection with the preexisting spectrum, as seen in the right panel of Figure 5.2.

Figure 5.3 shows how the flux of cosmic rays is shared between the different regions, for a seed spectrum scaling as p^{-4}. Besides the escaping flux F_e, also shown are the flux advected downstream F_{adv} as well as the net flux gained in the acceleration $F_{adv} + F_e - F_0$, where F_{adv} and F_0 are identified in Equation 5.29 as:

$$F_{adv} = \frac{2}{R_{tot}^2} \frac{\gamma_c}{\gamma_c - 1} P_{cr,2} \,, \tag{5.30}$$

$$F_0 = \frac{2}{R_{tot}} \frac{\gamma_c}{\gamma_c - 1} P_{c,0} \,. \tag{5.31}$$

Although the energy flux would quickly grow to unphysical values in the test-particle regime, accounting for the nonlinearity of the problem leads to a drastic reduction of the acceleration efficiency. The energy gain saturates at the level of about 40% and then decreases as the pressure of the seeds is further increased, for in this case most of the flux of preexisting particles is converted into kinetic shock modification and heat. The upstream escaping flux is always a few times larger than the flux advected downstream, which is expected since the solution is a concave spectrum.

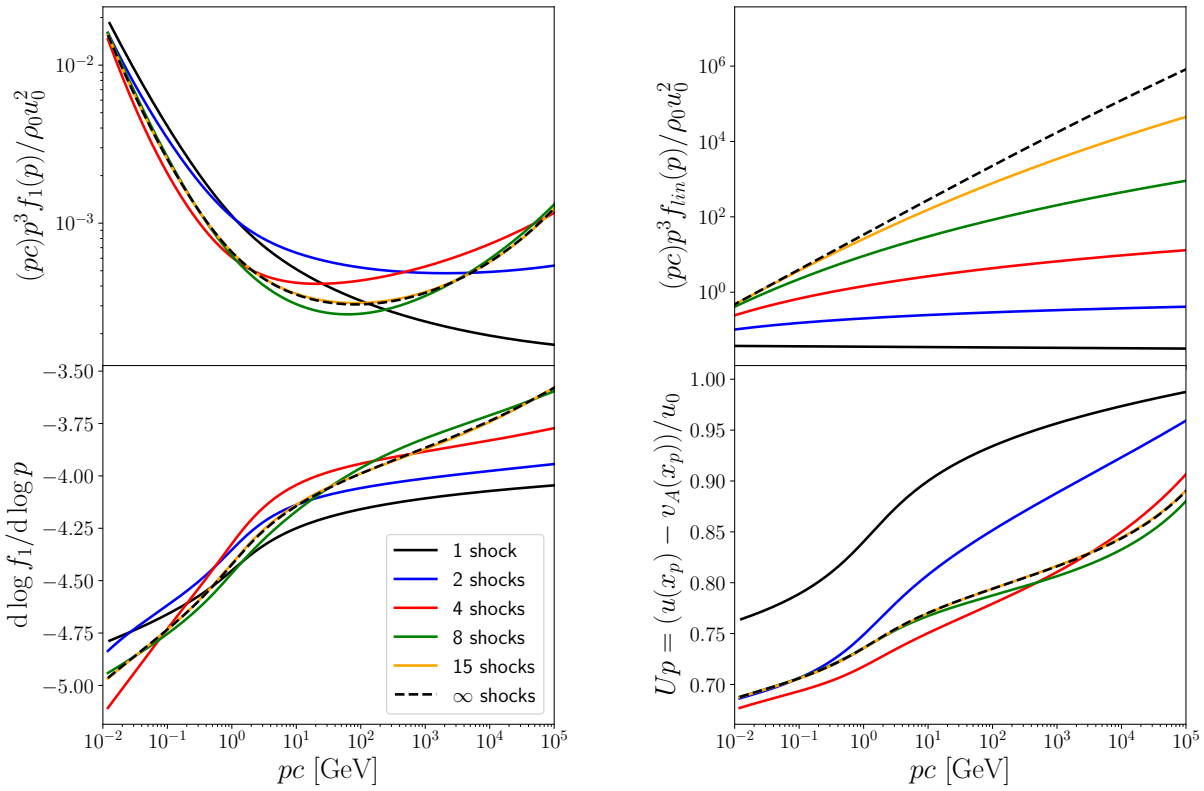

Figure 5.4: Spectrum of cosmic rays after multiple reaccelerations (top left panel) and corresponding spectral indices (bottom left panel) compared with linear diffusive shock reacceleration (top right panel). The bottom right panel displays the velocity felt by the particles as defined by Equation 5.19.

5.5 Particle acceleration by successive nonlinear shocks

5.5.1 Identical shocks

We now aim at investigating the acceleration of particles by multiple shocks. First we assume that all shocks are identical. This is a simplistic modelling as we expect for instance the medium to be heated by each shock if they all span the same volume, or the density to decrease if the volume expands. The idealistic solution is nevertheless interesting as a benchmark to understand more realistic scenarios, which we shall investigate in a moment.

Figure 5.4 shows the evolution of the spectrum of cosmic rays for $\mathcal{M}_0 = 20$, $T_0 = 10^6$ K ($u_0 = 3320$ km/s), $n_0 = 0.01$ cm^{-3}, $\xi = 3$, $p_{max} = 1$ PeV. There are no preexisting particles before the first shock, and particles are injected from the thermal pool at each shock. The bottom right panel displays the effective flow velocity felt by particles of momentum p. In Bohm's diffusion regime, the diffusion length is proportional to p such that x_p, the distance probed by the particles of momentum p ahead of the shock, can be identified with the distance up to a rescaling ($x_{p_{max}}$ being interpreted as the position of a fictitious free escape boundary). This plot therefore shows the velocity profile of the scattering centres, and one sees how the energetic particles slow down the flow upstream of the shock, leading to the formation of a precursor. The effective compression ratio of the subshock, S_{sub}, decreases rapidly after the first few shocks and stabilises around 2.4, which results in a steepening at low energies: the spectral index can be as high as

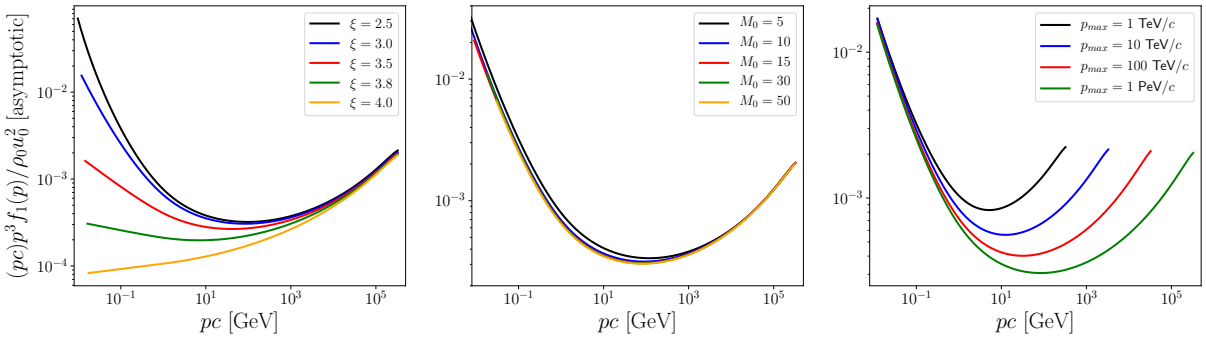

Figure 5.5: Asymptotic solution after multiple shock reaccelerations for various sets of parameters. Left: $M_0 = 20$, $p_{max} = 10^6$ GeV, varying ξ. Middle: $\xi = 3$, $p_{max} = 10^6$ GeV, varying M_0. Right: $M_0 = 20$, $\xi = 3$, varying p_{max}.

5. On the other hand, the total compression ratio increases after each shock before it stabilises around 4.6, which leads to an amplified hardening of the high energy bands. Asymptotically, the spectrum is harder than p^{-4} beyond 100 GeV and the spectral index reaches 3.6 at 1 PeV. This demonstrates a striking discrepancy compared with the linear evolution displayed for comparison on the top right panel of Figure 5.4 (see also left panel of Figure 5.1). As shown in the previous section, the linear treatment leads to a spectral hardening until the asymptotic p^{-3} distribution is reached.

Figure 5.5 shows the asymptotic solution (reached typically after about 10 reaccelerations) for various sets of parameters. It is striking that the high energy part of the spectrum above 100 GeV displays a somewhat universal shape, that is, a slight concavity, with a spectral index decreasing from about 3.9 to 3.5. As far as the injection parameter is concerned, it only affects the lower part of the spectrum, which is steeper for high injection efficiencies (small ξ). Furthermore, the asymptotic solution is nearly independent of the Mach number and, up to a rescaling, of the maximum momentum as well.

The evolution of the pressure of the downstream cosmic rays (in between the passage of two shocks, after adiabatic decompression) as function of the number of shocks which have already swept-up the medium is plotted in Figure 5.6 for various sets of parameters. While the comparison between the linear and nonlinear computation displayed on the top left panel demonstrates again the need for a nonlinear treatment of shock reacceleration, the three other panels show that the evolution of the pressure does not depend much on the parameters and can be described in three phases. During the first three shocks, the pressure increases, until it overshoots its asymptotic value. Then it decreases and stabilises after about 10 shocks. The reason behind the decrease of the downstream pressure is that, as discussed above, the acceleration efficiency decreases when the seed pressure is too large. Eventually a balance is set between the downstream advection and the upstream escape. The asymptotic fluxes are such that about 50% of the shock kinetic flux goes into cosmic rays, with about 10% advected downstream and 40% escaping upstream. This means that the reacceleration process saturates when the system approaches an equipartition of energy between the shock and the particles. This is the very reason behind the nearly universal character of the asymptotic solution. Only the injection of fresh particles modulates the low energy bands of the spectrum and the value of the cosmic ray pressure at saturation, which slightly increases as the injection efficiency increases (top right panel of Figure 5.6). This variation is nevertheless very moderate. Only for low injection efficiencies (e.g. $\eta \sim 10^{-12}$), the pressure of downstream cosmic rays is

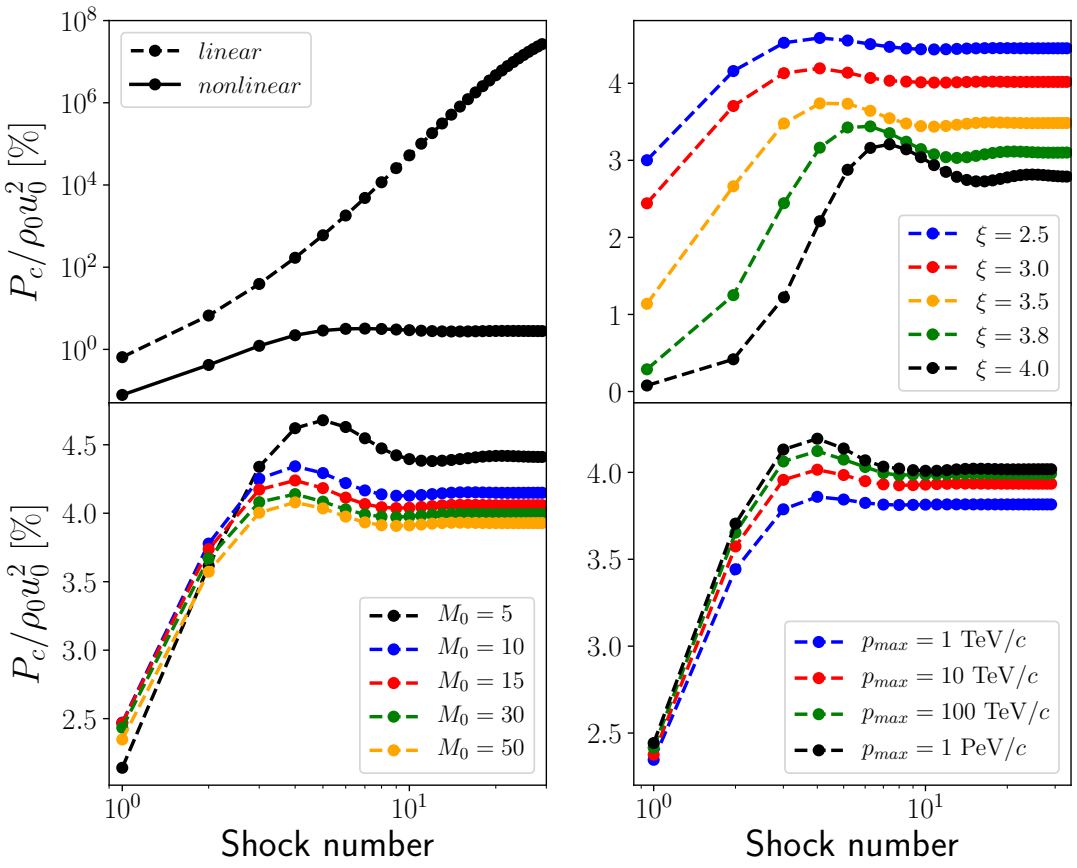

Figure 5.6: Evolution of the cosmic ray pressure after reacceleration by successive shocks. Top left panel: comparison between linear and nonlinear computations, for $\mathcal{M}_0 = 20$, $\xi = 4$, $p_{max} = 1$ PeV. Top right panel: $\mathcal{M}_0 = 20$, $p_{max} = 1$ PeV, varying ξ. Bottom left panel: $\xi = 3$, $p_{max} = 1$ PeV, varying M_0. Bottom right panel: $\mathcal{M}_0 = 20$, $\xi = 3$, varying p_{max}.

found to saturate below 1%. This is because in this case the asymptotic test-particle solution $f(p) \propto p^{-3}$ is reached before nonlinear effects regulate the energy balance. In particular, the energy of the particles always remains negligible compared to that of the shock and equipartition cannot be reached. However such small efficiency is not realistic and we conclude that nonlinear effects are generally unavoidable when dealing with multiple shocks. In this case, for standard values of the injection parameter ($\xi \sim 2-4$) the pressure of the cosmic rays remaining in the (decompressed) medium is always about $3-5\%$ of the shock ram pressure.

5.5.2 Heating

The spectra discussed in the previous section have been obtained in the idealistic situation where all shocks are identical. This is not expected in realistic environments. For instance, if all shocks span the same volume, the medium is expected to be heated. The postshock temperature including adiabatic decompression reads, as function of the upstream temperature T_0 (Amato and Blasi, 2006):

$$T_2 = T_0 R_{sub}^{1-\gamma}(1+\Lambda_B)\frac{\gamma+1+(1-\gamma)/R_{sub}}{\gamma+1+(1-\gamma)R_{sub}}\,, \tag{5.32}$$

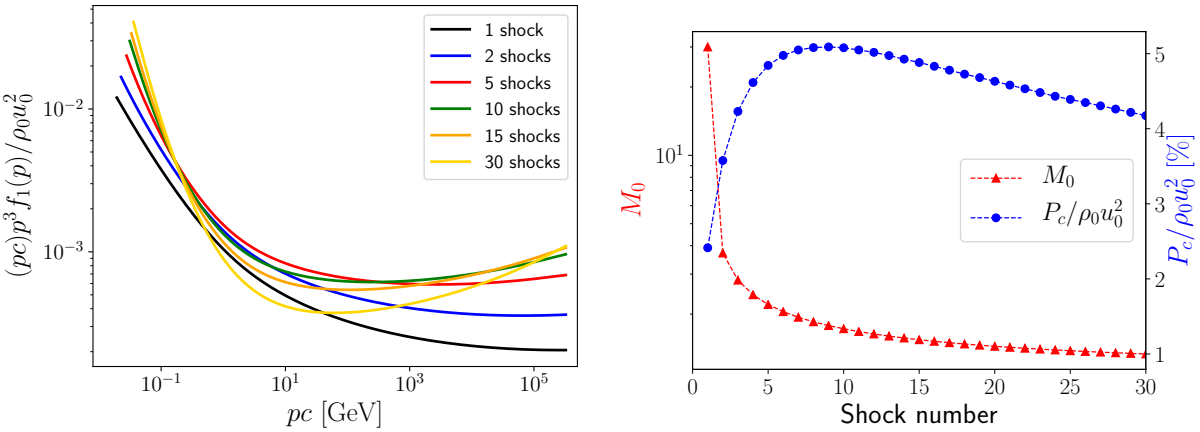

Figure 5.7: Evolution of the downstream cosmic ray spectrum (left), the shock Mach number (right, in red) and the postshock cosmic ray pressure (right, in blue) when the heating of the medium in between successive shocks is taken into account.

where Λ_B has been defined in Equation 3.41. In Figure 5.7, we plot the evolution of the shock Mach number and postshock cosmic ray pressure, accounting for the heating of the medium. The initial temperature is set to 10^6 K, the shock velocity is fixed to $u_0 = 5000$ km/s (i.e. the initial Mach number is set to 30) and the injection parameter is set to $\xi = 3$.

After the first few accelerations, the Mach number decreases rapidly and the reacceleration becomes inefficient. The spectra are steeper than in the situation where all shocks are identical. Although an asymptotic solution is also expected to be reached in this case, it takes much longer time for the system to converge.

5.5.3 Towards cosmic ray production in superbubbles

A more promising environment where multiple shock acceleration is expected to take place is a superbubble. Indeed, confined cosmic rays may be successively reaccelerated by supernova shocks inside superbubbles (Ferrand and Marcowith, 2010). Interestingly, the adiabatic expansion of the bubble compensates the heating of the medium due to the successive shocks, such that the interior temperature stays nearly constant in time (Parizot et al., 2004, see also Equation 1.11). On the other hand, the density decreases more rapidly: $n(t) \propto t^{-22/35}$. We computed again the reacceleration of cosmic rays by successive shocks taking into account this density drop with a constant temperature.

Figure 5.8 shows the evolution of the cosmic ray spectrum in an environment where the density decreases as $n_i \propto i^{-22/35}$, where i is the number of shocks which have swept-up the medium (we assume that the shocks accelerate the particles at regular intervals), and n_i is the density far upstream of the ith shock. What is shown is the spectrum just before the $(i+1)$th reacceleration (including the decompression of the medium), compared with the post-shock spectrum in the case where the ambient density is constant. The right panel of Figure 5.8 displays the evolution of the postshock pressure normalised to the ram pressure of the first shock. Because cosmic rays suffer enhanced adiabatic losses in between shocks, the pressure does not increase as rapidly as in the case of constant density and do not overshoots the asymptotic value. Nevertheless, the asymptotic pressure is identical to that computed in the ideal case of constant density, which is around 4% of the ram pressure of the first shock. Neither are the particle spectra displaying substantial modifications.

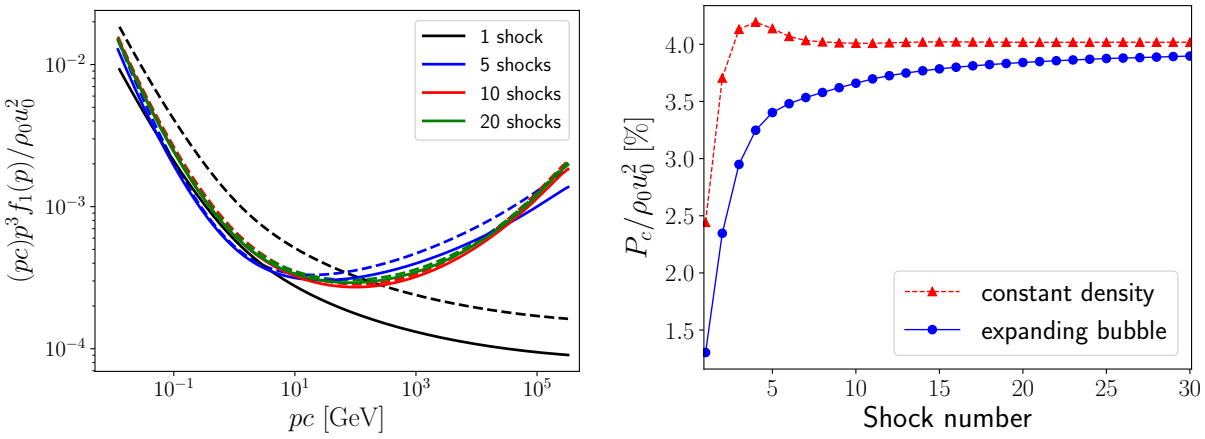

Figure 5.8: Left: Evolution of the cosmic ray spectrum during multiple shock acceleration in an expanding medium (solid lines) compared to the spectra computed in the case where all shocks are identical (dashed lines). Right: Evolution of the pressure of cosmic rays in an expanding medium. The parameters are $n_0 = 0.01$ cm^{-3}, $\mathcal{M}_0 = 20$, $\xi = 3$.

Reducing a superbubble to an expanding medium is once again a minimalistic approach. In particular, the average time interval between two supernova explosions is about $\Delta t = 35/N_*$ Myr $\approx 0.1 - 1$ Myr, where N_* is the number of massive stars in the cluster. As will be seen in the next chapter, the escape of GeV particles away from the region of acceleration is about 0.01 - 10 Myr, depending on the level of turbulence and the size of the bubble. In order to probe the modulation induced by the escape of the particles in between the reacceleration events, we assume that the escape time scales as $\tau_{esc}(p) = \tau(pc/1 \text{ GeV})^{-1/3}$, which is expected for a Kolmogorov turbulence (Ferrand and Marcowith, 2010, see also Section 2.3). Neglecting all processes but the escape, the transport equation averaged over the superbubble volume simply reads, in between supernova explosions: $\partial_t f = -f/\tau_{esc}$ (see Equation 2.61), which provides:

$$f(t) = f(t_i) e^{-\Delta t/\tau (pc/1 \text{ GeV})^{1/3}}, \tag{5.33}$$

where Δt is the average time interval between two supernova explosions and $f(t_i)$ is the decompressed postshock distribution after the passage of the ith shock.

Figure 5.9 shows the resulting cosmic ray spectra and pressure evolution. Whenever $\tau < \Delta t$, the production of cosmic rays is intermittent at all energy bands: there are nearly no particles remaining in between the shocks and the cosmic ray pressure right before a supernova explosion is close to zero. In this case, the particles are not reaccelerated and the superbubble is just a collection of isolated supernovae. On the other hand, if $\tau > \Delta t$, the "benchmark" asymptotic solution described in Section 5.5.1 is retrieved up to the momentum such that $\tau_{esc}(p) < \Delta t$. Beyond this momentum, the particles escape and are not reaccelerated.

One could typically hope to retrieve the concave asymptotic solution if e.g. the interval between two supernovae is $\Delta t \sim 100$ kyr and the escape time is $\tau \sim 10$ Myr. These are not unrealistic values for clusters hosting hundreds of massive stars in possibly very turbulent environments such as the galactic centre.

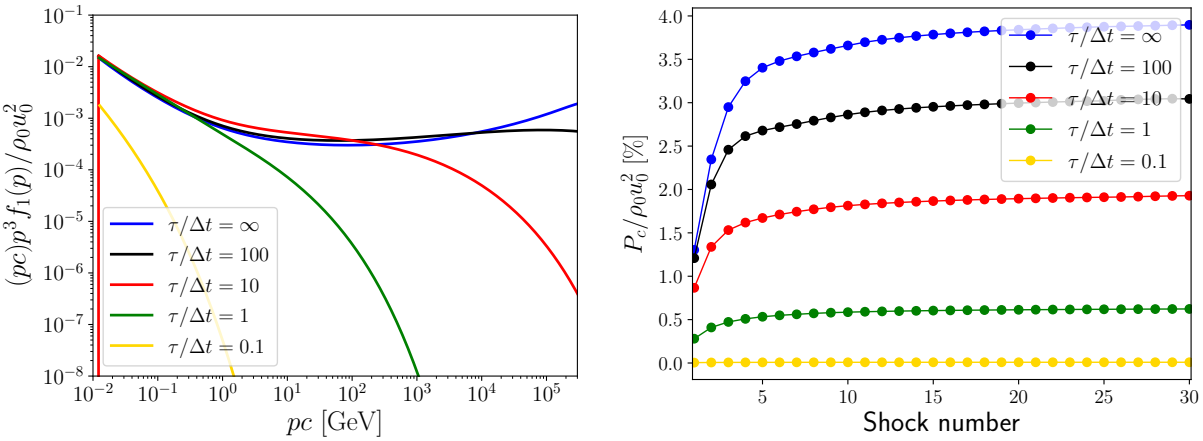

Figure 5.9: Asymptotic cosmic ray spectrum (left) and evolution of the pressure (right) during multiple shock accelerations in an expanding medium where the particles can escape in between the passage of two shocks. The parameters are $n_0 = 0.01$ cm^{-3}, $\mathcal{M}_0 = 20$, $\xi = 3$.

5.6 Summary

After having briefly reviewed the seminal works by Bykov et al. describing the acceleration of cosmic rays in a stochastic ensemble of coexisting shocks, we tackled the problem of the nonlinear reacceleration of particles by a succession of strong shocks, using a semi-analytical computation accounting for the streaming instability as well as the Alfvénic drift. We have shown that the linear framework provides a very inaccurate estimate of the solution. The presence of seeds can indeed strongly modify the shock structure and balance the shock pressure such that particle reacceleration becomes less efficient at either low or high energies, depending on the seed spectrum. This can lead to spectra either steep (for steep distributions of seeds), hard (for flat distributions of seeds), or with a sharp transition from a steep to a hard component (for hard distributions of seeds).

We then considered the acceleration of particles by multiple identical shocks. The spectrum converges towards an asymptotic solution, which is typically reached after 20 shocks. Remarkably, the asymptotic spectrum is nearly universal above 10 GeV. In particular, it does not depend on the injection efficiency and shock Mach number. The injection efficiency shapes the low energy bands, which are steeper for higher efficiencies. The asymptotic solution is eventually characterised by a spectral index of about 3.5 at the maximum energy. This is again very different from the linear solution, $f(p) \propto p^{-3}$, which could only be retrieved assuming very small injection fractions. Varying the injection parameter, one expects a transition between the universal linear solution and the universal nonlinear solution, as already pointed out by Ferrand et al. (2008).

The downstream cosmic ray pressure increases after a few shocks, then quickly stabilises around an asymptotic value. The latter is about 5% of the ram pressure of one shock. Interestingly, this value weakly depends on the injection efficiency. Even for very small efficiencies, a reacceleration by a few shocks is sufficient for the pressure of cosmic rays to reach a few percent of the shock energy.

We eventually generalised the analysis to the case of non-identical successive shocks. In a constant volume the medium is heated between each shocks, which leads to a rapid decrease of the shock Mach numbers: the reacceleration of the particles becomes inefficient. On the other hand, assuming an environment undergoing an adiabatic expansion, such as a galactic superbubble, we found results similar to the case of identical shocks.

Although the pressure of cosmic rays increases less rapidly, it still saturates at about 5% of the shock ram pressure. The particle spectrum converges towards the same asymptotic distribution, with a concave shape and universal spectral index around 3.5 at the maximum energy. Eventually, the particle escape between shocks was introduced, demonstrating that the asymptotic solution would form only in the case where particles are very efficiently confined. This computation will be the building block of a novel self-consistent model of particle acceleration in superbubbles, which will be now discussed.

References

Achterberg, A. (May 1990). "Particle acceleration by an ensemble of shocks". In: A&A 231.1, pp. 251–258.

Amato, E. and Blasi, P. (Sept. 2006). "Non-linear particle acceleration at non-relativistic shock waves in the presence of self-generated turbulence". In: MNRAS 371.3, pp. 1251–1258. DOI: 10.1111/j.1365-2966.2006.10739.x.

Bell, A. R. (Feb. 1978). "The acceleration of cosmic rays in shock fronts - II." In: MNRAS 182, pp. 443–455. DOI: 10.1093/mnras/182.3.443.

Blandford, R. D. (May 1980). "On the mediation of a shock front by Fermi-accelerated cosmic rays". In: ApJ 238, pp. 410–416. DOI: 10.1086/157998.

Blasi, P. (Feb. 2002). "A semi-analytical approach to non-linear shock acceleration". In: *Astroparticle Physics* 16.4, pp. 429–439. DOI: 10.1016/S0927-6505(01)00127-X.

Blasi, P. (2004). "Nonlinear shock acceleration in the presence of seed particles". In: *Astroparticle Physics* 21.1, pp. 45–57. ISSN: 0927-6505. DOI: https://doi.org/10.1016/j.astropartphys.2003.10.008.

Bykov, A. M. (Jan. 1997). "Primary Cosmic Rays Composition around the "Knee" in the Model of Particle Acceleration by Shock Front Ensembles in Galactic Superbubbles". In: *International Cosmic Ray Conference*. Vol. 4. International Cosmic Ray Conference, p. 365.

Bykov, A. M. and Fleishman, G. D. (Mar. 1992). "On non-thermal particle generation in superbubbles." In: MNRAS 255, pp. 269–275. DOI: 10.1093/mnras/255.2.269.

Bykov, A. M. and Toptygin, I. N. (Oct. 1990). "Theory of charge particle acceleration by a shock wave ensemble in a turbulent medium". In: *Zhurnal Eksperimentalnoi i Teoreticheskoi Fiziki* 98, pp. 1255–1268.

Bykov, A. M. and Toptygin, I. N. (Oct. 2001). "A Model of Particle Acceleration to High Energies by Multiple Supernova Explosions in OB Associations". In: *Astronomy Letters* 27.10, pp. 625–633. DOI: 10.1134/1.1404456.

Bykov, A. M. (Jan. 1999). "Nonthermal Particles in Star Forming Regions". In: *LiBeB Cosmic Rays, and Related X- and Gamma-Rays*. Ed. by R. Ramaty et al. Vol. 171. Astronomical Society of the Pacific Conference Series, p. 146.

Bykov, A. M. (Oct. 2001). "Particle Acceleration and Nonthermal Phenomena in Superbubbles". In: Space Sci. Rev. 99, pp. 317–326. DOI: 10.1023/A:1013817721725.

Bykov, A. M. and Toptygin, I. (Nov. 1993). "Reviews of topical problems: Particle kinetics in highly turbulent plasmas (renormalization and self-consistent field methods)". In: *Physics Uspekhi* 36.11, pp. 1020–1052. DOI: 10.1070/PU1993v036n11ABEH002179.

Bykov, A. M. et al. (Apr. 2020). "High-Energy Particles and Radiation in Star-Forming Regions". In: Space Sci. Rev. 216.3, 42, p. 42. DOI: 10.1007/s11214-020-00663-0.

Caprioli, D., Blasi, P., and Amato, E. (July 2009). "On the escape of particles from cosmic ray modified shocks". In: MNRAS 396.4, pp. 2065–2073. DOI: 10.1111/j.1365-2966.2008.14298.x.

Caprioli, D. and Spitkovsky, A. (Mar. 2014). "Simulations of Ion Acceleration at Non-relativistic Shocks. I. Acceleration Efficiency". In: ApJ 783.2, 91, p. 91. DOI: 10.1088/0004-637X/783/2/91.

Caprioli, D. (July 2012). "Cosmic-ray acceleration in supernova remnants: non-linear theory revised". In: J. Cosmology Astropart. Phys. 2012.7, 038, p. 038. DOI: 10.1088/1475-7516/2012/07/038.

Caprioli, D., Zhang, H., and Spitkovsky, A. (June 2018). "Diffusive shock re-acceleration". In: *Journal of Plasma Physics* 84.3, 715840301, p. 715840301. DOI: 10.1017/S0022377818000478.

Drury, L. O. and Voelk, J. H. (Aug. 1981). "Hydromagnetic shock structure in the presence of cosmic rays". In: ApJ 248, pp. 344–351. DOI: 10.1086/159159.

Eichler, D. (Apr. 1979). "Particle acceleration in collisionless shocks: regulated injection and high efficiency." In: ApJ 229, pp. 419–423. DOI: 10.1086/156969.

Ferrand, G. and Marcowith, A. (Feb. 2010). "On the shape of the spectrum of cosmic rays accelerated inside superbubbles". In: A&A 510, A101, A101. DOI: 10.1051/0004-6361/200913520.

Ferrand, G., Downes, T., and Marcowith, A. (Jan. 2008). "MARCOS, a numerical tool for the simulation of multiple time-dependent non-linear diffusive shock acceleration". In: MNRAS 383.1, pp. 41–56. DOI: 10.1111/j.1365-2966.2007.12511.x.

Kang, H. (June 2021). "Diffusive Shock Acceleration by Multiple Weak Shocks". In: *arXiv e-prints*, arXiv:2106.08521.

Kang, H. and Ryu, D. (June 2011). "Re-acceleration of Non-thermal Particles at Weak Cosmological Shock Waves". In: ApJ 734.1, 18, p. 18. DOI: 10.1088/0004-637X/734/1/18.

Klepach, E. G., Ptuskin, V. S., and Zirakashvili, V. N. (May 2000). "Cosmic ray acceleration by multiple spherical shocks". In: *Astroparticle Physics* 13.2-3, pp. 161–172. DOI: 10.1016/S0927-6505(99)00108-5.

Malkov, M. A. and Voelk, H. J. (Dec. 1996). "Renormalized Two-Fluid Hydrodynamics of Cosmic-Ray–modified Shocks". In: ApJ 473, p. 347. DOI: 10.1086/178149.

Melrose, D. B. and Pope, M. H. (Jan. 1993). "Diffusive Shock Acceleration by Multiple Shocks". In: *Proceedings of the Astronomical Society of Australia* 10.3, p. 222.

Parizot, E. et al. (Sept. 2004). "Superbubbles and energetic particles in the Galaxy. I. Collective effects of particle acceleration". In: A&A 424, pp. 747–760. DOI: 10.1051/0004-6361:20041269.

Spruit, H. C. (Apr. 1988). "Particle acceleration in a flow accreting through shock waves". In: A&A 194.1-2, pp. 319–327.

Vieu, T., Gabici, S., and Tatischeff, V. (2021a). "Nonlinear particle reacceleration by multiple shocks". In: *In preparation*.

Vieu, T., Gabici, S., and Tatischeff, V. (2021b). "Nonlinear particle reacceleration by successive shocks". In: *Proceedings of 37th International Cosmic Ray Conference — PoS(ICRC2021)*. Vol. 395, p. 148. DOI: 10.22323/1.395.0148.

White, R. L. (Feb. 1985). "Synchrotron emission from chaotic stellar winds." In: ApJ 289, pp. 698–708. DOI: 10.1086/162933.

Chapter 6

Cosmic ray production in superbubbles

This chapter aims at computing the acceleration of cosmic rays in superbubble environments, considering all the relevant ingredients. We use the methods and results of the previous chapters in order to account for the bubble structure and dynamics, the stochastic reacceleration and escape in turbulence, the acceleration and reacceleration around multiple strong shocks. The feedback of energetic particles onto the turbulence and large-scale flows is taken into account. Eventually, the model is refined by considering two regions with different properties. Typical superbubble cosmic ray and gamma-ray spectra are computed and discussed in the light of available observations. The results of this chapter will be published in Vieu et al. (2021a) (see also Vieu et al., 2021c).

6.0 Notations

In complex superbubble environments, the acceleration and transport of cosmic rays is driven by a rich physics from microphysical to galactic scales. Table 6.1 provides a guide to not get lost in the notations which will be defined and used throughout this chapter. Additionally, it provides typical values or order of magnitude estimates.

6.1 Superbubble properties

6.1.1 Bubble structure

Let us consider a cluster of hundreds of massive ($8-150 M_\odot$) stars distributed according to an initial mass function of index 2.3 (Salpeter, 1955). The mass of a star can be connected to its lifetime by using the numerical fit from the stellar evolution simulations performed by Limongi and Chieffi (2006): $\log_{10}(t\ [\mathrm{yr}]) = 9.598 - 2.879 \log_{10} M + 0.6679 (\log_{10} M)^2$, where M is the initial mass of the star in solar masses. Assuming that all stars in a cluster are born at the same time $t = 0$, it is possible to implement a Monte Carlo sampling to simulate the times at which they explode into supernovae. One of such realisations for a cluster of 100 massive stars is shown in the left panel of Figure 6.1. Such a number of massive stars represents the typical content of superbubbles (Lingenfelter, 2018). The most massive stellar clusters located near the galactic centre contain of the order of 10^3 massive stars (Krumholz et al., 2019).

Stars inject kinetic energy in the surrounding medium not only when they explode as supernovae, but also during their entire lives, mainly due to the presence of stellar winds (Cesarsky and Montmerle, 1983; Seo et al., 2018). As discussed in Chapter 1, an

CLUSTER AND SUPERBUBBLE		
*Initial number of massive stars	N_*	$100 - 1000$
Lifetime of the superbubble	$\mathcal{T}_{SB}$	35 Myr
Time-dependent mechanical power	$\mathcal{P}_{tot}$	$10^{38} - 10^{39}$ erg/s
Average mechanical power (winds and supernovae)	L_*	$10^{38} - 10^{39}$ erg/s
Fraction of the mechanical power working on the shell	ξ_b	22%
Radius of the superbubble	R_b	$50 - 150$ pc
*Normalised superbubble radius per star at 1 Myr	R_0	10 pc
Volume of the superbubble	V_{SB}	
*Density of the interstellar medium around the superbubble	n_{ISM}	$10 - 100$ cm^{-3}
Interior number density	n	$0.01 - 0.1$ cm^{-3}
Interior density	ρ	$0.2 - 2 \times 10^{25}$ g cm^{-3}
Interior temperature	T	5×10^6 K
MASSIVE STAR WINDS		
Wind mechanical power	$\mathcal{P}_w$	$10^{37} - 10^{38}$ erg/s
Radius of the wind termination shock	R_s	$1 - 10$ pc
Velocity of the wind outflows	V_w	2000 km/s
*Injection momentum at winds	p_0	5 MeV/c
*Maximum momentum at winds	p_w	10^5 GeV/c
*Wind acceleration efficiency	η_w	10%
SUPERNOVA REMNANTS (SNR)		
Supernova energy	E_{SN}	10^{51} erg
Mass of supernova ejecta	M_e	$10 M_\odot$
Initial velocity of supernova shocks	V_{SN}	3000 km/s
Velocity of SNR starting the Sedov-Taylor phase	u_0	1500 km/s
"Equivalent" volume spanned by "stationary" SNR	$\mathcal{V}_{SNR}$	1% V_{SB}
Fraction of cosmic rays reaccelerated at SNR	χ	1%
*Injection parameter of SNR shocks	ξ	3.5
Maximum momentum in SNR shocks	p_{max}	1 PeV/c
TURBULENCE		
Source of the turbulence at the largest turbulent scale	S	
Energy spectrum of the turbulence	W	
*Efficiency of turbulence generation	η_T	$1 - 30$%
*Relaxation time of the turbulence generated by SNR	τ_T	1 Myr
*Largest turbulent scale	λ	10 pc
Smallest turbulent wavenumber	k_0	
Non-thermal turbulence damping rate	Γ	
*Large scale magnetic field	B_0	10 µG
Random component of the magnetic field	δB	$1 - 10$ µG
Total magnetic field	B	$10 - 20$ µG
Turbulence level	η	$1 - 10$%
Alfvén velocity	v_A	$10 - 100$ km/s
Root-mean-square velocity	δu	$10 - 100$ km/s
PARTICLE TRANSPORT		
Particle distribution function	$f(x, p, t)$	
Particle spectrum	$n(p, t)$	
Particle velocity	v	$0.3 - 3 \times 10^8$ m/s
Particle kinetic energy	$\epsilon(p)$	10 MeV − 10 PeV
Spatial diffusion coefficient	D_x	10^{27-28} cm^2/s at 1 GeV/c
Momentum diffusion coefficient	D_p	1 (GeV/c)^2/Myr at 1 GeV/c
Escape time from the superbubble	τ	1 Myr at 1 GeV/c
Flux of particles coming from the interstellar medium	ϕ_{ISM}	
Flux of particles escaping in the interstellar medium	$\Phi(E)$	

Table 6.1: Notations used in this chapter. The third colum provides typical values. The input parameters of the model are highlighted in red with a star.

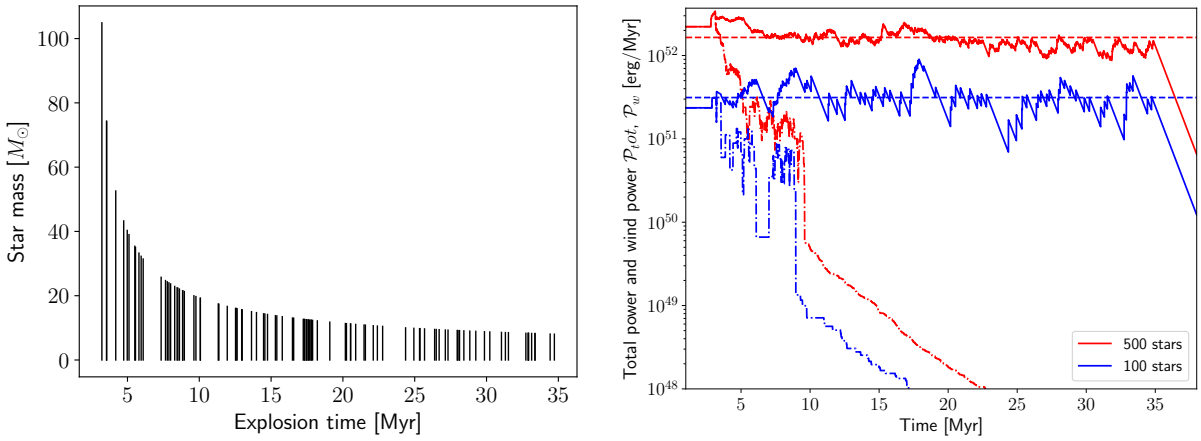

Figure 6.1: Left: Supernova explosion times as a function of stellar mass for a cluster of 100 stars in the range 8-150 $M_\odot$. Right: Evolution of the mechanical power of the cluster assuming a relaxation time $\tau_T = 1$ Myr for the supernova remnant perturbations (see Equations 6.2 and 6.7). The dash-dotted lines indicate the contribution of the winds, $\mathcal{P}_w$. The dashed lines indicate the average luminosities.

expanding superbubble filled by hot and diluted gas is blown around the cluster. It was shown in Section 1.2.1 that the radius of the superbubble evolves as (Castor et al., 1975; Weaver et al., 1977; McCray and Kafatos, 1987):

$$R_b(t) \approx 86\ \xi_b^{1/5} \left(\frac{L_*}{10^{38}\ \mathrm{erg/s}}\right)^{1/5} \left(\frac{n_{ISM}}{\mathrm{cm}^{-3}}\right)^{-1/5} \left(\frac{t}{\mathrm{Myr}}\right)^{3/5} \mathrm{pc}\,, \tag{6.1}$$

where L_* is the total average power injected in the superbubble by stellar winds and supernova explosions, n_{ISM} is the hydrogen number density of the surrounding medium, and ξ_b a numerical factor accounting for various loss processes, as discussed in Section 1.5. As shown by Figure 1.13, observations suggest $n_{ISM}/\xi_b \approx 450\ \mathrm{cm}^{-3}$. In the following we will assume $n_{ISM} = 100\ \mathrm{cm}^{-3}$, which is a typical density of giant molecular clouds where young clusters are expected to be born and expand (Parizot et al., 2004). This implies $\xi_b \approx 22\%$.

To estimate the wind mechanical power, denoted $\mathcal{P}_w$ in the following, we account for both the main sequence and Wolf-Rayet wind phases, while we neglect the red supergiant phase which gives a negligible contribution (Seo et al., 2018). Stellar evolution models provide an estimate of the wind power in either phase as (Seo et al., 2018):

$$\begin{aligned} \log_{10}\left(\frac{\mathcal{P}_{w,MS}(M)}{\mathrm{erg\ Myr}^{-1}}\right) &\approx -3.4\,(\log_{10} M)^2 + 15\log_{10} M + 34\,, \\ \mathcal{P}_{w,WR}(M) &\approx 6\times 10^{48} M^{1.2}\ \mathrm{erg\ Myr}^{-1}\,. \end{aligned} \tag{6.2}$$

While the duration of the main sequence is computed from the fits provided by Limongi and Chieffi (2006), the duration of the Wolf-Rayet phase is assumed to be 320 kyr, independently on the initial mass of the star provided it is higher than 20 $M_\odot$ (Seo et al., 2018).

As an example, for the typical stars in our cluster, $M \sim 20 M_\odot$ and the corresponding lifetime is around 20 Myr, such that the total wind energy in the main sequence is of the order 10^{49} erg while the total wind energy in the Wolf-Rayet phase is around 10^{50} erg.

For the most massive O stars, $M \sim 100 M_\odot$, the total wind energy reaches 10^{51} erg which is comparable to the mechanical energy of a supernova explosion.

The mechanical power of two randomly generated clusters containing respectively 100 and 500 massive stars is plotted in the right panel of Figure 6.1. In the early stage of the cluster ($t \lesssim 5$ Myr), the contribution of the Wolf-Rayet stars dominates, while in older superbubbles the supernovae are the main sources of mechanical power. Because the Wolf Rayet and supernova remnant phases last for a short time, the injection of mechanical energy in the bubble is intermittent, although the mean value is roughly constant in time. The wind power quickly drops after 10 Myr, which is the time at which all stars of mass higher than $20 M_\odot$ have exploded. Then there only remain main sequence stars. Eventually, the average power of supernovae over the lifetime of the cluster is 9×10^{35} erg/s/star while the average power of winds is 9×10^{34} erg/s/star, for a total average power of 10^{36} erg/s/star. The winds are therefore subdominant, yet non negligible, in particular because the input from supernovae is strongly intermittent. The total production of energy by a cluster of 100 massive stars is of the order 10^{53} erg. Note that the average power injected into the superbubble, $\int_0^{\mathcal{T}_{SB}} \mathrm{d}t \mathcal{P}_{tot}(t)/\mathcal{T}_{SB}$, is equal to the average luminosity (or mechanical power) of the cluster L_* which drives the dynamics of the bubble (see Equation 6.1).

If the average luminosity of a cluster of N_* massive stars is $L_* = 10^{36} N_*$ erg/s, Equation 6.1 can be rewritten as:

$$R_b(t) \approx R_0 N_*^{1/5} \left(\frac{t}{\mathrm{Myr}} \right)^{3/5} , \tag{6.3}$$

where $R_0 = 34\ \xi_b^{1/5} \left(n_{ISM}/\mathrm{cm}^{-3}\right)^{-1/5} \mathrm{pc} \approx 10$ pc. Assigning a numerical value to R_0 is sufficient to determine the entire dynamical evolution of the superbubble.

As the superbubble expands, its interior is diluted and cooled, while interstellar matter evaporates from the shell to the interior. We recall here the scalings derived in Section 1.2.1 (Equations 1.11, 1.12, see also Mac Low and McCray, 1988):

$$n(t) = 0.34\ \mathrm{cm}^{-3} \left(\frac{\xi_b N_*}{100} \right)^{6/35} \left(\frac{n_{ISM}}{100\ \mathrm{cm}^{-3}} \right)^{19/35} \left(\frac{t}{\mathrm{Myr}} \right)^{-22/35} , \tag{6.4}$$

$$T(t) = 4.8 \times 10^6\ \mathrm{K} \left(\frac{\xi_b N_*}{100} \right)^{8/35} \left(\frac{n_{ISM}}{100\ \mathrm{cm}^{-3}} \right)^{2/35} \left(\frac{t}{\mathrm{Myr}} \right)^{-6/35} . \tag{6.5}$$

Together with the expansion of the outer shock, the evolution of the density and the temperature describes the dynamical superbubble environment.

6.1.2 Turbulence generation

Inside the superbubble, the mechanical energy of the stars is converted into turbulence which cascades from the largest scale to the dissipation scale (see Section 1.3). We assume equipartition of the kinetic and magnetic energies in the waves and denote W the spectral energy density such that $\int \mathrm{d}k W(k) = \delta B^2/4\pi$. As discussed in Section 2.1.3, the dynamics of the turbulence can be described by the following nonlinear local energy transfer (Zhou and Matthaeus, 1990; Norman and Ferrara, 1996; Miller and Roberts, 1995; Ptuskin et al., 2005):

$$\partial_t W + \partial_k \left(\frac{a}{\sqrt{\rho}} k^{5/2} W^{3/2} \right) = -\Gamma(k) W + S\delta(k - k_0) , \tag{6.6}$$

where $a \approx 0.8$ is a numerical constant determined from experiments or simulations (e.g. Verma et al., 1996), ρ is the gas density, $2\pi/k_0$ is the largest turbulence scale, S is the power transferred from the stars to the turbulence at the largest scale and Γ is the damping rate.

We assume that both winds and supernovae convert a fraction η_T of their mechanical energy into magnetised waves, and that the conversion is exponentially suppressed for supernova remnants, such that the source term of the turbulence cascade is phenomenologically written as:

$$S = \frac{\eta_T}{V_{SB}(t)}\mathcal{P}_{tot}\,, \quad \mathcal{P}_{tot} = \sum_{i=1}^{N(t)} \mathcal{P}_w(M_i) + \sum_{N(t)+1}^{N_*} \frac{E_{SN}}{\tau_T} e^{-(t-t_i)/\tau_T}\,, \tag{6.7}$$

where $N(t)$ is the number of stars remaining in the cluster at time t, t_i is the time at which the star number i is expected to explode, $E_{SN} = 10^{51}$ erg is the energy of a supernova and τ_T is the relaxation time of the turbulence after a supernova explosion, which is assumed to be much smaller that the lifetime of the cluster. This recipe is similar to that adopted in Fang et al. (2019) (see also the discussion in Section 1.3 and references therein).

In the stationary regime, the general solution of Equation 6.6 reads:

$$W(k) = k^{-5/3}\left(\frac{\sqrt{\rho}S}{a}\right)^{2/3}\left(1 - \frac{1}{3}\left(\frac{\rho}{Sa^2}\right)^{1/3}\int_{k_0}^{k} \mathrm{d}k' \frac{\Gamma(k')}{k'^{5/3}}\right)^2 . \tag{6.8}$$

In the absence of damping, one retrieves the Kolmogorov scaling $W \propto k^{-5/3}$. The generalisation to another turbulence regime (e.g. Kraichnan) is straightforward. The test-particle solution provides an estimate of the energy density contained in the turbulence:

$$\frac{\delta B^2}{4\pi} \approx \rho \delta u^2 \approx \frac{3}{2}\left(\frac{\sqrt{\rho}S}{ak_0}\right)^{2/3} . \tag{6.9}$$

Considering turbulence strengths above this limit would violate energy conservation in the cluster. Equation 6.9 allows to estimate the turbulent magnetic field δB and velocity δu:

$$\delta B \lesssim (5\ \mu\mathrm{G})\left(\frac{n}{0.01\ \mathrm{cm}^{-3}}\right)^{1/6}\left(\frac{\eta_T\mathcal{P}_{tot}}{10^{51}\ \mathrm{erg/Myr}}\frac{\lambda}{10\ \mathrm{pc}}\right)^{1/3}\left(\frac{R_b}{50\ \mathrm{pc}}\right)^{-1}, \tag{6.10}$$

$$\delta u \lesssim (110\ \mathrm{km/s})\left(\frac{n}{0.01\ \mathrm{cm}^{-3}}\right)^{-1/3}\left(\frac{\eta_T\mathcal{P}_{tot}}{10^{51}\ \mathrm{erg/Myr}}\frac{\lambda}{10\ \mathrm{pc}}\right)^{1/3}\left(\frac{R_b}{50\ \mathrm{pc}}\right)^{-1}, \tag{6.11}$$

where $\lambda = 2\pi/k_0$ is the largest turbulent scale.

The density, power and radius of the cluster depend on the total number of stars N_* as well as the time t. From the scalings derived above we get to conclude that the random component of the velocity δu is weakly dependent on the total number of stars: $\delta u \propto N_*^{8/105}$, while it decreases with time as $\delta u \propto t^{-41/105}$. The sound speed being of the order of 100 km/s inside the superbubble, the turbulence is expected to consist in an ensemble of weak secondary shock waves in the early times of the cluster history, namely the first few million years. The transport of charged particles in strong supersonic turbulence has been investigated by Bykov et al. in a series of seminal articles and conference proceedings, as reviewed in Section 5.1. In the following we shall rather analyse the acceleration of particles in more evolved superbubbles, in which the turbulence

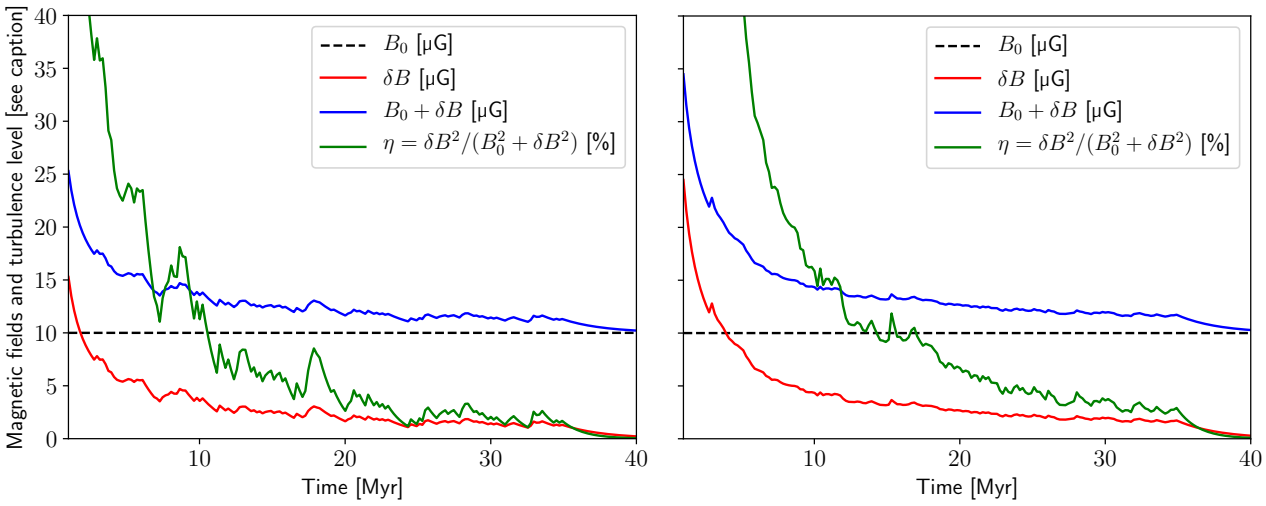

Figure 6.2: Evolution of the turbulent magnetic field and turbulence level in a typical superbubble with $N_* = 100$ (left) and $N_* = 500$ (right).

is expected to be subsonic. One should nevertheless keep in mind that the early phase of efficient particle acceleration in supersonic turbulence could last several million years and be a very efficient source of cosmic rays (e.g. Bykov et al., 1995; Bykov, 2001).

The evolution of the random component of the magnetic field is plotted in Figure 6.2 for two clusters containing respectively 100 and 500 massive stars, where we assumed a background field $B_0 = 10$ μG and an efficiency of turbulence generation $\eta_T = 30\%$. The quasi-linear theory is, strictly speaking, only valid when $\delta B < B_0$, or $\eta < 50\%$, where $\eta = \delta B^2/(B_0^2 + \delta B^2)$ is the turbulence level. This is verified after a few million years for a background field $B_0 = 10$ μG. On the other hand, the turbulence may remain strong during all the lifetime of the cluster if e.g. $B_0 = 1$ μG (still assuming $\eta_T = 30\%$).

The turbulence level decreases rapidly in the first million years as Wolf-Rayet stars explode and the wind power diminishes. Then it stabilises after about 10 Myr around a few percent (for $B_0 = 10$ μG, when only main sequence stars remain and the main sources of turbulence are the supernovae.

6.2 Particle acceleration and transport in superbubbles

In this section, the microphysical processes described in the previous chapters are applied to superbubble environments.

6.2.1 Particle acceleration at stellar wind termination shocks

We have seen in Section 1.2.1 that the stellar outflows may form a collective termination shock around a star cluster. The position of the termination shock R_s is determined by the equilibrium between the ram pressure of the collective wind and the pressure in the interior of the superbubble (Section 1.2.1), which provides, in terms of the parameters adopted in the present chapter:

$$R_s \approx \frac{(\xi_b L_*)^{-1/5} \mathcal{P}_w(t)^{1/2}}{(10^{36}\ \mathrm{erg/s})^{3/10}} \left(\frac{n_{ISM}}{100\ \mathrm{cm}^{-3}}\right)^{-3/10} \left(\frac{V_w}{10^3\ \mathrm{km/s}}\right)^{-1/2} \left(\frac{t}{1\ \mathrm{Myr}}\right)^{2/5} \mathrm{pc}\,, \quad (6.12)$$

where $L_* \approx 10^{36} N_*$ erg/s is the average mechanical power imparted by the winds and the supernovae which determines the pressure in the interior of the superbubble, while $\mathcal{P}_w(t)$ is the mechanical power of the winds, which determines the ram pressure of the termination shock. In the early phase of the cluster life, the radius of the termination shock may reach about 10 pc. On the other hand, after 10 Myr only main sequence stars remain and the wind power is subdominant, such that the collective termination shock can barely be sustained and shrinks to a sub-parsec size. For simplicity, we will therefore consider *loose clusters* in the following, assuming that the extent of the cluster (or that of the region of energy deposition) is of the order of 10 pc. In this case, a collective wind termination shock cannot form and the winds produce isolated strong shocks around each stars, with radii determined by Equation 6.12 provided the total wind power $\mathcal{P}_w$ is replaced by the power of the individual stars.

A fraction of the mechanical energy of the winds can be converted into cosmic rays via diffusive shock acceleration operating at the individual wind termination shocks (Cesarsky and Montmerle, 1983; Seo et al., 2018). Because winds do not produce a high energy density of particles, we assume that this acceleration process takes place in the test-particle regime. We can therefore describe the acceleration of particles at the wind termination shock as a continuous and time dependent injection of cosmic rays characterised by an injection rate of particles of momentum p equals to:

$$q_w(p) = \frac{\eta_w p^{-4} e^{-p/p_w}}{4\pi \mathcal{N}_w} \sum_{i=1}^{N(t)} \mathcal{P}_w(M_i)\,, \tag{6.13}$$

with $\eta_w \approx 10\%$ the fraction of the wind mechanical energy that goes into cosmic rays, $\mathcal{P}_w(M_i)$ the mechanical power of the wind ejected by the ith star in the cluster, p_0 the injection momentum, p_w the maximum one, and $N(t)$ the number of stars remaining in the cluster (i.e. not yet exploded) at time t. The maximum momentum achievable in a nearly stationary wind termination shock is expected to be limited by the size of the shock rather than its lifetime: $p_w \sim ZeBV_wR_s \sim 10^5$ GeV (e.g. Voelk and Biermann, 1988; Morlino et al., 2021). Finally, $\mathcal{N}_w$ is a normalisation constant given by the following integral:

$$\mathcal{N}_w = \int_{p_0}^{p_w} \mathrm{d}p\, \epsilon(p) p^{-2} e^{-p/p_w}, \tag{6.14}$$

where $\epsilon(p)$ is the kinetic energy of protons of momentum p.

6.2.2 Particle reacceleration at supernova remnant shocks

When a star explodes into a supernova, not only it injects fresh cosmic rays in the stellar cluster, but it also reaccelerates a fraction of the already existing particle distribution. The lifetime of a supernova remnant in the medium of density 0.01-0.1 cm^{-3} is of the order 10-100 kyr, which is short compared to the time of diffusion away from the cluster (Myr), hence we assume that the supernovae are instantaneous and compute cosmic ray propagation only between them (Ferrand and Marcowith, 2010). The cosmic ray spectrum after the passage of the supernova shock, $n_f(p)$, is written as:

$$n_f(p) = \mathcal{V}_{SNR}\, \mathcal{R} \left[\frac{n_i}{V_{SB}}\right] + \left(1 - \frac{\mathcal{V}_{SNR}}{V_{SB}}\right) n_i\,, \tag{6.15}$$

where n_i is the spectrum of cosmic rays preexisting before the supernova explosion, $\mathcal{V}_{SNR}$ is the volume spanned by the supernova remnant, $V_{SB} = 4\pi/3R_b^3$ is the volume of the superbubble and $\mathcal{R}$ the "reacceleration operator". In the test-particle limit, this operator simply reads (see Equation 5.14):

$$\mathcal{R}[f] = 4\int_{p_0}^{r^{1/3}p} \frac{\mathrm{d}p'}{p'} \left(\frac{r^{1/3}p}{p'}\right)^{-4} \left(f(p') + \eta_{SNR}\delta\left(p' - p_0\right)\right) , \tag{6.16}$$

which describes both the injection of particles from the thermal bath with an efficiency η_{SNR} at the injection momentum p_0 and the reacceleration of the preexisting distribution of particles. As seen in Chapter 5, the test-particle reacceleration operator cannot be applied in environments where multiple shocks are expected over small timescales. We indeed realised that in superbubbles, this would systematically lead to the violation of the energy conservation (most supernovae would transfer more than 10^{51} erg into non-thermal particles). The linear reacceleration operator must therefore be substituted by the nonlinear computation described in Section 5.3 (Vieu et al., 2021b). Let us briefly recall that in order to take into account the feedback of the cosmic ray pressure on the hydrodynamic profile and small-scale turbulence, two differential equations must be solved together with suitable boundary conditions. On one hand, the shock structure is modified by the non-thermal particles according to the conservation of momentum, while on the other hand the acceleration of the particles is driven by the transport equation integrated around the shock. We also recall that the injection efficiency η can be related to the injection momentum by imposing the continuity between the thermal and non thermal distributions of particles at the injection momentum (Blasi et al., 2005, see Section 3.2). Finally, adiabatic decompression is computed after the explosion of each supernova. As shown in Section 5.5, the reaccelerated spectrum tends towards a universal shape after a few successive reaccelerations. In consequence the injection parameter is not expected to play a major role. In the following, we will take an injection parameter $\xi = 3.5$, which is defined such that, in the absence of preexisting particles ahead of the shock, the remnant transfers about 10^{50} erg into non-thermal cosmic rays. Assuming that supernova remnants are strong shocks, the only remaining parameter is the maximum momentum. We constrain the latter in a simple and conservative approach, without assuming field amplification far upstream of the supernova shock[1]. As seen in Section 3.5, the most stringent limitation is the acceleration time. The latter depends on the dynamics of the supernova remnant, which is not straightforward to compute when the shock expands in an inhomogeneous medium. Disregarding these complications, we assume that the velocity is constant in the free expansion phase, which is a good approximation especially when the remnant expands in a wind density profile (e.g. Finke and Dermer, 2012; Gaggero et al., 2018). We then recover the situation described in Section 3.1. If the magnetic field is not amplified, the maximum momentum is achieved at the end of the free expansion phase, which coincides with the peak of the mechanical power of the shock and reads (see Equations 3.16 and 1.17):

$$p_{max} = 1.4 \text{ PeV} \frac{ZB}{10\ \mu\text{G}} \left(\frac{V_{SN}}{3000\ \text{km/s}}\right) \left(\frac{M_e}{10M_\odot}\right)^{1/3} \left(\frac{n}{0.01\text{cm}^{-3}}\right)^{-1/3} , \tag{6.17}$$

[1]The merging of the remnant with the ambient medium does generate turbulence inside the superbubble according to Equation 6.7, which amplifies the magnetic field *a posteriori*, and the resonant streaming instability does excite Alfvén waves in the shock precursor, as described in Section 3.7.1, but we assume that the field is not significantly amplified far away upstream during the expansion of the remnant, such that the maximum achievable momentum is not enhanced.

where n and B are respectively the density and the total magnetic field in the interior of the superbubble. Although this is admittedly a rough estimate, it allows to get rid of an otherwise free parameter without solving the time-dependent nonlinear problem of shock reacceleration accounting for the multiple environments the remnant experiences before entering the adiabatic phase. Besides, it contains all the relevant physical ingredients. The maximum momentum is indeed expected to increase with enhanced magnetic field and in low density media which provide longer acceleration times.

As seen in Chapter 5, a substantial fraction of the non-thermal energy leaks upstream, carried by high-energy particles beyond the maximum momentum. Because these particles will quickly escape from the superbubble (within typically 10 kyr), they are not expected to affect the overall cosmic ray content and we disregard them in the present analysis. However, they should interestingly provide an intermittent input of very high energy particles in the galaxy, leaving a signature in the region of the knee which is observed in the galactic cosmic ray spectrum.

The only remaining quantity to constrain is the volume spanned by the supernova remnant, $\mathcal{V}_{SNR}$, which determines the fraction of cosmic rays reaccelerated by the expanding shock (Equation 6.15). In the hot rarefied medium characterising the superbubble interior, a supernova remnant becomes subsonic before becoming radiative (Mac Low and McCray, 1988). In principle, $\mathcal{V}_{SNR}$ should therefore correspond to the volume spanned by the supernova remnant before the forward shock weakens. However, diffusive shock acceleration is solved under the hypothesis of stationarity and the Mach number at which the shock "weakens" is not well defined, although it is typically expected to lie in between 1-10. Instead of keeping it as a free parameter, we rather impose that the kinetic energy of the stationary strong shock multiplied by the volume $\mathcal{V}_{SNR}$ equals the energy of the supernova explosion:

$$\rho \mathcal{V}_{SNR} u_0^2/2 = 10^{51}\ \mathrm{erg}\,, \tag{6.18}$$

which ensures that the energy of the stationary shock will never exceed the energy budget of the time-dependent supernova. The fraction of reaccelerated cosmic rays thus reads:

$$\frac{\mathcal{V}_{SNR}}{V_{SB}} \approx \min\left(5.9\left(\frac{R_b(t)}{20\ \mathrm{pc}}\right)^{-3}\left(\frac{n(t)}{0.01\ \mathrm{cm}^{-3}}\right)^{-1}\left(\frac{u_0}{1500\ \mathrm{km/s}}\right)^{-2}, 1\right)\,, \tag{6.19}$$

where t is the age of the superbubble in Myr and $u_0 \approx 1500$ km/s is the velocity of the supernova remnant shock at the beginning of the Sedov-Taylor phase, which is independent on the density and thus stays nearly constant throughout the superbubble evolution (Parizot et al., 2004). Equation 6.18 could have been equivalently obtained by imposing that the acceleration process stops when the Mach number of the supernova shock falls below $\mathcal{M}_{min} \approx 2.5\left(\frac{u_0}{1500\ \mathrm{km/s}}\right)^{7/2}\left(\frac{T}{10^6\mathrm{K}}\right)^{-1/2}$, which is consistent with the intuitive definition of a "weak" shock. Assuming $N_* = 100$ and $n_{ISM} = 100\ \mathrm{cm}^{-3}$, and using the scaling described above, Equation 6.19 becomes: $\mathcal{V}_{SNR}/V_{SB} \approx \min\left(0.16(t/\mathrm{Myr})^{-1.17}, 1\right)$, which means that only a few percent of the cosmic ray content will be reaccelerated by a given remnant.

To summarise, in order to reduce an expanding supernova to a stationary shock, we assume that *(i)* the stationary shock velocity is equal to the velocity of the supernova at the beginning of the Sedov-Taylor phase ($u_0 = 1500$ km/s), *(ii)* the stationary shock disappears when its integrated kinetic energy $\rho \mathcal{V}_{SNR} u_0^2/2$ is equal to the energy of the supernova explosion (10^{51} erg), *(iii)* particles are injected from the thermal bath with a

stationary efficiency such that in the absence of preexisting particles 10^{50} erg are transferred into cosmic rays ($\xi = 3.5$), *(iv)* the time-independent maximum energy achieved by the freshly injected particles as well as that beyond which reaccelerated particles escape upstream is about that reached at the end of the free expansion phase[2], *(v)* we disregard the upstream flux of very high energy particles assuming that they quickly leave the superbubble.

6.2.3 Stochastic acceleration

When they propagate inside the superbubble, particles experience resonant scattering against the hydromagnetic waves (Chapter 2). Each scattering deflects the particles in such a way that on average, an effective diffusion takes place both in space and momentum. The momentum diffusion operator reads:

$$\partial_t f = \frac{1}{p^2}\partial_p \left(p^2 D_p \partial_p f(p)\right) , \tag{6.20}$$

where $f(p)$ is the distribution function averaged over the spherical coordinates μ and ϕ:

$$f(p) = \frac{1}{4\pi}\int_0^{2\pi} \mathrm{d}\phi \int_{-1}^{1} \mathrm{d}\mu\, f(p,\mu,\phi)\,, \tag{6.21}$$

where μ is the pitch-angle cosine and ϕ the gyrophase, and D_p is the pitch-angle averaged diffusion coefficient: $D_p(p) = 1/2\int_{-1}^{1}\mathrm{d}\mu D_p(p,\mu)$. These normalisations ensure that the number density of the particles reads $n = 4\pi\int \mathrm{d}p p^2 f(p)$.

The quasi-linear theory of particle diffusion in turbulence provides the following expression for the pitch-angle averaged diffusion coefficient D_p (Equation 2.55):

$$D_p = \frac{\pi^2 Z^2 e^2 v_A^2}{v}\int_{ZeB/p}^{\infty}\frac{\mathrm{d}k}{k}\left(1-\left(\frac{ZeB}{kp}\right)^2\right)W(k)\,, \tag{6.22}$$

where W describes both co- and counter-propagating waves of equal energy. Here and in the following the background magnetic field B_0 which appears in the formulae derived in Chapter 2 is systematically supplemented by the perturbation δB computed according to Equation 6.10 and we write the total field $B = B_0 + \delta B$. This allows to consistently account for the case of strong turbulence, $\delta B \gtrsim B_0$, where the quasi-linear theory only makes sense locally, for particles follow the mean resulting field. An accurate description of the strong turbulence regime is beyond the scope of this work. We recall that for the parameters considered in this analysis, the turbulence is strong only in the early phase of the superbubble evolution.

Once again, in the case where the energy of the diffusing particles is similar to that of the turbulence, one must account for the backreaction of the particles on the turbulence, which is expected to damp the waves. The procedure to include this nonlinear effect has been described in Section 2.4. Let us recall that the non-thermal wave damping term was derived as (Equation 2.70):

$$\Gamma(k) = \frac{8\pi^3 Z^2 e^2 v_A^2}{k}\int_{ZeB/k}\mathrm{d}p\, p f(p)\,. \tag{6.23}$$

[2]In principle the energy of the reaccelerated particles is not limited by the acceleration time but by the finite size of the shock. However both criteria provide very similar estimates at the beginning of the Sedov-Taylor phase.

Injecting this into Equation 6.8 provides the spectrum of the turbulence, which in turn determines the diffusion coefficient D_p. From the stationary solution given by Equation 6.8, and assuming that the turbulence spectrum is steep enough for Equation 6.22 to be approximated within a factor of order unity as $D_p \approx \pi^2 v_A^2 Z^2 e^2 W(ZeB/p)/3v$, we obtain:

$$D_p \approx \frac{\pi k_0^{1/3} p^{5/3}}{12v} \left(\frac{ZeB}{k_0}\right)^{1/3} \left(\frac{S}{a\rho}\right)^{2/3} \left(1 - \frac{2\pi^2}{5} \left(\frac{ZeB}{\rho^2 a^2 S}\right)^{1/3} \int_p \mathrm{d}p' f(p') p'^{8/3}\right)^2 . \quad (6.24)$$

The feedback of the particles on the turbulence reduces the density of the waves and can even terminate the turbulence cascade at a finite scale. Indeed, it may happen that for high enough cosmic ray energy densities the quantity in the parenthesis in Equation 6.24 vanishes at small momenta. Low energy particles will not be able to resonate anymore with the magnetised waves, and their momentum diffusion coefficient should vanish.

To obtain the turbulence spectrum, and thus the momentum diffusion coefficient, we solved the stationary version of Equation 6.6. The timescale of the energy transfer at the scale $2\pi/k$ is $\tau = \rho/(a\sqrt{Wk^3})$. For a Kolmogorov spectrum, this timescale is always much smaller than the scattering time of the particles on the magnetic waves and the hypothesis of stationarity is well justified.

Together with stationarity, other simplifications have been done in the above derivation. We assumed that all modes of the turbulence followed a Kolmogorov-type cascade, whereas in realistic cosmic environments two cascades may coexist, one describing the dynamics of Alfvén waves and the other describing the fast magnetosonic modes. The latter should be described by a Kraichnan spectrum rather than a Kolmogorov scaling (Ptuskin et al., 2003).

6.2.4 Spatial diffusion and escape

When they propagate in the turbulent medium, not only particles are reaccelerated by stochastic scatterings on magnetic waves, but they also experience an effective spatial diffusion until they escape in the interstellar medium. Under the quasilinear hypothesis, the following approximate relation between the spatial and momentum diffusion coefficients is obtained for a Kolmogorov turbulence (Equation 2.57)[3]:

$$D_x D_p \approx 0.2 v_A^2 p^2 . \quad (6.25)$$

This relation, derived for a power law turbulence spectrum $W(k) \propto k^{-5/3}$, is also valid if small scales are damped, providing the largest scales do follow a Kolmogorov scaling. In the test-particle regime, Equation 6.24 eventually provides the following estimate:

$$D_x \approx 10^{28} \beta \left(\frac{p}{m_p c}\right)^{\frac{1}{3}} \left(\frac{B}{10\ \mu\mathrm{G}}\right)^{\frac{5}{3}} \left(\frac{\eta_T L_*}{10^{51}\ \mathrm{erg/Myr}}\right)^{-\frac{2}{3}} \left(\frac{n}{0.01\ \mathrm{cm}^{-3}}\right)^{-\frac{1}{3}} \left(\frac{R_b}{100\ \mathrm{pc}}\right)^2 \mathrm{cm}^2/\mathrm{s} . \quad (6.26)$$

In the case where the cosmic ray energy density is so high that the turbulence cascade terminates at a large scale such that D_p vanishes (this happens when the quantity in parenthesis in Equation 6.24 vanishes, see also Section 2.4.1), the above expression breaks down. In this case, low energy particles do not scatter on waves anymore, but rather

[3]The "standard" relation $D_x D_p = v_A^2 p^2/9$ is only valid in Bohm's regime.

follow the field lines of the background field. In a highly turbulent medium[4], the background field has a coherence length of the order of $0.77/k_0$ (Casse et al., 2001). Low energy particles following the background field do experience a random walk with mean displacement $0.77/k_0$. From a macroscopic point of view, this gives rise to an effective spatial diffusion with diffusion coefficient about $0.3v/k_0$. We conveniently extrapolate the coefficient between the low and high energy regimes as:

$$D_x \approx \left(\frac{5D_p}{v_A^2 p^2} + \frac{3k_0}{v} \right)^{-1} . \tag{6.27}$$

The quasilinear relation given by Equation 6.25 is retrieved whenever the particles scatter on magnetic waves, while in the absence of waves one gets $D_x \approx 0.3v/k_0$. In the intermediate regime, i.e. at scales close to the termination of the turbulence cascade, the density of waves is small: part of the particles scatter on the waves while the others diffuse along the background field. The macroscopic diffusion coefficient is averaged over both processes.

In reality, the diffusion of cosmic rays below the inertial turbulence cascade is a more complicated process than the simple picture presented above, in particular because the anisotropic streaming along the background field is expected to trigger the so-called streaming instability, such that the particles will scatter on the waves they produce. Accounting for the streaming instability requires the knowledge of the spatial gradient of the distribution function along the magnetic field lines, which is beyond the scope of this work. Furthermore, it is not straightforward to solve the turbulence cascade including the growth of the streaming instability. For simplicity, we assume that the background field is chaotic enough to efficiently isotropise the low energy particles, such that the streaming instability can be neglected. Moreover, although it is crucial to account for the feedback of the energetic particles on the hydromagnetic waves, the issue of particle diffusion away from the inertial range of the turbulence is in fact very scarcely raised in the parameter space considered in the present analysis.

We eventually average the transport equation of cosmic rays over the volume of the superbubble such that the spatial diffusion reduces to a leakage with characteristic escape time $\tau = R_b^2/(6D_x)$. The complete averaged transport equation of cosmic rays in the superbubble then reads:

$$\partial_t n = -\frac{n}{\tau} + \frac{1}{p^2}\partial_p \left(p^2 D_p \partial_p n \right) + \frac{1}{p^2}\partial_p \left(p^2 \left[\left.\frac{\mathrm{d}p}{\mathrm{d}t}\right|_{\mathrm{Ad.}} + \left.\frac{\mathrm{d}p}{\mathrm{d}t}\right|_{\mathrm{Int.}} \right] n \right) + q_w \, , \tag{6.28}$$

where $n = V_{SB} f(p)$ is the cosmic ray spectrum in the superbubble. The first loss rate in the right-hand side accounts for the adiabatic decompression of the cosmic ray spectrum in the expanding medium, $\left.\frac{\mathrm{d}p}{\mathrm{d}t}\right|_{\mathrm{Ad.}} = (\epsilon(p)/v)\dot{R}_b/R_b$ (e.g. Finke and Dermer 2012 or Appendix B of Aharonian 2004). The second loss rate $\left.\frac{\mathrm{d}p}{\mathrm{d}t}\right|_{\mathrm{Int.}}$ encodes the losses due to the Coulomb interactions and to the production of pions (Mannheim and Schlickeiser, 1994).

The computation of the cosmic ray dynamics in the superbubble follows the procedure used by Ferrand and Marcowith (2010). In between supernova explosions, the spectrum evolves according to Equation 6.28 implemented within a forward Euler scheme (a Crank-Nicholson scheme can not be used since the momentum diffusion is nonlinear). Whenever

[4]In this case, the quasi-linear approximation used to compute the diffusion of high energy particles on the waves is understood as a local approximation.

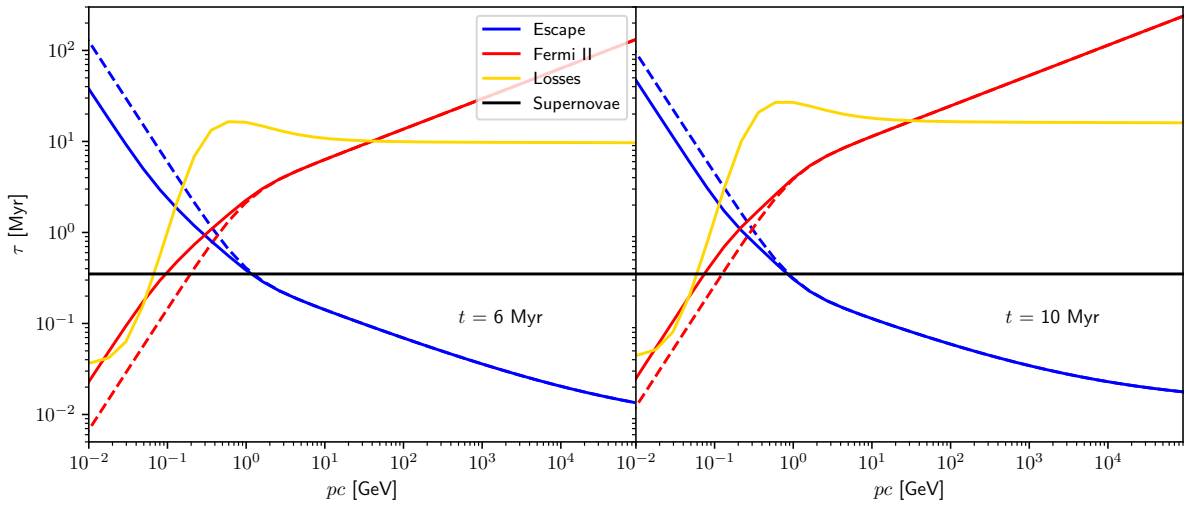

Figure 6.3: Typical timescales of the fiducial superbubble (see the parameters highlighted in red in Table 6.1) for $N_* = 100$, $\eta_T = 30\%$, and two different times (left: 6 Myr, right: 10 Myr). The solid lines correspond to the nonlinear computation accounting for the cosmic ray feedback on the turbulence spectrum, to be compared with the dotted lines displaying the test-particle expectation. The horizontal black line indicates the typical time interval between two supernovae in a cluster of 100 massive stars.

a supernova explodes, the reacceleration of the particles is computed according to the formalism detailed in Section 5.3 (Vieu et al., 2021b). All other physical processes are neglected during the supernova explosion.

6.3 Results

6.3.1 Timescales

Figure 6.3 displays the timescales of stochastic (Fermi II) acceleration $p^2/(2D_p)$ as well as the escape time τ. At high energies ($p \gtrsim 10$ GeV), the standard Kolmogorov scalings are always retrieved. Below 10 GeV, the cascade can be damped if there are enough massive stars in the cluster. In this case, the stochastic acceleration is less efficient than expected in the test-particle limit, while the escape is faster. Sub-GeV energies are driven by the stochastic reacceleration while the escape dominates above GeV bands.

For completeness we added the timescale of the proton losses, including Coulomb collisions, protons-protons interactions, as well as adiabatic decompression. Proton losses are only relevant at the smallest energies. Let us eventually note that two processes have been neglected in this first approach: the contribution of the interstellar cosmic rays leaking inside the superbubble (Tolksdorf et al., 2019) as well as the modification of the diffusion through the magnetised shell (Bouyahiaoui et al., 2019). These will be discussed in the end of the present chapter.

6.3.2 Cosmic ray energetics in superbubbles

Figure 6.4 displays the energetics of the fiducial superbubble described by the parameters highlighted in red in Table 6.1. About 10% of the mechanical power is transferred into cosmic rays. For small clusters ($N_* < 100$), the production of cosmic rays becomes

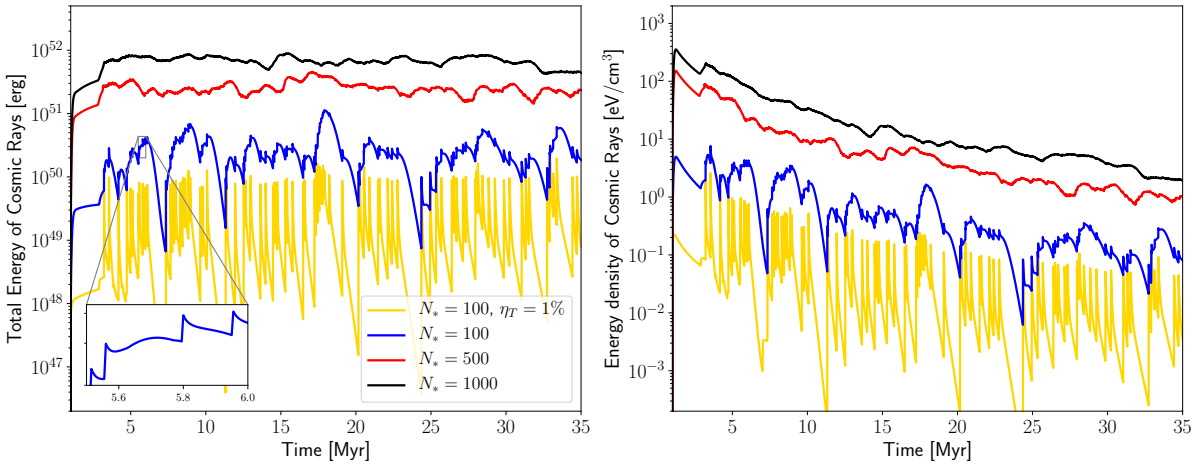

Figure 6.4: Time evolution of the total energy (left) and energy density (right) of cosmic rays inside the superbubble for clusters containing initially 100, 500 and 1000 stars. All the results are obtained with $\eta_T = 30\%$ except those shown by the yellow curves for which $\eta_T = 1\%$.

intermittent, in particular if the turbulence is not efficiently generated, as shown by the yellow curve where we set $\eta_T = 1\%$. In this case the particles are not confined and the superbubble is closer to a collection of individual supernova shocks.

As shown by the zoomed-in window in the left panel of Figure 6.4, the acceleration of cosmic rays proceeds in two steps. First, diffusive shock acceleration at supernova remnant shocks injects nonthermal particles inside the superbubble. In the next few 10 kyr, the high energy particles rapidly escape. Meanwhile, low energy particles are reaccelerated in the magnetic turbulence. After around 100 kyr, this second order reacceleration compensates the escape and the total energy increases progressively. However, the process of stochastic reacceleration is only effective at low energies, such that when a substantial fraction of the particles have been reaccelerated, the escape dominates once again and the total energy decreases, until a new star enters the Wolf-Rayet phase.

The right panel of Figure 6.4 displays the time evolution of the cosmic rays energy density inside the superbubble. Densities of the order of 1 to 10 eV/cm^3 are expected in rather small clusters ($N_* < 100$), while larger clusters gathering hundreds of stars may contain a cosmic ray energy density higher than 100 eV/cm^3.

The result of the computation also shows that even when accounting for nonlinear effects, fresh cosmic rays are mainly injected by supernova remnants (e.g. 95% for $\eta_w = 0.1$ or 78% for $\eta_w = 0.5$). The fraction is slightly smaller for more massive clusters (e.g. 64% for a cluster of 500 stars with $\eta_w = 0.5$) because the nonlinear effects are stronger. Yet, the supernovae are dominant in most cases. We also recall that our modelling of the winds as a background injection does not take into account the backreaction of the particles on the shock, which means that the fraction of the particles accelerated by the (linear) winds is the highest we could expect, although the effect of nonlinearities on the fresh injection of particles is rather limited and test-particle results are expected to remain valid within typically 10%.

The energy transfer between the winds and the cosmic rays proceeds mainly indirectly through the stochastic reacceleration in turbulence. Since the particles are confined in the superbubble, this process is very efficient. Nearly all the energy injected from the stars to the turbulence is reinjected into cosmic rays. This could explain the high gamma-ray fluxes detected in e.g. G25.18+0.26 (Katsuta et al., 2017), without requiring an

unrealistically small diffusion coefficient. This statement has to be confirmed by further studies including the inhomogeneity of the turbulence and distribution function. Indeed, if the stars are gathered at the centre of the cluster, they are expected to excite Alfvén waves only in a small region of space. On the other hand, the density of cosmic rays is expected to be higher close to the centre of the bubble, such that most of the particles could still be efficiently reaccelerated.

Because the main source of matter inside the superbubble is the evaporation of interstellar material at the shell interface, most of the material accelerated in the superbubble by supernova remnants is expected to be of galactic composition. A discrepancy is however expected because of the efficient injection of Wolf-Rayet enriched material in the early phase of the cluster life. Although the fraction of cosmic rays accelerated at wind termination shocks is only about 5-10% of that accelerated at supernova remnants, this may be enough to account for the observed overabundance of ^{22}Ne over ^{20}Ne in the galactic cosmic rays, in particular if very massive stars collapse without exploding (Kalyashova et al., 2019; Gupta et al., 2020; Tatischeff et al., 2021).

6.3.3 Intermittency

The time evolution of the particle distribution function is shown in Figure 6.5 for various initial numbers of massive stars. The low energy bands ($p \lesssim 0.1$ GeV) are always intermittent because low energy particles are stochastically reaccelerated in the turbulence as soon as they are injected into the superbubble. Intermediate energies are less intermittent because the stochastic acceleration is less efficient and the escape is slow. In particular, for standard clusters containing hundreds of massive stars, the GeV band is nearly stationary, except if the turbulence level is low (bottom panel of Figure 6.5), in which case even these rather low energies are not confined and escape between supernova explosions. High energies are very intermittent because the escape is faster than the interval between two supernova explosions. Three regimes of cosmic ray production should therefore be distinguished. Whenever the stochastic acceleration time is lower than the average time interval between two supernovae, i.e. $p^2/2D_p(p) < \Delta t_{SN}$, the cosmic ray production is expected to be intermittent. This regime extends up to the momentum p_1 defined by $p_1^2/2D_p(p_1) = \Delta t_{SN}$. In the test-particle approximation, we obtain:

$$\beta(p_*)^3 p_1 = 4 \text{ MeV} \left(\frac{N_*}{100}\right)^{-3} \left(\frac{\eta_T L_*}{10^{51} \text{ erg/Myr}}\right)^2 \left(\frac{\mathcal{T}_{SB}}{35 \text{ Myr}}\right)^3 \times \left(\frac{n}{0.01 \text{ cm}^{-3}}\right)^2 \left(\frac{B}{10 \text{ µG}}\right) \left(\frac{R_b}{50 \text{ pc}}\right)^{-6} . \quad (6.29)$$

Because the damping of the turbulence by non-thermal particles is generally moderate, the test-particle approximation is expected to give reliable estimates on average, even though the nonlinear timescale of diffusion may decrease considerably right after a supernova explosion.

Then, if both the stochastic acceleration time as well as the escape time are larger than the average time interval between two supernovae, i.e. $p^2/2D_p(p), R_s^2/6D_x(p) < \Delta t_{SN}$, the cosmic ray production is expected to be nearly stationary. This regime extends up to

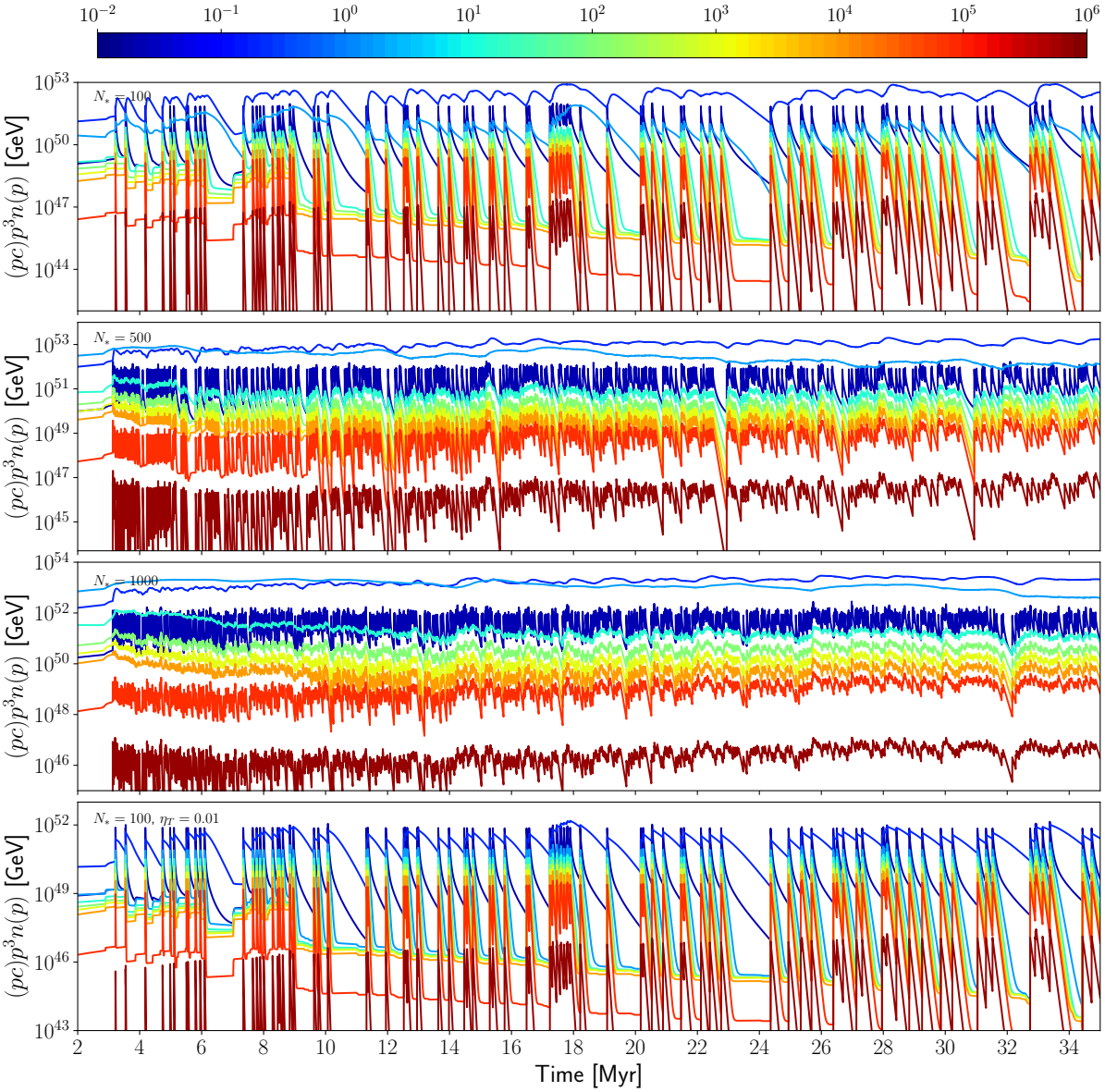

Figure 6.5: Time evolution of the particle distribution function. The parameters of the superbubble are highlighted in red in Table 6.1. Top panel: 100 massive stars. Second panel: 500 massive stars. Third panel: 1000 massive stars. Bottom panel: 100 massive stars, with $\eta_T = 1\%$ instead of 30%. Colours correspond to different momenta (see the colour scale in units of GeV/c at the top). Dark blue: 10 MeV/c. Blue: 0.13 GeV/c. Light blue: 1.6 GeV/c. Turquoise blue: 20 GeV/c. Green: 240 GeV/c. Yellow: 2.9 TeV/c. Orange: 35 TeV/c. Red: 0.43 PeV/c. Dark red: 5.3 PeV/c.

the momentum p_2 defined by $R_s^2/6D_x(p_2) = \Delta t_{SN}$, which translates into:

$$p_2 = 0.09 \text{ GeV} \left(\frac{N_*}{100}\right)^3 \left(\frac{\eta_T L_*}{10^{51} \text{ erg/Myr}}\right)^2 \left(\frac{\mathcal{T}_{SB}}{35 \text{ Myr}}\right)^{-3} \left(\frac{n}{0.01 \text{ cm}^{-3}}\right) \left(\frac{B}{10 \text{ µG}}\right)^{-5}. \tag{6.30}$$

Finally, for $p > p_2$, the escape dominates and the cosmic ray production is expected to be intermittent again. The three regimes can be identified in Figure 6.3, comparing the Fermi II acceleration time (red curve), the escape time (blue curve) and the time interval between supernovae (black line). If the black line is below the other timescales, supernovae can sustain the reacceleration and escape. In other cases, intermittent reacceleration or escape is expected.

It may happen that $p_2 < p_1$. In this case, there are not enough stars to sustain a stationary cosmic ray production against the escape, even at intermediate energies. This translates into an intermittent production of cosmic rays at all energies, as it is the case for the cluster of 100 stars with inefficient turbulence generation ($\eta_T = 1\%$, see bottom panel of Figure 6.5).

For our fiducial clusters containing respectively 100, 500 and 1000 massive stars, Equations 6.29 and 6.30 provide $p_1 \approx 0.1$, 0.04, 0.01 GeV and $p_2 \approx 1$ GeV, 3 TeV, 1 PeV, which is consistent with the curves shown in Figure 6.5. In these cases, the test-particle estimates are proved to be reliable indicators within one order of magnitude.

Eventually, one notices in the top and bottom panels of Figure 6.5 that the winds provide a stationary threshold on top of the intermittent emission due to supernova explosions. Although this contribution is subdominant below TeV energies, it is non negligible at the highest energies, where the escape is efficient.

6.3.4 Spectra

Examples of spectra resulting from our nonlinear computation are shown in Figure 6.6. The overall shape agrees qualitatively with the conclusions drawn by Ferrand and Marcowith (2010), that is, a hard component at low momenta competes with a steep component at high momenta. We denote p_* the momentum of the transition. As we expressed the turbulence spectrum as function of the mechanical energy of the stars rather than as function of the background magnetic field, our expression for p_* differs from that given in Ferrand and Marcowith (2010) even in the test-particle regime:

$$\beta(p_*)^3 p_* \approx 0.1 m_p c \left(\frac{B}{10 \text{ µG}}\right)^{-2} \left(\frac{\eta_T L_*}{10^{51} \text{ erg/Myr}}\right)^2 \left(\frac{n}{0.01 \text{ cm}^{-3}}\right)^{-1/2} \left(\frac{R_b}{100 \text{ pc}}\right)^{-3}. \tag{6.31}$$

One notices that p_* decreases as the superbubble expands, which is a consequence of the dilution of the mechanical energy of the stars in an increasing volume. In the fiducial cluster of 100 massive stars considered in this work, p_* is found around a few to tens of GeV. In typical clusters of several hundreds of stars, p_* can hardly be higher than a few tens of GeV, even considering unrealistic turbulence generation efficiencies because in this case nonlinearities are expected to regulate the stochastic acceleration process by damping the waves.

The shapes of the superbubble spectra are overall well understood by the timescales of the competing reacceleration and escape processes. One may wonder why the high energy "universal" asymptotic solution of successive shock reacceleration computed in Chapter 5 is never retrieved, in particular for the cluster of 1000 massive stars, where the average

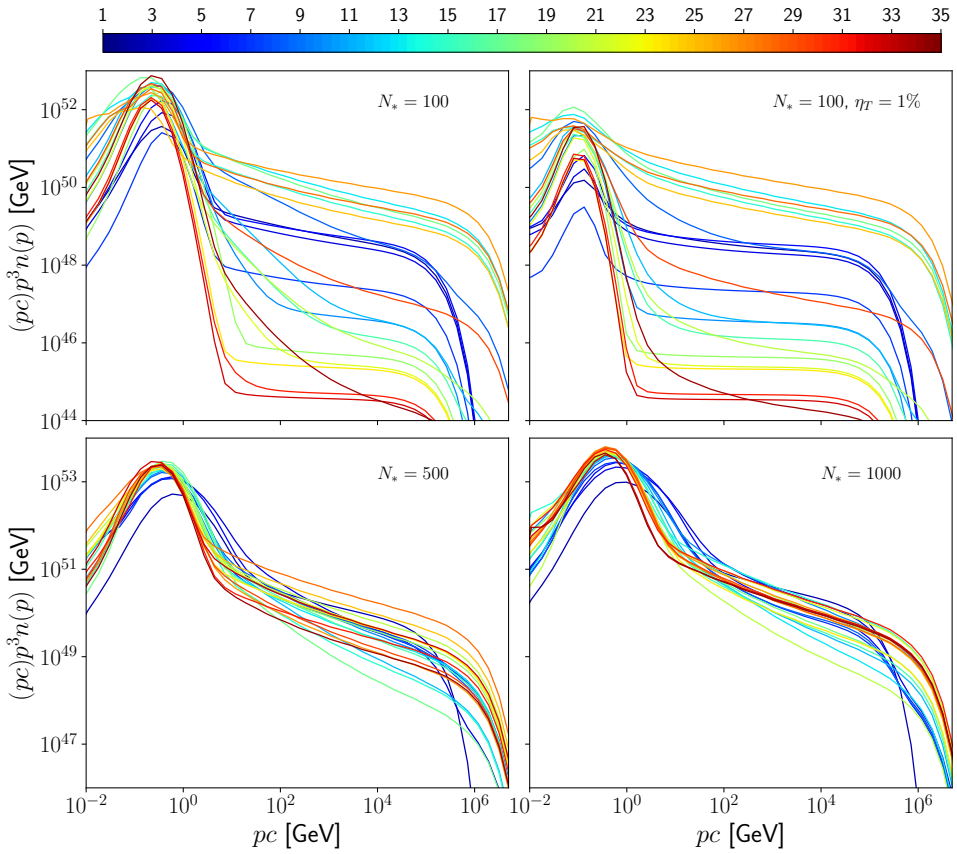

Figure 6.6: Instantaneous superbubble spectra. Each curve corresponds to a different time represented by the colour scale in units of Myr at the top. The parameters of the superbubble are that highlighted in red in Table 6.1, with varying number of stars. Top left panel: $N_* = 100$. Top right panel: $N_* = 100$ with $\eta_T = 1\%$. Bottom left panel: $N_* = 500$. Bottom right panel: $N_* = 1000$.

time interval between supernovae is about 30 kyr, i.e. $\tau_{GeV}/\Delta t \approx 100$. This is because we implicitly assumed, by considering the average cosmic ray spectrum $n(p)$ instead of the distribution function $f(x,p)$, that the (re)accelerated cosmic rays instantaneously homogenise inside the superbubble. Under these circumstances, preaccelerated particles have small chances to be reaccelerated by the next supernova remnant shock, which only spans a few percent of the superbubble volume. Such a situation corresponds to a loose cluster, with large distances between the stars. The case of a compact cluster will be discussed using of a two-zone model in Section 6.4.2.

Finally, although the contribution from the winds is globally subdominant, it yet provides a non-negligible injection of cosmic rays at the highest energies under the form of a constant component of spectral index 4.3.

When integrated over the lifetime of the cluster, the spectra display an enlarged "Fermi II bump" and then a steep high energy tail above 10-100 GeV, as shown in Figure 6.7, where the spectra have been corrected as $\Phi(E) = 4\pi p^2 n(p)/(v(p)\tau(p))$. This corresponds to the cosmic ray flux escaping from the cluster in the interstellar medium, except above 1 PeV where we disregarded the very high energy flux escaping upstream of supernova remnants. Interestingly, the high energy flux is a power law scaling as $\Phi(E) \propto E^{-2.2}$, which would reproduce the $E^{-2.7}$ scaling measured around the Earth if one assumes that the diffusion coefficient of cosmic rays in the interstellar medium scales as $D(E) \propto E^{0.5}$,

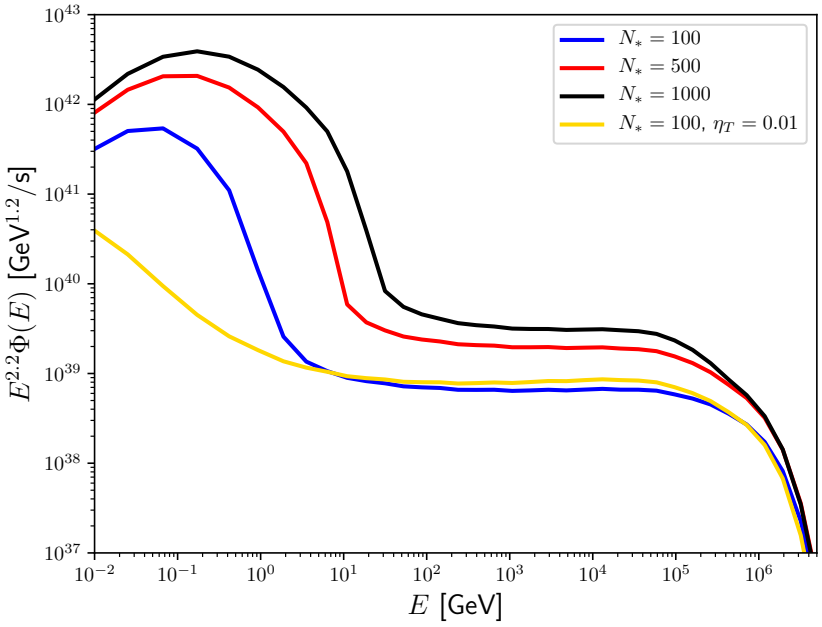

Figure 6.7: Average flux of cosmic rays escaping the superbubble.

as expected in the Iroshnikov-Kraichnan regime of turbulence. Eventually, the transition between the maximum energy achievable in wind termination shocks (about 100 TeV) and that achieved at supernova remnants (about 1 PeV), produces a spectral break between 0.1 and 1 PeV which has a certain resemblance to the knee observed in the galactic cosmic ray spectrum.

6.4 Two-zone model

In this section we show that it is possible to refine the modelling in order to compute supernova reacceleration in compact clusters in a more realistic way as well as to consider the effect of the supershell of the superbubble

6.4.1 Diffusion in a two-zone model

Let us split the interior of the spherical superbubble into two zones, as schemed in Figure 6.8. The left panel presents the general setup while the two other panels display two limit cases of physical interest, which will be discussed below. In this section we stick to a general formalism, assuming that the inner region has a radius R_1 and the outer region has a radius R_b, which is the radius of the superbubble. The boundaries of both areas are therefore separated by a length equal to $R_b - R_1$. Both regions are characterised by diffusion coefficients D_1 and D_2. We eventually denote f_1 and f_2 the average distributions of particles in both regions such that the corresponding energy densities are $n_1 = V_1 f_1$ and $n_2 = V_2 f_2$, where $V_1 = 4/3\pi R_1^3$ and $V_2 = V_{SB} - V_1$ with V_{SB} the volume of the superbubble.

The transport of cosmic rays in the superbubble is then described as a two-zone diffusion-losses model. The transport equation reads:

$$\partial_t f_i = \nabla \cdot (D_i \cdot \nabla f) + \mathcal{D}_i[f_i] + \mathcal{L}_i[f_i] + f_{inj}(t)\,, \tag{6.32}$$

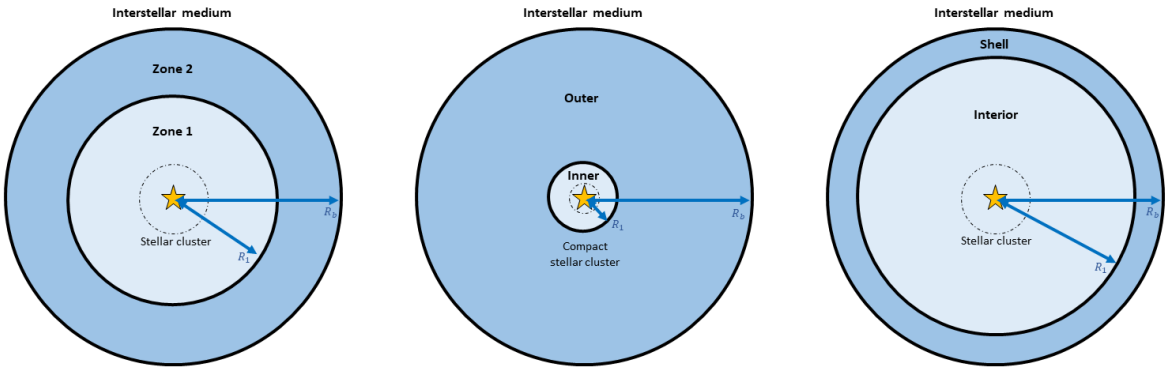

Figure 6.8: Left: Sketch of the two-zone model. Middle: Limit case of a compact cluster, where zone 1 is the region of supernova reacceleration. Right: Limit case of a supershell.

where $i = 1$ (resp. $i = 2$) in the inner (resp. outer) region, $\mathcal{D}_i[f_i] = (1/p^2)\partial_p\left(p^2 D_{p,i}\partial_p f_i\right)$ is the stochastic reacceleration operator, with $D_{p,i}$ the momentum diffusion coefficient and $\mathcal{L}_i$ an operator encoding the various loss processes in both zones. Instead of solving directly Equation 6.32, we average the densities. Denoting τ_{12} the typical time it takes for particles to diffuse from zone 1 to zone 2 (and conversely), and τ_2 the escape time from zone 2 to the interstellar medium, we obtain the following system of differential equations:

$$\left\{\begin{array}{rcl} \partial_t n_1 &=& \frac{n_2-n_1}{\tau_{12}} + \mathcal{D}_1[n_1] + \mathcal{L}_1[n_1] + q_w\,, \\ \partial_t n_2 &=& \frac{n_1-n_2}{\tau_{12}} - \frac{n_2}{\tau_2} + \mathcal{D}_2[n_2] + \mathcal{L}_2[n_2] + \phi_{ISM}\,, \end{array}\right. \tag{6.33}$$

where ϕ_{ISM} is the flux of interstellar particles entering the outer region.

To compute the typical residence time of particles in between zone 1 and zone 2, let us assume that there exists a constant injection of particles Q at $r = 0$, with a free escape boundary at $(R_1 + R_b)/2$. The solution of the stationary diffusion equation in spherical symmetry, $\partial_r(r^2 D\partial_r f) = r^2 Q\delta(r)$, reads:

$$\left\{\begin{array}{l} r < R_1 \quad \text{(zone 1)} \implies f = \frac{Q}{4\pi D_1}\left(\frac{1}{R_1} - \frac{1}{r}\right) + \frac{Q}{4\pi D_2}\left(\frac{2}{R_1+R_b} - \frac{1}{R_1}\right)\,, \\ r > R_1 \quad \text{(zone 2)} \implies f = \frac{Q}{4\pi D_2}\left(\frac{2}{R_1+R_b} - \frac{1}{r}\right)\,. \end{array}\right. \tag{6.34}$$

Integrating this solution from 0 to R_1 and then from R_1 to $(R_1 + R_b)/2$, we obtain N, the total number of particles in between both regions:

$$N = \frac{QR_1^2}{6D_1}\left(1 + \frac{\rho_b}{\delta} + \frac{\rho_b^2}{4\delta}\right)\,, \tag{6.35}$$

where we set $\rho_b \equiv (R_b - R_1)/R_1$ and $\delta \equiv D_2/D_1$. The typical residence time is therefore identified as:

$$\tau_{12} = \frac{R_1^2}{6D_1}\left(1 + \frac{\rho_b}{\delta} + \frac{\rho_b^2}{4\delta}\right)\,, \tag{6.36}$$

which can also be interpreted as the time it takes for a particle to be transferred from one zone to the other.

Eventually, we compute the escape time from zone 2 to the interstellar medium by integrating the transport equation over the volume of zone 2, assuming that the spatial diffusion coefficient in the interstellar medium is much larger than that in zone 2. This provides, by virtue of the divergence theorem:

$$\partial_t n_2 = \oiint (D_2 \cdot \nabla f) \cdot \mathrm{d}\boldsymbol{S} + \mathcal{D}_2\left[n_2\right] + \mathcal{L}_2\left[n_2\right]\,. \tag{6.37}$$

Then we estimate the gradient of particles across the surface $S_b = 4\pi R_b^2$ by means of a linear extrapolation as $\nabla f_2 \sim 2\alpha(f_{ISM} - n_2/V_2)/(R_b - R_1)$, with α a geometrical factor. The surface integral becomes trivial and we eventually get:

$$\partial_t n_2 = \frac{6\alpha D_2 R_b^2 (V_2 f_{ISM} - n_2)}{(R_b^2 + R_b R_1 + R_1^2)(R_b - R_1)^2} + \mathcal{D}_2\left[n_2\right] + \mathcal{L}_2\left[n_2\right] - \iint_{S_1} (D_2 \cdot \nabla f) \cdot \mathrm{d}\boldsymbol{S}\,, \quad (6.38)$$

where f_{ISM} is the diffuse cosmic ray distribution function in the interstellar medium and S_1 the surface of the interface between the two zones. The surface integral over the inner surface S_1 encodes the transfer of particles from zone 1 to zone 2 which has been already computed. From Equation 6.38 we identify the escape time from zone 2 to the interstellar medium as well as the flux of interstellar particles entering the superbubble:

$$\tau_2 = \frac{(R_b^2 + R_b R_1 + R_1^2)(R_b - R_1)^2}{6\alpha D_2 R_b^2}\,, \quad (6.39)$$

$$\phi_{ISM} = \frac{4\pi}{3\tau_2}\left(R_b^3 - R_1^3\right) f_{ISM}\,. \quad (6.40)$$

In the limit case $R_1 \ll R_b$, one should set $\alpha = 1$ to get $\tau_2 = R_b^2/(6D_2)$ which is the diffusion time in spherical symmetry. On the other hand, if $R_1 \approx R_b$, one should set $\alpha = 4$ in order to get $\tau_2 = ((R_b - R_1)/2)^2/(2D_2)$, which is the diffusion time in one dimension.

Now that all timescales have been determined, Equation 6.33 can be written in matrix form and solved iteratively. Such two-zone model can be used to compute for instance the acceleration and transport of cosmic rays in a superbubble where turbulence is only efficiently generated around the stellar cluster, or to account for the residence time of particles in the inner region spanned by successive supernova remnants, or to model the shielding of the interstellar cosmic rays by the dense shell, or last but no least, to probe the modulation of the cosmic ray spectra induced by the supershell with associate non-thermal emission of photons.

6.4.2 Cosmic ray reacceleration in compact clusters

As mentioned earlier, the one-zone model does not properly account for the reacceleration of cosmic rays in compact clusters, for it is implicitly assumed that the accelerated particles homogenise instantaneously in the whole superbubble after the passage of a remnant. The two-zone model can be used to describe the reacceleration process more accurately. Indeed, the inner region can be identified with the volume spanned by supernova remnants $\mathcal{V}_{SNR}$[5]. The radius of supernova remnants is typically 10% the radius of the superbubble such that this situation is close to the limit case $R_1 \ll R_b$ sketched in the middle panel of Figure 6.8. For simplicity we assume that the turbulence is homogeneous in both zones, although in reality it should probably be stronger in the inner zone close to the energy deposition region. Eventually, we neglect the flux of interstellar particles leaking inside the superbubble ($\phi_{ISM} = 0$)[6]. These two simplifications allow to directly compare the output of the two-zone model with the previous results. Moreover, there is no additional free parameter to be introduced.

[5]Because this volume depends on the density of the superbubble interior, it is time-dependent and the radius of the inner region is defined dynamically.

[6]This assumption is generally justified as the energy density of the particles confined in the shell is expected to be much larger than the interstellar cosmic ray energy density.

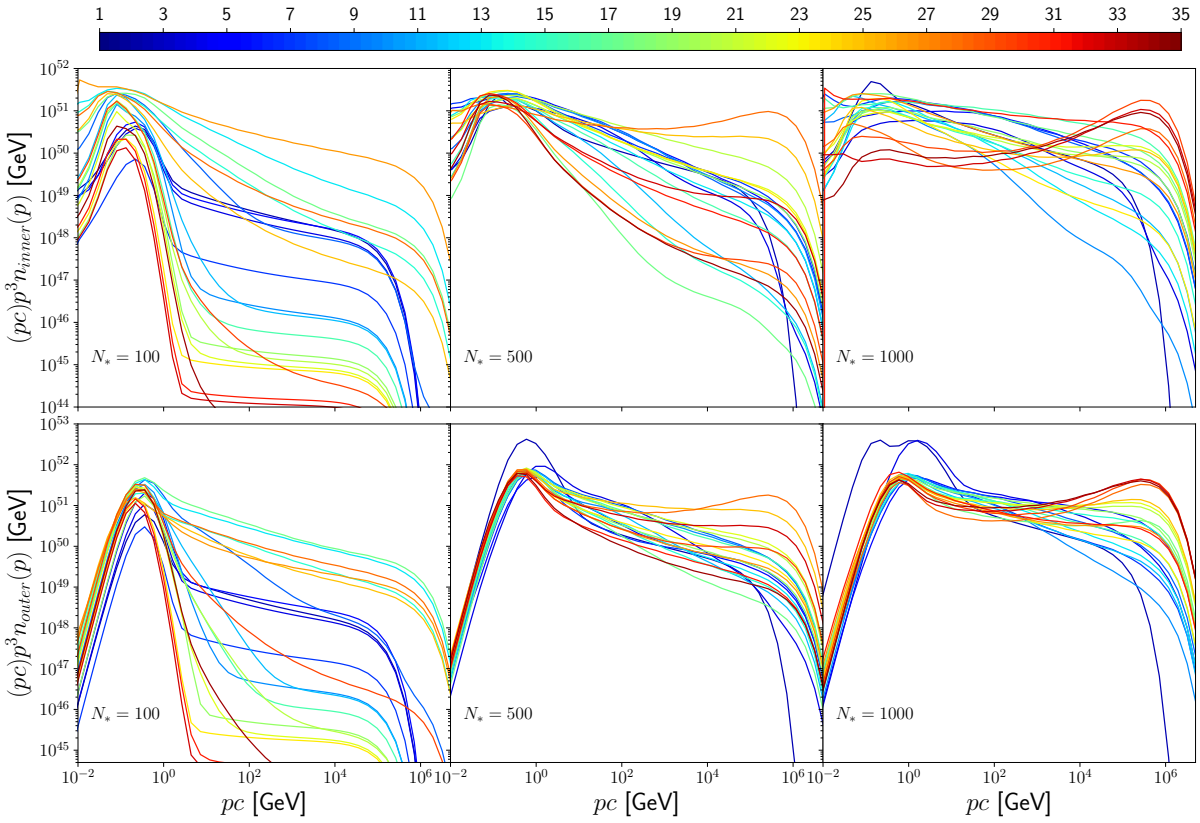

Figure 6.9: Average spectra around a compact cluster modelled as a two-zone model (inner/outer). Each curve corresponds to a different time represented by the colour scale in units of Myr at the top. The number of massive stars is assumed to be 100 (left), 500 (middle) and 1000 (right). The top panels show the spectrum in the inner region spanned by supernova remnants while the bottom panels show the spectrum in the outer region, which fills most of the superbubble volume.

Figure 6.9 displays the spectra obtained in this refined model. The first thing to notice is that the overall normalisation is about one to two orders of magnitude below that obtained using a one-zone model (Figure 6.6). The energy transfer between the supernovae and the cosmic rays is much less efficient because of the backreaction of the cosmic rays onto the shocks in the inner region. Indeed, preaccelerated cosmic rays do not have time to entirely dilute inside the superbubble between two supernova explosions. The particle energy density in the inner region is high, which slows down the shock precursor and makes the acceleration of low-energy particles less efficient (see Chapter 5). On the other hand, if the massive stars are numerous enough, the time interval between supernovae can be smaller than the escape time at intermediate or even high energies and the spectra are efficiently reaccelerated without leaving the region. As expected from the "benchmark" asymptotic solution discussed in Chapter 5, the spectrum resulting from the reacceleration by successive shocks is concave, with a high energy slope close to 3.5 in the case where the escape of the particles is completely neglected. As shown in the middle panel of Figure 6.9, concave spectra are indeed intermittently retrieved in a cluster containing initially 500 massive stars. For a cluster of 1000 stars, as shown in the right panel of Figure 6.9, the reacceleration is very efficient and the benchmark asymptotic spectrum may be achieved up to the highest energies. Then the concave spectrum realised in the inner region is transferred in the outer region, where low energy

bands experience a stochastic reacceleration. The particles will eventually interact with the shell and concave gamma-ray spectra should be expected, which could be a typical signature of massive compact clusters.

Besides, young compact clusters may sustain a collective wind termination shock on a few parsec size. The frontal collision between supernova remnants exploding inside the cluster and the wind termination shock is well described by the set-up discussed in Chapter 4 (if the velocity of the supernova shock is twice that of the stellar outflow, the shocks are exactly in the configuration pictured in Figure 4.1). It is expected that the collision will further reaccelerate preexisting particles of high energies in the region spanned by the remnant. In order to describe this reacceleration without violating the energy balance, the time-dependent problem of shock collision must be solved accounting for the feedback of the particles on both shocks. This goes beyond the framework considered in Chapter 4 and we will not include this process in the self-consistent model developed in the present chapter. It is nevertheless worth keeping in mind that it could enhance the concavity of the spectra, strengthening our conclusions.

Interestingly, hard gamma-ray spectra with slight concavities were recently observed in the G25 region (Katsuta et al., 2017). Although the nature of the source is yet unclear, it was suspected that a star forming region could be responsible for this extended emission. Such spectra are indeed possible signatures of shock reacceleration in a superbubble surrounding the hypothetical G25.18+0.26 young stellar association.

6.4.3 Modelling the supershell

The two-zone model can also be used to account for the effect of the dense supershell in which the interstellar matter and magnetic field swept-up by the superbubble forward shock accumulates. The interstellar magnetic field is compressed and strengthened in the direction tangential to the shell. In order to escape in the interstellar medium, particles must diffuse mainly perpendicularly to this strong background field. As discussed in Section 2.2.5, deriving the expression for a perpendicular diffusion coefficient from first principles is far from being trivial. On the other hand, heuristic arguments as well as numerical simulations suggest that $D_\perp \approx (\delta B/B)^{\alpha_B} D_\parallel$, with $\alpha_B \approx 4$ (e.g. Casse et al., 2001; Mertsch, 2020). Therefore, the diffusion coefficient in the shell could well be orders of magnitude below that in the superbubble interior, which would enhance the confinement of the particles. This can be accounted for in the two-zone model as the parameter δ in Equation 6.36 is precisely the ratio of the diffusion coefficients. Eventually we need to specify the shell density and thickness. For simplicity we assume that the thickness is equal to 10% of the superbubble radius at any time, that is, $\rho_b = 0.1$. The hydrogen number density in the shell n_H follows by assuming that all the mass swept-up by the superbubble forward shock has accumulated in the shell, which provides $n_H = n_{ISM}/((1+\rho_b)^3 - 1) \approx 3 n_{ISM}$. In the following we assume $n_{ISM} = 10$ cm^{-3}.

Equation 6.36 predicts that the confinement of the particles will be enhanced when $\rho_b/\delta > 1$. Indeed the left panels of Figure 6.10 show that for $\delta = 0.01$, the emission in a superbubble hosting 100 massive stars is much less intermittent, which results in overall smoother and steeper spectra because the flat wind component is always subdominant. For a high "shell confinement coefficient" $\rho_b/\delta = 10^3$ (right panels of Figure 6.10), the particles are strongly confined. In this case, the cosmic ray energy density in the shell is so high that the turbulence cascade terminates close to the injection scale: the shell is not turbulent. This demonstrates that low values of the parameter δ (that is, strong

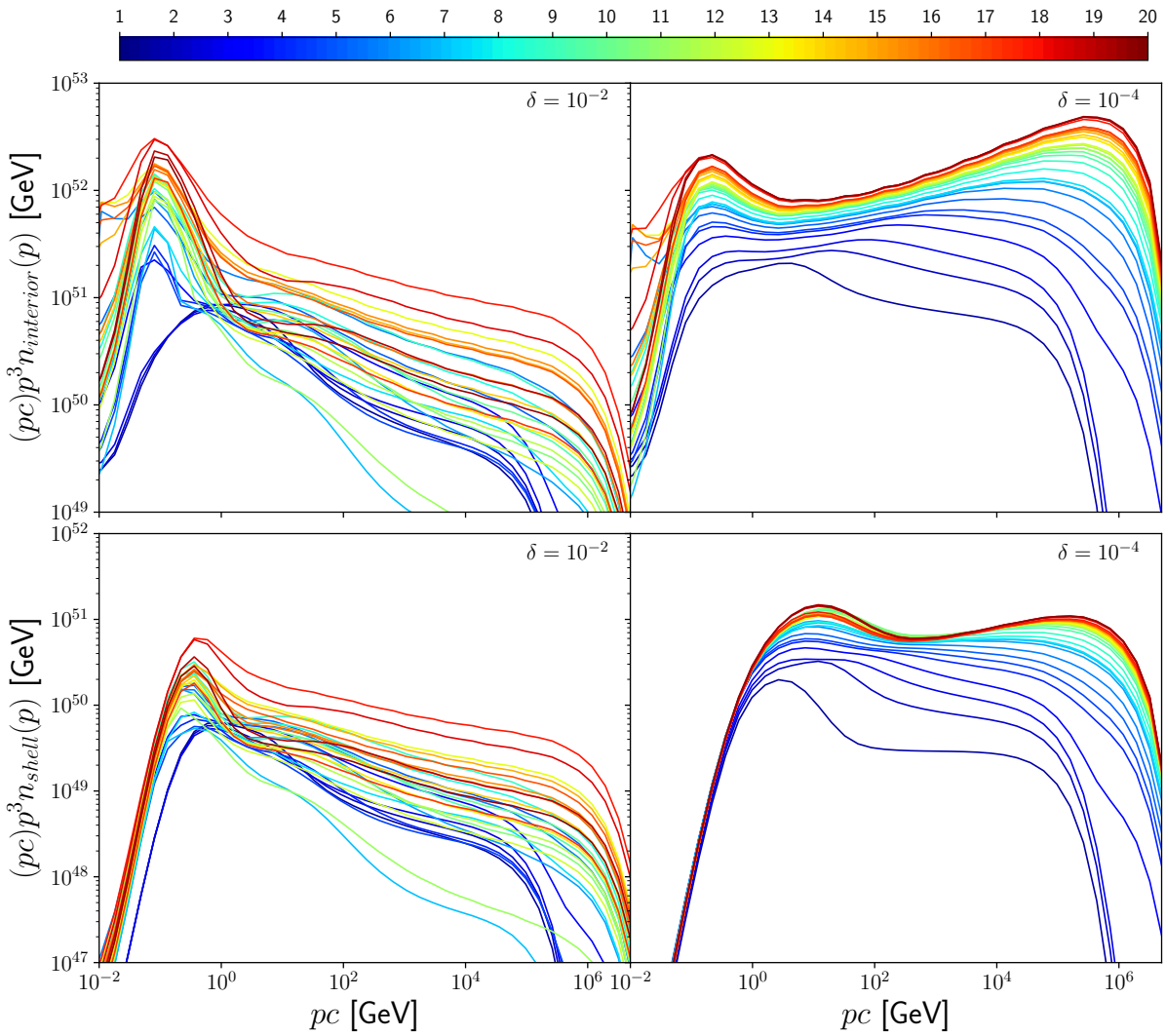

Figure 6.10: Average spectra in a two-zone (top panels: interiors, bottom panels: shells) model with two different values of the shell confinement coefficient $\rho_b/\delta = 10$ (left panels), 1000 (right panels). Each curve corresponds to a different time represented by the colour scale in units of Myr at the top.

confinements) are not unrealistic, although a self-consistent model computing δ from first principles and accurately accounting for the backreaction of the particles on the perpendicular transport remains to be developed.

Whenever the shell efficiently enhances the confinement, the particles reaccelerated at supernova remnants stay inside the superbubble in such a way that the interior is characterised by a homogeneous concave spectrum which converges toward the asymptotic solution discussed in Chapter 5. Eventually, one notices that low energies are screened below 1 GeV because of the enhanced losses suffered within the dense shell.

6.5 Superbubble contribution to galactic cosmic rays

Let us provide a first estimate of the contribution of superbubbles enclosed by supershells to galactic cosmic rays. The differential flux of particles reaching the Earth from

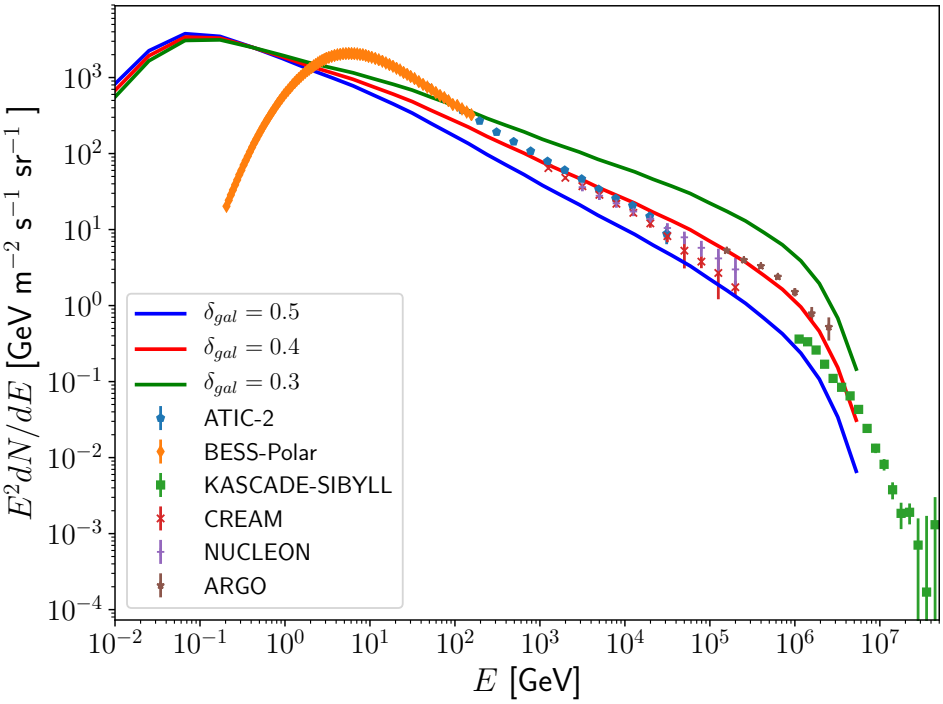

Figure 6.11: Superbubble contribution to the galactic cosmic ray proton spectrum, assuming a galactic diffusion coefficient with index $\delta_{gal} = 0.5$ (blue), $\delta_{gal} = 0.4$ (red), $\delta_{gal} = 0.3$ (green).

superbubbles is estimated as:

$$\frac{\mathrm{d}N}{\mathrm{d}E} = \frac{f_{SB}}{\langle V_{SB} \rangle} \frac{T_{disk}(p) c}{\tau_2} p^2 n_{shell}(p) \,, \tag{6.41}$$

where $f_{SB} \approx 20\%$ is the volume filling factor of the hot gas in the solar vicinity (Ferrière, 1998), $\langle V_{SB} \rangle \approx 0.004$ kpc^3 is the volume of a typical superbubble, $T_{disk}(p) \approx 3(p/\mathrm{GeV})^{-\delta_{gal}}$ Myr is the residence time in the galactic disk, with $\delta_{gal} \approx 0.3 - 0.5$. Equation 6.41 provides an order of magnitude estimate of the flux normalisation without introducing any arbitrary parameter. Figure 6.11 shows the differential flux computed from the shell energy density n_{shell} obtained in the previous subsection for $N_* = 100$ and a confinement parameter $\rho_b/\delta = 10$ (bottom left panel of Figure 6.10).

As seen in Figure 6.11, the flux normalisation is close to that of the available data. The main parameter driving the cosmic ray density in superbubbles is the injection efficiency at supernova remnants, that is the fraction of thermal particles injected in the accelerator. Increasing the injection efficiency is however not expected to change the result dramatically, for shock acceleration becomes less efficient in the nonlinear regime. The agreement between this first prediction and the data is overall acceptable and this preliminary estimate of the contribution of superbubbles to the galactic cosmic rays show that they can account for the observed cosmic ray flux with a realistic residence time and thus a realistic galactic diffusion coefficient.

Let us eventually recall that the superbubble contribution to the galactic cosmic ray spectrum computed beyond 1 PeV is not reliable, for we neglected the flux of particles escaping upstream of supernova remnants beyond the maximum energy. An accurate description of this component requires to solve the time-dependent reacceleration problem in the nonlinear regime, at least phenomenologically, which could provide an additional

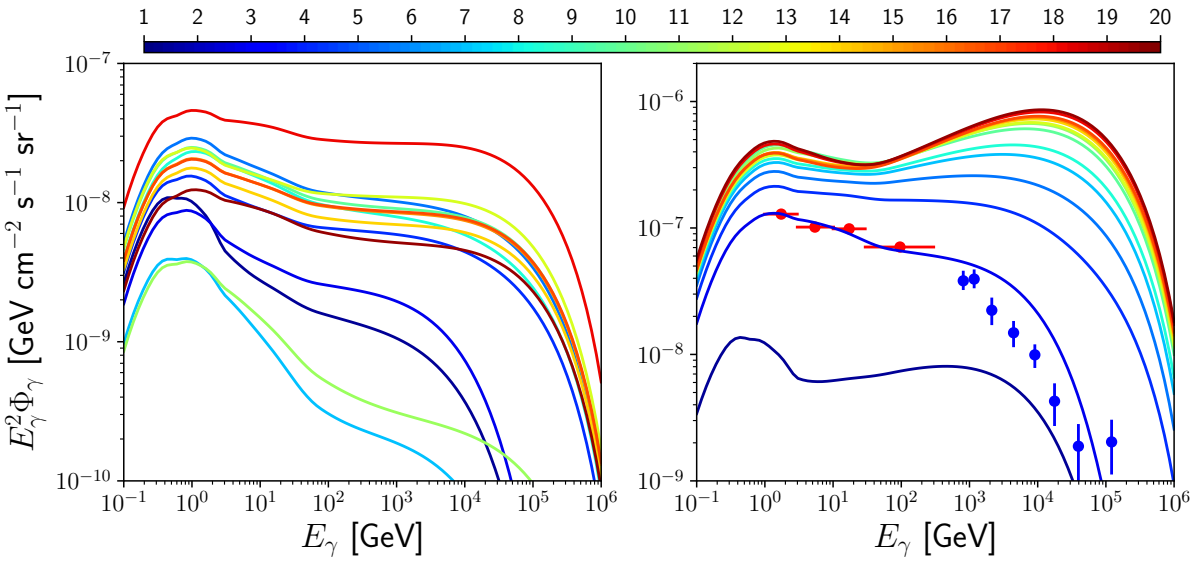

Figure 6.12: Gamma-ray spectral energy distributions from p-p interactions in a standard superbubble shell of hydrogen number density $n_H = 30$ cm^{-3} ($n_{ISM} = 10$ cm^{-3}), with a shell confinement coefficient $\rho_b/\delta = 10$ (left panel), and 1000 (right panel). The source is a loose cluster of 100 massive stars located at 1.5 kpc from the Earth. Spectra are plotted at various times from 1 to 20 Myr corresponding to the various colours from blue to red (see the colour scale at the top). The data points show the gamma-ray flux measured in the Cygnus region: Fermi-LAT data in red (Abdollahi et al., 2020) and HAWC data in blue (Abeysekara et al., 2021).

steep power law component at energies close to that of the knee. Such promising analysis is left for future work.

6.6 Gamma-ray spectra

The gamma-ray emission of supershells due to neutral pion decay can eventually be computed from the cosmic ray energy spectra as:

$$\Phi_\gamma(E_\gamma) = \frac{n_H c}{4\pi D_S^2} \int_{T_{p,min}} \mathrm{d}T_p 4\pi p^2 n_{shell}(p(T_p)) \epsilon_{nh}(T_p) \frac{\mathrm{d}\sigma_{pp}}{\mathrm{d}E_\gamma}(T_p, E_\gamma)\,, \tag{6.42}$$

where n_H is the hydrogen number density of the shell, D_S is the distance of the source, $T_{p,min}$ the threshold energy for neutral pion production in proton-proton interactions, $\mathrm{d}\sigma/\mathrm{d}E_\gamma$ is the differential cross-section of gamma-ray production and ϵ_{nh} is the nuclear enhancement factor accounting for nucleus-nucleus interactions. The computation follows the prescription of Kafexhiu et al. (2014).

Figure 6.12 shows the resulting gamma-ray spectral energy distributions for a cluster of 100 massive stars and two values of the parameter δ. It is striking to see how the modification of a single parameter can produce many different spectral shapes. In standard superbubbles surrounding loose clusters, the cosmic rays are not very efficiently reaccelerated (left panel). The fluxes escaping through the shell produce rather steep power law gamma-ray spectra, with a low normalisation and characterised by a strong intermittency. The flux is generally below the detection threshold of the Fermi-LAT telescope, which could explain why several massive star clusters are not associated with gamma-ray

emissions (Maurin et al., 2016), and in particular the well-known Orion-Eridani superbubble (Joubaud et al., 2020). On the other hand, with an enhanced shell confinement coefficient ρ_b/δ, the cosmic rays are trapped in the shell, which results in a more efficient production of gamma-rays (right panel). The spectra at early times, driven by stellar winds, are slightly steeper than E^{-2} (e.g. $\Phi_\gamma \propto E^{-2.1} - E^{-2.2}$), which is consistent with what is observed in the Cygnus-X star forming region. In particular, the spectrum at 3 Myr shows a very good agreement with the normalisation and shape of the spectral energy distribution measured in the Cygnus region, although we did not adjust any parameter to obtain the best fit. A thorough comparison with Fermi and HAWC data is left for future work. Eventually, hard power law or concave spectra are expected if the cosmic rays are efficiently confined and reaccelerated, as it starts to be the case for $\rho_b/\delta = 1000$ (right panel of Figure 6.12) after about $5 - 10$ Myr. This is expected if the perpendicular diffusion is suppressed in the shell or if the particles are efficiently reaccelerated in compact clusters. Slightly concave gamma-ray spectral energy distributions were observed in the G25 region (Katsuta et al., 2017). Flat gamma-ray spectra were observed in the very compact and very massive Westerlund 2 young star cluster (Aharonian et al., 2007; Yang et al., 2018). Eventually, flat gamma-ray spectra extending up to TeV energies were observed in the Westerlund 1 region, in the vicinity of the most massive star cluster of our galaxy (Abramowski et al., 2012; Ohm et al., 2013). It seems that all these observations, despite differing quantitatively or even qualitatively, could be explained by superbubble proton spectra. Our superbubble modelling will allow to constrain the properties of the supershells, turbulence, and massive star clusters in order to reproduce gamma-ray data. In particular, the model being self-consistent, it predicts not only spectral shapes but realistic normalisations as well. Eventually, the PeV protons do produce ultra high energy photons above the sensitivity of the LHAASO observatory, which recently detected a photon of 1.4 PeV in the direction of the Cygnus OB2 massive cluster (Cao et al., 2021). In a near future, this new observatory is expected to provide unvaluable data in the highest energy bands, to be confronted with the present model.

6.7 Summary

Using a self-consistent model accounting for all relevant ingredients rederived from first principles, we computed the acceleration of protons in superbubble environments. We extended the model of Ferrand and Marcowith (2010) in order to account for the dynamical evolution of the environment as well as the stellar winds, the losses and the effect of the shell. We also refined the model to include the backreaction of the particles onto the turbulence and onto the shocks, the latter being properly computed using an up-to-date semi-analytical model of nonlinear diffusive shock reacceleration. Our model complements the work of Bykov (2001) who focused on the early phase of stochastic acceleration in strong supersonic turbulence.

We found that the stars efficiently transfer their energy into non-thermal particles by means of shock acceleration as well as stochastic acceleration in turbulence, especially around compact clusters where particles are efficiently reaccelerated in the inner region and in the case where a dense magnetised supershell prevents the particles to escape in the interstellar medium. High cosmic ray energy densities are generally achieved in the superbubble, which calls for nonlinear models, and in some cases the turbulence can be completely suppressed by the non-thermal particles confined in the shell.

When the confinement is less efficient, e.g. in the limit of a thin supershell or in

small clusters, the typical spectra are rather intermittent, displaying a typical "Fermi II bump" from the injection energy to the GeV band, and then transitions toward a steep power law produced by the nearly stationary wind contribution as well as the intermittent supernovae modulated by the escape. Providing the level of turbulence is about a few percent, which requires the stars to transfer a few tens of percent of their mechanical power into hydromagnetic waves, the low energy particles are efficiently reaccelerated, which gives rise to steep escape fluxes typically scaling as $E^{-2.2}$, which is close to what is needed in order to account for the diffuse cosmic ray spectrum observed near Earth. When the confinement of the particles is enhanced, the spectra harden with typically flat gamma-ray signatures, or even small concavities with somewhat hard components (about $E^{-1.8}$ at high energies) due to the successive reaccelerations of the confined particles.

The variability of the spectra from cluster to cluster, and also during the lifetime of a given cluster, provides a simple answer to the puzzling discrepancies between the recent gamma-ray observations. Indeed, some superbubbles are not detected in gamma-rays (e.g. the Orion-Eridani superbubble, the Rosette nebula), others display rather steep power law spectra (e.g. the Cygnus region), or flat energy distributions (e.g. the Westerlund 1 and 2 regions), and some data even suggest slight concavities (e.g. in the G25 region). The specific gamma-ray signature of a superbubble can therefore be used to constrain the properties of a given massive star cluster (its number of massive stars, if it is compact or loose...), the surrounding environment (the magnetic field, the turbulence level...), as well as the properties of the supershell (the thickness, the density...). Although the model depends on several parameters, some of them such as the cluster and shell properties can hopefully be constrained by multiwavelengths observations. The main difficulty is probably to infer the properties of the turbulence (intensity and spectrum), which at the moment are unknown. Using our model, gamma-ray spectra could be used indirectly to constrain the diffusion coefficients. Indeed, the momentum diffusion coefficient drives the slope at low energies by means of the stochastic reacceleration, while the spatial diffusion coefficient drives the slope at high energies as well as the intensity of the gamma-ray flux, because it determines the efficiency of the confinement. Such analysis could be applied to the Cygnus region.

Eventually, the overall contribution of superbubbles to the galactic cosmic ray population can be estimated using Monte-Carlo samplings. Thorough statistical computations confronted to the observed cosmic ray spectrum could be used to probe the most likely superbubble parameters, in particular the magnetic fields, turbulence levels and shell properties, as well as their variance. The modulation of the galactic spectrum due to the local bubble could also be included in such computation using our two-zone modelling. Indeed, this model allows to compute the screening of the interstellar flux of cosmic rays when it penetrates a dense supershell, an idea which was already raised in the 80's (Streimatter et al., 1985). The depletion of sub-GeV bands due to the losses in the shell could for instance account for the low-energy cutoff measured by the Voyager probe (Cummings et al., 2016).

References

Abdollahi, S. et al. (Mar. 2020). "Fermi Large Area Telescope Fourth Source Catalog". In: ApJS 247.1, 33, p. 33. DOI: 10.3847/1538-4365/ab6bcb.

Abeysekara, A. U. et al. (Mar. 2021). "HAWC observations of the acceleration of very-high-energy cosmic rays in the Cygnus Cocoon". In: *Nature Astronomy*. DOI: 10.1038/s41550-021-01318-y.

Abramowski, A. et al. (Jan. 2012). "Discovery of extended VHE gamma-ray emission from the vicinity of the young massive stellar cluster Westerlund 1". In: A&A 537, A114, A114. DOI: 10.1051/0004-6361/201117928.

Aharonian, F. et al. (June 2007). "Detection of extended very-high-energy gamma-ray emission towards the young stellar cluster Westerlund 2". In: A&A 467.3, pp. 1075–1080. DOI: 10.1051/0004-6361:20066950.

Aharonian, F. A. (2004). *Very high energy cosmic gamma radiation : a crucial window on the extreme Universe*. DOI: 10.1142/4657.

Blasi, P., Gabici, S., and Vannoni, G. (Aug. 2005). "On the role of injection in kinetic approaches to non-linear particle acceleration at non-relativistic shock waves". In: MNRAS 361.3, pp. 907–918. DOI: 10.1111/j.1365-2966.2005.09227.x.

Bouyahiaoui, M., Kachelriess, M., and Semikoz, D. V. (Jan. 2019). "Vela as the source of Galactic cosmic rays above 100 TeV". In: J. Cosmology Astropart. Phys. 2019.1, 046, p. 046. DOI: 10.1088/1475-7516/2019/01/046.

Bykov, A. M., Ptuskin, V. S., and Toptygin, I. N. (Jan. 1995). "Spectrum of Ultra-High Energy Cosmic Rays Acceleration in Superbubbles". In: *International Cosmic Ray Conference*. Vol. 3. International Cosmic Ray Conference, p. 337.

Bykov, A. M. (Oct. 2001). "Particle Acceleration and Nonthermal Phenomena in Superbubbles". In: Space Sci. Rev. 99, pp. 317–326. DOI: 10.1023/A:1013817721725.

Cao, Z. et al. (May 2021). "Ultrahigh-energy photons up to 1.4 petaelectronvolts from 12 gamma-ray Galactic sources". In: *Nature*. ISSN: 1476-4687. DOI: 10.1038/s41586-021-03498-z.

Casse, F., Lemoine, M., and Pelletier, G. (Nov. 2001). "Transport of cosmic rays in chaotic magnetic fields". In: Phys. Rev. D 65.2. ISSN: 1089-4918. DOI: 10.1103/physrevd.65.023002.

Castor, J., McCray, R., and Weaver, R. (Sept. 1975). "Interstellar bubbles." In: ApJ 200, pp. L107–L110. DOI: 10.1086/181908.

Cesarsky, C. J. and Montmerle, T. (Oct. 1983). "Gamma-Rays from Active Regions in the Galaxy - the Possible Contribution of Stellar Winds". In: Space Sci. Rev. 36.2, pp. 173–193. DOI: 10.1007/BF00167503.

Cummings, A. C. et al. (Nov. 2016). "Galactic Cosmic Rays in the Local Interstellar Medium: Voyager 1 Observations and Model Results". In: ApJ 831.1, 18, p. 18. DOI: 10.3847/0004-637X/831/1/18.

Fang, K., Bi, X.-J., and Yin, P.-F. (Sept. 2019). "Possible origin of the slow-diffusion region around Geminga". In: MNRAS 488.3, pp. 4074–4080. DOI: 10.1093/mnras/stz1974.

Ferrand, G. and Marcowith, A. (Feb. 2010). "On the shape of the spectrum of cosmic rays accelerated inside superbubbles". In: A&A 510, A101, A101. DOI: 10.1051/0004-6361/200913520.

Ferrière, K. (Aug. 1998). "The Hot Gas Filling Factor in Our Galaxy". In: ApJ 503.2, pp. 700–716. DOI: 10.1086/306003.

Finke, J. D. and Dermer, C. D. (May 2012). "Cosmic-Ray Electron Evolution in the Supernova Remnant RX J1713.7-3946". In: ApJ 751.1, 65, p. 65. DOI: 10.1088/0004-637X/751/1/65.

Gaggero, D. et al. (Apr. 2018). "Time evolution of gamma rays from supernova remnants". In: MNRAS 475.4, pp. 5237–5245. DOI: 10.1093/mnras/sty140.

Gupta, S. et al. (Apr. 2020). "Realistic modelling of wind and supernovae shocks in star clusters: addressing $^{22}Ne/^{20}Ne$ and other problems in Galactic cosmic rays". In: MNRAS 493.3, pp. 3159–3177. DOI: 10.1093/mnras/staa286.

Joubaud, T. et al. (Mar. 2020). "The cosmic-ray content of the Orion-Eridanus superbubble". In: A&A 635, A96, A96. DOI: 10.1051/0004-6361/201937205.

Kafexhiu, E. et al. (Dec. 2014). "Parametrization of gamma-ray production cross sections for p p interactions in a broad proton energy range from the kinematic threshold to PeV energies". In: Phys. Rev. D 90.12, 123014, p. 123014. DOI: 10.1103/PhysRevD.90.123014.

Kalyashova, M. E. et al. (Nov. 2019). "Wolf-Rayet stars in young massive star clusters as potential sources of Galactic cosmic rays". In: *Journal of Physics Conference Series*. Vol. 1400. Journal of Physics Conference Series, p. 022011. DOI: 10.1088/1742-6596/1400/2/022011.

Katsuta, J., Uchiyama, Y., and Funk, S. (Apr. 2017). "Extended Gamma-Ray Emission from the G25.0+0.0 Region: A Star-forming Region Powered by the Newly Found OB Association?" In: *The Astrophysical Journal* 839.2, p. 129. DOI: 10.3847/1538-4357/aa6aa3.

Krumholz, M. R., McKee, C. F., and Bland-Hawthorn, J. (Aug. 2019). "Star Clusters Across Cosmic Time". In: ARA&A 57, pp. 227–303. DOI: 10.1146/annurev-astro-091918-104430.

Limongi, M. and Chieffi, A. (Aug. 2006). "The Nucleosynthesis of ^{26}Al and ^{60}Fe in Solar Metallicity Stars Extending in Mass from 11 to 120 M_{solar}: The Hydrostatic and Explosive Contributions". In: ApJ 647.1, pp. 483–500. DOI: 10.1086/505164.

Lingenfelter, R. E. (Nov. 2018). "Cosmic rays from supernova remnants and superbubbles". In: *Advances in Space Research* 62.10, pp. 2750–2763. DOI: 10.1016/j.asr.2017.04.006.

Mac Low, M.-M. and McCray, R. (Jan. 1988). "Superbubbles in Disk Galaxies". In: ApJ 324, p. 776. DOI: 10.1086/165936.

Mannheim, K. and Schlickeiser, R. (June 1994). "Interactions of cosmic ray nuclei". In: A&A 286, pp. 983–996.

Maurin, G. et al. (June 2016). "Embedded star clusters as sources of high-energy cosmic rays . Modelling and constraints". In: A&A 591, A71, A71. DOI: 10.1051/0004-6361/201628465.

McCray, R. and Kafatos, M. (June 1987). "Supershells and Propagating Star Formation". In: ApJ 317, p. 190. DOI: 10.1086/165267.

Mertsch, P. (Aug. 2020). "Test particle simulations of cosmic rays". In: Ap&SS 365.8, 135, p. 135. DOI: 10.1007/s10509-020-03832-3.

Miller, J. A. and Roberts, D. A. (Oct. 1995). "Stochastic Proton Acceleration by Cascading Alfven Waves in Impulsive Solar Flares". In: ApJ 452, p. 912. DOI: 10.1086/176359.

Morlino, G. et al. (Mar. 2021). "Particle acceleration in winds of star clusters". In: MNRAS. DOI: 10.1093/mnras/stab690.

Norman, C. A. and Ferrara, A. (Aug. 1996). "The Turbulent Interstellar Medium: Generalizing to a Scale-dependent Phase Continuum". In: ApJ 467, p. 280. ISSN: 1538-4357. DOI: 10.1086/177603.

Ohm, S., Hinton, J. A., and White, R. (Sept. 2013). "Gamma-ray emission from the Westerlund 1 region". In: MNRAS 434.3, pp. 2289–2294. DOI: 10.1093/mnras/stt1170.

Parizot, E. et al. (Sept. 2004). "Superbubbles and energetic particles in the Galaxy. I. Collective effects of particle acceleration". In: A&A 424, pp. 747–760. DOI: 10.1051/0004-6361:20041269.

Ptuskin, V. S. et al. (July 2003). "Dissipation of Hydromagnetic Waves on Energetic Particles: Impact on Interstellar Turbulence and Cosmic Ray Transport". In: *International Cosmic Ray Conference*. Vol. 4. International Cosmic Ray Conference, p. 1929.

Ptuskin, V. et al. (2005). "Propagation model for cosmic ray species in the Galaxy". In: *Advances in Space Research* 35.1. Mars International Reference Atmosphere, Living With a Star and Fundamental Physics, pp. 162–166. ISSN: 0273-1177. DOI: https://doi.org/10.1016/j.asr.2003.08.051.

Salpeter, E. E. (Jan. 1955). "The Luminosity Function and Stellar Evolution." In: ApJ 121, p. 161. DOI: 10.1086/145971.

Seo, J., Kang, H., and Ryu, D. (Apr. 2018). "The Contribution of Stellar Winds to Cosmic Ray Production". In: *Journal of Korean Astronomical Society* 51.2, pp. 37–48. DOI: 10.5303/JKAS.2018.51.2.37.

Streimatter, R. E. et al. (Feb. 1985). "Cosmic ray propagation in the local superbubble." In: A&A 143, pp. 249–255.

Tatischeff, V. et al. (June 2021). "The Origin of Galactic Cosmic Rays as Revealed by their Composition". In: *arXiv e-prints*, arXiv:2106.15581.

Tolksdorf, T. et al. (July 2019). "Cosmic Rays in Superbubbles". In: *The Astrophysical Journal* 879.2, p. 66. DOI: 10.3847/1538-4357/ab24c6.

Verma, M. K. et al. (1996). "A numerical study of the nonlinear cascade of energy in magnetohydrodynamic turbulence". In: *Journal of Geophysical Research: Space Physics* 101.A10, pp. 21619–21625. DOI: https://doi.org/10.1029/96JA01773.

Vieu, T., Gabici, S., and Tatischeff, V. (2021a). "Cosmic ray production in superbubbles". In: *In preparation*.

Vieu, T., Gabici, S., and Tatischeff, V. (2021b). "Nonlinear particle reacceleration by multiple shocks". In: *In preparation*.

Vieu, T., Gabici, S., and Tatischeff, V. (2021c). "The cosmic ray content of superbubbles". In: *Proceedings of 37th International Cosmic Ray Conference — PoS(ICRC2021)*. Vol. 395, p. 147. DOI: 10.22323/1.395.0147.

Voelk, H. J. and Biermann, P. L. (Oct. 1988). "Maximum Energy of Cosmic-Ray Particles Accelerated by Supernova Remnant Shocks in Stellar Wind Cavities". In: ApJ 333, p. L65. DOI: 10.1086/185289.

Weaver, R. et al. (Dec. 1977). "Interstellar bubbles. II. Structure and evolution." In: ApJ 218, pp. 377–395. DOI: 10.1086/155692.

Yang, R.-z., de Oña Wilhelmi, E., and Aharonian, F. (Apr. 2018). "Diffuse gamma-ray emission in the vicinity of young star cluster Westerlund 2". In: A&A 611, A77, A77. DOI: 10.1051/0004-6361/201732045.

Zhou, Y. and Matthaeus, W. H. (1990). "Models of inertial range spectra of interplanetary magnetohydrodynamic turbulence". In: J. Geophys. Res. 95.A9, pp. 14881–14892. DOI: https://doi.org/10.1029/JA095iA09p14881.

Conclusions and perspectives

General summary

Galactic cosmic rays are most likely produced by the powerful activity of massive stars, either directly at shock waves or indirectly in the turbulence. It is therefore very natural to believe that these particles are accelerated within the regions in which massive stars form and evolve, most of them remaining in stellar clusters during tens of million years. In star forming regions, stellar clusters carve superbubbles, characterised by a hot ionised and turbulent interior spanned by multiple shocks (Chapter 1). These environments are favourable sites of particle acceleration. Recent gamma-ray observations, for instance in the Cygnus region, have called for in-depth theoretical modelling of the mechanisms of cosmic ray production in superbubbles. Developing such a model was the main goal of the present work.

After reviewing the fundamentals of particle acceleration and transport in turbulence (Chapter 2) and at shock waves (Chapter 3), I have shown how the acceleration mechanisms may differ in low-density turbulent cavities hosting hundreds of massive stars. First of all, strong shocks may collide within a superbubble. This not only happens when stellar winds interact within a cluster, but also when a supernova expands toward the collective wind termination shock which may form around a compact cluster, or when two supernova shocks exploding nearly simultaneously converge toward each other. Whenever expanding shocks are considered, the time-dependency of the situation must be accounted for, which was done in Chapter 4. I concluded that the acceleration of particles from the thermal bath would not differ from the acceleration at a single shock, apart from a slight broadening of the high-energy cutoff. This is because particles become energetic enough to diffuse from one shock to the other only in the latest times of the collision. On the other hand, if preaccelerated particles are confined in the region, they can experience both shocks already at the beginning of the process, which is expected to result in a pronounced hardening of the particle spectrum at high energies. Such high-energy hardening, with an asymptotic solution scaling as p^{-3} (generally steeper in reality), is expected when collective effects are considered. Such collective mechanisms of acceleration extend from the interaction of stellar winds to the stochastic reacceleration of the particles by multiple shocks, either with a spatial intermittency (strong supersonic turbulence, Bykov 2001) or with a temporal intermittency (successive supernova shocks spanning the same region, Ferrand and Marcowith 2010). In these situations, the repeated acceleration of particles can be very efficient and the cosmic ray pressure is expected to reach the level of the hydrodynamic pressure, with fluxes close to equipartition. This calls for nonlinear modelling of the processes. In Chapter 5, I performed the first investigation of the nonlinear reacceleration of cosmic rays by multiple shocks, properly accounting for the development of a precursor ahead of the shocks due to the cosmic rays slowing down the flows. Remarkably, the spectra were shown to quickly reach a universal concave solution

with spectral index about 3.5 around the maximum energy, independently on the shock Mach number, the injection efficiency, and the maximum achievable momentum. The cosmic ray pressure would saturate at the level of a few percent of the shock ram pressure in the downstream region. This model of shock reacceleration was then applied to realistic dynamical superbubble environments in Chapter 6. Although superbubbles are complex environments which require a number of parameters to be described accurately, hydrodynamic theories, thermodynamic considerations and particularly numerical simulations, as well as optical, infrared, and X-ray observations allow to put constraints on most of the variables. Several parameters are in fact source-dependent, including the initial number of massive stars in the cluster, the density of the surrounding medium and the properties of the magnetised turbulence, namely its wave spectrum and intensity. Assuming fiducial values for these parameters, I analysed the acceleration of cosmic rays in superbubbles using a semi-analytical model which included the most relevant processes in order to describe either loose or compact clusters. The production of cosmic rays was shown to result from the complex interplay between shock acceleration at winds or supernova remnants and subsequent stochastic reacceleration in weak turbulence. Particles injected at shock fronts are reaccelerated to GeV energies when they propagate inside the superbubble, until they escape beyond the supershell. This gives rise to a bumpy feature in the low energy bands and a rather steep component at high energy on average, unless the confinement of the particles is enhanced. The latter may happen in very massive compact clusters or in presence of a magnetised supershell surrounding the superbubble. In these cases, the particles are efficiency reaccelerated, which produces a spectral hardening.

The energy transfer between the massive stars and the particles, which proceeds both directly via shock acceleration and indirectly via the hydromagnetic turbulence, is found to be efficient. High cosmic ray energy densities are reached inside typical superbubbles ($1-10^3$ eV/cm^3), which call for nonlinear models. By taking into account the feedback of the particles onto the expanding shocks and turbulent hydromagnetic waves, I developed the first self-consistent model of particle acceleration in evolved superbubbles, which is meant to complement the works of Bykov and collaborators (e.g. Bykov, 2001). The intermittent and source-dependent proton spectra result in various classes of gamma-ray spectra, from steep and low-intensity spectra to some with concave shapes and high intensities, in qualitative agreement with the available data such as the spectral energy distributions measured in the Cygnus cocoon (Abdollahi et al., 2020; Abeysekara et al., 2021) and around the Westerlund 1 and 2 clusters (Aharonian et al., 2007; Abramowski et al., 2012). Finally, I provided a first estimate of the overall contribution of superbubbles to the galactic cosmic ray spectrum, in particular showing that these sources can indeed account for the flux measured near Earth.

Perspectives

The model, although consistently accounting for most of the crucial ingredients, has several limitations which are likely not critical but, on the contrary, open doors on promising axes of improvements and future developments. Here are some topics of investigations in the continuation of the present work:

(i) Nonlinear particle acceleration and reacceleration in time-dependent spherical converging shocks;

(ii) Successive shock reacceleration accounting for the dynamical evolution of supernova remnants in superbubbles;

(iii) Nonlinear particle reacceleration at clustered stellar winds;

(iv) Particle acceleration and transport in inhomogeneous superbubbles;

(v) Particle acceleration and transport in supersonic hydromagnetic turbulence;

(vi) Cosmic-ray production in star-forming regions;

(vii) Indirect investigation of the hydromagnetic turbulence in star-forming regions and superbubbles using gamma-ray observations;

(viii) Acceleration of heavy elements in superbubbles and the composition of galactic cosmic rays;

(ix) Detailed modelling of the contribution of superbubbles to the galactic cosmic ray spectrum.

These research axes could be classified in three categories.

(1) Improving the modelling of collective effects such as colliding shocks, successive reaccelerations, stellar winds (points *(i)-(iii)*). Indeed, in order to be included in a self-consistent framework, the system of colliding shocks must be solved accounting for the backreaction of the particles. In addition, the high-energy hardening of the spectra suggests that a substantial fraction of the energy escapes the system, which should be explicitly included in the model, considering the effect of the finite geometry of the shocks which is probed by high-energy particles. As far as the reacceleration by successive shocks is concerned, we did develop a nonlinear framework, however in the stationary regime. This is a major caveat, as most of the crucial parameters such as the shock velocity, the injection efficiency and the maximum achievable momentum, are not well defined (see the discussion in the end of Section 6.2.2). Supernova remnants evolving inside superbubbles are very different from isolated supernovae expanding in the interstellar medium. First they expand inside dense winds, then they may collide with the wind termination shock surrounding compact star clusters, and eventually they reach the nearly uniform low-density interior of the superbubble. Because the medium is not homogeneous, nor scale-invariant, the evolution of the clustered supernovae is most likely not self-similar and should display several phases. To properly describe such evolution is an axis of research in itself. Given that most supernovae are believed to explode within star clusters and superbubbles (Higdon and Lingenfelter, 2005), this topic is of utmost importance not only for the field of astroparticle physics but also for the investigation of the stellar feedback onto the dynamics of the galaxy. Regarding the acceleration of particles in superbubbles, the dynamical evolution of supernova remnants should be applied to successive shock reacceleration, including the time-dependency of the shock properties in a phenomenological way. This would allow in particular to properly compute the high energy escape spectrum. Although the latter is not expected to strongly impact the gamma-ray emission of the superbubbles considered in the present work, for the high-energy particles will escape without suffering important losses, this may not be the case if a dense supershell efficiently screens the escape. Besides, this high-energy component is expected to contribute to the cosmic ray spectrum around the knee, and could even be the dominant galactic source of particles in PeV bands.

There are also possibilities of improvement regarding the modelling of cosmic ray acceleration at wind termination shocks. While we only introduced this contribution as a

background injection, reacceleration effects could play a role (Klepach et al., 2000), and this should be again computed in a nonlinear framework. Besides, the collective wind termination shock sustained by Wolf-Rayet stars in the first few million years of a cluster history could be rather weak (Chevalier and Clegg, 1985), which would produce steep power law background spectra.

(2) Improving the modelling of the superbubble environment (points *(iv)-(vi)*). In the framework used in Chapter 6, the interior of the superbubble was assumed to be homogeneous. This is most likely not the case in reality. The turbulence is probably stronger close to the cluster and may not be diluted in the whole superbubble as quickly as assumed in Chapter 6. This may have important consequences on the confinement and reacceleration of the particles. Besides, streaming instabilities around stellar winds, and in particular in presence of a collective wind termination shock, may locally induce a Bohm regime of turbulence, which would confine the particles even more efficiently, making PeV energies easier to reach (Morlino et al., 2021). I have shown in the end of Chapter 6 how a two-zone model could be used to coarsely account for such an inhomogeneity. However, an accurate computation should inevitably account for the spatial transport of the particles. Streaming instabilities inside the superbubble, not only around the shock waves, could also be accounted for. These are expected to excite the turbulence and enhance the confinement of the particles (e.g. Nava et al., 2016), which would compete with the damping due to the stochastic reacceleration of non-thermal particles. This could again change the turbulence regime, especially at small-scales. The turbulence will be modified even more dramatically if it does not dilute quickly inside the large superbubble volume but remains close to the stellar cluster. The stars could indeed sustain a supersonic turbulence during a time much longer than what we estimated, possibly until the end of the cluster life. Due to the interactions with dense clumps or the collisions between shocks, a substantial fraction of the mechanical energy of the stellar outflows and supernova shocks may indeed decay into weak stochastic shocks before reaching the low-density interior of the superbubble (Parizot et al., 2004). It would be interesting to investigate this situation using a two-zone model. The inner region would be characterised by strong stellar outflows producing a strong supersonic turbulence under the form of spatially and temporally intermittent primary and secondary shocks covering a broad range of Mach numbers (Bykov and Toptygin, 1990). The outer region would be characterised by a weak turbulence regime as discussed in Chapter 6. Eventually, one could add a third zone in order to describe the shell. The framework developed in this thesis allows to conveniently introduce these ingredients without much complication and keeping the computation time within reasonable scales (several hours). This is a major strength of the model which I would like to underline again: it can be easily supplemented by additional ingredients.

Eventually, one could consider star forming regions as collections of superbubbles and shells. Our model could be included in e.g. a Monte-Carlo sampling of several cavities of various sizes, between which particles would be able to transfer within typical timescales. The multiple supershells could strongly modulate the resulting spectra. Several clusters could be included with imperfect temporal correlations, which is closer to realistic environments (for instance the Cygnus-X region hosts several clusters of ages ranging from about 3 to 8 Myr).

(3) Confronting the model with data (points *(vii)-(ix)*). The model discussed in the present work can be confronted to gamma-ray data as well as direct cosmic ray measurements near Earth. Indeed, the particles interacting with the dense supershell sur-

rounding the superbubble produce neutral pions which decay into gamma-ray radiation. While I only speculated at the end of Chapter 6 about the possible agreement of the model with the available gamma-ray data, a logical continuation of the present work is to perform a careful comparison of the model predictions and gamma-ray observations. This would require to adapt the model to the acceleration of electrons and to account for specific point-sources hosted in star-forming regions such as pulsar-wind nebulae. Eventually, not only this could be used to constrain the properties of the turbulence in the observed star forming regions, but also to account for the ultra-high energy emission recently detected in the Cygnus-X region by the LHAASO observatory (Cao et al., 2021), which strongly motivates to pursue the investigation of superbubbles and star forming regions as cosmic ray sources. We are looking forward to see the publication of more data.

Finally, the model can be confronted to the diffuse cosmic ray spectrum measured near Earth. Although I provided a first estimation of the superbubble contribution at the end of Chapter 6, a careful analysis must be performed using a realistic Monte-Carlo sampling implementing statistical data on superbubbles and clusters (e.g. Portegies Zwart et al., 2010; Krumholz et al., 2019). The modulation induced by the local supershell could also be accounted for using our two-zone model in order to confront the model predictions at low energies with Voyager data. Eventually, while we only considered the acceleration of protons, the model can further be adapted to compute the acceleration of heavier ions. Recent works on the composition of superbubbles (e.g. Tatischeff et al., 2021) could then be used to properly estimate the overall contribution of superbubbles to the galactic cosmic rays, deriving isotopic ratios (in particular the ^{22}Ne/^{20}Ne ratio) and the total cosmic ray spectrum expected to reach the Earth, at the end of the galactic journey, answering the very question which has been asked for more than a century on the origin of cosmic rays.

References

Abdollahi, S. et al. (Mar. 2020). "Fermi Large Area Telescope Fourth Source Catalog". In: ApJS 247.1, 33, p. 33. DOI: 10.3847/1538-4365/ab6bcb.

Abeysekara, A. U. et al. (Mar. 2021). "HAWC observations of the acceleration of very-high-energy cosmic rays in the Cygnus Cocoon". In: *Nature Astronomy*. DOI: 10.1038/s41550-021-01318-y.

Abramowski, A. et al. (Jan. 2012). "Discovery of extended VHE gamma-ray emission from the vicinity of the young massive stellar cluster Westerlund 1". In: A&A 537, A114, A114. DOI: 10.1051/0004-6361/201117928.

Aharonian, F. et al. (June 2007). "Detection of extended very-high-energy gamma-ray emission towards the young stellar cluster Westerlund 2". In: A&A 467.3, pp. 1075–1080. DOI: 10.1051/0004-6361:20066950.

Bykov, A. M. and Toptygin, I. N. (Oct. 1990). "Theory of charge particle acceleration by a shock wave ensemble in a turbulent medium". In: *Zhurnal Eksperimentalnoi i Teoreticheskoi Fiziki* 98, pp. 1255–1268.

Bykov, A. M. (Oct. 2001). "Particle Acceleration and Nonthermal Phenomena in Superbubbles". In: Space Sci. Rev. 99, pp. 317–326. DOI: 10.1023/A:1013817721725.

Cao, Z. et al. (May 2021). "Ultrahigh-energy photons up to 1.4 petaelectronvolts from 12 gamma-ray Galactic sources". In: *Nature*. ISSN: 1476-4687. DOI: 10.1038/s41586-021-03498-z.

Chevalier, R. A. and Clegg, A. W. (Sept. 1985). "Wind from a starburst galaxy nucleus". In: Nature 317.6032, pp. 44–45. DOI: 10.1038/317044a0.

Ferrand, G. and Marcowith, A. (Feb. 2010). "On the shape of the spectrum of cosmic rays accelerated inside superbubbles". In: A&A 510, A101, A101. DOI: 10.1051/0004-6361/200913520.

Higdon, J. C. and Lingenfelter, R. E. (Aug. 2005). "OB Associations, Supernova-generated Superbubbles, and the Source of Cosmic Rays". In: ApJ 628.2, pp. 738–749. DOI: 10.1086/430814.

Klepach, E. G., Ptuskin, V. S., and Zirakashvili, V. N. (May 2000). "Cosmic ray acceleration by multiple spherical shocks". In: *Astroparticle Physics* 13.2-3, pp. 161–172. DOI: 10.1016/S0927-6505(99)00108-5.

Krumholz, M. R., McKee, C. F., and Bland-Hawthorn, J. (Aug. 2019). "Star Clusters Across Cosmic Time". In: ARA&A 57, pp. 227–303. DOI: 10.1146/annurev-astro-091918-104430.

Morlino, G. et al. (Mar. 2021). "Particle acceleration in winds of star clusters". In: MNRAS. DOI: 10.1093/mnras/stab690.

Nava, L. et al. (Oct. 2016). "Non-linear diffusion of cosmic rays escaping from supernova remnants - I. The effect of neutrals". In: MNRAS 461.4, pp. 3552–3562. DOI: 10.1093/mnras/stw1592.

Parizot, E. et al. (Sept. 2004). "Superbubbles and energetic particles in the Galaxy. I. Collective effects of particle acceleration". In: A&A 424, pp. 747–760. DOI: 10.1051/0004-6361:20041269.

Portegies Zwart, S. F., McMillan, S. L. W., and Gieles, M. (Sept. 2010). "Young Massive Star Clusters". In: ARA&A 48, pp. 431–493. DOI: 10.1146/annurev-astro-081309-130834.

Tatischeff, V. et al. (June 2021). "The Origin of Galactic Cosmic Rays as Revealed by their Composition". In: *arXiv e-prints*, arXiv:2106.15581.

Résumé substantiel

Résumé chapitre par chapitre

Introduction : Les rayons cosmiques

Les rayons cosmiques, des particules chargées (protons, noyaux, électrons...) qui atteignent les hautes couches de l'atmosphère terrestre, sont détectés depuis plus d'un siècle. Leur origine reste cependant sujette à débat. On a longtemps pensé que les supernovae, explosions résultant de l'effondrement des étoiles massives, pouvaient représenter les sources principales via un mécanisme d'accélération par diffusion des particules autour des ondes de choc. Cependant, ce scénario est remis en cause depuis plusieurs années, en particulier parce qu'il ne parvient pas à expliquer les énergies gigantesques (PeV) atteintes par certaines particules. Les rayons cosmiques sont des acteurs de premier-plan dans l'écosystème galactique, en particulier car ils peuvent ioniser les nuages moléculaires et exciter la turbulence magnétique, régulant ainsi la dynamique des nuages moléculaires et la formation des étoiles. Pourtant, l'origine de ces particules reste un mystère et la plupart des rayonnements électromagnétiques associés, en particulier l'émission gamma de certaines régions de la galaxie, demeure mal comprise. D'un autre côté, on pense que la plupart des étoiles massives naissent et évoluent au sein d'amas stellaires. Au cours de leur vie, les amas émettent des vents qui creusent des bulles interstellaires. Ces bulles grossissent durant des millions d'années, sculptant les nuages moléculaires en des complexes contenant plusieurs cavités que l'on appelle des superbulles. Ces environnements sont caractérisés par un plasma chaud (10^6 K), raréfié et probablement très turbulent, balayé par de multiples ondes de choc. Cela en fait des milieux particulièrement favorables à l'accélération de particules. Le but de cette thèse est de modéliser la production de rayons cosmiques dans les superbulles.

Chapitre 1 – Les superbubbles : formation et évolution

On comprend globalement les phénomènes qui régissent la dynamique des bulles interstellaires et des superbulles, depuis l'effondrement des nuages moléculaires jusqu'à l'éclatement des cavités dans le halo galactique, en passant par la formation des amas stellaires, l'évolution des étoiles massives, les explosions de supernovae ainsi que l'expansion des bulles dans des milieux complexes. Bien que la plupart des observations puisse être qualitativement discutée, on manque toujours d'un modèle réaliste et prédictif des amas stellaires et des superbulles, et des déviations conséquentes entre les mesures et les résultats théoriques sont encore mal comprises.

Les superbulles sont régies par une forte interaction entre la thermodynamique des plasmas, leurs instabilités hydrodynamiques, la conduction thermique, les champs magnétiques et les particules énergétiques. La bulle gonfle car l'énergie mécanique des étoiles est

convertie en énergie thermique qui pousse la coquille dense entourant la cavité. Cependant les étoiles produisent également de la turbulence et des particules énergétiques, tandis que les propriétés du plasma chaud sont affectées par la conduction thermique, l'évaporation de la matière à la frontière de la bulle, le chauffage de poussières etc. Le milieu interstellaire, pressurisé et magnétisé, réagit contre la coquille, ce qui induit des instabilités, lesquelles modifient à nouveau les mécanismes internes. Tous ces processus sont intriqués dans plusieurs boucles non-linéaires. De plus, les superbulles que l'on observe par exemple dans la région d'Orion-Eridani ou du Cygne sont loin d'être de simples cavités sphériques, mais se présentent plutôt sous la forme de réseaux de cavités creusées au sein de nuages moléculaires denses et étendus que l'on associe à des nébuleuses abritant généralement plusieurs amas et sous-amas stellaires organisés hiérarchiquement. Même au sein d'un amas donné, les étoiles massives ne naissent pas exactement en même temps et les bulles interstellaires se forment séquentiellement autour des étoiles massives avant de fusionner successivement des petites aux grandes échelles. S'il est impossible de correctement modéliser la dynamique de ces régions analytiquement, les simulations numériques peinent à capturer avec précision toutes leurs caractéristiques. Etant donné cette complexité, il n'est pas surprenant que les modèles peinent à reproduire les observations, même si de nombreux progrès ont été réalisés dans les dernières décennies. En particulier, de plus en plus de bulles interstellaires sont détectées en rayons X mous dans notre galaxie ainsi que dans le Grand Nuage de Magellan et d'autres galaxies plus lointaines. Les travaux théoriques, numériques et observationnels des dernières décennies suggèrent notamment qu'une partie conséquente de l'énergie mécanique des étoiles pourrait être stockée dans la turbulence et les rayons cosmiques et non dans le plasma thermique.

Chapitre 2 – Rayons cosmiques et milieux turbulents

Le transport des particules chargées dans des milieux faiblement turbulents peut être décrit grâce à la théorique quasi-linéaire, qui consiste à supposer que les particules suivent les lignes du champ magnétique d'arrière-plan non turbulent. La fonction de distribution des particules est perturbée par les interactions répétées entre les particules et les perturbations hydromagnétiques, lesquelles isotropisent rapidement la distribution de particules, induisent une diffusion spatiale et réaccélèrent les particules. Des formules analytiques peuvent être obtenues dans le cas d'une turbulence unidimensionnelle. Bien que le transport perpendiculaire aux lignes de champ magnétique soit plus délicat à modéliser, il peut être décrit à partir d'argument heuristiques. La dynamique de la turbulence, et en particulier la réaction non-linéaire des particules sur les ondes hydromagnétiques, peut être incorporée dans ce cadre théorique. Les particules chargées peuvent exciter ou amortir la turbulence, selon l'énergie et le courant qu'elles transportent.

Chapitre 3 – L'accélération des particules dans des chocs

Ce chapitre passe brièvement en revue la théorie de l'accélération des particules par diffusion autour des ondes de choc. Les particules gagnent de l'énergie dans les inhomogénéités du plasma, et en particulier lorsqu'elles franchissent les discontinuités induites par les chocs. Le milieu étant turbulent, les particules diffusent de part et d'autre de la discontinuité et peuvent ainsi franchir le choc de nombreuses fois. La compétition entre le gain d'énergie et la probabilité qu'a une particule de se laisser définitivement entraîner par le plasma en aval du choc produit un spectre en loi de puissance, $f(p) \propto p^{-4}$ pour les chocs

forts. Des énergies de l'ordre du PeV ne peuvent être atteintes dans ces systèmes que si les niveaux de turbulence sont importants, auquel cas les particules sont efficacement confinées près des chocs et gagnent de l'énergie rapidement. Des niveaux de turbulence élevés sont en effet attendus si le champ magnétique est amplifié en amont du choc, ce qui peut être dû à des instabilités déclenchées par les particules elles-mêmes. Quand la réaction des particules sur le choc est prise en compte, les spectres prennent une forme concave et la plupart de l'énergie s'échappe en amont.

L'équation de transport des particules en présence d'inhomogénéités ainsi que les équations de conservation du fluide fournissent un cadre théorique permettant de réaliser des calculs semi-analytiques dans de nombreuses configurations. En particulier, une fois que la solution pour une injection monochromatique est calculée, la réaccélération d'une distribution de particules préexistant à l'expansion d'un choc peut être calculée à son tour, ce qui est utile en particulier pour modéliser la réaccélération des particules confinées au sein de superbulles.

Chapitre 4 – L'accélération des particules dans des collisions de chocs

Dans une tentative de résoudre analytiquement le problème non stationnaire de l'accélération des particules dans une collision entre chocs, nous concluons que le spectre des particules accélérées est très proche de la solution canonique p^{-4} obtenue en considérant un choc isolé, à l'exception d'une faible déviation aux hautes énergies. Le formalisme mathématique développé dans ce chapitre est cependant très général et notre approche peut être utilisée pour résoudre de nombreux problèmes similaires. Cela s'applique notamment à la réaccélération de particules préexistantes. Sous certaines conditions, des spécificités spectrales comme un durcissement du spectre peuvent apparaître aux hautes énergies.

Chapitre 5 – L'accélération des particules par de multiples chocs

Au moyen de calculs semi-analytiques, nous considérons le problème de la réaccélération non-linéaire des particules par une succession de chocs. La présence de particules préexistantes en amont des chocs modifie fortement la structure hydrodynamique du plasma, de telle sorte que l'accélération des particules devient moins efficace. Les spectres résultants peuvent être mous, durs ou concaves selon la distribution des particules préexistantes. Lorsque l'on considère de nombreuses réaccélérations successives, le spectre des rayons cosmiques converge vers une solution quasi universelle qui diffère grandement de celle prédite par la théorie linéaire. Ceci n'est pas surprenant étant donné qu'après le passage de quelques chocs la pression des particules devient similaire à la pression hydrodynamique, et ce quelle que soit l'efficacité d'injection des particules. La solution asymptotique est concave avec un indice spectral autour de 3.5 à l'énergie maximale. Nous avons également pris en compte l'évolution des propriétés du milieu au fur et à mesure que les chocs le balayent, soit en supposant que la densité est constante et que la température augmente, soit en considérant une température constante et en supposant que la densité diminue, ce qui se rapproche d'un modèle de superbulle. Nous avons finalement montré que si l'échappement des particules entre le passage de deux chocs est pris en compte, la solution asymptotique n'est que partiellement réalisée.

Chapitre 6 – La production de rayons cosmiques dans les superbulles

Nous utilisons un modèle auto-consistant de superbulle prenant en compte tous les ingrédients pertinents afin de calculer l'accélération des protons. Nous prenons notamment en compte l'évolution dynamique de l'environnement, les vents stellaires, les pertes et la coquille dense qui entoure la cavité. Nous incluons également la réaction non-linéaire des particules sur la turbulence ainsi que sur les chocs. Nous concluons que les particules sont accélérées efficacement, soit directement via les ondes de choc, soit indirectement via la turbulence. Les rayons cosmiques confinés dans les superbulles représentent une densité d'énergie conséquente, d'autant plus en présence d'une coquille qui ralentit l'échappement des particules. Lorsque le confinement est peu important, les spectres sont intermittents. Une bosse due à la réaccélération stochastique dans la turbulence apparaît aux énergies intermédiaires tandis que les hautes énergies sont caractérisées par une loi de puissance plutôt molle. L'émission diffuse résultante se comporte comme $E^{-2.2}$, ce qui est proche de ce que l'on attend pour expliquer le spectre des rayons cosmiques observé sur Terre. Lorsque le confinement est plus efficace, les spectres durcissent, produisant des signatures gammas en E^{-2} voire même de faibles concavités avec des composantes dures ($E^{-1.8}$) aux hautes énergies. La variabilité des spectres apporte une réponse simple au problème posé par les écarts conséquents reportés entre les différentes observations réalisées en rayons gamma. En effet, plusieurs superbulles ne sont pas détectées en rayons gamma, comme la superbulle d'Orion-Eridani ou la nébuleuse de la Rosette, d'autres présentent des spectres en lois de puissance plutôt molles, comme la région du Cygne, ou plutôt dures, comme les régions Westerlund 1 et 2 ainsi que G25. Les signatures gamma d'une superbulle peuvent ainsi être utilisées pour contraindre les propriétés d'un amas d'étoiles et du milieu environnant, en particulier le spectre et l'intensité de la turbulence.

Bilan général

Les rayons cosmiques galactiques sont en toute probabilité produits, soit directement soit indirectement, par l'activité des étoiles massives. Il est donc naturel de penser que ces particules sont accélérées dans les environnements où les étoiles massives se forment et évoluent. Dans les régions de formation d'étoiles, les amas stellaires creusent des superbulles caractérisées par un milieu chaud, ionisé et turbulent balayé par de nombreux chocs (Chapitre 1). Ces environnements sont des sites favorables d'accélération de particules. Afin d'interpréter les récentes observations en rayons gamma, nous devons développer des modèles théoriques des mécanismes de production des rayons cosmiques dans les superbulles. Ceci est le but principal de cette thèse.

Après avoir passé en revue les théories fondamentales décrivant l'accélération et le transport des particules dans la turbulence (Chapitre 2) et autour des ondes de chocs (Chapitre 3), j'ai montré comment les mécanismes d'accélération peuvent différer au sein de cavités raréfiées et turbulentes abritant des centaines d'étoiles massives. Tout d'abord, des chocs peuvent entrer en collision au sein de superbulles. Cela peut arriver lorsque deux vents interagissent, ou lorsqu'une supernova se propage jusqu'au choc terminal entretenu par les vents autour de l'amas, ou encore lorsque deux supernovae explosent quasi simultanément. Lorsque deux chocs convergent l'un vers l'autre, la dépendance temporelle du système doit être prise en compte, ce qui est décrit dans le Chapitre 4. J'ai conclu que l'accélération des particules lors d'une collision entre deux chocs ne présentait pas de par-

ticularité réellement notable par rapport au cas d'un choc isolé, car les particules ne sont capables de se propager d'un choc à l'autre que lors des derniers instants de la collision. Cependant, si des particules ont été préaccélérées avant la collision et sont restées dans la région, ce qui peut être le cas dans les superbulles, un durcissement prononcé du spectre peut apparaître aux hautes énergies. Un tel durcissement, avec une solution asymptotique théorique en p^{-3}, est une caractéristique générale de l'accélération des particules par des chocs multiples. De tels mécanismes ne se limitent pas à l'interaction de vents stellaires ou à la collision de supernovae, mais incluent également la turbulence supersonique, qui décrit un ensemble de chocs stochastiques, ainsi que l'accélération de particules par des chocs balayant successivement le milieu. Dans ce cas, l'énergie des particules atteint rapidement celle des chocs, de sorte que l'influence des particules sur les chocs doit être prise en compte et le modèle devient non-linéaire. Le Chapitre 5 a eu précisément pour but de développer un modèle d'accélération des particules par chocs successifs dans le régime non-linéaire, en prenant correctement en compte le développement d'un précurseur en amont du choc, dû à la pression des rayons cosmiques ralentissant le fluide. De manière remarquable, il est apparu que les spectres convergent après le passage de quelques chocs vers une solution concave quasiment universelle. Ce modèle de réaccélération a ensuite été appliqué à une superbulle réaliste en prenant en compte l'évolution dynamique de l'environnement (Chapitre 6). Bien que les superbulles soient des environnements complexes dont la description nécessite l'introduction de nombreux paramètres, les théories hydrodynamiques, thermodynamiques, ainsi que les simulations numériques et les observations en diverses longueurs d'onde permettent de contraindre la plupart des variables. Certains paramètres comme le nombre d'étoiles massives présentes dans l'amas stellaire, la densité du milieu interstellaire et les propriétés de la turbulence magnétique, peuvent varier d'une source à l'autre. En supposant des valeurs typiques pour ces paramètres, j'ai analysé l'accélération des rayons cosmiques dans les superbulles en utilisant un modèle semi-analytique qui inclut les processus physiques les plus pertinents. Les rayons cosmiques sont d'abord accélérés dans les chocs, puis réaccélérés à des énergies de l'ordre du GeV tandis qu'elles se propagent dans la superbubble, jusqu'à s'échapper au-delà de la coquille entourant la cavité. Cette dynamique se traduit par une bosse dans le spectre des rayons cosmiques au niveau des faibles énergies. Aux plus hautes énergies, les spectres moyens sont plutôt raides, sauf si le confinement des particules est accru, ce qui se produit dans les amas très massifs et compacts, ou en présence d'une coquille magnétisée autour de la cavité. Dans ce cas, les particules sont efficacement réaccélérées, ce qui produit un durcissement du spectre des rayons cosmiques.

Le transfert d'énergie entre les étoiles massives et les particules, qu'il soit induit directement par l'accélération autour des chocs ou indirectement dans la turbulence hydromagnétique, est généralement efficace. Dans les superbulles, la densité énergétique des rayons cosmiques peut atteindre des niveaux très importants ($1 - 10^3$ eV/cm^3) et la réaction des particules sur les chocs et sur la turbulence doit être prise en compte. J'ai ainsi développé le premier modèle auto-consistant d'accélération de particules dans des superbulles évoluées, qui vise à compléter les travaux de Bykov et collaborateurs. Les spectres des protons, intermittents et variables d'une source à l'autre, produisent différentes classes de spectres de rayons gamma en accord qualitatif avec les observations réalisées au cours de la dernière décennie. Enfin, en obtenant une première estimation de la contribution globale des superbulles au spectre des rayons cosmiques, j'ai montré que ces sources peuvent en effet reproduire le flux mesuré autour de la Terre. Cela encourage la poursuite de ce travail de modélisation des superbulles et régions de formation d'étoiles

en tant qu'accélérateurs de particules, dans le but de résoudre le mystère de l'origine des rayons cosmiques.